The Dissertation Committee for Ran Chen Certifies that this is the approved version of the following dissertation:

GROUNDWATER INFLOW INTO ROCK TUNNELS

Committee:

Fulvio Tonon, Supervisor

Peter Eichhubl

Ellen Rathje

John M. Sharp

Jorge G. Zornberg

GROUNDWATER INFLOW INTO ROCK TUNNELS

by

Ran Chen, B.E.; M.E.

Dissertation

Presented to the Faculty of the Graduate School of

The University of Texas at Austin

in Partial Fulfillment

of the Requirements

for the Degree of

DOCTOR OF PHILOSOPHY

The University of Texas at Austin

August 2010

Acknowledgements

First, I would like to thank Dr. Tonon, Eichhubl, Rathje, Sharp, and Zornberg for serving on my doctoral committee.

Most ideas contained in this document originated during conversations with Dr. Tonon, whose knowledge and experience in rock fractures and water inflow are the foundations of this work. Thank you also for being a friend and for offering your continued support throughout my time at UT. Thanks to Dr. Sharp, too, for questioning some aspects of natural fracture systems during my comprehensive exam and guiding me to study more references. Thanks to Dr. Marret for helping me understand fracture spatial characterization, providing me with several papers and sharing fracture data at Pedernales Fall State Park. Thanks to Dr. Srinivasan for instructive discussions on fracture simulation during his course. Thanks to Dr. Eichhubl and Dr. Laubach for sharing their group discussion with me. Thanks to Dr. Zornberg and Dr. Rathje for critical questioning me during my qualifying and comprehensive exams and giving many ideas and suggestions.

I would also like to thank a number of people who provided technical support or shared their ideas and experiences. Thanks are due to my fellow graduate students: Seung Han Kim, Sang Yeo Seo, and Xiaomin You for questioning me and providing ideas during group meetings; John Hooker for fracture discussions and thin sections work; Heejung Youn for rock testing; and Pooyan Asadollahi and Yuannian Wang for programming and course study.

This work was financed by the International Tunneling Consortium (ITC). Thanks are due to all members of ITC. Additional thanks to J. F. Shea Company for providing

me with an internship in the summer of 2009 to collect data. Research data (fracture maps, water flow data and geotechnical information) were provided by Cobb County (GA) and Caltrans.

Most importantly, thanks are due to my most important partner, my wife Xinyi, who provided an unbounded quantity of help and moral support that saw me through to the end of what has been a long and winding road. Thanks also to my parents and parents-in-law for helping us take care of our son Daniel in our hard time.

Groundwater Inflow into Rock Tunnels

Publication No._____

Ran Chen, Ph.D.

The University of Texas at Austin, 2010

Supervisor: Fulvio Tonon

Prediction of groundwater inflow into rock tunnels is one of the essential tasks of tunnel engineering. Currently, most of the methods used in the industry are typically based on continuum models, whether analytical, semi-empirical, or numerical. As a consequence, a regular flow along the tunnel is commonly predicted. There are also some discrete fracture network methods based on a discontinous model, which typically yield regular flow or random flow along the tunnel. However, I observed that in hard rock tunnels, flow usually concentrates in some areas, leaving much of the tunnel dry. The reason for this is that, in hard rock, most of the water flows in rock fractures; fractures typically occur in a clustered pattern rather than in a regular or random pattern. I develop a new method in this work that can model the fracture clustering and reproduce the flow concentration. After an elaborate literature review, a new algorithm is developed to simulate fractures with clustering properties by using geostatistics. Next, I discuss a discrete fracture network that was built and simplified. In order to solve the flow problem in the discrete fracture network, an existing analytical-numercial method must be improved. Two case studies illustrate the procedure of fracture simulation. Several ideal

tunnel cases and one real tunnel project are used to validate the flow analysis. I determine that fracture clustering can be modeled and flow concentration reproduced by using the proposed technique.

Table of Contents

List of Tables

List of Figures

INTRODUCTION

Groundwater inflow into rock tunnels has been an extensive research topic in tunnel engineering for the last half century. Since Goodman et al. (1965) introduced groundwater mechanics into tunneling to predict the tunnel water inflow analytically and carried out some model tests, many researchers and engineers produced a large amount of work and developed many methods to compute or predict the water inflow into tunnels. Most of these methods are analytical and are easily understood and applied. Heuer (1995) developed a practical semi-empirical method to predict water inflow into tunnels by using empirical graphs, an analytical approach corrected by applying empirical coefficients. It is the most widely-used method in the current tunnel industry. However, analytical solutions can only be obtained under many assumptions, including material properties, flow states, and boundary conditions. Relaxation of any assumption will lead to an inconceivably complicated solution or, worse, no analytical solution. Numercial methods based on the continous assumption were first used to solve groundwater flow into tunnels in the early 1970s. Many problems, such as tunnels in layered ground, with complicated boundary shapes and under time-dependent total head, can currently be easily solved with the available computational procedure.

In hard rock, most of the water flows along fractures. Continuum models may not apply in this kind of material. Therefore, discontinous models were adopted to represent the fractured rock media. Snow (1969) first developed one discrete model in which the fracture network was represented by three orthogonal families of infinite planes, with constant or random spacings. After that, more than a dozen discrete fracture network models were developed that combined different rock fracture properties. Two of the most

widely used models are the Beacher model (1977) and the Dershowitz model (1988). The latter gradually grew into the commercial software FracMan (by Golder Associates Inc.).

Recently, Raymer (2005) stated that "[In hard rock tunnels], *most of the inflow occurs in a few places, some of the inflow occurs in many places, and much of the tunnel is dry*". The reason for this is that, in hard rock, water only flows in connected fractures; because these fractures are clustered, water inflow typically concentrates in the fracture cluster zones. This phenomenon cannot be modeled by any continous model, whether analytical or numerical, and may be not reproduced by some discontinous models if actual rock fractures are clustered and these models are not able to appropriately simulate clustering.

Therefore, in this research, I propose and develop a new approach that models the fracture clustering and reproduces the flow concentration. With this aim in mind, the first two chapters review and summarize most of the literature in groundwater inflow into tunnels and in rock fractures. In Chapter 3, a proposed fracture simulation algorithm is given, starting from its theoretical background and followed by two cases studies. The discrete fracture network generation and flow analysis are described in Chapter 4. In the last chapter, the developed simulation methods are applied to some ideal tunnel cases and one real tunnel project. Conclusions and suggestions for future work are also included in this chapter.

CHAPTER 1: FRACTURE PROPERTIES INFLUENCING FLUID FLOW IN FRACTURED ROCK

In this section, rock fracture characterizations are described, including orientation, size distribution and fracture spatial arrangement.

1.1 Definitions and approaches to fracture detection

According to the definition given by Priest (1993), "a discontinuity is here defined as any significant mechanical break or fracture of negligible tensile strength in a rock." "The term discontinuity makes no distinctions concerning the age, geometry or mode of origin of the feature." "The decision as to whether a particular mechanical break is 'significant' must be made subjectively on the basis of specific knowledge of a particular site and in the context of the proposed engineering activity. This requirement generally places a lower limit of between 1 and 100mm on discontinuity size and excluded such features as pore spaces, micro-cracks and cleavage planes in crystals; such features are here regarded as part of the rock material."

However, from a geological perspective, a range of terms have been adopted to describe discontinuities. These terms include faults (Price, 1966), "obvious signs of differential movement of the rock mass on either side of the plane"; joints, "cracks and fractures in rock along which there has been extremely little or no movement"; as well as bedding, cleavage, fissure and other features.

In this chapter, the term "fracture" is used as an analogical definition to the geology term "discontinuity," but they are not completely the same. In this chapter, "fracture" is defined as all natural cracks in the rock, including not only joints and faults, but also macrofracture and microfractures, no matter whether it has been closed or not.

Here the definition of microfracture is (Laubach, 1997): macrofracture is the fracture visible with the unaided eyes, whereas microfracture is the fracture which is smaller than those are visible with the unaided eyes.

This chapter is structured as follows: Section 1.1.1 gives an overview of the fracture properties, their definitions and detection approaches. In Section 1.2, orientation sampling and distribution are summarized, followed by a description of micro- and macro- fracture orientation. Several distributions for fracture size are detailed first in Section 1.3, followed by length, displacement/throw/heave/aperture, spacing, length-aperture relationship and sampling bias, which are each introduced individually. In the last section, the characterization of fracture spatial arrangement is summarized according to traditional methods and recent research.

1.1.1 OVERVIEW OF FRACTURE PROPERTIES AND THEIR DEFINITIONS

The fracture properties that have the greatest influence to the fluid flow in fractured rock are listed as follows:

1.1.1.1 Orientation

Orientation of a fracture can be presented by its strike and dip angle or dip direction and dip angle. It can also be expressed by the normal direction of the fracture. Graphically, one of the simplest forms of representation is the rose diagram (Attewell and Farmer, 1976; Cawsey, 1977). However, the disadvantage of rose diagrams is that they contain no information on dip angle. The other technique used to represent three-dimensional orientation is stereographic or hemispherical projection (Duncan, 1981; Phillips, 1971). A plane can be represented by a curve in hemispherical projection, and a line can be represented by a point in it. Typically, all fractures in one set are assumed to be parallel, although they are not in reality.

1.1.1.2 Size distribution (shape, length/diameter/height, aperture/displacement)

To describe the geometry of an individual fracture, shape and length/diameter/height and displacement/throw/heave/aperture are needed. Size is one of the most difficult properties of a fracture to measure accurately, because only by completely dismantling a given rock mass is it possible to trace and to measure the complete area of each fracture. This has never been done satisfactorily for a rock mass (Priest, 1993). Circular discs, ellipses, squares, rectangles and polygons all can be assumed as the fracture shape. Sampling difficulties have so far made it impossible to prove or disprove any hypothesis of the fracture shape. Disc or rectangle hypotheses are commonly used because of their easy expression. Because of special boundary conditions, sometimes fractures are assumed to be an infinite plane; blade-like, slot-like or penny-shaped.

In regard to fractures, one direction is always considered much shorter than the other two. Length or diameter or height is often used to describe its dimension in those two larger directions. Which parameter is going to be used, length or diameter or height, depends on what kind of shape the fracture is. In fracture measurements, the trace length, which is the intersection of fracture and observational surface, is often measured instead of the true length. Stereology allows one to reconstruct the fracture size distribution from the trace distribution (Warburton, 1980b, Tonon and Chen, 2007). Displacement or throw or heave is typically used in faults or shear-mode fracture and aperture is used in open-mode fracture. Similarly, displacement or throw or heave or aperture is often measured on an observational surface in which case maximum value can be obtained or just one value along a line, such as scanline or borehole.

1.1.1.3 Frequency, spacing and intensity

As for the quantitative distribution of fractures, frequency, spacing and intensity are the fundamental measures of the degree of fracturing in a rock mass.

Frequency can be expressed in terms of the number of fractures that are observed or are predicted to occur in a unit volume, a unit area or a unit length of a sample from a given rock mass. Volumetric frequency is the most fundamental of these three fracture frequencies, because it is orientation independent. If the occurrence of a fracture in a rock mass can be represented by the occurrence of a point located at the centroid on the fracture, the volumetric frequency is the average number of these points per unit volume of rock sample. Because of generally impractical volumetric frequency measurements, in most cases volumetric frequency is estimated from measurements of areal or linear frequency taken at exposed planar rock faces. Since many rock exposures are planar, or very nearly so, it is often feasible to express the frequency of fractures in terms of their areal frequency. Similarly, the occurrence of each fracture on an exposed face can be represented by the mid-point of its trace. The areal frequency is the average number of these points per unit area of the exposure. In addition, the simplest, and most commonly used, measure of fracture frequency is the linear frequency, defined as the average number of fractures intersected by a unit length of sampling line. However, the resulting values of areal and linear frequency are biased by the orientation of the sampling plane or line. More details about bias and artifacts in sampling are shown in the following section.

Spacing, the average fracture-to-fracture distance along the fracture normal direction, is how the degree of fracturing is typically described for opening fractures (Narr and Suppe, 1991). Commonly, apparent spacings can be measured along the borehole or the scanline on the outcrop. Apparent spacings can be corrected to true spacing by a certain correct factor that is related to the angle between scanline (or borehole) and the normal of fractures (Priest, 1993, page 122). The average spacing can be calculated by dividing the total length of scanline (or borehole) by the total number (N) of fracture spacings.

Intensity has units of inverse length (L^{-1}) and is a ratio of the number of fractures, the sum of fracture lengths, the sum of fracture surface areas to the length, area, or the

volume of observation, respectively (Mauldon et al., 2001). For one-dimensional observation domains (i.e., scanline or borehole), fracture intensity has the same value as frequency.

Dershowitz and Herda (1992) extend the traditional fracture spacing and intensity measures to a class of fracture intensity measures in one, two and three dimensions without requiring reference to specific sets or orientations.

1.1.1.4 Spatial arrangement

Gomez and Marrett (Gomez and Marrett, written communication) define spatial arrangement of fractures this way: how fractures are positioned relative to one another in space, where each set groups all fractures with common characteristics (e.g., orientation and cement fill) and genesis. The notion of spatial arrangement refers to the presence, or absence, of patterns in fracture position in space. Fracture position along a scanline is obtained by combining the spacing between nearest-neighbor fractures and the sequence of spacings. La Pointe (1993) summarizes several methods for reconstructing a fractured rock mass from limited pattern descriptors and observations for fluid flow. Gomez and Marrett (written communication) summarize the traditional analyses of fracture arrangement in space; Hare and Marrett (written communication) develop the spectral analysis of fracture arrangement; and Marrett et al. (written communication) develop the correlation analyses of fracture arrangement.

1.1.1.5 Cementation (Filling)

Cementation is the process of deposition of dissolved mineral components in the interstices of sediments. Cementing materials may include silica, carbonates, iron oxides, or clay minerals. Cementation occurs in fissures or other openings of existing rocks in the groundwater zone and is a dynamic process more or less in equilibrium with a dissolution or dissolving process. Degree of fracture pore-space preservation in large fractures is one essential ingredient of permeable fracture networks.

According to Laubach et al. (1995), cementation can be classified as synkinematic and postkinematic. Synkinematic cementation occludes fracture porosity during the fracture growth, while postkinematic cementation of extension fractures occludes fracture porosity after cessation of fracture growth.

1.1.2 APPROACHES TO FRACTURE DETECTION

1.1.2.1 Natural fracture systems

There are two distinct natural fracture systems that can be identified in the field (e.g., outcrops, boreholes, excavation planes): shear-mode fractures (faults) and open-mode fractures. Open-mode fractures can be subdivided as veins and joints.

In some cases, faults (shear-mode fractures) are often recognized only in outcrops and not in cores (Ortega and Marrett, 2000). Shear fractures are commonly rectilinear and consist of two mutually crosscutting sets of conjugate strike-slip faults forming acute angles of 70° to 25°. The shear fractures are characterized by the presence of cataclasite.

Veins (open-mode mineralized fractures) often show sinuous traces and are typically grouped in swarms. Hooked vein connections between fractures suggest open-mode propagation under nearly isotropic remote stresses (Olson, 1993).

Joints are open-mode fractures interpreted to be associated with the release of confining pressure and/or the changes in temperature.

1.1.2.2 Fracture detection methods

As the sampling dimension is considered, there are one-, two- and three-dimensional fracture sampling methods. Because of the property of natural rock and fracture, it is very difficult to get three-dimensional sampling information accurately. One-dimensional samplings (e.g., scanlines in outcrops or thin sections, sections in geological maps, boreholes) and two-dimensional samplings (e.g., outcrops, excavation

planes, thin sections, cross section of seismic reflection) are the most common methods used to observe fractures.

As the sampling scale is considered, there are macro- and micro- scale measurements. Macro-scale method includes seismic reflection, air photos, geological maps, outcrops, excavation planes (e.g., tunnels, slopes), cores, image logs, etc. Micro-scale method only includes thin section observation, which can be a petrographic or Scanning Electron Microscope (SEM) image. More details are stated in the following part of this section.

1.1.2.2.1 Macrofactures

Macrofractures in the surface and subsurface can be detected by various means, ranging from simple extrapolation of surface observation to sophisticated seismic and electromagnetic soundings. The Committee on Fracture Characterization and Fluid Flow (1996) provides a general overview of geophysical fracture detection methods, as shown in Table 1.1.

Table 1.1 Macrofacture detection methods (From the Committee on Fracture Characterization and Fluid Flow, 1996)

Method	Length Scale of Investigation and Resolution	Remarks
Differential methods	0.1–5,000 m	Most of the methods below best detect actual flow if performed both before and after a known stimulus.
Elastic methods: seismic band (10-100 Hz)	100–5,000 m	Zero shear modulus in fracture fluid is critical.
P-wave reflection (2D)	[1–2 λ (velocity)][a] [1/4 λ (amplitude)]	Surface methods best detect horizontal fractures; fracture shape is critical.
P-wave reflection (3D)	[1–2 λ (velocity)] [1/8 λ (amplitude)]	Very subtle features recognizable in patterns.
S-wave reflection (2D)	[1–2 λ (velocity)] [1/4 λ (amplitude)]	Surface methods best detect vertical aligned fractures.
P-wave vertical seismic orofiling (VSP) (including offset, reverse)	[<1 λ (velocity)]	Minimizes overburden difficulties; fractures cause tube waves.
S-wave 3C vertical seismic profiling (VSP)	[< 1 λ (velocity)]	Minimizes overburden difficulties.
P-wave tomography	10–100 m [1/2 λ (velocity)]	Zero shear modulus in fracture fluid is critical.
Cross-hole reflections	10–100 m [1/2 λ (velocity)]	Zero shear modulus in fracture fluid is critical.
Coupled methods	100–5,000 m [< 1 λ (velocity)]	Iteration of reflection and transmission inversion steps.

Table 1.1 (continued)

Elastic methods: sonic band (2-20 kHz)	0.1–10 m	Zero shear modulus in fracture fluid is critical.
P-wave transmission (acoustic Log, 1D)	[1–2 λ (velocity)] [1–2 λ (amplitude)]	Best detects fractures oriented transverse to rays.
Acoustic waveform Log, *P* and *S*	[1–2 λ (velocity)] [1–2 λ (amplitude)]	Best detects fractures oriented transverse to rays.
Acoustic emissions	10–100 m [1–10 m]	Emissions accompany fracture growth (e.g., during hydrofrac pumping operations).
Elastic methods: ultrasonic band (200-2,000 kHz)	0.1–5 m	Fracture aperture is critical.
Borehole televiewer	10–30 cm [0.3–5 cm]	Detects fractures in boreholes.
Electrical methods	10–300 m	Contrasting resistivity of fracture-filling fluid is critical.
Electric sounding	[1–10 m]	Best detects horizontal fractured zones.
Electric profiling	[1–10 m]	Best detects vertical or dipping fractured zones.
Electric resistivity tomography	[1–10 m]	Still under development.
Formation microscanner (FMS)	[0.1–3 cm]	Best detects open fractures.
Electromagnetic methods	[10–300 m]	Contrasting resistivity of fracture-filling fluid is critical.
Electromagnetic sounding	[3–10 m]	Best detects horizontal fractured zones.
Electromagnetic profiling	[3–10 m]	Best detects vertical or dipping fractured zones.
Electromagnetic tomography	[3–10 m]	Best detects conductive anomalies, like fluid-filled fractures.
Radar methods	3–100 m	Contrasting resistivity of fracture-filling fluid is critical.
Ground-penetrating radar (reflection)	[0.1–5 m]	Conductive overburden presents difficulties, limits penetration.
Borehole radar (reflection)	[1–5 m]	Determines both location and orientation from a single borehole.
Radar tomography (transmission)	[2–10 m]	May be used to image velocity, attenuation, or differences over time.
Conventional well logs	0.1-10 m	Near-borehole environment.
Neutron log	[0.1 m]	Detects clay and porosity in fracture washouts.
Resistivity log	[0.1 m]	Detects clay in fractures and washouts.
Density log	[0.1 m]	Detects clay in fractures and washouts.
Gamma ray log	[0.1 m]	Detects radioactive fillers, rock-type identification.
Caliber log	[0.01 m]	Detects borehole enlargement.
Temperature log	[0.01 m]	Detects temperature changes owing to flow in fracture system.
Fluid conductivity log	[0.01 m]	Detects salinity changes owing to flow in fracture system.
Fluid replacement log	1–100 m [1–10 m]	Detects salinity changes owing to flow in fracture system.
Geological observation	0.1–500 km	Surface lineations, structures, etc., may indicate fractures at depth.
Satellite airborne imaging	1–500 km [1–100 m]	Direct observation of lineaments and inference of fractures from geological structures.
Core inspection	[0.1–10 cm]	Core may not be representative.
Optical imaging	[0.1–10 cm]	Borehole fluid must be clear.
Tiltmeter methods	100–2,000 m	Expansion of fracture by hydrofrac pumping operations is critical.
Flowmeters	1–100 m	Directly detects fracture flow.
Heat-pulse flowmeter	[1–10 m]	Directly detects fracture flow.
Electromagnetic flowmeter	[1–10 m]	Still under development.
Acoustic doppler flowmeter	[1–10 m]	Still under development.

[a]λ is the wavelength of seismic or sonic energy.

It is worth noting that, in Table 1.1, geological observation not only includes satellite airborne imaging and core inspection, but also the observation in outcrops (e.g.,

road cuts or river cuts) and excavation planes (e.g., tunnels), which are commonly used by geologists and civil engineers. In this research, observation in outcrops and tunnels are the main methods employed to detect the macrofractures. One-dimensional detection can be done along the scanline in the outcrop or the tunnel wall, whereas two-dimensional detection is implemented in a certain surface domain of the outcrop or the tunnel wall.

1.1.2.2.2 Microfactures

The methodologies to image microfractures include: random photomicrographs throughout the thin section, systematic transects in predefined orientations and/or mosaics covering small portions of the thin section. Standard operating procedures are described by Milliken (1994). As for microfractures, the petrography microscope and the Scanning Electron Microscope (SEM) are the two most common techniques. Microfracture data can be collected from thin sections that come from subsurface or surface oriented samples.

The first step in microfracture analysis is the preparation of suitable samples and subsequent thin sections. Based on the observations of Laubach (1997) and Marrett et al. (1999), we may assume in many cases that microfractures that are in the same set as macrofractures have many similar properties (orientation, degree of cementation, fracture history, etc.) to macrofractures, and micro- and macro- fractures together follow certain predictable distributions in length, aperture/displacement and spacing. Therefore, thin sections can be cut parallel to stratification, providing microscopic views comparable to two-dimensional macroscopic outcrops.

The second step is to image the rock. For many applications, it involves collecting images at a high magnification then stitching the images together into a mosaic. According to different fracture cementation, mineral composition, a petrography microscope and/or the scanning electron microscope (SEM) are often used to observe microfractures.

1.1.2.2.2.1 Petrographic image

In some rocks, cement-filled microfractures are readily visible using transmitted-light microscopy (as Figure 1.1).

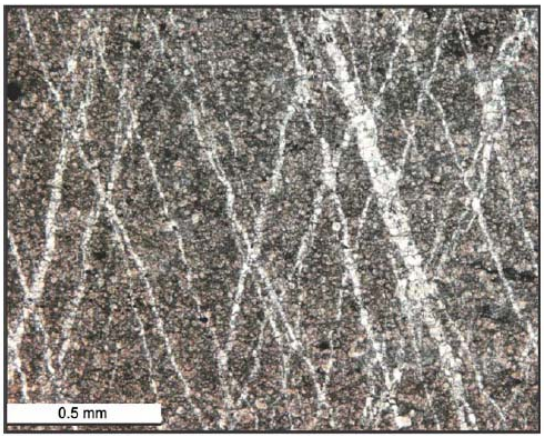

Figure 1.1 Transmitted-light image of microfractures (from Gomez and Laubach, 2006)

We can use petrographic microscopes and a digital camera to generate mosaic images. A graduated mechanical stage can be used to make controlling the position of the thin section easier, facilitating alignment and proper overlap of individual images for image stitching. Image collection using petrographic microscopes could be automated. A digital or paper copy of an entire individual thin-section image helps register features on adjacent thin sections.

1.1.2.2.2.2 SEM and SEM-CL image

In the last twenty years, many researchers have used a scanning electron microscope (SEM) to observe microfractures in the rock. The use of SEM allowed observation of microfractures not readily visible using conventional microscopic techniques (Laubach, 1997). For instance, quartz-lined opening-mode microfractures (lengths of microns to millimeters) in quartz-cemented sandstones commonly are not visible using standard petrographic methods, but systematic mapping of these microfractures is possible using photomultiplier-based electron beam-induced luminescence (scanned cathodoluminescence) imaging when microfracture data are

collected systematically from small areas of a thin section (Laubach, 1997; Laubach and Milliken, 1996).

It is difficult for conventional optical cold-cathode luminescence stages with fixed-position electron beams to obtain high-quality images of quartz because of low light emission. In contrast, cathodoluminescence imaging in an SEM (SEM-CL) reveals subtle compositional and defect variations in silicate minerals. SEM-mounted collectors and detection systems can collect the low levels of light available to produce high-resolution (~100 nm) images; they can also distinguish detrital quartz and subsequently precipitated authigenic quartz at the micron scale (Laubach, 1997). The thin sections are polished with aluminum and covered with a carbon coating (dark blue degree) for study under the SEM-CL. Owing to the stable observing conditions, high magnifications, and sensitive light detection that characterize this detection method, SEM-CL permits rapid collection of images having a higher resolution than those of conventional light-microscope systems.

SEM/SEM-CL imaging of microfractures is a useful structural technique because microfracture strike, length, maximum mechanical aperture and crosscutting relations can be discerned in the photographs (Ortega, 1997). An SEM-CL image of microfractures is shown as Figure 1.2.

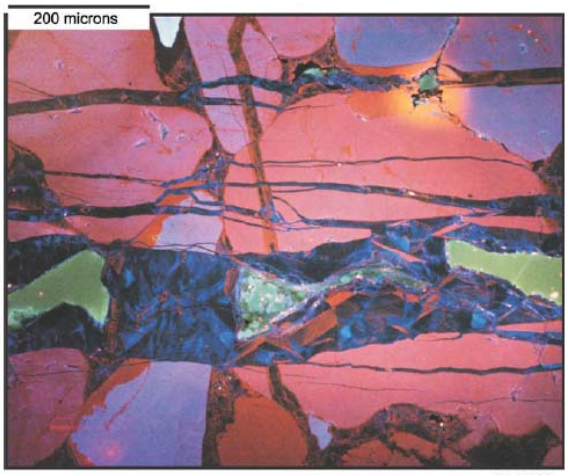

Figure 1.2 SEM-CL image of microfractures (from Gomez and Laubach, 2006)

However, sometimes SEM-CL cannot illuminate the details of microfracture morphology necessary to classify microfractures. For example, the presence of highly luminescent minerals in the rock (e.g., quartz) adversely affects image quality. Also, the recognition of microfracture continuity is complicated by difficulties in distinguishing certain segments of microfractures.

SEM/SEM-CL detectors image only small sample areas relative to fracture-population patterns, and the effort required to image a representative area of the sample at these magnifications impedes the use of microfractures. Image collection and stage-control-automation software for SEMs helps remove this impediment.

Gomez and Laubach (Gomez and Laubach, 2006) present the method of mapping and measuring microfractures on the transmitted-light or SEM thin section. This method comprises four main steps. First, a thin section or polished slab is generated. Second, images are acquired using software that drives a transmitted-light or SEM stage. Third, microfractures are digitized using commercial digitizing software and export fracture coordinates to a spreadsheet. Fourth, the spreadsheet-based software quantifies and displays attributes of all or part of the fracture population. This method makes microfracture analysis more accessible and effective.

1.2 Orientation

In this section, the orientation of fractures is introduced, including measurement method, typical distribution and some description models.

Orientation is one of the most important characteristics of fractures. Because it is not easy to get all the orientations of each fracture at the location we are interested in, it is necessary to measure fracture orientation at other rock locations (e.g., outcrops, boreholes, thin sections, etc) and build up a statistical model that represents the fracture

orientation characteristics of the rock mass. In most cases, the statistical model is based on the fact that geological processes usually generate one or more fracture sets in which fractures nearly have the same strike and dip angle (parallel).

1.2.1 ORIENTATION SAMPLING

In outcrops or any excavation plane, the orientation of a fracture can be measured at the point of intersection with the scanline by means of a magnetic compass and clinometer device fitted with a spirit level (ISRM, 1978; Ragan, 1985). The orientation can be expressed in degrees as the dip direction (3 digits) and dip angle (2 digits) of the fracture. The orientation of fractures in the boreholes can be obtained from the oriented core or from image logs.

As for the microfracture orientations, generally we can only get strikes of fractures from thin section in the local coordinate system and determine the strikes in the geological system according to the relative orientation relationship between thin section and oriented rock sample.

1.2.2 ORIENTATION REPRESENTATION

There are graphical and vectorial methods to represent the fracture orientation. Graphical representation includes the rose diagram, the histogram for fracture dip angle and stereographic projection.

The rose diagram is one of the simplest forms of graphical representation (Attewell and Farmer, 1976; Cawsey, 1977). The whole circle is divided into convenient class intervals, and the number of dip direction values in each class interval is counted. The results are plotted as wedges that have a radial extent that proportional to the frequency in each class interval. Although the rose diagram can express all strike

directions and indicate the dominating direction(s), the dip directions and dip angles are not depicted.

The histogram for fracture dip angle can overcome the disadvantage of missing dip angle information in the rose diagram method by selecting data from the more significant class intervals and then plotting a histogram of dip angle. In this plot, the dominating dip angle can be found in a dip direction interval. However, this method often needs more than one plot to represent all significant orientations (dip directions and dip angles).

Stereographic projection is the other technique to represent three-dimensional orientation (Duncan, 1981; Phillips, 1971) in two dimensions. A plane can be represented by a curve in hemispherical projection, and a line can be represented by a point in it. The orientation of each fracture can be expressed by its normal and, in turn, a point in the hemispherical projection plane. If points appear in a cluster in the hemispherical projection plane, the fractures that have normals as these points can be seen as the same fracture set because they are nearly parallel.

Vectorial methods provide a powerful tool for the representation and analysis of fracture orientation data. It is convenient to consider the downward directed unit vector normal to the fracture plan. Typically, the direction cosines of the normal can express its direction and, in turn, the orientation of the fracture plane.

1.2.3 ORIENTATION DISTRIBUTION

Researchers describe a number of models to provide good fits to orientation data, such as Fisher distribution (Fisher, 1953), Bingham distribution (Einstein and Baecher, 1983; Mardia, 1972) and Normal distribution (Belfield and Sovich, 1995). Fisher distribution is widely used by researchers and is described below.

Fisher distribution (Fisher, 1953), in a fundamental analysis of orientation statistics, assumed that a population of orientation values was distributed about some true

value. This assumption is equivalent to the idea of fracture normals being distributed about some true value within a set. He determines that the probability density distribution can be expressed by:

$$f(\theta) = \frac{K \sin\theta \cdot e^{K\cos\theta}}{e^{K} - e^{-K}} \tag{1.1}$$

where θ is the angle between the normal to one fracture and the "true" value, and K is the Fisher's constant, a measure of the degree of clustering, or preferred orientation, within the population. Fisher (1953) shows that K can be estimated by:

$$\frac{e^{K} + e^{-K}}{e^{K} - e^{-K}} - \frac{1}{K} = \frac{|\mathbf{r_n}|}{N} \tag{1.2}$$

where $\mathbf{r_n}$ is the resultant vector of N unit normal vectors of fractures, N is the number of fractures in the sample.

The probability that a random orientation value makes an angle of between θ_1 and θ_2 with the true orientation given by:

$$P(\theta_1 < \theta < \theta_2) = \int_{\theta_2}^{\theta_2} f(\theta)\, d(\theta) \tag{1.3}$$

1.2.4 RELATION OF MICRO- AND MACRO- FRACTURE ORIENTATION AND MACROFRACTURE ORIENTATION PREDICTION

Sometimes it is difficult to obtain fracture orientation in outcrops because of erosion, vegetation and clay coverage or filling. Also, fracture orientation data are sparse in boreholes because few subvertical fractures intersect vertical bores (Laubach, 1997).

To overcome these limitations of macrofractures, researchers found that, at times, microfractures can be used as a proxy to predict macrofracture orientations, because microfractures are widespread even in small specimens obtained from borehole cores or underground excavations. Microfracture orientations from each sample can be initially plotted as rose diagrams and compared with the associated macrofracture orientations. In

some cases the preferential orientation of all the microfractures in a sample corresponds with the orientation of the macrofractures developed in the same bed (Laubach, 1997; Laubach, 2003; Ortega and Marrett, 2000), which suggest that under some circumstances the extrapolation of fracture attributes from the microscale to the macroscale is justified. Laubach (1997) provided a comprehensive discussion of microfracture morphology and origin. Ortega and Marrett (2000) suggest that transgranular and transcement microfractures (Laubach, 1997) have the highest suitability as proxies of macrofractures, because they are most likely to have formed under the same remote stress conditions as the macrofractures. This strike comparison in areas dominated by one set of macrofractures often indicates that it is feasible to predict macrofracture orientation using microfracture orientation data from properly oriented samples.

In some cases, microfracture orientations are more complex than the macrofracture orientations. This complexity in part reflects the material heterogeneity at the microscopic scale and the tectonic history that affected these rocks. In this case, more caution is needed in comparing the macrofracture and microfracture orientations (Ortega and Marrett, 2000). Ortega and Marrett suggest that the microfracture orientations can be weighted according to lengths to enhance the agreement between macrofracture and microfracture orientations.

An uncertainty for using microfractures as proxies for large fractures is the variable abundance of those microfractures that most reliably indicate the strike of large fractures, namely those having straight traces across multiple grain boundaries. In some rocks these are numerous, and strike can be readily determined from samples. Rocks having a low density of such fractures, on the other hand, may require extensive sampling to obtain dependable information. Rigorous analysis of variation in microfracture abundance is needed to devise appropriate sampling strategies.

1.3 Size distribution

In this section, size distributions of fractures are summarized according to existing literature, including trace length, spacing, aperture and their relations.

Fracture size characterizations can be described by shape, planar dimension (height, diameter, trace length, etc.), kinematic dimension (aperture, displacement, throw, heave) and spatial dimension (spacing, frequency).

In the following part of this chapter, length distribution, aperture/displacement/throw/heave distribution, the relation between the two and spacing/frequency will be described.

Several common distributions are introduced first, such as normal distribution, log-normal distribution, negative exponential distribution, negative logarithmic relationship, uniform distribution, power-law distribution gamma distribution and Lévy-stable distribution. Two different frequency statistic methods, discrete frequency distribution and cumulative frequency distribution, are also introduced.

1.3.1 DEFINITIONS OF SEVERAL DISTRIBUTIONS

1.3.1.1 Normal distribution (N)

The normal distribution, also called the Gaussian distribution, can be defined by two parameters: the mean (μ) and variance (σ^2). The standard normal distribution is the normal distribution with a mean of zero and a variance of one. The graph of probability density of normal distribution is a bell curve that resembles a bell and is symmetric with the mean (μ).

The probability density function (pdf) of normal distribution can be written as:

$$p(x) = \frac{1}{\sigma\sqrt{2\pi}} \exp\left(-\frac{(x-\mu)^2}{2\sigma^2} \right) \tag{1.4}$$

The cumulative density function (cdf) of normal distribution can be written as:

$$P(x) = \frac{1}{2}\left(1 + erf\left(\frac{x-\mu}{\sigma\sqrt{2}} \right) \right) \tag{1.5}$$

where *erf* is the "error function" which is defined as

$$erf(z) = \frac{1}{\sqrt{\pi}} \int_0^z e^{-t^2} dt \tag{1.6}$$

1.3.1.2 Log-normal distribution (LN)

The log-normal distribution is the single-tailed probability distribution of any random variable whose logarithm is normally distributed. If Y is a random variable with a normal distribution, then X = exp(Y) has a log-normal distribution; likewise, if X is log-normally distributed, then log(X) is normally distributed.

The probability density function (pdf) of log-normal distribution can be written as:

$$p(x) = \frac{1}{x\sigma\sqrt{2\pi}} \exp\left(-\frac{(\ln(x)-\mu)^2}{2\sigma^2} \right) \tag{1.7}$$

The cumulative density function (cdf) of log-normal distribution can be written as:

$$P(x) = \frac{1}{2}\left(1 + erf\left(\frac{\ln(x)-\mu}{\sigma\sqrt{2}} \right) \right) \tag{1.8}$$

where *erf* is the "error function" in Eq.(1.6)

1.3.1.3 Negative exponential distribution (NE) or exponent distribution

The probability density function (pdf) of negative exponential distribution can be written as:

$$p(x,\lambda) = y = \begin{cases} \lambda e^{-\lambda x}, x \geq 0 \\ 0 \quad\quad , x < 0 \end{cases} \tag{1.9}$$

The cumulative density function (cdf) of negative exponential distribution can be written as:

$$P(x,\lambda) = Y = \begin{cases} 1 - e^{-\lambda x}, x \geq 0 \\ 0 \quad\quad , x < 0 \end{cases} \tag{1.10}$$

If logarithm is taken of both sides of the probability density function, it will become:

$$\log\left(p(x,\lambda)\right) = \log(y) = \log(\lambda) - \lambda x, \text{ for } x \geq 0 \tag{1.11}$$

If we plot $\log(y)$ and x in the linear coordinate system, or plot y and x in the log-linear coordinate system, a line with a negative slope can be shown to represent this distribution.

1.3.1.4 Negative logarithmic relationship (NL)

A negative logarithmic relationship between x and y can be expressed as:

$$y = a - b\log(x) \tag{1.12}$$

where a and b are constant and b is greater than zero. If we plot x and y in the log-linear coordinate system, a line with a negative slope (-b) represents this relationship.

1.3.1.5 Uniform distribution (U)

The probability density function (pdf) of uniform distribution can be written as:

$$p(x) = y = \begin{cases} \frac{1}{b-a}, \text{for } a \le x \le b, \\ 0 \quad\quad , \text{for } x < a \text{ or } x > b \end{cases} \tag{1.13}$$

The cumulative density function (cdf) of uniform distribution can be written as:

$$P(x) = Y = \begin{cases} 0 \quad\quad , x < a \\ \frac{x-a}{b-a} \ , a \le x < b \\ 1 \quad\quad , x \ge b \end{cases} \tag{1.14}$$

1.3.1.6 Power-law distribution (PL)

A power-law is a relationship that exhibits the property of scale invariance. The most common power-laws have the form:

$$f(x) = y = ax^k \tag{1.15}$$

where a and k are constants. k is called the scaling exponent, denoting the fact that a power-law function (or, more generally, a kth order homogeneous polynomial) satisfies the criterion

$$f(cx) \propto f(x) \tag{1.16}$$

where c is a constant. That is, scaling the function's argument changes the constant of proportionality as a function of the scale change, but preserves the shape of the function itself. This relationship becomes clearer if we take the logarithm of both sides (or, graphically, plotting on a log-log graph)

$$\log(f(x)) = \log(y) = k\log(x) + \log(a) \tag{1.17}$$

This expression has the form of a linear relationship with slope k, and scaling the argument induces a linear shift (up or down) of the function, and leaves both the form and slope k unchanged.

1.3.1.7 Gamma distribution (G)

The probability density function (pdf) of the gamma distribution can be expressed in terms of the gamma function parameterized in terms of a shape parameter k and scale parameter θ:

$$f\left(x;k;\theta\right)=x^{k-1}\frac{e^{-x/\theta}}{\theta^{k}\Gamma\left(k\right)},\ \text{for}\ \ x>0\ and\ k,\theta>0. \tag{1.18}$$

where $\Gamma\left(z\right)$ is the Gamma function which is defined as

$$\Gamma\left(z\right)=\int_{0}^{\infty}t^{z-1}e^{-t}dt \tag{1.19}$$

The cumulative density function (cdf) of uniform distribution can be written as:

$$F\left(x;k;\theta\right)=\int_{0}^{x}f\left(u;k;\theta\right)du=\frac{\gamma\left(k,x/\theta\right)}{\Gamma\left(k\right)} \tag{1.20}$$

where $\gamma\left(a,x\right)$ is the lower incomplete gamma function which is defined as

$$\gamma\left(z,x\right)=\int_{0}^{x}t^{z-1}e^{-t}dt \tag{1.21}$$

Gamma distribution has both scaling and exponential properties:

Scaling: for any t > 0 it holds that tx is distributed $F\left(x;k;t\theta\right)$, demonstrating that θ is a scale parameter.

Exponential: The Gamma distribution is a two-parameter exponential family with natural parameters k−1 and −1/θ.

1.3.1.8 Lévy-stable distribution (L)

The probability density function (pdf) of the Lévy-stable distribution can be expressed as

$$p\left(x\right)=\frac{1}{\pi}\int_{0}^{\infty}\exp\left[-\left(Ct\right)^{\alpha}\right]\cos\left(tx\right)dt \tag{1.22}$$

where α is the Lévy index, lying in the range $0<\alpha\leq 2$, and C is a parameter that describes the width of the distribution, when $\alpha=2$, the Lévy probability density, is

equivalent to a Gaussian distribution. Small α values correspond to broader distributions with longer tails and more extreme values. This distribution has a power-law tail where for large x', the probability of encountering a size x>x' is
$P(x > x') \sim (x')^{-\alpha}$ with $0 < \alpha < 2$.

1.3.1.9 Discrete and cumulative frequency distribution (DFD and CFD)

1.3.1.9.1 Discrete frequency distribution (DFD)

DFD is typically generated by dividing the range (covering the minimum and maximum values that the variable takes) of a data set into a set of mutually exclusive (non-overlapping) intervals of equal width, listing them in increasing order and assigning to each interval the number of measurements (frequency) that fall in each interval. Graphs of DFD are commonly shown in the form of histograms. In statistics of a variable, a histogram is a bar graph of a frequency distribution in which the heights of the bars are proportional to the interval frequencies.

There are two different ways to express the discrete frequency with the same data. One uses the number of measurements per interval, while the other uses the number of measurements per interval divided by the total number of measurements, which yields an estimate of the probability that a measurement in a statistical sample will fall into a particular interval.

1.3.1.9.2 Cumulative frequency distribution (CFD)

CFDs are one of the most popular analytical techniques used to quantify statistical properties of fracture attributes. Cumulative frequency is used to determine the number of observations that are equal to or greater than a particular value in a data set. It tells how often the value of the random variable is equal to or greater than a particular reference value.

In the research of the fracture, the first step commonly used to generate a cumulative frequency distribution of a fracture attribute of interest (e.g., aperture, length, spacing) is to sort all measurements of the fracture attribute from largest to smallest, and then calculate the cumulative number by assigning increasing numbers (increments of one) to each measurement of fracture attribute. Secondly, duplicate values of the fracture attribute should be distilled so that only the largest value of cumulative number is retained. This creates a table with pairs of values of fracture attribute and cumulative number. The cumulative number indicates how many fractures in the sample have an attribute equal to or larger than the corresponding value of fracture attribute. The third step is to divide the cumulative number by the dimension of observation domain (e.g., scanline length for a one-dimensional sampling) to obtain the cumulative frequency of the fracture attribute under study. Normalization to calculate cumulative frequency is similar to the one commonly used for histograms in DFD; instead of normalizing by the total number of measurements, however, it is done using the size of the observation domain.

Cumulative frequency fracture-size distributions are commonly illustrated using log-linear and log-log graphs. In many cases, lines can be fit to linear trends of data points in both types of graphs, implying that either exponential or power (fractal) laws, respectively, can be used to model fracture-size distributions. Different authors have supported one or the other type of distribution with particular data sets. However, no model typically fits entire data sets, a result that commonly is interpreted to reflect various sampling limitations (Ortega and Marrett, 2000).

1.3.2 LENGTH

Here, I use the term “length” to express a generalized meaning for the planar dimension of the fracture. For example, considering a three-dimensional fracture size, length can be the diameter if the fracture has a disk shape; the height and width if the

fracture has a rectangular shape; the major axis and minor axis if the fracture has an elliptical shape; and the correlative dimensions if the fracture has any other kind of shape. Considering a two-dimensional fracture size, the length can be so-called "trace length," which is the intersection of the fracture and the observation plane. Strictly speaking, there is no one-dimensional fracture length size. That is because there is just one point that has no size when a line intersects with the fracture. However, we can obtain the fracture length population along a scanline (one-dimensional). All these fractures are those which intersect with the scanline. Therefore, sometimes we call this length population a one-dimensional length sampling. However, this means the sampling domain is one-dimensional, while length measurements are still two-dimensional. If there is no special mention, length population always refers to a two-dimensional length sampling, which means all lengths are measured on a certain confined planar area, such as a geological map, an outcrop, a cross section of a rock mass, a thin section of a rock sample, and so on. Circular scanline technique will be described in Section 1.3.5. Sampling bias such as censoring and truncation will be introduced in Section 1.3.6.

Many researchers have worked with the length distribution of fractures. Summary of fracture length distribution is shown in Table 1.2. Faults, joints and veins are all included, almost of which are two-dimensional samplings of CFD population. Almost all types of length observation methods are included, such as satellite images, aerial photographs, geological maps, seismic maps, outcrops, cores and SEM thin sections. However, the length observation in cores is relatively rare because macrofracture lengths cannot be obtained in the majority of cases due to lengths exceeding the core diameter. The length observation on thin sections is also uncommon because thin sections are usually unsuitable for microfracture length observation and analysis because thin section images are often not wide enough to identify the two ends of microfractures.

From Table 1.2, it can be found that no matter what types of fracture are present, log-normal distribution or power-law distribution are the most common length distributions.

The distribution of fracture lengths observed in many studies appears to be log-normal, such as Baecher and Lanney, 1978; Baecher et al., 1977; Cruden, 1977a; Dershowitz and Einstein, 1988; Einstein and Baecher, 1983; Hudson and Priest, 1983; Priest and Hudson, 1976; Priest and Hudson, 1981; and Warburton, 1980a. In theory, differences in the observed distribution of fracture lengths are the result of differences in the mechanical processes creating the fractures. For example, Dershowitz and Einstein (1988) argue that a uniform stress distribution would lead to exponential distributions, while multiplicatory processes such as breakage may lead to a log-normal distribution.

Cladouhos and Marrett (1996) give out fracture growth and linkage models to develop a power-law distribution of fracture length from a population that initially does not cause the power-law distribution. Actually, many researchers show that the distribution of fracture lengths appears to be power-law, such as Barton and Zoback, 1992; Belfield and Sovich, 1995; Berkowitz, 2002; Bour and Davy, 1999; Clark et al., 1995; Clark et al., 1999; Gillespie et al., 1993; Gross, 1993; Gudmundsson, 1987a; Harris et al., 2003; Hatton et al., 1994; Johnston and McCaffrey, 1996; Marrett, 1997; and Wong et al., 1989. The scaling exponents of all these power-law distributions are in the range of about 0.5~2.5. The valid range of power-law distributions are often over two orders of magnitude. Some even can reach over 5 orders of magnitude, which means some data cover from millimeter scale to kilometer scale. Power-law length distributions are often referred to as "self-similar" and their exponents as "fractal dimensions." When the exponent is equal to 2, we call this is a 'strictly self-similar' system.

It is worthy to mention that, in outcrops fracture length measurement is often complicated by the challenge of defining what constitutes an individual fracture where multiple fracture strands connect. Ortega and Marrett (2000) offer criterion for

identifying fracture terminations uniquely. Because of the limitation of accessing all fracture lengths (e.g., erosion and vegetation), fracture length data are also collected along scanlines or outcrops. Two-dimensional fracture distributions can be obtained by the estimating approach (Marrett, 1996) of using one-dimensional scanline data.

As for the power-law distribution, some researchers consider that the scaling exponent is different at the different scale of fracture length. For instance, Ortega and Marrett (2000) find that, according to the correlation coefficient analysis, the smallest fracture lengths in the data set are best modeled by an exponential function, and larger fracture lengths are best modeled by a power-law function. Many analyses of analogous changes in length distributions concluded that the changes reflected a censoring bias in the sampling procedure (e.g., Baecher and Lanney, 1978; Barton and Zoback, 1992). However, censoring was minimized in the experiment of Ortega and Marrett (2000) by studying nearly 100 long fractures within an area having dimensions more than an order of magnitude greater than the length of the longest fractures observed. The power-laws that provide the best fits to fracture lengths have different exponents for longer and longest fractures with a change in exponents at the scale of the mechanical layer thickness. Ortega and Marrett (2000) interpret the change in power-law exponent to be a real phenomenon. Therefore, caution is needed in upscaling the prediction of fracture lengths by using power-law from the observation scale.

Researchers also show some other uncommon length distributions. For example, Davy (1993) analyzes the fault length distribution from the San Andreas fault system and shows that exponential function, power-law and log-normal distribution do not fit data over the whole range of lengths between 1 and 100 km. The best fit was obtained with a gamma function, mixing power-law and exponential function. Some researchers show negative exponential distribution (Aler et al., 1996; Baecher et al., 1977; Call et al., 1976; Cruden, 1977b; Kulatilake et al., 1993; Priest and Hudson, 1981; Robertson, 1970). Other

researchers (Aler et al., 1996; Hudson and Priest, 1979) give the normal distribution of fracture length. Table 1.3 shows the list of some other distributions.

Table 1.2 Summary of fracture length distributions

(Note: PL – Power-law, LN – Log-normal)

NO	location	rock type	fracture mode	Frequency distribution	distribution	distribution parameter	range	Observation method	From	note
1	Butten Western Ireland	Limestone	Vein	CFD	PL	-0.8	1-50m	Low level aerial photographs of pavement & high resolution fracture maps	Odling et al., 1999 figure 4	Probably: 1m is resolution effect, 50m is a censoring effect Subparallel, strongly clustered,
2	Butten Western Ireland	Limestone	Joint	CFD	LN	-	-	Low level aerial photographs of pavement & high resolution fracture maps	Odling et al., 1999 figure 4	Confined within 1.2m thick limestone unit Anticlustering, relatively regular spacing
3	Fault-bounded Hornelen basin of western norway	Sandstone	Joint	CFD	Individual sample: LN Together: PL	PL: -2.1	PL: 4~5 magnitude (extension aerial data)	Outcrop hand-mapping & low level aerial photographs taken from deffent observation heights	Odling et al., 1999 figure 5 a)	
4	Cambrian-Ordovician sandstone of the Tayma region of NW Saudi Arabia	Sandstone	Joint and fault	CFD	Individual sample: LN Together: PL	PL: -2.34	PL: 4~5 magnitude (nine maps)	Frature maps generated at different scales and resolutions from outcrop mapping and interpretation of low level aerial photographs, standard aerial stereoscopic photographs and satellite images	Odling et al., 1999 figure 9)	
5	A quarry at Rordal, North Jylland in Denmark	Chalk	Joint	CFD	(2D) LN			aerial photographs	Odling et al., 1999 figure 12)	
6	The Black Warrior Basin, Alabama	Sandstome (Pennsylvanian Pottsville Formation)	Fransgranular micro-fracture	CFD	(2D) PL LN	PL: -2.179	PL: 0.07~0.22mm	SEM-CL in the sidewall cores	Laubach & Gale, 2006 Fig. 7 B)	From: 1300m deep PL: using Marrett et al., 1999 method Exponential function also fits, correlation coefficients for the two fits are insistinguishable
7	Utah in USA Gulf of Suez in Egypt		Extensional fault	CFD	(2D) PL	-	10cm~1000km	Maps, outcrop	Koestler, 1994	Study from different onshore areas to fill-in the information gap between the scale of seismic

	Bornholm in Denmark Somerset in England									resolution and core samples
8	Gulf of Sues	sandstone	Fracture and fault	CFD	(2D) PL	Slope:-3	5~20000m	Outcrop Oil field fault map Geologic fault map	Heffer & Bevan, 1990 fig 2	There are gaps between three data
9	North Sea North America Literature throughout he world (30 data sets)		Fracture and fault	CFD	(2D) PL	Slope:-3	10^{-4}~10^{5}m	In-house seismic maps Outcrop surveys	Heffer & Bevan, 1990 fig 3	
10	Cappanawalla, The Burren, Co. Clare, Ireland	Carboniferous limestone	Vein	CFD	(2D) LN	$\overline{s} = 0.706$ SD=0.416	-	Aerial photography and digital map	Gillespie et al., 2001 Fig. 8a	No in sample is 1117. Sample area is $3.6\times10^{4}\,m^{2}$
11	Sheshymore, The Burren, Co. Clare, Ireland	Carboniferous limestone	vein	CFD	(2D) PL	1487; -1.007	2-70m	Aerial photography and digital map	Gillespie et al., 2001 Fig. 8a	No in sample is 3439. Sample area is $1.144\times10^{5}\,m^{2}$
12	Sheshymore, The Burren, Co. Clare, Ireland	Carboniferous limestone	Vein (filtered)	CFD	(2D) PL	630.3; -0.749	2-70m	Aerial photography and digital map	Gillespie et al., 2001 Fig. 8a	No in sample is 1770. Sample area is $1.144\times10^{5}\,m^{2}$ This is the filtered (exclude those with an ambiguous origin)
13	Cappanawalla, The Burren, Co. Clare, Ireland	Carboniferous limestone	Joint	CFD	(2D) LN	$\overline{s} = 0.437$ SD=0.442	-	Aerial photography and digital map	Gillespie et al., 2001 Fig. 8a	No in sample is 15254. Sample area is $2.708\times10^{6}\,m^{2}$
14	Sheshymore, The Burren, Co. Clare, Ireland	Carboniferous limestone	Joint (filtered)	CFD	(2D) LN	$\overline{s} = 0.722$ SD=0.392	-	Aerial photography and digital map	Gillespie et al., 2001 Fig. 8a	No in sample is 4087. Sample area is $1.144\times10^{5}\,m^{2}$ This is the filtered (exclude those with an ambiguous origin)
15	Neogene fault, in the Boso and Miura Peninsulas, Japan	-	fault	CFD	PL	Slope: -2.1	about 9km~120km		Scholz & Cowie, 1990 Fig 2 a	
16	Bul (1), Gulf of Mexico, Amoco Prod. Co.	-	fault	CFD	(2D) PL	Slope: -1.67	4km~24km		Cladouhos & Marrett, 1996 Fig.1	A=3600km^{2}
17	Text (25), Gulf of Mexico, Amoco Prod. Co.	-	fault	CFD	(2D) PL	Slope: -1.66	4km~28km		Cladouhos & Marrett, 1996 Fig.1	A=5100km^{2}

18	Ang (B), Gulf of Mexico, Mexico, Amoco Prod. Co.	-	fault	CFD	(2D) PL	Slope: -2.07	6km~30km		Cladouhos & Marrett, 1996 Fig.1	A=6200km^2
19	Boso and Miura Peninsulas, Japan	-	fault	CFD	(2D) PL	Slope: -0.97	1km~8km		Cladouhos & Marrett, 1996 Fig.1	A=280km^2 Cited from Kakimi (1980)
20	Yucca Mountain, Nevada	-	fault	CFD	(2D) PL	Slope: -1.21	0.2km~5.5km		Cladouhos & Marrett, 1996 Fig.1	A=120km^2 Cited from Scott and Castellanos (1984)
21	Chimney Rock, Utah	-	fault	CFD	(2D) PL	Slope: -0.67	0.15km~2km		Cladouhos & Marrett, 1996 Fig.1	A=29km^2 Cited from Krantz (1988)
22	Basin-Range, NV	-	fault	CFD	(2D) PL	Slope: -1.84	12km~50km		Cladouhos & Marrett, 1996 Fig.1	A=290000km^2 Cited from Stewart (1980)
23	Laramide, WY	-	fault	CFD	(2D) PL	Slope: -1.11	7km~60km		Cladouhos & Marrett, 1996 Fig.1	A=250000km^2 Cited from Blackstone (1988)
24	Middle Atlas aquifer, Northern Morocco	Limestone and dolomite	fracture	CFD	(2D) PL	2.8 -1.99	1~10km		Rouai, 2006 Fig.5	N=976
25	US active surface fault		fault	CFD	(2D) PL	-1.76	10~20km		Hatton et al., 1993Fig 1	Cited from Shaw & Gartner, 1986
26	North Sea fields	Jurassic horizons affected by end-Jurassic extension	fault	CFD	(2D) PL	-1.37 or -1.59	~700-10000m	Seismic reflection data	Yielding et al., 1996 Fig 9	-1.37 is obtained by extrapolating tips -1.59 is obtained by adding a nominal tip length (350 mat each end) to all faults
27	West Norway	Sandstone (Devonian)	Joint system	CFD	(2D) PL	-2.1	1~>3000m	maps in the field and from low-level aerial photography taken from different heights.	Odling, 1997 Fig. 6	Individual samples show LN distributions, a natural lower cut-off to the PL at around 1 m individual distributions is attributed to a combination of truncation and and censoring effects
28	the Ligurian Alps (Italy).	metamorphic and sedimentary rock units		CFD	(2D) PL	-2.15	0.2m~24000m	outcrop site aerial images satellite images	Cravero et al., 2006 Fig 12	There is a data gap from 2m~200m
29	Reykjanes	lava		CFD	(2D)	-0.8986		Tectonic map	Gudmundsson,	

	Peninsula, southwest Iceland				PL				1987a fig 8	
30	Horda Platform, northern North Sea		fault	CFD	(2D) PL	-2.0	More than 1 order of magnitude	Seimic datasets	Yielding et al., 1992 fig 10	Yielding et al. (1992) & Heffer and Bevan (1990) suggest the slope of fault trace length exponent may be universal.
31	Pelican field, North Sea, offshore, United Kingdom		fault	CFD	(2D) PL	NE-SW: -1.42 NNW-SSE: -1.69 E-W: -1.10	More than 1 order of magnitude	Seimic datasets	Gauthier & Lake, 1993 fig. 7B	Three sets
32	Westwater Springs Canyon		Opening mode fracture	CFD	(2D) PL	-1.98	More than 3 order of magnitude	SEM and macrofracture	Ortega & Marrett, 2000 Fig 12	

Table 1.3 Other trace length distributions used in the literature

Distribution	From
Uniform	Aler et al., 1996; Hudson & Priest, 1979
Negative exponential	Aler et al., 1996; Baecher et al., 1977; Call et al., 1976; Cruden, 1977b; Kulatilake et al., 1993; Priest & Hudson, 1981; Robertson, 1970
Normal	Aler et al., 1996; Hudson & Priest, 1979
Gamma distribution	Baecher et al., 1977; Davy, 1993; Kulatilake et al., 1993
Lévy-stable distribution	Belfield, 1998

1.3.3 DISPLACEMENT/THROW/HEAVE/APERTURE

We often use "displacement" to describe the relative moving distance of both sides of faults; "throw" to refer to the amount of vertical displacement due to faulting; and "heave" as the horizontal offset of faults (Ries, 1915). "Aperture" refers to the relative opening distance in the direction perpendicular to the fracture wall. Aperture can be suitable to the opening-mode fracture, such as joints and veins. In some cases, shear fractures also can have an aperture and even have the greatest hydraulic aperture in the shallow subsurface. We can call all these relative moving distances (displacement, throw, heave and aperture) the "kinematic dimension" of the fracture, which has a different meaning for different fracture modes or offset components.

It is very difficult to obtain the real "kinematic dimension" by using three-dimensional sampling because we cannot disassemble the rock mass completely to get the size properties of all fractures. One-dimensional or two-dimensional observation is still the major means of sampling apparent kinematic dimensions instead of the real ones. If two-dimensional sampling is used, the observation objective is the maximum kinematic dimension, which is the maximum value (displacement or aperture) along the whole fracture in the observation domain. However, if one-dimensional sampling is adopted, the only value of the kinematic dimension along scanlines or boreholes is collected. Similar to the length population analysis, discrete or cumulative frequency distribution can be used in the analysis of kinematic dimension. Marrett et al. (1999) show that sampling artifacts can be minimized through collecting data along one-dimensional scan lines, which eliminates the need for identifying fracture terminations.

Like fracture length distribution, kinematic dimensions also follow several different distributions for different rock types, fracture modes, diagenesis processes, stress states, etc. The summary of fracture displacement/aperture is shown in Table 1.4, in which the most common distributions (log-normal and power-law) are listed.

Power-law is the most common distribution of displacement or aperture. The scaling exponents of power-law for two-dimensional CFD distribution are in the range of about -0.5 ~ -1.5. The scaling range of power-law of open-mode fracture aperture by using traditional observational methods often covers less than three orders of magnitude, such as from the millimeter scale to meters. In recent years, some researchers use thin sections of rock samples to obtain the wider valid range of power-law, which can be over four to five orders of magnitude. For example, Marrett et al. (1999) combine data from multiple observational scales by the use of the hand lens, the comparator, the petrographic microscope, and the scanning electron microscope with a cathode luminescence detector (SEM-CL) to collect data sets over more than five orders of magnitude.

Table 1.4 Summary of fracture displacement/aperture distributions

(Note: PL – Power-law)

NO	Location	rock type	fracture mode	Frequency distribution	distribution	distribution parameter	range	Observation method	From	Note
1	Cajon Pass scientific drill hole, near San Bernadino, California	Crystalline Rock	Joint	CFD	(1D) PL	-1.4	15-100mm	High-quality borehole televiewer (BHTV)	Barton & Zoback, 1992 Fig 6b	4km from the San Andreas fault, at 1750-3460 m deep The drop off in frequency of fracture with apertures <15mm is largely a function of detection limit of the BHTV and the resolution of the technique.
2	An East Texas Austin Chalk reservoir	chalk	Joint	CFD	(1D) PL		0.01~1mm Almost two order of magnitude	Microscanner logs (in horizontal wells)	Belfield & Sovich, 1995 Fig. 4	Unit is 2600m deep and 26m thick Deviations from PL behavior occur around the 0.01 mm threshold level of the microscanner
3	The Black Warrior Basin, Alabama	Sandstome (Pennsylvanian Pottsville Formation)	Fransgranular micro-fracture	CFD	(2D) PL	-0.9613	0.002~0.01mm	SEM-CL in the sidewall cores	Laubach & Gale, 2006 Fig. 7 A)	From: 1120m deep PL: using Ortega, 1997 method
4	The Black Warrior Basin, Alabama	Sandstome (Pennsylvanian Pottsville Formation)	Fransgranular micro-fracture	CFD	(1D) PL	-1.1766	0.018~0.02mm	SEM-CL in the sidewall cores	Laubach & Gale, 2006 Fig. 7 C)	From: 1300m deep PL: using Ortega, 1997 method Azimuth: 030-050
5	The Black Warrior Basin, Alabama	Sandstome (Pennsylvanian Pottsville Formation)	Fransgranular micro-fracture	CFD	(1D) PL	0.0052, -1.112	0.015~0.17mm	SEM-CL in the sidewall cores	Laubach & Gale, 2006 Fig. 7 D)	From: 1300m deep PL: using Ortega, 1997 method Azimuth: 070-110
6	Westerly Granite	Granite (igneous)	Micro joint	CFD	(1D) PL	0.044, -0.843	0.03~2.17μm	SEM	Wong et al., 1989 Fig. 8	
7	Rutland Quartzite	Quartzite (metamophic)	Micro joint	CFD	(1D) PL	0.255, -0.804	0.25~80.39μm	SEM	Wong et al., 1989 Fig. 8	
8	Curraghinalt	Graphitic pelite Graphitic semi-pelite quartzose semi-pelite	vein	CFD	(1D) PL	-	0.03~80cm		McCaffrey et al., 1994	No detail parameters

		psammite								
9	Northeastern Mexico	Sandstone (Middle Triassic to Lower Jurassic La Boca Formation)	Joint (opening mode fracture)	CFD	(1D) PL	~0.0035; -1.30	0.002mm~6 mm	Outcrop; Thin section (SEM-CL)	Laubach & Ward, 2006	Microfracture populations alone are well fit by a power-law across roughly two orders of magnitude.
10	Gleninagh, The Burren, Co. Clare, Ireland	Carboniferous limestone	Vein thickness	CFD	(1D) PL	-0.62	0.5-10mm	Aerial photography and digital map	Gillespie et al., 2001 Fig. 12a	Line length is 156.58 m
11	Mobil Blakeney-Krueger No. 1 well, Texas	Ozona Sandstone	Extension fractures	CFD	(1D) PL	19.3 -0.769	0.00023~2.5 mm 4 orders of magnitude	10 power hand lens and a comparator Microscope	Marrett et al., 1999 Fig. 1A	surveys were conducted at two scales: visual and microscopic observation number: 235/0.0186m + 98/0.55m
12	Pedernales Falls State Park, Texas	Marble Falls Limestone	Extension fractures	CFD	(1D) PL	1.88 -1.042	0.007~18mm 3.4 orders of magnitude	10 power hand lens and a comparator SEM-CL	Marrett et al., 1999 Fig. 1B	surveys were conducted at two scales: visual and microscopic observation number: 117/0.407m + 639/21.54m
13	Yucca Mountain, Nevada	Tuff (Miocene Paintbrush Group)	Basin and Range fault	CFD	(1D) PL	8.10 -0.731	0.04m~3200 m 4.9 orders of magnitude	a 7.9-km-long, 7.6-m-diameter tunnel; fault mapping; cross sections; reports	Marrett et al., 1999 Fig. 2	Each fracture having a trace length on the tunnel walls in excess of 1 m was quantified two populations of faults were studied at the regional scale number: 523/4.78km + 9,39/14,146km
14	NE Venezuela	Limestone (Cretaceous Apon Formation)	Opening mode fractures	CFD	(1D) PL	3.6773 -1.0295	0.006mm~4 mm 2.8 orders of magnitude	outcrop	Gale et al., 2005	Kinematic aperture small fractures are all sealed, whereas larger fractures in outcrop contain degraded hydrocarbons
15	Alaska margin	Turbidite (Kodiak Formation, Late Cretaceous to earlyTertiary)	vein	CFD	(1D) PL	Slope: -1.33	0.3~35mm		Clark et al., 1995 Fig.2 A	Measure along 24 scan lines
16	Neogene fault, in the Boso and Miura Peninsulas, Japan	-	fault	CFD	(1D) PL	Slope: -1.2	about 13cm~400cm		Scholz & Cowie, 1990 Fig 2 b	
17	Viking Graben	Late	Fault	CFD	(1D)	Slope: about	50m~5000m		Walsh et al.,	

	(Northern North Sea)	Jurassic/earliest Cretaceous Episode	Dip-slip displacement		PL	-0.8,-0.9			1991 Fig 1a	
18	Onjuko	-	fault	CFD	(1D) PL	Slope: -0.6~-0.8	0.09m~3m		Kakimi, 1980	
19	Gulf of Mexico	Late Cenozoic marine strata	Listric normal growth fault	CFD	(2D) PL	Slope: -1.3~-1.5	200m~1500 m		Marrett & Allmendinger, 1992 Fig. 1B	The data were derived from structural contour maps based on extensive seismic profile and drill-hole data
20	La Escalera Canyon, the Sierra Madre Oriental, Mexico	carbonate	Opening mode fracture	CFD	(1D) PL	-0.685	0.05~20mm	Field data	Ortega et al., 2006 Fig 6	
21	Barnhart field, Reagan County, west Texas	dolostones (the Lower Ordovician Ellenburger Group)	Opening mode fracture	CFD	(1D) PL	-0.7328 ~-0.935	Two orders of magnitude	SEM-CL	Gale & Gomez, 2007 Fig 14	Two wells, four samples, four distributions
22	The Monterrey Salient of the Sierra Madre Oriental of Mexico	Dolostone (Lower Cretaceous Cupido Formation)	Opening mode fracture	CFD	(1D) PL	-1.1(micro) -0.97(macro)	0.01~1mm (micro) 0.05~4mm (macro)	transmitted-light microscope	Gomez & Laubach, 2006 Fig 7b	Fractures are filled mainly by crystalline calcite that contrasts with the dolomitic rock mass such that most microfractures are visible using a transmitted-light microscope
23	the footwall of the Moine thrust zone in northwestern Scotland	Sandstone (Cambrian Eriboll)	Opening mode fracture	CFD	(1D) PL	-1.018~ -1.05	Two orders of magnitude	SEM-CL	Gomez & Laubach, 2006 Fig 9a-b	
24	North Sea fields	Jurassic horizons affected by end-Jurassic extension	fault	CFD	(2D) PL	-1.34	20-1000m	Seismic reflection data	Yielding et al., 1996 Fig 13	
25	South Yorkshire Coalfield		fault	CFD	(2D) PL	-1.1~-1.53	2.5 orders of magnitude		Watterson et al., 1996 Fig 9	
26	Sierra Madre Oriental, Mexico	dolostone (Lower Cretaceous Cupido Formation)	Opening mode fracture	CFD	(1D) PL	-1.152	0.01mm~20 mm	Outcrop Thin section	Gale et al., 2004Fig. 3C	No gap: outcrop (high- and low-resolution data) and thin section
27	Oketibbeha	Ordovician	Opening mode	CFD	(1D)	-1.402	0.0008~0.015	Thin section	Gale et al.,	

	County, Mississippi	Knox Group dolostone	fracture		PL		mm		2004Fig. 4b	
28	La Codosera, Spain	Devonian Sandstones and slates	Vein thickness	CFD	(1D) PL	-0.95~-1.5	>1 order of magnitude	Routine logging of drill holes	Sanderson et al., 1994 Fig 3 and 4	
29	Entire northern North Sea		Faut displacement	CFD	(1D) PL	-0.9	100~6000m Almost 2 orders of magnitude	Measure on a seismic section	Yielding et al., 1992fig 2	
30	northern North Sea Oilfield		Faut throw	CFD	(1D) PL	-0.85	25~600m	on 56 parallel seismic lines	Yielding et al., 1992fig 3	Sampling on the same horizon on 56 parallel seismic lines
31	northern North Sea		Faut throw	CFD	(1D) PL	-0.9(band) Individual (-0.4~-0.95)	0.01~1000m	21 data sets	Yielding et al., 1992fig 5	21 different datasets: 11 seismic datasets, 2 coal mine, 4 outcrop and 4 wells
32	Frio County, Pearsall field	Austin Chalk	Opening mode fracture	CFD	(1D) PL	-0.6786	0.04~0.5mm	Horizontal core	Gale, 2002fig 2	
33	Grove Ceeek, Waxahachie, morth central Texas	Austin Chalk	Opening mode fracture	CFD	(1D) PL	-0.5575	0.04~70mm	outcrop	Gale, 2002fig 2	

1.3.4 RELATIONSHIP BETWEEN LENGTH AND APERTURE/DISPLACEMENT

The relationship of displacement or aperture as a function of length is important for a variety of applications that depend on the mechanical and hydraulic properties of faults and fractures. Many researchers have worked with the relationship between length and aperture/displacement (Cowie and Scholz, 1992; Dawers et al., 1993; Gillespie et al., 1992; Marrett and Allmendinger, 1991; Scholz and Cowie, 1990; Vermilye and Scholz, 1995; Walsh and Watterson, 1988). Summary of this relationship is shown in Table 1.5.

For the length and displacement relationship of faults, in general, the scaling of maximum displacement u as a function of length l takes the power-law form, $u = kl^v$, where k and v are constants. Scholz and Cowie (1990) and Dawers et al. (1993) considered following a linear relation, which means the exponent of power-law of this relation is 1.0. Walsh and Watterson (1988) proposed a model for fault growth that predicts this exponent of displacement and trace length is 2. However, Marrett and Allmendinger (1991) show that the least-squares best-fit to this data was 1.58, and also compile other data, none of which were used by Walsh and Watterson (1988), to find empirically that the exponent is 1.46. The data shows that displacement varies over six orders of magnitude and trace length varies by nearly five orders of magnitude. Clark and Cox (1996) applied regression techniques to perform a rigorous statistical analysis and examined the same data as earlier studies (Marrett and Allmendinger, 1991; Scholz and Cowie, 1990; Walsh and Watterson, 1988) and find that most of the data examined are consistent with a linear relationship (a power-law exponent of unity) between fault displacement and length, and that exponents of 1.5 or 2 are clearly inconsistent with the data.

For opening-mode fractures, many attempts have been made to quantify the relation between aperture and length for extension fractures and result in significant disagreement.

According to the linear elastic fracture mechanics (Pollard and Aydin, 1988), aperture and length scale linearly with each other. Some observations are also consistent with a linear relation between aperture and length (Vermilye and Scholz, 1995), however other results (Hatton et al., 1994; Johnston, 1992) indicate a nonlinear relation. Renshaw and Park (1997) suggest that the aperture of a fracture indicates the energy available for fracture growth and controls fracture permeability, and that the relationship between aperture and fracture length can therefore be used to infer the factors affecting fracture formation at different length scales. Their study of the scaling properties of tensile fractures in the Krafla fissure swarm, Iceland, revealed a distinct break in slope in the aperture-length scaling relationship, corresponding to fractures a few meters in length; this break in slope was interpreted qualitatively as indicative of non-universal, scale-dependent growth mechanisms. Hatton et al.'s (1993) studies of more complex vein and open tension fracture arrays suggest a more general power-law relationship where the exponent is positive and may take on a range of values less than or greater than 1.0. Johnston and McCaffrey (1996) study five areas with widely varying structural fracture geometries in a variety of host rock types. They find vein sizes obey the empirical relationship: $L = kT^a$ (where L = length in mm, T = thickness in mm), $20 < k < 2000$ mm^{1-a}, for small veins $0.6 < a < 1.0$ (usually between 0.7 and 0.8) and for large veins $a > 1$, as shown in Figure 1.3. This suggests that veins amplify initially by inflation and subsequently by elongation.

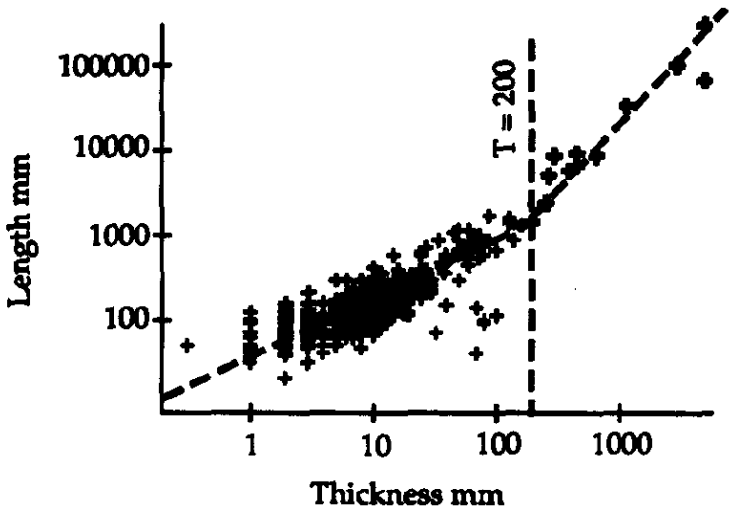

Figure 1.3 Vein length and thickness relationship (From Johnston and McCaffrey, 1996)

Main et al. (1999) suggest that the power-law exponent may change significantly at a characteristic length for a variety of reasons, for example when cracks begin to interact, or when cracks grow to a length comparable to a characteristic size in the brittle layer. Such a break of slope requires a second straight line, requiring two extra model parameters, as shown in Figure 1.4. Actually, the trends of Figure 1.3 and Figure 1.4 are the same, because coordinate axes are flipped.

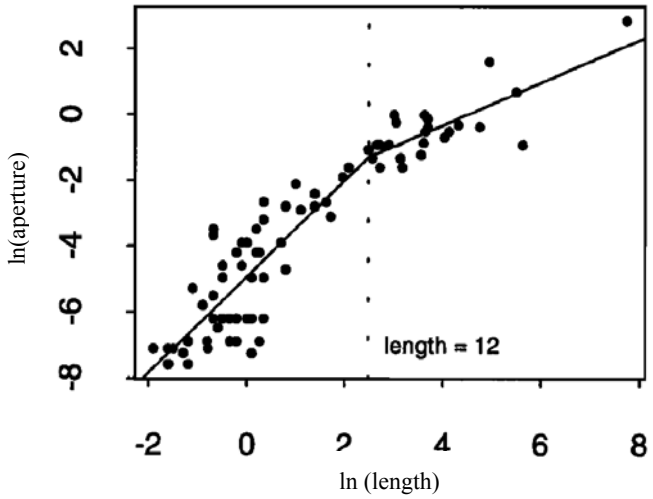

Figure 1.4 Fracture aperture (opening displacement) and length relationship (From Main et al., 1999) (aperture and length are in meters)

As shown in Figure 1.5, data collected by Marrett et al. (1997) from microfractures in low-porosity sandstones using the SEM-CL technique (Laubach and Milliken, 1996; Laubach, 1997) extend the range of available data by three orders of magnitude.

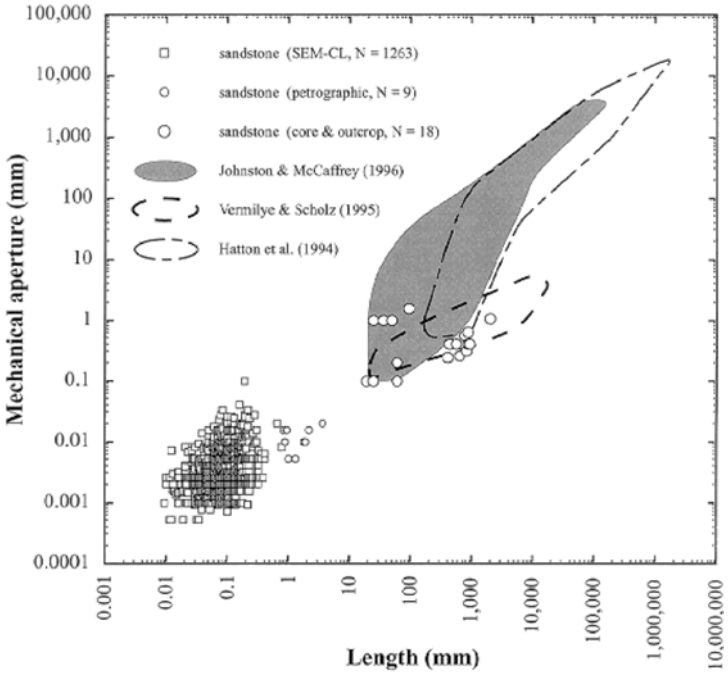

Figure 1.5 Mechanical aperture vs length for extension fractures (From Marrett and Laubach, 1997)

However, in the research of opening mode fractures in Middle Triassic to Lower Jurassic La Boca Formation sandstone, in northeastern Mexico, Laubach and Ward (2006) found no simple relation between length and aperture, but did find that long individual fractures and multi-segment arrays have small apertures relative to their length.

Almost all data sets of length and displacement or aperture relationship show considerable scatter, part of which might reflect sampling limitations (e.g., measurement along chords of fracture surfaces) and differences in fracture linkage host layer thickness and host rock strength.

Table 1.5 Summary of relationship between length and displacement or aperture

(Note: PL – Power-law, LN – Log-normal)

NO	Location	rock type	fracture mode	distribution	distribution parameter	Observation method	From	Note
1	Fault-bounded Hornelen basin of western norway	sandstone	joint		Aspect ratio: 8.0	Outcrop hand-mapping & low level aerial photographs	Odling et al., 1999 figure 5 b)	
2	Cappanawalla & Sheshymore, The Burren, Co. Clare, Ireland	Carboniferous limestone	vein	(1D) LN	$\overline{s}$ =3.66 SD =0.48	Aerial photography and digital map	Gillespie et al., 2001 Fig. 12b	No in sample is 18 (Shesh.) & 12 (Capp.). Consistent with the multi-segment veins by Vermilye & Scholz, 1995
3	Many locations	-	fault	PL	Slope=2 (1.58)		Walsh & Watterson, 1988fig.3	least-squares best-fit to the data was 1.58.
4	Neogene fault, in the Boso and Miura Peninsulas, Japan	-	fault	PL	Slope=about 1		Scholz & Cowie, 1990 Eq.4	
5	Many locations	-	fault	PL	1.46		Marrett & Allmendinger, 1991 Fig. 1	
6	Croagh Patrick	In quartzite	vein	PL	0.83		Johnston & McCaffrey, 1996 Fig 2a	measured parallel to the transport direction and perpendicular to the zone, i.e. the ac kinematic plane. n = 431
7	Loughshinny	Carboniferous calcarenites and Brigantian age calcisiltites	vein	PL	1.01		Johnston & McCaffrey, 1996 Fig 2c	n = 158
8	Bridges of Ross	In sandstone	Quartz vein	PL	0.77		Johnston & McCaffrey, 1996 Fig 2e	n = 300
9	Mace Head	In granite	Quartz vein	PL	0.67		Johnston & McCaffrey, 1996 Fig 2h	n = 16
10	North Sea fields	Jurassic horizons affected by end-Jurassic extension	fault	(2D) PL or linear	Slope=1.1 Or 1.0	Seismic reflection data	Yielding et al., 1996 Fig 14	A linear relationship and the power-law both fit the data well

11	northern North Sea			PL	$D \propto L^{1.5}$	6 datasets	Yielding et al., 1992fig 8	6 datasets This relationship agrees with the slopes of 1D and 2D fault throw. $L \propto D^{2/3}$, $C_1 \approx C_2$ -2/3
12	Pelican field, North Sea, offshore, United Kingdom		fault	PL	0.8	Seimic datasets	Gauthier & Lake, 1993 fig. 7A	

1.3.5 SPACING/FREQUENCY/ INTENSITY

Fracture spacing is the distance between two immediately adjacent fractures (nearest-neighbors) of the same set along a straight line (commonly known as scanline) perpendicular to the fractures (e.g., Priest and Hudson, 1976; Rives et al., 1992; Gross and Engelder, 1995).

Average spacing ($\overline{S}$) is calculated by summing all the spacings between nearest-neighbor fractures (S_i) and dividing by the total number (N) of fracture spacings (e.g., Narr, 1996):

$$\overline{S} = \frac{1}{N}\sum_{i=1}^{N} S_i \approx \frac{L}{N} = \frac{1}{F} \tag{1.23}$$

Fracture intensity is a ratio of the number of fractures, sum of fracture lengths, or sum of fracture surface areas to the length, area, or volume of observation, respectively (Mauldon et al., 2001). Therefore, fracture intensity has units of inverse length. Fracture intensity is most commonly determined from one-dimensional observation domains (i.e., scanlines) by dividing the number of fractures (N) by the total length (L) of the scan line:

$$F = N / L \tag{1.24}$$

The summary of some fracture spacing distributions is listed in Table 1.9. From this table, we see that negative exponential, log-normal and power-law are the most common distributions in the fracture spacing.

The physical processes controlling fracture spacings are relatively easy to understand compared to the physical mechanisms controlling fracture lengths. Fracture spacings can be due to regular deterministic or a stochastic process. Deterministic processes result in functional forms represented by geometric series, and random processes are manifest as uniform distributions (Hudson and Priest, 1983). Priest and Husdon (1981) give general examples of physical phenomena that would result in a particular functional form for measured fracture spacing in borehole data. Homogeneous

rock would produce a random distribution of fracture spacing and lead to negative exponential distributions. Some other researchers find the spacing population follows negative exponential distribution, such as Baecher et al. (1977), Cruden, (1977a), Dershowitz and Einstein (1988), Einstein and Baecher (1983), Hudson and Priest (1983), Pineau (1985), and so on.

Log-normal distribution is obtained by some researchers, such as Becker and Gross (1996), Johnston (1992), Narr and Suppe (1991), Pascal et al. (1997), Rives et al. (1994), and Sen and Kazi (1984). The power-law distribution of fracture spacings is observed in the study of Barton and Zoback (1990), Gillespie et al., (1999), Barton and Zoback (1992), Belfield and Sovich (1995), etc. Other uncommon distributions are also obtained by few researchers, such as normal distribution (Ji and Saruwatari, 1998) and gamma distribution (Castaing et al., 1996; Gross, 1993; Huang and Angelier, 1989).

The fracture intensity (or the average spacing) varies with changes in resolution of observation (Ortega et al., 2006). That is because the number of fractures observed in a domain will increase as the threshold size for fracture detection decreases. Therefore, fracture intensity (and average spacing) is scale dependent and is only meaningful if the fracture-detection threshold is quantified. Here, "scale dependent" means that the fracture intensity and average spacing depend on the observation scale (more small fractures at small scale), which is different from the "scale dependence" in Dershowitz and Herda's (1992), where scale means observation region scale, and overall fracture numbers do not change with the observation region size.

Dershowitz and Herda (1992) extend the traditional fracture spacing and intensity measures to a class of fracture intensity measures in one, two, and three dimensions without requiring reference to specific sets or orientations under the following two assumptions:

1) Fracture distributions and locations are independent of the sampling domain;

2) Fracture aperture is significantly smaller than the diameter.

All measures are summarized in Table 1.6.

Table 1.6 Measures for fracture intensity (After Dershowitz and Herda, 1992)

Dimensions of Sampling Region		Dimension of Fracture Measure: 0 Number of fracture	1 Fracture 1D size	2 Fracture area	3 Fracture volume
1	Line measure (borehole or scanline)	P10 [L^{-1}]	P11 [L^{0}]	/	/
2	Area Measure (trace plane)	P20 [L^{-2}]	P21 [L^{-1}]	P22 [L^{0}]	/
3	Volume measure (rock mass)	P30 [L^{-3}]	P31 [L^{-2}]	P32 [L^{-1}]	P33 [L^{0}]

Density Intensity Porosity

P10 is the inverse of the traditional fracture spacing measured along a scanline. Fracture spacing is a very difficult measure to interpret because it is dependent upon the relationship between the orientation of fracture and the orientation of the line along which spacing is measured. For sets of parallel fractures, the spacing measured in the field is corrected based on the angle θ between the mean pole of the fractures and the observation scanline (Priest, 1993, page 122). P10, as well as the fracture mean spacing is orientation-dependent. Because of assumption 1, P10 is scale independent.

P20 is the number of traces per unit area. P20 depends on the distribution of fracture size and as a result is scale dependent at scales smaller than the maximum fracture trace length.

P30 is the number of fracture centers per unit volume. Like P20, P30 is scale dependent and changes with the size of the region being analyzed for regions smaller than the maximum fracture size. Dershowitz and Herda (1992) comment that P30 is useful

only where fractures are much smaller than the region being analyzed, such that fracture centers represent individual fractures.

P21 is fracture trace length per area of exposure. It is scale independent because it directly incorporates fracture size, but it is orientation dependent.

P22 is the fracture area per unit area of exposure, which is the fracture porosity in two dimensions. Dershowitz and Herda (1992) do not give its orientation- and scale-dependence. However, like P11, it should be scale independent and orientation independent (for parallel fractures).

P32 is the fracture area per unit volume of rock mass. Like P21, it is scale independent because it directly incorporates fracture area, and it is orientation independent because it is a 3D measure.

P33 is the fracture volume per unit volume of rock mass, which is the fracture porosity in 3D. Like P11 and P22, it is scale independent, and orientation independent because it is a 3D measure.

The orientation and scale independence of all measures are summarized in Table 1.7. In this table, P20 is scale dependent when observing that region scale is less than the maximum trace length. Mauldon and Dershowitz (2000) improve the strategy for counting fracture numbers in the observed region. An unbiased estimate of P20 (trace density) is given by one half the number of trace ends divided by the window area (Mauldon and Dershowitz, 2000). The estimator P20 becomes scale-independent because the fracture number will not be under- or over-estimated when the domain changes dimension.

In addition, Mauldon et al. (1999) develop a new sampling method: circular scanline (shown in Figure 1.6). The use of circular scanlines eliminates the orientation bias associated with straight scanlines while still achieving the time efficiency of scanlines. Mauldon et al. (1999) also describe an unbiased estimator, n/4r, for trace intensity (P21) based on a count of trace intersections with a circular scanline, where n is

the number of intersections between fracture traces and a circular scanline of radius r. This estimator allows us to use a one-dimensional sampling region (still scanline and intersection counting) to estimate the two-dimensional intensity parameter P21.

Table 1.7 Dependence of measures for fracture intensity

(Note: "?" indicates that dependence is defined by the author)

	Orientation-dependent	Region scale-dependent
P10	Yes	No
P20	Yes	Yes (at scales <max trace length)
P30	No	Yes (at scales <max fracture size)
P21	Yes	No
P22	?No (for parallel fractures)	?No
P32	No	No
P33	No	No

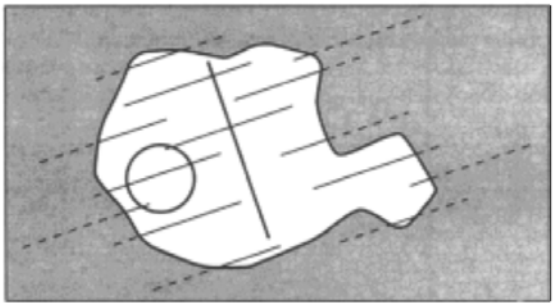

Figure 1.6 Circular scanline and straight scanline

Dershowitz and Herda (1992) also present some converting relationships between these measures. The author summarizes them in Table 1.8, where "*" indicates multiplication, "!" indicates that this value is only valid for the uniform distribution of fracture orientation, $\overline{L} = \int_0^\infty L f_L(L)\,dL$, $\overline{A} = \int_0^\infty A f_A(A)\,dA$, $\overline{V} = \int_0^\infty A t f_A(A) f_t(t)\,dA dt$, and $f_L(L)$, $f_t(t)$ and $f_A(A)$ are the probability density functions of fracture length, aperture and wall area.

In Table 1.8, C_{P2} and C_{P3} are coefficients found by the methods of stochastic geometry (Santalo, 1976). Dershowitz and Herda (1992) obtain C_{P2} and C_{P3} by simulating boreholes with different orientations within fracture networks simulated with the

FracMan discrete fracture model, as shown in Figure 1.7 and Figure 1.8. Notice that P22 on the y axis label of Figure 1.7 is P21 in this dissertation, and S_f in Figure 1.7 and Figure 1.8 is the average spacing, 1/P10. For a uniform distribution of fracture orientation, C_{P3}, is 2.0. For most fracture geometries, it will vary between 1.0 and 3.0. In parallel fracture cases, C_{P3} is $\csc(\theta)$ (Terzaghi, 1965), where θ is the angle between scanline and fracture normal.

Table 1.8 Converting between measures for fracture intensity

	P10 =	P20 =	P30 =	P11 =	P21 =	P31 =	P22 =	P32 =	P33 =
P10 *	1				C_{P2}			C_{P3}	
P20 *	⁄	1			$\overline{L}$				
P30 *	⁄	⁄	1					$\overline{A}$	
P11 *	⁄	⁄	⁄	1					
P21 *	⁄	⁄	⁄	⁄	1			$4/\pi$!	
P31 *	⁄	⁄	⁄	⁄	⁄	1			
P22 *	⁄	⁄	⁄	⁄	⁄	⁄	1		
P32 *	⁄	⁄	⁄	⁄	⁄	⁄	⁄	1	$\overline{V}/\overline{A}$
P33 *	⁄	⁄	⁄	⁄	⁄	⁄	⁄	⁄	1

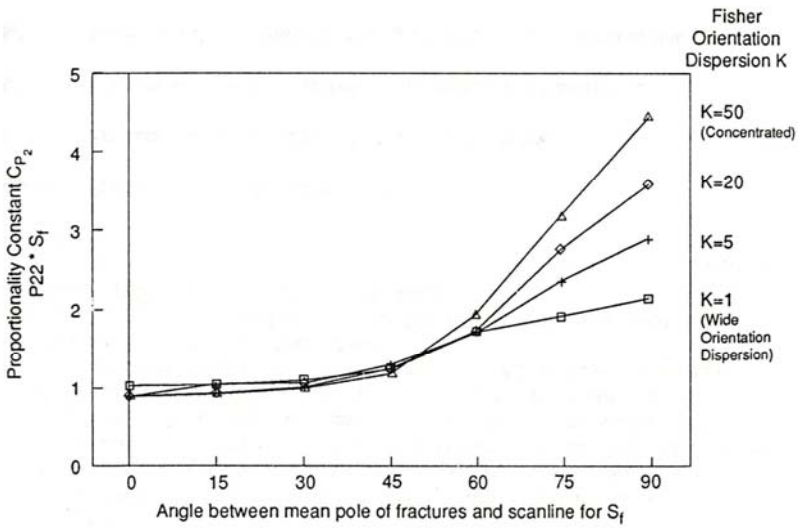

Figure 1.7 Parameter C_{P2} (From Dershowitz and Herda, 1992)

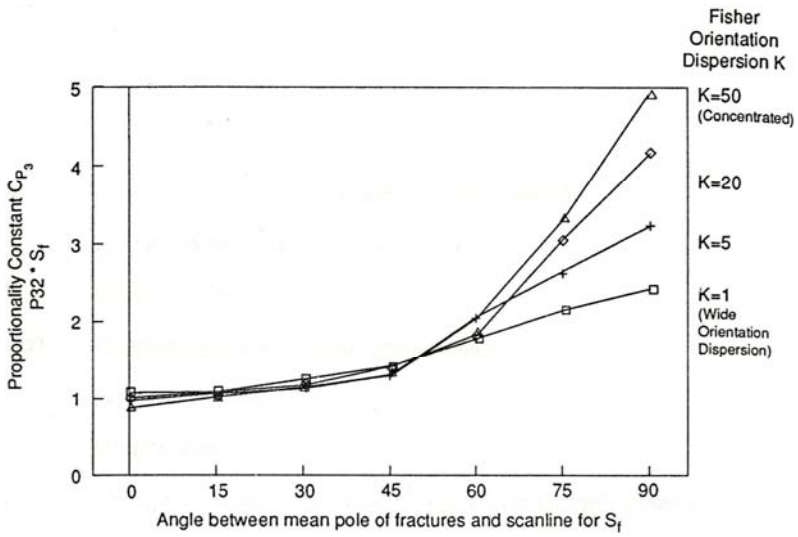

Figure 1.8 Parameter C_{P3} (From Dershowitz and Herda, 1992)

Table 1.9 Summary of fracture spacing distributions

(Note: PL – Power-law, LN – Log-normal, N–Normal, NL–Negative logarithmic, NE–Negative expoent)

NO	Location	rock type	fracture mode	Frequency distribution	distribution	distribution parameter	Observation method	From	Note
1	A quarry at Rordal, North Jylland in Denmark	chalk	joint	CFD	Clustered to anti-clustered	C_v=0.6~1.3	aerial photographs	Odling et al., 1999 figure 12)	Due to the presence of two orthogonal joint sets and the high joint density, connectivity is very high.
2	Cajon Pass scientific drill hole, near San Bernadino, California	Crystalline Rock	Joint	CFD	PL	-1.03	BHTV	Barton & Zoback, 1992	4km from the San Andreas fault, at 1750-3460 m deep
3	An East Texas Austin Chalk reservoir	chalk	Joint	CFD	PL	-	Microscanner logs (in horizontal wells)	Belfield & Sovich, 1995 Fig. 5	Unit is 2600m deep and 26m thick Spacing follows PL until average spacing is reached (0.3m). Fracture spacing is resolution dependent.
4	Cappanawalla, The Burren, Co. Clare, Ireland	Carboniferous limestone	Vein	CFD	PL	K=23.68 D=-0.69	Aerial photography and digital map	Gillespie et al., 2001 Fig. 9a	No in sample is 160. Line length is 599.08 m C_v=2.19
5	Sheshymore, The Burren, Co. Clare, Ireland	Carboniferous limestone	vein	CFD	?PL	-0.88	Aerial photography and digital map	Gillespie et al., 2001 Fig. 9a	No in sample is 103. Line length is 282.89 m C_v=1.14
6	Cappanawalla, The Burren, Co. Clare, Ireland	Carboniferous limestone	Joint	CFD	LN	$\overline{S}$=-0.037 SD=0.334	Aerial photography and digital map	Gillespie et al., 2001 Fig. 9a	No in sample is 120. Line length is 139.30 m C_v=0.63
7	Sheshymore, The Burren, Co. Clare, Ireland	Carboniferous limestone	Joint	CFD	LN	$\overline{S}$=-0.001 SD=0.299	Aerial photography and digital map	Gillespie et al., 2001 Fig. 9a	No in sample is 202. Line length is 241.1 m C_v=0.59
8	Sheshymore, The Burren, Co. Clare, Ireland	Carboniferous limestone	Joint (filtered)	CFD	N	$\overline{S}$=3.02 SD=1.562	Aerial photography and digital map	Gillespie et al., 2001 Fig. 9a	No in sample is 52. Line length is 149.38 m This is the filtered (exclude those with an ambiguous origin)

									C_v =0.48
9	Frio County, Pearsall field	Austin Chalk	Opening mode fracture	CFD	LN		Kinlaw normal core (204 fractures)	Gale, 2002fig 4	
10	Frio County, Pearsall field	Austin Chalk	Opening mode fracture	CFD	NL		Kinlaw oblique core (51 fractures)	Gale, 2002fig 4b	
11	Grove Ceeek, Waxahachie, morth central Texas	Austin Chalk	Opening mode fracture	CFD	NL		Outcrop (136 fractures)	Gale, 2002fig 4a	
12	Pedernales Falls State Park, Texas	Marble Falls Limestone	Extension fractures	CFD	LN			Gomez & Marrett, Manuscript Draft fig 3b	
13	Sweden	Granite (Stripa)	fractures	DFD	LN		Outcrop (tunnel) and core (1324 fractures)	Rouleau & Gale, 1985 Fig 8	Examined spacing for each fracture set
14		Limestone and Calcareous sandstone	Tension tectonic joints	DFD	Gamma and apparent NE		outcrop	Huang & Angelier, 1989	NE due to limitation in measuring small spacing in air photos Limestone: 800 joints Sandstone: 400, 107 joints
15	Santa Mana basin and Santa Ynez Mountains of the Transverse Ranges province of California	Chert, dolostone, porcelanite	Rock joints	DFD	LN		outcrop	Narr & Suppe, 1991 fig 4	596 joints Spacing normalized by the median spacing for each set
16	Scarborough and Whitby, on the coast of North Yorkshire, U.K.	Limestone, shale, mudstone, siltstone	joints	DFD	LN, NE, N		Outcrop Physical and numerical models	Rives et al., 1992 fig 4	320 joints (outcrop) 314 (model) Distributions evolve from NE to LN normal with increasing strain
17	Arroyo Burro	dolostone	veins	DFD	LN and PL		Outcrop and thin section	Gross & Engelder, 1995 fig 14	70, 155 (outcrop) 37, 47 (thin section) Distributions differ for outcrop (LN and PL) and thin section (PL)
18	Many location	sandstone	joints	DFD and CFD	N, PL, and NE		outcrop	Gillespie et al., 1993 fig 2, 10,11,12	Combining different fracture sets gives a NE distribution
19	NW Sardinia, Italy		veins	DFD	LN		outcrop	Simpson, 2000 fig 4b, 5ef	

1.3.6 SAMPLING BIAS OF FRACTURE SIZE

There are four biases affecting the estimation of fracture size: length bias, orientation bias, truncation bias, and censoring.

Length bias means small fractures will be underrepresented because there is a lower probability of intersecting smaller fractures than larger fractures. Orientation bias means that fractures parallel to the sampling plane will be underrepresented. Truncation bias means that fractures shorter than a predetermined length are usually not mapped.

A censoring bias is introduced because the sample area is finite, and the fracture traces may not be completely visible (Baecher et al., 1977). Censoring bias is most important for longer fractures, which are generally the more conductive fractures. With respect to censoring bias, fracture traces can be divided into three groups: (1) traces with both endpoints visible; (2) traces with one endpoint visible; and (3) traces with no endpoints visible. The trace length distribution of the first group can be determined. These fractures have a maximum length determined by the dimensions of the sample area. For the second group a distribution of minimum lengths can be estimated. For the third group all that is known is that the fracture traces are larger than the sample dimensions.

Priest and Hudson (1981) develop methods to analyze trace length data and get the bias-corrected estimating mean trace length regardless of whether the trace length distribution is known or not (see Priest, 1993 Section 6.3 and 6.4 for details).

Some analytical solutions to the censoring problem have been obtained by assuming a distributional form for the trace lengths (Long and Billaux, 1987; Einstein et al., 1979). Similarly, if a distributional form is assumed for the fracture areas, one can use the corrected trace length distribution to estimate the parameters of the area distribution (Long and Billaux, 1987). Dershowitz et al. (1991) developed an automated procedure for generating fractures of a given size distribution and sampling the system the same way

the field data were sampled. The prospective area distributions can be easily modified until a good (but necessarily unique) match to the field data is found. If only borehole measurements are available, problems associated with obtaining estimates of fracture size can be severe.

1.4 Spatial arrangement

Spatial arrangement is a fundamental characteristic for a set of natural fractures. The spatial arrangement of fractures in a fracture set is defined by how fractures are positioned relative to one another in space, where each set groups all fractures with common characteristics (e.g., orientation and cement fill) and genesis (e.g., Twiss and Moores, 1992). It is important for a range of geologic problems, such as fluid flow through fractured aquifers, petroleum reservoirs, and hydrothermal systems. It constrains fracture-growth processes and affects fracture permeability. The neglect of spatial correlation in fracture patterns can severely alter the flow in a rock mass, which is not governed by the average permeability of the rock mass, but by the existence of a highly permeable channel made up of highly clustered fractures (La Pointe, 1993). The advantages of considering spatial correlation are (1) an ability to reproduce the high connectivity and conductivity of channels that arise due to spatial correlation; and (2) reducing, and more precisely, constraining the error of estimation (La Pointe, 1993). In this section, fracture spatial arrangement analysis and simulations are introduced based on the contributions of La Pointe (1993) and Marrett et al. (2005, 2006).

1.4.1 TRADITIONAL SIMULATION METHODS

La Pointe (1993) summarizes most fracture pattern simulation methods that fall into two broad classes (stochastic-geometric and stochastic-mechanistic) depending on

their probability theories. For the purpose of this research, only stochastic-geometric methods are covered here.

1.4.1.1 Spatially uncorrelated processes

The simplest method to characterize rock mass jointing began in the 1970s (Baecher et al., 1977) and consists of idealizing jointing as a spatially uncorrelated point process to create a fracture network from probability distributions of fracture attributes. These processes, or schemes for reproducing fracture patterns, are spatially uncorrelated in that the quantity of fractures per unit area or volume, their orientations and trace lengths in a region of any size are independent of the geometry of fractures in any other region of similar size. One implication is that the presence of a large fracture occurring at any point with a particular orientation indicates nothing about the size or orientation of nearby fractures. Each fracture is entirely independent of the others. The most commonly used spatially uncorrelated models involve Poisson point, line or plane processes.

1.4.1.2 Geostatistical Methods

Geostatistical methods resemble the point processes (Section 1.4.1.1) with the significant difference that the location of the fractures and their other geometrical and hydromechanical attributes have spatial correlation; that is, they are not spatially independent processes. Spatial correlation implies that the geometry and attributes of a particular fracture or group of fractures are similar to neighboring fractures and less similar to distant ones, and that this similarity decreases as the relative distance between fractures increases. Certain features of fracture patterns in rock suggest this type of spatial correlation, which can be quantified by calculating a variogram, which will be introduced in Chapter 3.

Geostatistical quantification of fracture patterns was first recognized independently by Miller (1979) and La Pointe (1980), and subsequently demonstrated for

a wide variety of rock units by others. The first attempt to simulate rock fracturing through geostatistics was by La Pointe (1981), and was subsequently improved upon by others (Chilès, 1988; Long and Billaux, 1987). Experience indicates that there are several options for incorporating spatial correlation properties into the simulation.

La Pointe (1993) states that there are also both theoretical and operational difficulties in using forms of geostatistics to create fracture patterns. Geostatistical simulation methods often require that the variables have a particular functional form. For example, the turning bands method produces realizations that have a Gaussian spatial law, which is ill suited to simulate any phenomena that do not possess the high degree of spatial continuity that a Gaussian distribution implies. The practical difficulty in using geostatistical methods is defining the correlation structure in the directions of interest. This difficulty is two-fold (length and direction). First, the robust calculation of the variogram requires linear samples on the order of twice the length of the maximum dimension of the region over which the pattern is to be simulated, unless there is a compelling reason to suggest that spatial correlation is not present at larger scales. Such long, linear exposures are often very difficult to find in underground exposures. However, sometimes a borehole has been logged or cored over a sufficiently long interval to provide a statistically useful linear sample of the fracture population. The problem is that boreholes tend to be nearly vertical, and the correlation properties in the vertical direction are rarely transformable to the horizontal direction, which is usually the direction of interest. In essence, a borehole samples a very different population of fractures, with different hydromechanical properties, than the ones that would be sampled by a horizontal borehole or along the walls of an underground exposure.

In this research, I solve the first difficulty by using the indicator Gaussian sequential simulation (Section 3.1.5.5), which does not require a particular distribution function. For the second challenge, I use fracture measurements at the beginning of the tunnel excavation section from which spatial correlation in the direction of interest can be

obtained. The simulation can be implemented sequentially during the tunnel excavation by conditioning the simulation model with the information collected in the excavated section. These ideas will be expanded upon in Chapters 3 and 5.

1.4.1.3 Fractals

Fractal geometry is the other way to quantify the spatial or temporal dispersion of a quantity, and how this dispersion may change with the scale of observation. It is a useful mathematical model when the histogram of the quantity is a declining power-law, which describes a set of objects in which there are fewer big objects than small ones, and when the spatial relation between objects of different sizes exhibit regularities that transcend the scale of observation. Geometric aspects of a natural fracture pattern that suggest that fractals are an appropriate tool include (La Pointe, 1993): (1) the qualitative observation that there are many more small fractures than large fractures, and the quantitative findings that measured trace lengths often conform to a negative exponential distribution; (2) big fractures do not generally occur near other big fractures, but are spaced at large intervals, so that, on average, the size of a fracture is proportional to its spacing—large faults have a large spacing, microcracks have a very small spacing; (3) abutting relations, orientations and relative abundances of fractures appear to be repeated over many scales of observation; and (4) the fracture porosity of a given mechanical layer in a specific structural setting may be more or less homogeneous, since the stress is homogeneous and the mechanical properties of the rock are homogeneous—this implies that the space-filling properties of the fracture voids might also be homogeneous at different scales and locales, and hence, fractal.

The first application of fractal geometry to fracture network geometry was an attempt to characterize outcrop fracture pattern geometry in support of nuclear waste repository studies (Barton and Larson, 1985). This work was followed by several other studies, such as Chilès (1988).

1.4.2 RECENT RESEARCH IN SPATIAL ARRANGEMENT ALONG A SCANLINE

The following three papers discuss fracture spatial arrangement in terms of aperture on a one-dimensional scanline; the authors summarize traditional analysis methods and develop two innovative methods (correlation analyses and spectral analyses):

1. Traditional Analyses of Fracture Spatial Arrangement (Gomez and Marrett, Manuscript)

2. Correlation Analyses of Fracture Spatial Arrangement (Marrett et al., Manuscript)

3. Spectral Analyses of Fracture Spatial Arrangement (Hare and Marrett, Manuscript)

Fracture position along a scanline is obtained by combining the spacing between nearest-neighbor fractures and the sequence of spacings. Traditional techniques that only address fracture spacing (average, median, coefficient of variation, discrete and cumulative frequency distributions) are best suited to quantify regularly spaced fractures. Coefficient of variation and interval counting are partially successful for other types of arrangement, such as random arrangements and some cases of non-random clustering. Frequency distributions can detect such arrangements, but do not effectively quantify them. Among traditional techniques, coefficient of variation and interval counting are least affected by the minimum size (threshold) of fractures sampled. The other techniques are strongly scale-dependent, because spacing values change significantly with threshold. As a consequence, most analyses of spatial arrangement are only meaningful if the size range is stated for measured fractures.

Most traditional techniques for analyzing the fracture spatial arrangement are flawed in two ways: they ignore spacing sequence and fracture size. Spectral analysis overcomes these limitations by quantifying fracture abundance in terms of both position (i.e., translation of the analyzing wavelet along a scanline) and scale of observation (i.e.,

dilation of the analyzing wavelet). Additionally, spectral analysis allows both the size and position of fractures to be analyzed simultaneously, something that is unattainable using traditional techniques. Analysis of natural fracture data shows that clusters exist across a broad spectrum of scales, such that the largest fracture clusters are made of smaller fracture clusters, which in turn consist of still smaller clusters, and so on. This multi-scaled arrangement of clusters suggests that fractures represent a natural fractal, which can be quantified using the variance of wavelet amplitudes.

Correlation analysis is a new technique that overcomes the two limitations mentioned above and additionally quantifies spatial organization by normalizing to expected values for randomly arranged fractures. The techniques differ in terms of computational intensity, robustness of results, ability to detect anti-correlation, and use of fracture size data. Variation of spatial organization across a broad range of length scales facilitates distinguishing clustered and periodic arrangements from random arrangements. Self-organized arrangements can be distinguished from arrangements due to extrinsic organization. Comparison of results that account for fracture size with results that ignore fracture size demonstrates that spatial organization is dominated by the sequence of fracture spacings, rather than coordination of fracture size with position. Fracture size and position are not completely independent, however, because large fractures are more clustered than small fractures are.

1.4.2.1 Traditional analysis of fracture arrangement in space

1.4.2.1.1 Arithmetic Mean (Average or Mean)

Average spacing ($\overline{S}$) is calculated by summing all the spacings between nearest-neighbor fractures (S_i) and dividing by the total number (n) of fracture spacings (e.g., Narr, 1996):

$$\overline{S} = \frac{\sum_{i=1}^{n} S_i}{n} = \frac{L - \sum_{i=1}^{n} b_i}{n} \approx \frac{L}{n} \tag{1.25}$$

where L is the length of the scanline; b_i is fracture aperture.

The average spacing depends only on the sum of all fracture spacings and the number of fracture spacings measured, regardless of the sequence of fracture spacings or their individual values, so it ignores the position of each fracture with respect to fractures other than its nearest neighbors. The average spacing of fractures can indicate the typical value of fracture spacings, but not how the observed spatial arrangement compares with regularly spaced, randomly arranged, or systematically clustered fractures. The closer a spatial arrangement of fractures is to a regularly spaced set of fractures, the more representative the average spacing is.

The significance of the average fracture spacing is also limited by the fact that it ignores the wide spectrum of fracture sizes found in many natural fracture sets. Apertures can range up to at least four orders of magnitude and lengths up to at least three orders of magnitude. The implicit assumption, almost never fulfilled in estimations of average fracture spacing, is that all fractures along the scanline were detected. In fact, there will be a fracture-size threshold, below which fractures are sampled incompletely or not at all. Therefore, most natural fracture sets will not have a unique value of average fracture spacing; instead, average spacing will vary depending on the aperture threshold used during data acquisition or later analysis. As shown in Figure 1.9, for example, because there is one-to-one relationship (reciprocal) between cumulative frequency and average spacing, which are both scale related to the fracture aperture, Ortega et al. (2006) recommended the use of cumulative frequency distributions of fracture aperture to estimate the average fracture spacing. This is accomplished by inverting the value of the cumulative frequency (number of fractures above the aperture threshold per unit length of scanline).

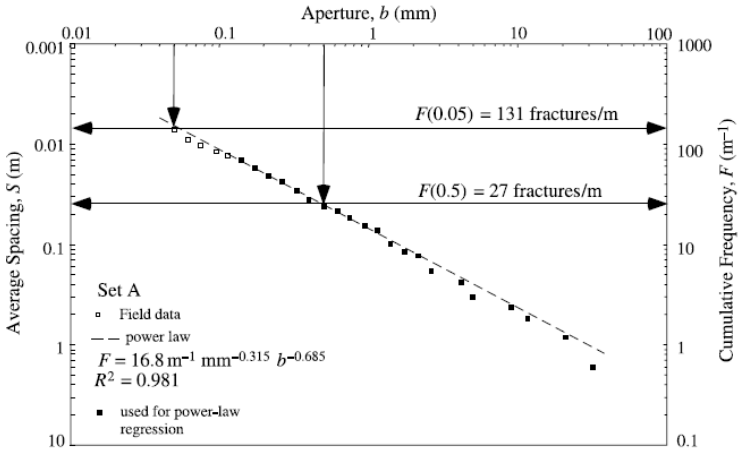

Figure 1.9 Cumulative frequency/average spacing vs. fracture size (From Ortega et al., 2006)

Although, this approach explicitly accounts for fracture size, it does not overcome the fundamental limitation of average fracture spacing as a statistic, in that it ignores the spatial position of fractures and cannot distinguish between random and non-random spatial arrangements.

1.4.2.1.2 Median

The median (S_m) is the middle value when a data set is arranged in order of size; it is the number that separates the largest half of a sample or a population from the smallest half. This implies that in order to calculate the median spacing, no information about the position of individual fractures in the scanline or about the sequence of fracture spacings is required.

The median has not been used directly to quantify the spacing between nearest-neighbor fractures along a scanline but instead has been used through what Narr (1991) called the fracture spacing index (FSI), the slope to the regression line of jointed-layer thickness versus median joint spacing (Narr and Suppe, 1991; Gross et al., 1995). The reason for using the median instead of the arithmetic mean for fracture characterization was stated by Narr and Suppe (1991): “The median is a better and more stable estimator

of the center of these asymmetric (log-normal) populations of joint spacing than is the arithmetic mean."

However, the fact that fracture spacing values commonly show large dispersion indicates that no single number, including the median, can represent many fracture sets in a meaningful way. Like average spacing, the median spacing ignores the position of each fracture with respect to fractures other than its nearest neighbors. The median only indicates the center value of the statistical sample, regardless of the range and distribution of fracture spacings. This is emblematic of the fact that there is not a unique median of fracture spacings; rather it is inherently scale-dependent.

1.4.2.1.3 Standard Deviation and Coefficient of Variation

The standard deviation (σ) is the most commonly reported measure of variability or dispersion in a set of data. The more widely the values vary, the larger the standard deviation. The standard deviation is defined as:

$$\sigma = \sqrt{\sum_{i=1}^{n}\left(S_i - \overline{S}\right)^2 \Big/ \left(n-1\right)} \tag{1.26}$$

In the case of a random arrangement of fracture, $\sigma = \overline{S} \approx L/n$, if fracture locations follow a Poisson's process, the spacing follows negative exponential distribution, which has the same value for mean and standard deviation.

Although the standard deviation can be used directly to characterize the variability of fracture spacings, it can also be expressed in proportion to the mean to yield the coefficient of variation (C_V). For a random arrangement of fractures,

$$C_V = \frac{\sigma}{\overline{S}} = 1 \tag{1.27}$$

In probability theory and statistics, the coefficient of variation is a measure of dispersion of a probability distribution. For fracture spacing analysis, the coefficient of variation is a dimensionless number that allows comparison of data sets having significantly different average spacings. The C_V in practice scales the standard deviation

by the size of the mean, making it possible to compare fracture data sets acquired at different places and/or at different scales.

Gillespie et al. (2001) appropriately proposed using the coefficient of variation to quantify the degree of clustering for a fracture data set. For fractures arranged according to a Poisson's process, the mean and the standard deviation are equal, therefore $C_V = 1$. If fractures are more clustered than random, then the arrangement of fractures will have a large σ compared with the corresponding S, with small spacings located inside the clusters and large spacings between the clusters, making $C_V > 1$. In contrast, if fractures are anti-clustered (i.e., more regularly spaced than random) then σ will be small when compared to S and therefore $C_V < 1$ (Gillespie et al., 2001).

Although in some cases C_V can distinguish a fracture spacing data set from random, it cannot determine how many clusters there are nor what cluster spacing is or what kind of organization (e.g., fractal) the clusters have because C_V ignores the spatial position of fractures.

1.4.2.1.4 Interval (box) counting

Interval counting, the one-dimensional equivalent of box counting in a plane (e.g., Barton and Larsen, 1985; Walsh and Watterson, 1993), is a classic technique for quantifying fractal patterns in space. The outcome of interval counting for fractures typically produces a nominal estimate of a fractal dimension for the spatial arrangement of fractures, or alternatively a rejection of the hypothesis that fractures follow a fractal arrangement in space. In principle, interval counting might identify and characterize a fractal arrangement of fractures.

Interval counting is achieved by tiling a scanline into intervals of uniform length and counting the number of intervals (N_b) that contain at least one fracture. This procedure is repeated for a wide range of interval sizes (r). If the spatial arrangement of fractures constitutes a natural fractal, then the resulting data should form a line in a log-log graph of interval count versus interval size:

$$N_b = ar^{-d} \tag{1.28}$$

where d is a fractal dimension. A set of data from natural fractures can only follow such a non-trivial power-law for a limited range of interval sizes, due to the fact that a finite number of fractures (n) are represented in a scanline of finite length (L). These effects impose upper bounds on the interval count, such that N_b cannot exceed n for $r \leqslant S$ nor L/r for $r \geqslant S$. On a log-log graph of interval count versus interval size, the upper bounds appear as lines that demarcate trivial fractal dimensions of 0 and 1, respectively, with a crossover at $r = S$. In the case of fractures that show perfectly regular spacing, interval counting results will follow the upper bounds. This must occur, because if $r \leqslant S$ then no counting interval can contain two fractures, so the number of intervals containing a fracture will equal the number of fractures. Alternatively, if $r \geqslant S$ then no counting interval can be devoid of a fracture, so the number of intervals containing a fracture will equal the number required to cover the entire scanline.

In the case of randomly located fractures, interval counting results will follow the law:

$$N_b = \frac{L}{r}\left[1 - e^{-n\frac{r}{L}}\right] \tag{1.29}$$

For a data set from natural fractures, an interval count larger than the value predicted by Eq. (1.29) indicates that fractures are more regularly spaced than a random arrangement (i.e., anti-clustered) at a length scale corresponding to the interval size. On the other hand, a count smaller than the value predicted by Eq. (1.29) indicates that fractures are more clustered than a random arrangement.

1.4.2.2 Correlation analysis of fracture arrangement in space

Statistical analyses of fracture spacing, the fracture-perpendicular distance from one fracture to the next in a set of parallel fractures, along scanlines are potentially flawed in two different ways: they ignore both the sequence of fracture spacings and

fracture sizes. Box counting is affected by significant artifacts (Harris et al., 1991; Gillespie et al., 1993; Brooks, 1994) and has limited predictive power (Gomez and Marrett, Manuscript). Marrett et al. (Manuscript) present new techniques that overcome such limitations and additionally quantify spatial organization by normalizing to expected values for randomly arranged fractures. The techniques differ in terms of computational intensity, robustness of results, ability to detect anti-correlation, and use of fracture size data. Variation of spatial organization across a broad range of length scales facilitates distinguishing clustered and periodic arrangements, opposite forms of organization, from random arrangements.

The new techniques Marrett et al. (Manuscript) present are derived from the correlation sum (e.g., Grassberger, 1983; Hentschel and Procaccia, 1983; Hilborn, 1994) and the geostatistical semivariogram (e.g., Deutsch and Journel, 1998; Jensen et al., 1997), except that in both cases normalization to statistically random fracture arrangements provides the most physical insight. Both approaches explicitly address fracture positions, so they implicitly account for sequence of fracture spacings.

1.4.2.2.1 Normalized Semivarigram

Geostatistical techniques (e.g., Deutsch and Journel, 1998; Jensen et al., 1997) permit simultaneous analysis of quantities of interest (such as fracture size) and their variation in space.

Consider aperture measurements made along a continuous scanline where the fracture locations are additionally recorded, as shown in Figure 1.10. Then the resulting data can be represented as a binary indicator sequence (I) as a function of position along the scanline (x) by dividing the scanline into linear elements that lie entirely within a fracture aperture ($I = 1$) or between fractures ($I = 0$).

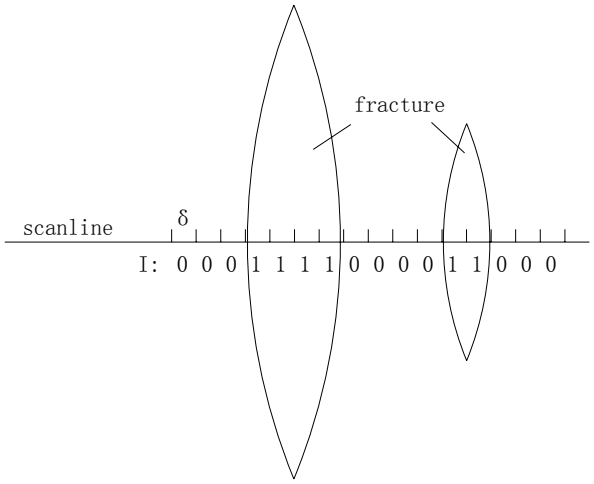

Figure 1.10 Sktech for binary indicator sequence

An element size (δ) is needed to faithfully represent the differences between the smallest apertures we can measure. The resulting indicator sequence provides a quantitative description of all fracture locations and apertures. Geostatistical analysis (e.g., Carr, 1995) of indicator sequences for fractures can be accomplished by calculating the indicator semivariance (γ) for a range of length scales (λ), sometimes referred to as lags or correlation lengths:

$$\gamma(\lambda) = \sum_{i=1}^{(L-\lambda)/\delta} \frac{\left[I(x_i) - I\left(x_{i+\lambda/\delta}\right) \right]^2}{2(L-\lambda)/\delta} \tag{1.30}$$

where L is the length of the scanline. From the equation, high correlation between fractures yields low semivariance. Nomalizing the observed semivariance difference by the expected semivariance difference (see Marrett et al., Manuscript, for details) yields an a priori estimate of the spatial correlation of fractures as a function of length scale.

1.4.2.2.2 Normalized Correlation Sum

The correlation sum (e.g., Grassberger, 1983; Hentschel and Procaccia, 1983; Hilborn, 1994), also known as the two-point correlation integral, can be used to analyze the spatial arrangement of a fracture set in the absence of fracture size information (e.g., Davy et al., 1992; Bour and Davy, 1999; Bonnet et al., 2001). Marrett et al. (Manuscript)

provide an intuitively meaningful interpretation of the correlation sum by normalizing the observed correlation sum with expected values for a random arrangement.

For the correlation sum, each fracture in a scanline is represented by the distance from the start of the scanline to the near (x_i) and far (y_i) margins of the fracture, such that $y_i - x_i$ equals the aperture of the ith fracture, although the aperture per se is otherwise ignored. The correlation sum (C) is simply the fraction of all fracture pairs for which the fracture separation ($x_j - y_i$) is less than the length scale (λ_k) under consideration:

$$C(\lambda_k) = \frac{2}{N(N-1)} \sum_{i=1}^{N} \sum_{j=i+1}^{N} H\left[\lambda_k - (x_j - y_i)\right] \tag{1.31}$$

where N is the total number of fractures along the scanline and H is the Heaviside step function (See Appendix A). A more meaningful interpretation of the correlation sum can be gained through a comparison with the expected correlation sum for fractures located randomly on a scanline, which is:

$$C_{random}(\lambda_k) = \frac{\lambda_k}{L}\left(2 - \frac{\lambda_k}{L}\right) \tag{1.32}$$

Normalizing the observed correlation sum by the expected correlation sum yields an a priori estimate of the spatial correlation of fractures as a function of length scale. Normalized correlation sum will fall below 1 for length scales at which fractures are anti-correlated, and will plot above 1 for positive correlation.

1.4.2.2.3 Normalized Correlation Count

The normalized correlation sum is poor at characterizing periodic behavior, such as regular spacing of fractures, because the integral/summation operator cancels positive correlation with anti-correlation at progressively longer length scales. For this reason, Marrett et al. (Manuscript) develop a variation of the correlation sum by analyzing its differences. The correlation count (c) is defined as the difference between two values of the correlation sum:

$$c(\lambda_k) = c(\lambda_{k+m}) - c(\lambda_{k-m}) \tag{1.33}$$

where m can be adjusted to avoid null results. The correlation count amounts to a binned version of the correlation sum, with boundaries of length-scale bins represented by λ_k. Consequently, the correlation count is the fraction of all fracture pairs for which the fracture separation is less than λ_{k+m} but more than λ_{k-m}. Unlike the correlation sum, which can only increase with increasing length scale, the correlation count can increase or decrease. Using logarithmic graduations of length scale, the correlation count follows a power-law having the same exponent and a comparable range as found with the correlation sum. Namely, the correlation count is just as useful as the correlation sum regarding assessment of fractal scaling. Like the correlation sum, normalization of the observed correlation count with expected values for fractures located randomly on a scanline yields a more physically meaningful interpretation in the form of spatial correlation:

$$c_{random}\left(\lambda_k\right) = \frac{\lambda_{k+m} - \lambda_{k-m}}{L}\left(2 - \frac{\lambda_{k+m} + \lambda_{k-m}}{L}\right) \tag{1.34}$$

The normalized correlation count is more effective than the sum at detecting fractures with approximately regular spacing. In this case, peaks of spatial correlation greater than 1 occur at a length scale corresponding to the dominant fracture spacing and its multiples, and troughs of values less than 1 occur at intermediate length scales. In order to be statistically significant, peaks and troughs should reach beyond confidence intervals for equivalent random arrangements.

1.4.2.2.4 Weighted Correlation Count

Marrett et al. (Manuscript) develop an additional approach to account for fracture size in correlation count analysis by weighting results according to fracture size. The weighted correlation count (c') is defined as:

$$c'\left(\lambda_k\right) = C'\left(\lambda_{k+m}\right) - C'\left(\lambda_{k-m}\right) \tag{1.35}$$

where

$$C'(\lambda_k) = \frac{2}{\left(\sum_{i=1}^{N} b_i\right)^2 - \sum_{i=1}^{N}\left(b_i^2\right)} \sum_{i=1}^{N}\sum_{j=i+1}^{N} b_i b_j H\left[\lambda_k - \left(x_j - y_i\right)\right] \tag{1.36}$$

and b_i is the kinematic aperture of the ith fracture. Weighting by fracture size has the effect of emphasizing correlation between large fractures at the expense of small fractures. Spatial correlation can be estimated by normalizing the weighted correlation count to expected values for fractures located randomly on a scanline.

1.4.2.3 Spectral analysis of fracture arrangement in space

Hare and Marrett (Manuscript) develop an approach for wavelet analysis that can be applied to fracture data to overcome the limitation of traditional analyses of fracture arrangement in space. Wavelet techniques quantify fracture abundance in terms of both position (i.e., translation of the analyzing wavelet along a scanline) and scale of observation (i.e., dilation of the analyzing wavelet). Additionally, the new method of analysis allows both the size and position of fractures to be analyzed simultaneously, something that is unattainable using traditional techniques. Analysis of natural fracture data shows that clusters exist across a broad spectrum of scales, such that the largest fracture clusters are made of smaller fracture clusters, which in turn consist of still smaller clusters, and so on. This multi-scaled arrangement of clusters suggests that in some cases fractures represent a natural fractal, which can be quantified using the variance of wavelet amplitudes. Because this method is not related to this dissertation, the original paper can be refered if interested.

The techniques described in Section 1.4.2.2 and 1.4.2.3 are useful to characterize fracture spatial arrangements. However, they are awkward for the inverse process—simulation. In this research, geostatistics are used to simulate fracture spatial arrangements in Chapters 3 and 5.

CHAPTER 2: CURRENT STATE OF THE ART AND STATE OF PRACTICE OF GROUNDWATER INFLOW INTO TUNNELS

This chapter summarizes literature related to tunnel groundwater inflow. Conceptual models, assumptions, governing equations, and boundary conditions are also included.

Prediction of water inflow into tunnels is one of the essential tasks of underground engineering. Inflow predictions determine pumping requirements and the extent to which groundwater control measures will be needed. However, accurate prediction of water inflow into rock tunnels during construction is a major challenge, because all of the controlling factors may not be accurately determined ahead of time (Heuer, 1995). For instance, the permeability distribution of fractured crystalline rocks is very heterogeneous, ranging over many orders of magnitude and on many scales. Only a few highly conductive pathways control the total groundwater flow in the rock mass surrounding a deep tunnel.

2.1 Problems in tunnel construction due to water inflow

Problems during tunnel construction due to water inflow mainly include like following four aspects (Goodman et al., 1965; Heuer, 1995; Löw, 2002; Zhang and Franklin, 1993):

2.1.1 The drawdown of piezometric levels in overlying soil strata leads to consolidation settlement of compressible soils, subsidence and foundation damage, lowering of the water table, draining of surface wells, and the drying up of springs and

lakes. These problems may apply a significant cost for the tunnel owner, and may lead to lengthy claims that may stop or seriously delay tunnel construction.

2.1.2 A second problem is the erosion of fresh concrete that is placed for final lining (liner deterioration). Corrosion of reinforcement steel by salt water in undersea tunnels requires extensive planning for protection of the concrete until it sets. This problem can occur for inflows in the range of 3 L/min/m (4.16 gal/min/ft), or more, of the tunnel. Groundwater flow also interferes with the bonding of shotcrete to wet rock. Furthermore, it causes erosion of filling materials from joints and shear zone or the rock material itself. Moderate inflows also can produce such problems.

2.1.3 Difficult and unsafe tunneling conditions and difficulty of working in wet conditions of heavy inflow result in reduced worker efficiency, a slow rate of advance, reduced efficiency of the muck removal system, mechanical equipment downtime, collecting and handling water in the tunnel, providing treatment before discharge at the surface, and difficult blasting. These problems can occur for inflows in the range of several hundred to several thousand L/min.

2.1.4 Conditions of high flow, water pressure, and gradient of the total head i (body force = $i\gamma_w$) can undermine the structural stability of the rock mass around the tunnel.

2.2 Groundwater inflow features in rock tunnels

Groundwater flow around and into tunnels is driven by gradients of total head, which are mainly composed of two components, the elevation head and pressure head

(generally, the velocity head can be ignored). The total head at the boundary of an open tunnel corresponds to the tunnel elevation plus the atmospheric pressure head. The pressure head component in a saturated formation is always greater than the atmospheric pressure in the open tunnel. This implies that for every open tunnel lying below the water table only flow into the tunnel can occur and the tunnel can never lose any fluid to the saturated formation. Exceptions are in tunnels above the groundwater table or in pressure tunnels where the fluid pressure inside the tunnel often exceeds the formation fluid pressure (Löw, 2002).

As shown in the following, water flow in tunnels can be classified in terms of the different locations where the inflow occurs and the different flow types or phases as hydraulic features change.

2.2.1 HEADING INFLOW AND WALL SIDES INFLOW

2.2.1.1 Heading inflow

Heading inflow is the water inflow into the tunnel through the tunnel face. Heading inflow is usually greater initially than long-term steady state because of:

- Three dimensional flow (water flows in from ahead of the tunnel, as well as from the sides);
- Higher hydraulic gradient. Higher water pressure exists closer to the advancing tunnel face. This means a higher hydraulic gradient causes a higher water flow rate through the rock mass. With time, as the tunnel advances, the initial transient hydraulic gradient condition decreases to a long-term steady-state condition.
- Storage depletion. Water stored in voids in the rock mass adjacent to the tunnel contributes to initial in flow, but drains out over a period of time.

The magnitude of initial heading inflow and the time required for it to decrease to a long-term steady-state condition are determined by a complex interaction of such factors as permeability of the rock mass, storage coefficient describing volume of water stored in voids, three-dimensional variability of permeability and storage coefficient, recharge characteristics, and rate of advance of tunnel heading.

Heuer (1995) gives an approximate estimate of heading inflow q_h:

$$q_h = F_h \times q_s \tag{2.1}$$

where the heading inflow factor F_h is a number between about 1 and 5 (shown as Table 2.1), and more permeable rock zones tend to give up their water more easily. q_s is the steady state inflow per unit tunnel length.

The typical values of the heading inflow factor of different rock permeabilities are shown in Table 2.1.

Table 2.1 The typical heading inflow factor value (After Heuer 1995)

Geologic interpretation	Equivalent permeability k_e cm/sec	Heading inflow factor F_h
Rock material	<1.0E-6	1.0
Few joints, tight	1.0E-6 ~ 3.0E-6	
	3.0E-6 ~ 1.0E-5	
Typical joint conditions	1.0E-5 ~ 3.0E-5	1.2
	3.0E-5 ~ 1.0E-4	1.5
	1.0E-4 ~ 3.0E-4	2.0
Influence of structural disturbance or special origin	3.0E-4 ~ 1.0E-3	3.0
	1.0E-3 ~ 3.0E-3	4.0
	>3.0E-4	5.0

There are analytical and closed-form methods to calculate the time necessary to reach a steady state for simple conditions, such as an infinitely long tunnel in a uniform aquifer, but numerical methods must be used for more complex situations. Actual water flow behavior seems to vary widely in different rock tunnels, even from place to place in the same tunnel, depending upon specifies of the rock fracture system and other boundary

conditions. In some cases, rapid bleed-off occurs within a matter of days, and sometimes only hours, while in other cases it requires weeks and months (Heuer, 1995).

Laughton (1998) evaluated the qualitative impact of groundwater inflow on tunnel boring machine (TBM) operations. He suggests dividing estimated water inflow at the tunnel heading into three categories, similar to Goodman et al. (1965) and the California Department of Water Resources (DWR) as shown in Table 2.2.

Table 2.2 Heading inflow impact on TBM operations

Category	Consequence (Laughton)	Quantity of inflow (Laughton)		Total inflow (DWR, Goodman et al.)	
		L/min per meter of tunnel	gpm per foot of tunnel	L/min	gpm
Small inflow	No problem	< 3	<4	22~110	100~500
Moderate inflow	Minor Problem	3~35	4~50	110~330	500~1500
High inflow	Major Problem	>35	>50	>330	>1500

2.2.1.2 Inflow through the tunnel walls

Referring to conditions that exist during construction, most of the existing conceptual flow models describe inflow through the tunnel walls. More details will be shown in Section 2.3 of this chapter.

2.2.2 FLOW STAGE CATEGORY

As total head and pressure around a tunnel in an aquifer develops over time, the flow pattern and tunnel inflow rate can be classified into several regimes or phases. Many researchers have worked with different flow stages and different boundary conditions. The main contribution list is shown in Table 2.3.

In most cases, an unlined tunnel section represents an inner boundary condition inside an aquifer that can be described by a constant pressure head value, instead of a constant discharge value.

Table 2.3 Main contribution list in different flow stage category

Category		Constant total head boundary	Non constant total head boundary (local or regional water table drawdown)	
			Confined flow	Unconfined flow
Transient flow	Early radial flow	Jacob & Lohman, 1952		
	Early linear flow	Can be derived following the approach Murdoch & Franco, 1994	Kawecki, 2000	Kawecki, 2000
Long term flow		Goodman et al., 1965 Zhang & Franklin, 1993 Lei, 1999	Late linear flow: Löw, 2002	Dupuit Horizontal flow: Goodman et al., 1965

2.2.2.1 Phase 1: early radial flow

If, before tunneling, the total head is constant and if we assume that the tunnel opening is created simultaneously over the entire section length under consideration, then we can expect purely radial flow into the tunnel since the early stages of the inflow process, as shown in the lower graphs of Figure 2.1.

Jacob and Lohman (1952) described the solution for the transient radial flow for well flow with asymptotic constant total head test. The transient flow model for a tunnel can be obtained by rotating the well flow model 90 degrees, as shown in Figure 2.1. The reason for the validity of this operation is that both the well model and the tunnel model share the same governing equation and boundary conditions in this transient flow phase, until the perturbation in the equipotential lines reaches any boundary, such as the ground water surface and the impervious bottom.

Indeed, the solution of Jacob and Lohman (1952) assumes infinite radial flow and is valid as long as the total head change in the aquifer, induced by the drainage of the tunnel, does not reach any boundary, i.e., the circular equipotential line does not reach the

upper boundary (groundwater table in an unconfined aquifer or upper impermeable layer in a confined aquifer) and the lower boundary (lower impermeable layer).

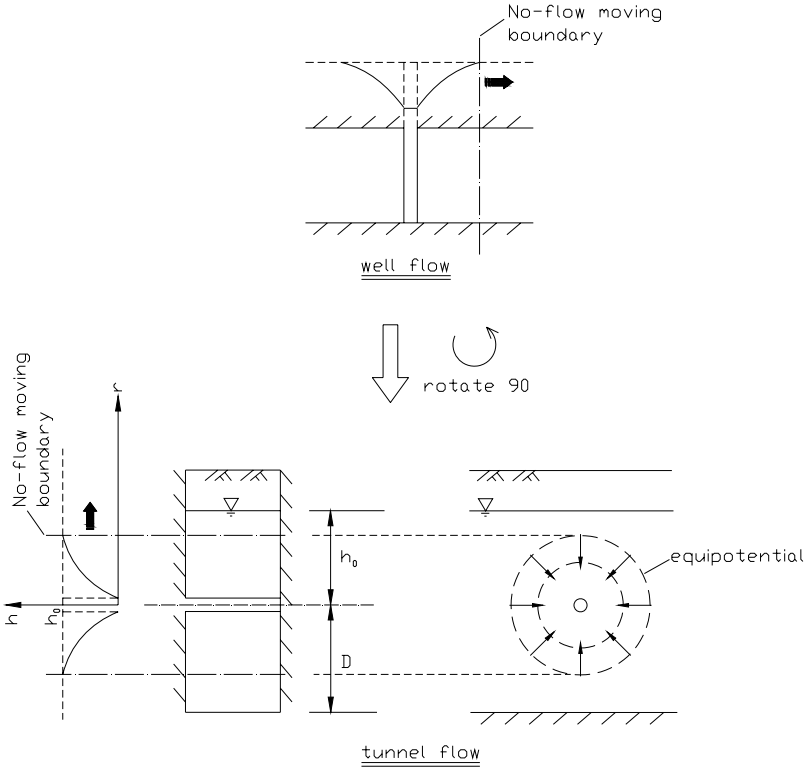

Figure 2.1 Sketch of transient radial flow in the well and tunnel

2.2.2.2 Phase 2: early linear flow

In this phase, the total head (the water table in unconfined aquifer case) will start to decline as soon as the pressure drop from the draining tunnel reaches the water table.

If constant total head boundary conditions apply above the tunnel, the early linear flow that links the radial flow model of Jacob and Lohman (1952) (Section 2.3.2.1.1) to the long-term steady-state solution of Goodman (1965) (Section 2.3.2.3.1) or Lei (1999) (Section 2.3.2.3.1.3) can be derived analytically in the Laplace space by following the approach of Murdoch and Franco (1994). However, for many tunnels where local or regional water table drawdown can be observed, assumptions made in the analytical

solution of Murdoch and Franco (1994) do not hold. Therefore, numerical groundwater flow simulations are often used to describe the flow system and tunnel inflow rate evolution for cases that have more complicated boundary conditions.

First order estimations of water table drawdown and tunnel inflow rate can be made for the case when the flow pattern can be approximated by a superposition of linear horizontal flow with vertical flow to the tunnel. Kawecki (2000) developed a set of equations for this case that are based on approximations derived for horizontal oil wells in confined aquifers (Section 2.3.2.2). In the opinion of this author, Kawecki's method is an approximate one for tunnel flow, because the pressure head at the tunnel wall is constant, whereas in horizontal oil wells the discharge rate is constant. The solution in unconfined aquifers can be obtained by substituting certain parameters in the confined solution. Kawecki (2000) does not include vertical groundwater recharge in the solutions, which can be an important factor for the location of a free water table above a draining tunnel. Therefore, these solutions overestimate water table drawdown and underestimate tunnel inflow, as long as there is groundwater recharge from the surface.

2.2.2.3 Phase 3: long-term flow

Long-term flow can be seen as steady-state flow in which the total head in the ground does not, or does insignificantly, change in time. Boundary conditions may vary from case to case, for example constant total head boundary in the whole domain or variable total head in the domain.

If the total head is constant, the only situation in which no water table drawdown occurs is when the upper boundary corresponds to an extended surface water body—a lake or the sea—or a prolific aquifer. For small ratios of tunnel inflow to surface recharge, the drawdown will also be minor and the groundwater surface may be treated as a constant total head boundary. When steady-state conditions have been reached, the

steady-state discharge formulations of Goodman (1965) or Lei (1999) may be used. The sketch of this long-term flow can be seen in Figure 2.2, in which the upper boundary remains fixed regardless of whether it is located above or below the ground surface.

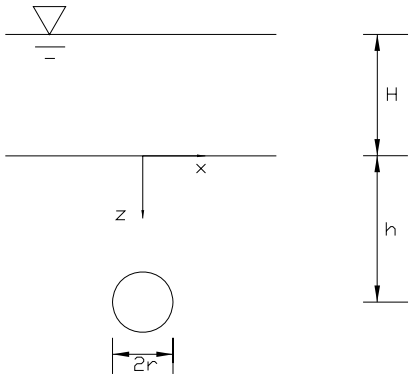

Figure 2.2 Sketch of long-term flow (constant total head boundary case)

On the other hand, if the water table retains its funnel shape after the early linear flow stage, the flow can be seen as steady-state flow/long-term flow. For unconfined aquifers, approximate solutions are available for Dupuit horizontal flow and a parabolic (Goodman et al., 1965) (Section 2.3.2.3.1) or elliptical (Perrochet and Musy, 1992) (Section 2.3.2.3.2.4) drawdown surface. When the aquifer is unconfined and drawdown reaches the tunnel crown, the flow sketch is shown in Figure 2.3.

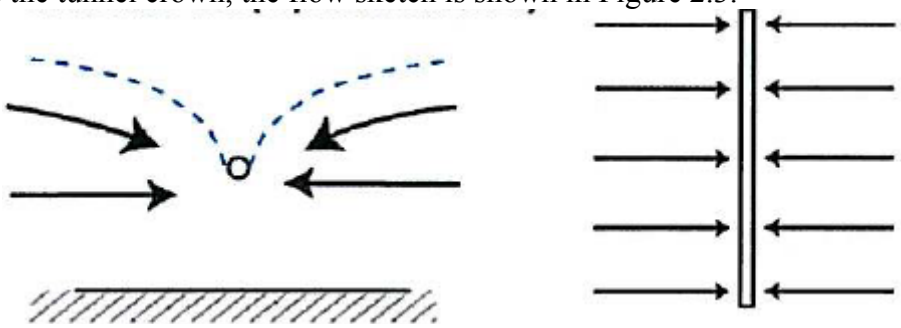

Tunnel end view Plane view

Figure 2.3 Sketch of long-term flow (non-constant total head boundary case)

2.2.3 GOVERNING EQUATIONS IN A DARCIAN MEDIUM

2.2.3.1 Darcy's law

In a point of a three-dimensional space, the flow rate vector is described by its three components v_x, v_y and v_z (see Figure 2.4).

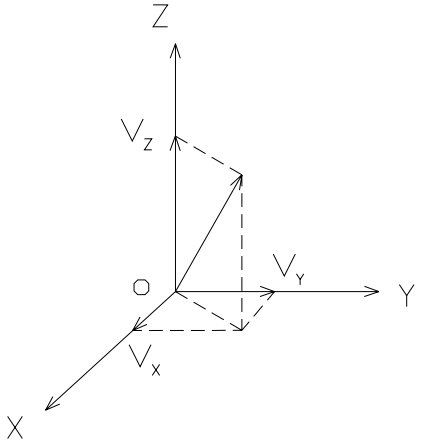

Figure 2.4 Flow rate vector

The generalization of Darcy's law is:

$$\begin{aligned} v_x &= -k_{xx}\frac{\partial h}{\partial x} - k_{xy}\frac{\partial h}{\partial y} - k_{xz}\frac{\partial h}{\partial z} \\ v_y &= -k_{yx}\frac{\partial h}{\partial x} - k_{yy}\frac{\partial h}{\partial y} - k_{yz}\frac{\partial h}{\partial z} \\ v_z &= -k_{zx}\frac{\partial h}{\partial x} - k_{zy}\frac{\partial h}{\partial y} - k_{zz}\frac{\partial h}{\partial z} \end{aligned} \tag{2.2}$$

where h is the total head, and $k_{xx}, k_{xy}, k_{xz}, k_{yx}, k_{yy}, k_{yz}, k_{zx}, k_{zy}, k_{zz}$ are the components of the hydraulic conductivity tensor.

If the x,y,z-directions are the principal directions of permeability, Eq.(2.2) then reduces to:

$$\begin{aligned} v_x &= -k_x\frac{\partial h}{\partial x} \\ v_y &= -k_y\frac{\partial h}{\partial y} \end{aligned} \tag{2.3}$$

$$v_z = -k_z \frac{\partial h}{\partial z}$$

2.2.3.2 Equation of continuity

If the fundamental physical principle of conservation of mass is applied to the element in Figure 2.5, the difference between inward flow amount and outward flow amount equals the difference in stored water (if water is considered incompressible), i.e.:

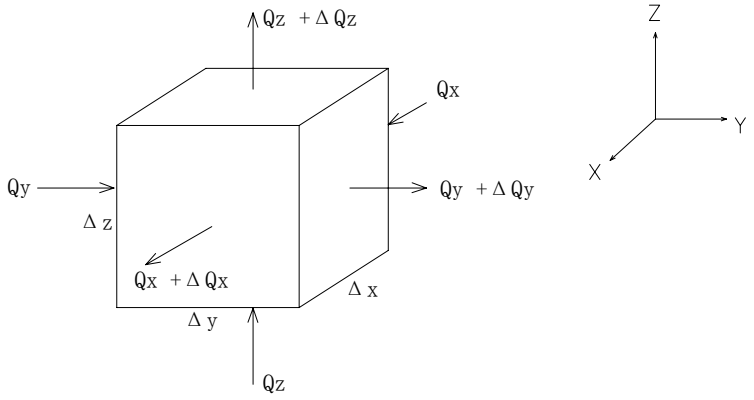

Figure 2.5 Flow amount in and out of element

$$\Delta Q_x + \Delta Q_y + \Delta Q_z + \Delta Q_S + G = 0 \tag{2.4}$$

where $\Delta Q_x = \rho v_x \Delta y \Delta z \Delta t$, $\Delta Q_y = \rho v_y \Delta x \Delta z \Delta t$, $\Delta Q_z = \rho v_z \Delta x \Delta y \Delta t$; ΔQ_S is the storage increment in this element, $\Delta Q_S = \rho S_s \Delta h \Delta x \Delta y \Delta z$. S_s [L^{-1}] is specific storage, and G is the source/sink term, $G = \rho S_G \Delta x \Delta y \Delta z \Delta t$. S_G [T^{-1}] is the strength of source/sink.

2.2.3.3 Flow equations

By substituting Eq.(2.3) into Eq.(2.4), one obtains,

$$S_s \frac{\partial h}{\partial t} = -\left[-\frac{\partial}{\partial x}\left(k_x \frac{\partial h}{\partial x} \right) - \frac{\partial}{\partial y}\left(k_y \frac{\partial h}{\partial y} \right) - \frac{\partial}{\partial z}\left(k_z \frac{\partial h}{\partial z} \right) \right] - S_G \tag{2.5}$$

If the hydraulic conductivity is spatially uniform and isotropic, Eq.(2.5) can be simplified as follows:

$$S_s \frac{\partial h}{\partial t} = k \nabla^2 h - S_G \tag{2.6}$$

where ∇^2 is Laplace operator.

Futher, if there is no sink/source in the element, Eq.(2.5) becomes:

$$S_s \frac{\partial h}{\partial t} = k\nabla^2 h \tag{2.7}$$

which is Laplace's equation.

If steady state flow is considered, Eq.(2.5), (2.6) and (2.7) become, respectively,

$$\frac{\partial}{\partial x}\left(k_x \frac{\partial h}{\partial x}\right) + \frac{\partial}{\partial y}\left(k_y \frac{\partial h}{\partial y}\right) + \frac{\partial}{\partial z}\left(k_z \frac{\partial h}{\partial z}\right) - S_G = 0 \tag{2.8}$$

$$k\nabla^2 h - S_G = 0 \tag{2.9}$$

$$\nabla^2 h = 0 \tag{2.10}$$

2.2.4 THE IMPORTANCE OF TUNNEL ADVANCE RATE

Anagnostou (1995) pointed out that except for the case of highly permeable ground or very slow excavation, the excavation advance rate *v* must be taken into consideration as an additional parameter of the mathematical model because the alteration of the hydraulic head field takes place simultaneously with the process of excavation. The finite-element method was used to solve the diffusion equation for this seepage flow problem. I reformulated the governing equations within a frame of reference that advances together with the tunnel heading to remedy some disadvantages pertaining to the traditional fixed coordinate system.

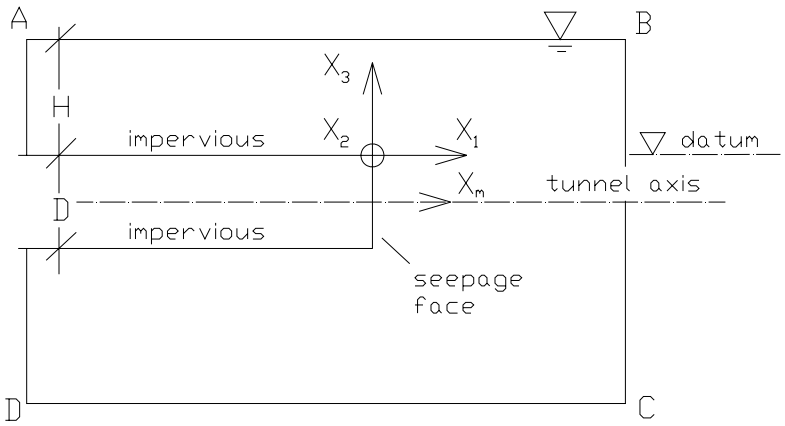

Figure 2.6 Geometric lay-out with the co-ordinate system

Assumptions:

A. Circular cross-section tunnel with impervious side wall and seepage tunnel face;

B. For the following model 2, the capillary fringe is neglected (i.e., the free surface is an abrupt interface between air and water).

C. The total stress tensor remains constant (i.e., the displacement field and the hydraulic head field can be uncoupled).

Governing equations:

Basic equation in the fixed coordinate system (Eq.(2.5) with $S_G = 0$):

$$S\frac{\partial h}{\partial t} = \frac{\partial}{\partial x_i} k \frac{\partial h}{\partial x_i} \tag{2.11}$$

Transformed equation in the co-ordinate system moving with the tunnel:

$$S\frac{\partial h^*}{\partial t} - Sv_m \frac{\partial h^*}{\partial x_m^*} = \frac{\partial}{\partial x_i^*} k \frac{\partial h^*}{\partial x_i^*} \tag{2.12}$$

At the quasi-steady state (a steady state is assumed when the flow is close to a steady state), the following equation holds:

$$\frac{\partial}{\partial x_m^*} k \frac{\partial h^*}{\partial x_m^*} + Sv \frac{\partial h^*}{\partial x_1^*} = 0 \tag{2.13}$$

where, S is the storage coefficient of the aquifer;

h is the total head, h^* is the total head in the face-fixed frame of reference;

x_i is co-ordinate axis, x^*_i is co-ordinate axis in the face-fixed frame of reference (i=1,2,3);

x_m is the tunnel axis, x^*_m is the tunnel axis in the face-fixed frame of reference;

k is the intrinsic permeability;

v is the excavation advance rate, v_m is the vector in direction of advance.

Initial and boundary conditions:

Let x be a point in the domain ABCD.

Model 1: the position of the water table remains constant

$$h(x,0) = H$$

$$h(x,t) = \begin{cases} H,\ for\ t \geq 0\ and\ x\ at\ BCDA(far\ field\ boundary) \\ H,\ for\ t \geq 0\ and\ x\ at\ AB \end{cases}$$

$$q(x,t) = 0,\ for\ t \geq 0\ and\ x\ at\ tunnel\ wall$$

$$h(x,t) = x_3,\ for\ t \geq 0\ and\ x\ at\ tunnel\ face$$

Model 2: the aquifer is not recharged (i.e., the groundwater table is variable)

$$h(x,0) = H$$

$$h(x,t) = \begin{cases} H,\ for\ t \geq 0\ and\ x\ at\ BCDA(far\ field\ boundary) \\ x_3\ (free\ face),\ for\ t \geq 0\ and\ x\ at\ AB \end{cases}$$

$$q(x,t) = 0,\ for\ t \geq 0\ and\ x\ at\ tunnel\ wall$$

$$h(x,t) = x_3,\ for\ t \geq 0\ and\ x\ at\ tunnel\ face$$

Solutions and comments:

Model 1: the position of the water table remains constant

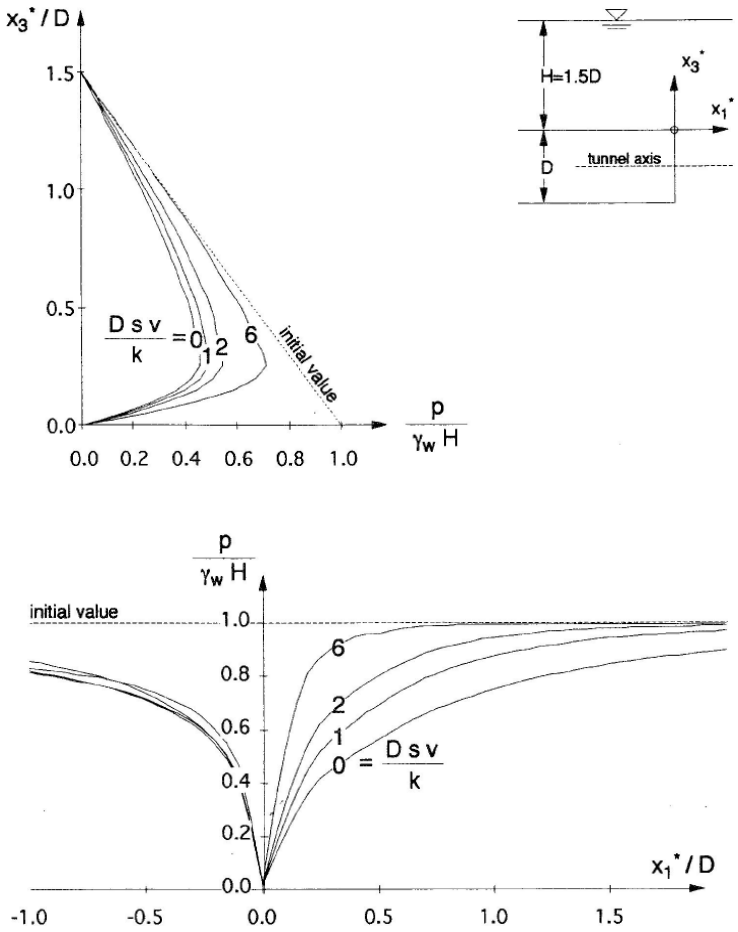

Figure 2.7 Pressure distribution above, behind and ahead of the tunnel face (From Anagnostou, 1995)

A. The gradient of the water pressure in the ground ahead of the tunnel face (i.e., at $x_1^* > 0$) increases with DSv/k. The lower the permeability and the higher the compressibility (i.e., the specific storage coefficient S) of the ground, the greater the seepage forces acting on the face (the values of D and v are assumed to be fixed);

B. The advance rate v does not influence significantly the water pressure alongside the tunnel ($x_1^* < 0$);

C. The higher the parameter DSv/k, the closer to the hydrostatic distribution will be to that above the tunnel, the more steeply will the total head rise ahead of the tunnel face;

D. When $x_1^* < 0$, the total head increases due to the departing tunnel face; when $x_1^* > 0$, the head decreases due to the approaching face.

Figure 2.8 shows the water inflow Q at the tunnel face (normalized by $k\pi D^2/4$) as a function of the dimensionless parameters DSv/k and H/D. For specific ground conditions (S, k and H) and tunnel diameter D, the water inflow increases with the advance rate v. For D=10m, H=30m and S=10^{-4}m^{-1}, the water inflow Q is plotted against the permeability k for rapid excavation (v=500 m/month) and steady-state conditions (v=0). As shown in Figure 2.9, the deviation of the two lines is considerable only when k<10^{-7}m/s. However, within this low-permeability range, the predicted water inflow amounts to less than 10 l/min and are not problematic in practice. This is a major conclusion that validates the use of models that do not consider the tunnel advance rate (i.e., most of the analytical models discussed in the following part of this chapter).

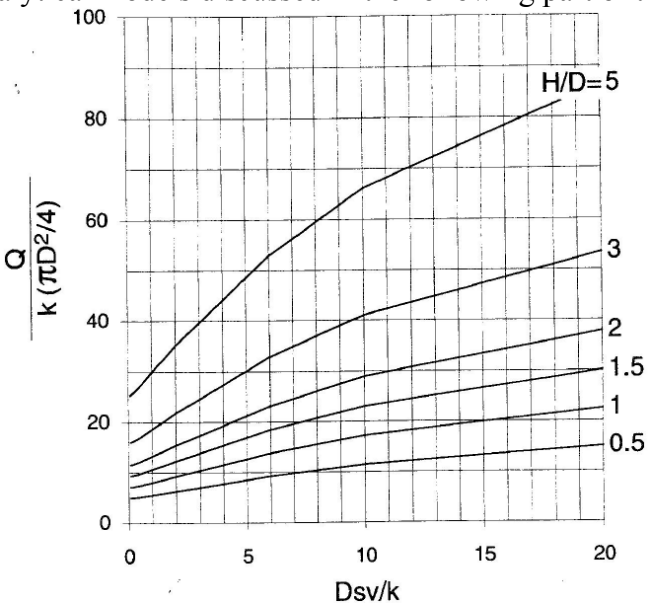

Figure 2.8 Heading inflow at the tunnel face as a function of the dimensionless parameters DSv/k and H/D (From Anagnostou, 1995)

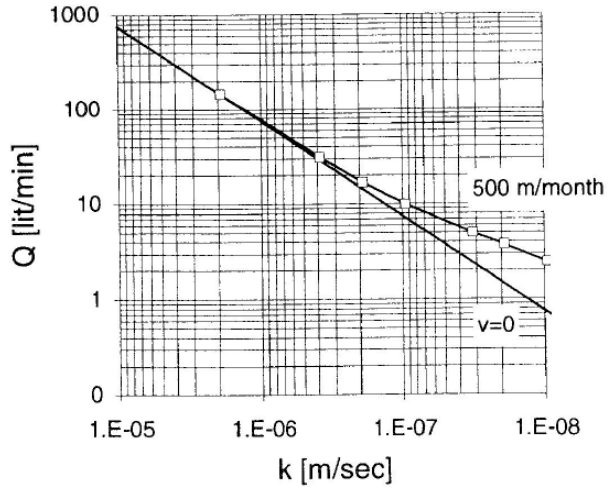

Figure 2.9 Heading inflow Q as a function of permeability k (D = 10 m; H = 30 m; S = $10^{-4}m^{-1}$) (From Anagnostou, 1995)

Model 2: aquifer is not recharged, i.e. the groundwater table is variable

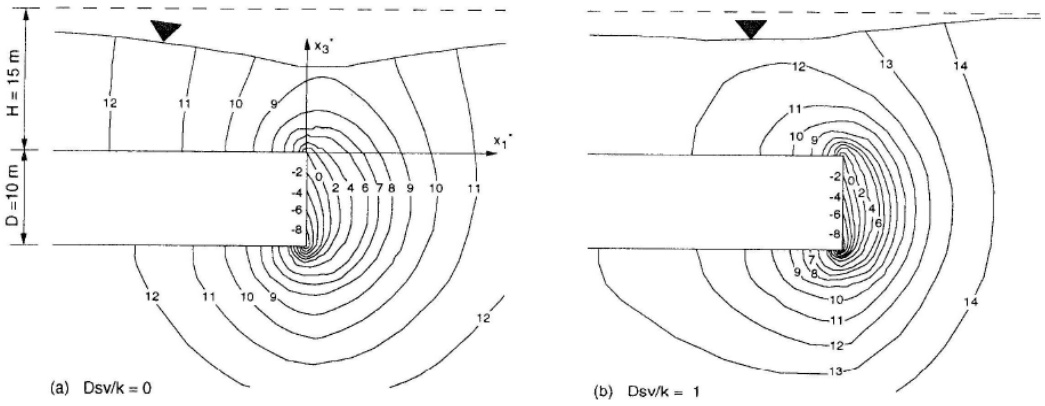

Figure 2.10 Equipotential lines and free surface in the plane of symmetry (D=10m; H=15m): (a) $DSv/k = 0$; (b) $DSv/k = 1$

A. In the case of continuous excavation (Figure 2.10 (b)), the head gradients are higher, the water table is not as depressed as in the case of v=0, and the maximum

drawdown takes place at $x_1^* < 0$ (i.e., a slight time-lag exists between excavation and maximum drawdown);

B. The free surface in Figure 2.10 (b) is steady with respect to a frame of reference that is fixed to the tunnel face, but it is unsteady with respect to a spatially fixed frame of reference. The free surface is not a flow surface, and the equipotential lines of the total head field are not perpendicular to the free surface.

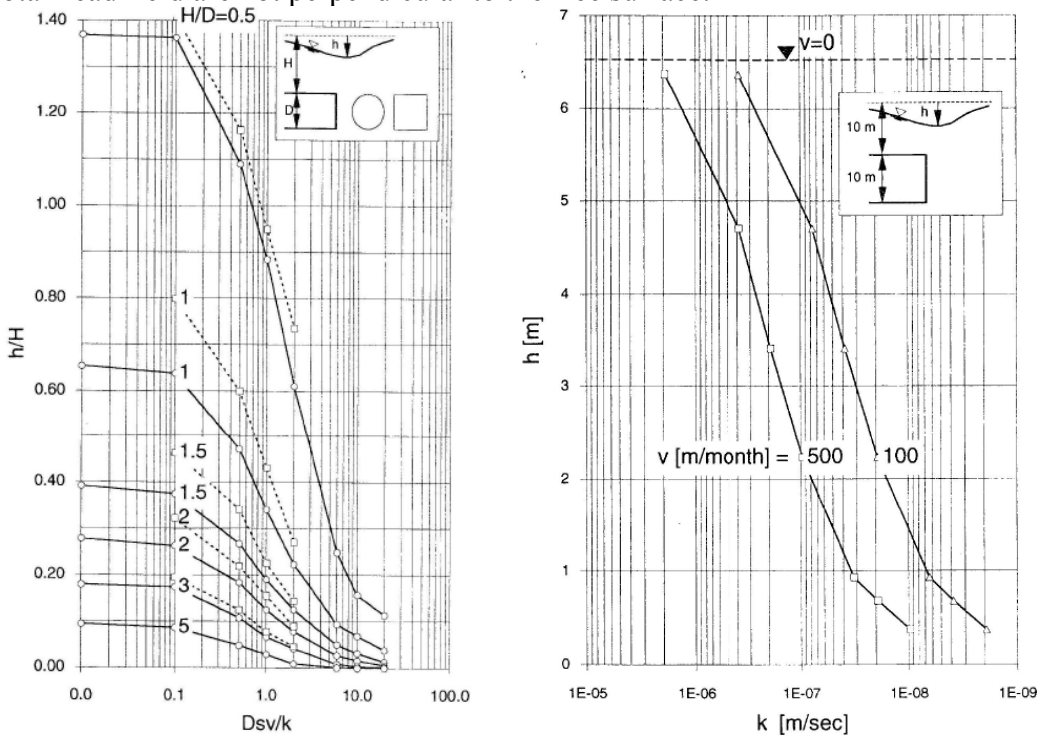

(a) (b)

Figure 2.11 (a) Maximum drawdown h of the water table as a function of dimensionless parameters DSv/k and H/D (solid lines for circular section, dashed lines for rectangular section); (b) Maximum drawdown h of the water table as a function of permeability k (D=10m; H=10m; $S=10^{-4}m^{-1}$) (From Anagnostou, 1995)

Figure 2.11 (a) shows that:

A. The higher the conductivity k and the lower the storativity S of the ground, the more the water table will be depressed;

B. In the range $DSv/k > 0.10$, the advance rate controls water drawdown; the influence of the advance rate in Model 2 is more pronounced than in Model 1;

C. The shape of the tunnel face is inconsequential.

Figure 2.11 (b) shows a practical example considering a tunnel with D=10m, H=10m and $S=10^{-4}m^{-1}$. The computed steady-state value (v=0) of the maximum drawdown h amounts to approximately 6.5 m. This value holds for typical excavation advance rates as well (e.g., v=100m/month), provided that the hydraulic conductivity k is higher than 5×10^{-6} m/s. In the case of a low-permeable ground mass ($k=10^{-7}$ m/s) and rapid excavation (v=500 m/month), the drawdown amounts to about 2 m (i.e., a common steady state computation would considerably overestimate the effect of the tunnel excavation on the water table).

2.3 Models and methods for continuous Darcian medium

2.3.1 INTRODUCTION

Several simple mathematical models have been published that can explain or predict the temporal behavior of groundwater inflow to tunnels in rocks with homogeneous hydraulic conductivity and Darcian flow. Most of these models assume two-dimensional flow in a plane perpendicular to the tunnel axis and constant total head boundary conditions at the tunnel wall, which is assumed to have a circular geometry.

The existing analytical solutions mainly apply to the early transient flow and long-term flow in simplified situations, such as homogeneous (hydraulic conductivity, storage coefficient and transmissivity), isotropic, infinite aquifers, constant boundary conditions, etc. However, the transient flow (including flow through the tunnel face and

through the wall of the tunnel) and long-term flow in more complicated aquifer and boundary conditions commonly need to use numerical methods, such as finite difference method, finite element method and boundary element method.

2.3.2 ANALYTICAL METHODS

Analytical solutions for inflow prediction are more convenient than numerical modeling because they allow a rapid parametric study of design alternatives and rock characteristics, which are often incompletely defined at the feasibility and even at the design stage. However, the available analytical solutions cover few conditions and are often restrictive in their assumptions.

All analytical models decribed in the following are summarized in Appendix B.

2.3.2.1 Transient flow models

This model is mainly used to describe the first phase of transient radial flow and is described by the well-known asymptotic constant total head test solution of Jacob and Lohman (1952). This model assumes that the aquifer is an ideal, infinite, confined, isotropic aquifer with a homogenous transmissivity and storativity; the flow is radial from infinity to the tunnel wall and the solution is valid as long as the pressure change in the aquifer, induced by the drainage of the tunnel, does not reach any boundary.

2.3.2.1.1 Constant head test solution of Jacob and Lohman (1952)

Jacob and Lohman give a mathematical theory for the discharge of a well subject to constant drawdown as shown in Figure 2.12. This theory is based on the solution by L. P. Smith (1937) of the analogous problem in heat conduction.

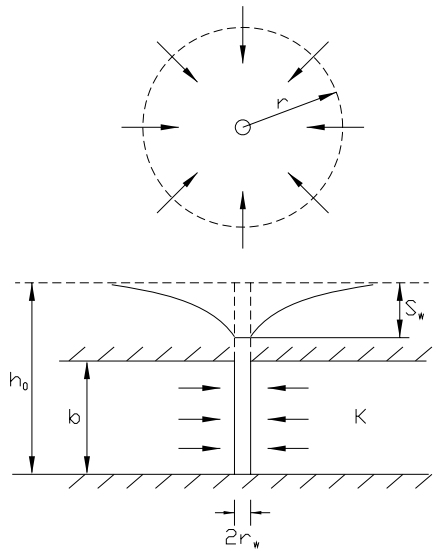

Figure 2.12 Sketch of flow induced by constant drawdown

Assumptions:

A. The aquifer is infinite and confined; its thickness is uniform,
B. The transmissibility and compressibility are uniform,
C. Initial total head is uniform throughout the aquifer, and
D. At zero time the total head at the well wall drops instantaneously to some lower constant value.

Equation and initial/boundary conditions:

The differential equation governing the non-steady flow may be obtained by rewriting Eq.(2.7) in cylindrical coordinates:

$$\frac{\partial^2 h}{\partial r^2} + \frac{1}{r} \cdot \frac{\partial h}{\partial r} = \frac{S}{T} \frac{\partial h}{\partial t}, \tag{2.14}$$

where h [L] is the total head in the flow field, S is the storage coefficient of the aquifer, and T [L^2 T^{-1}] is the transmissibility of the aquifer, i.e., the product of the hydraulic conductivity K [LT^{-1}] and its thickness b [L].

The initial and boundary conditions are

$$h\big|_{t=0} = h_0$$
$$h\big|_{r=\infty,t>0} = h_0 \tag{2.15}$$
$$h\big|_{r=r_w,t>0} = h_0 - s_w,$$

where h_0 [L] is the uniform initial value of total head, t [T] is the time, r [L] is the distance from the well, s_w [L] is the drawdown at the well, and r_w [L] is the radius of the well.

For the tunnel case, the model can be obtained by rotating the well model 90 degrees, as shown in Figure 2.13.

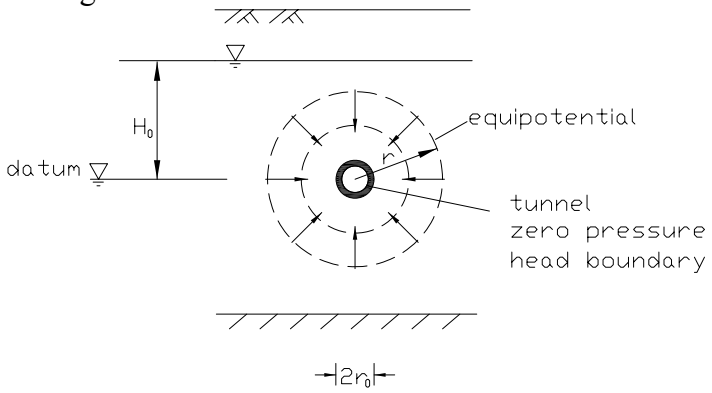

Figure 2.13 Tunnel transient flow model

In this case, the initial boundary condition and the boundary condition at infinity are H_0, instead of h_0. The drawdown s_w is exactly equal to H_0 if the tunnel wall is a zero pressure head boundary and the datum is set at the tunnel axis.

Derivation and solution:

By resorting to Green's functions and integral transforms to find the solution of the heat conduction problem, Jacob and Lohman (1952) obtain the solution of the governing equation that satisfies the initial and boundary conditions

$$Q = 2\pi T s_w \cdot G(\alpha), \tag{2.16}$$

where Q is the discharge of the well and where

$$\alpha = \frac{Tt}{Sr_w^{\,2}}.$$

The value of the function $G(\alpha)$ is given by the following integral

$$G(\alpha) = \frac{4\alpha}{\pi}\int_0^{\infty} xe^{-\alpha x^2}\left\{\frac{\pi}{2} + \tan^{-1}\left[\frac{Y_0(x)}{J_0(x)}\right]\right\}dx, \qquad (2.17)$$

in which $J_0(x)$ and $Y_0(x)$ are Bessel functions of zero order of the first and second kinds, respectively, as shown in Appendix C.

Discussion:

The integral Eq.(2.17) is not tractable by any of the ordinary means of integration. Jacob and Lohman (1952) resorted to numerical methods, replacing the integral by a summation, and compared the results with other, asymptotic solutions.

For small values of α (or small relative values of t), G approaches $1/\sqrt{\pi\alpha}$. For large values of α (or large relative values of t), G approaches $2/W\left(\frac{1}{4\alpha}\right)$, where $W(\bullet)$ is the so-called well function, which is expressed as $W(x) = \int_x^{\infty}\frac{e^{-s}}{s}ds$ (s is integral variable). For large relative values of t, the function $W\left(\frac{Sr_w^{\,2}}{4Tt}\right)$ can be further approximated by $2.30\log\left(\frac{2.25Tt}{Sr_w^{\,2}}\right)$. The difference is only about 0.02 percent of W at $\alpha = 200$, where the difference between G and 2/W is 5 percent of G. Thus, to almost the same approximation, G can be replaced by $2/\left[2.30\log\left(\frac{2.25Tt}{Sr_w^{\,2}}\right)\right]$, instead of $2/W$, and the discharge can be determined from

$$Q = 4\pi Ts_w / \left[2.30\log\left(\frac{2.25Tt}{Sr_w^{\,2}}\right)\right] \qquad (2.18)$$

This is the well-known Jacob Formula.

2.3.2.1.2 Perrochet solution to tunnel or well discharge under constant drawdown

Perrochet (2005a) develops a simple analytical formula to calculate transient discharge inflow rates into a tunnel or a well under constant drawdown.

Assumptions:

A. Apply all the assumptions of Jacob and Lohman (1952)

B. Assume that the effect of the specified drawdown strictly vanishes beyond a no-flow moving boundary located at a time-dependent distance, $r = R(t)$, and the drawdown propagation can be treated as successive steady-state snapshots of the drawdown s(r, t) over the distance R(t) (Figure 2.14 (b)). As for the tunnel case, shown in Figure 2.14 (b), it is also assumed that there is no drawdown beyond a no-flow moving boundary located at a time-dependent distance, $r = R(t)$, and the drawdown at $r = R(t)$ is $H_0 - h(r,t)$, which can also be treated as successive steady-state snapshots over this distance.

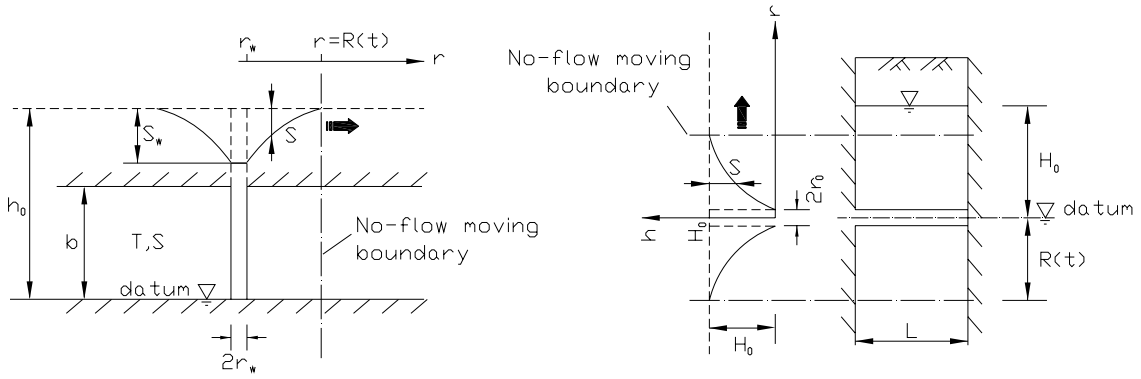

(a) well case (b) tunnel case

Figure 2.14 Constant drawdown flow (no-flow moving boundary)

Equation and initial/boundary conditions:

As schematized in Figure 2.14, the domain of interest is $r_0 \le r < R(t)$. Perrochet (2005a) considers the radial form of the diffusion equation

$$\frac{1}{r}\frac{\partial}{\partial r}\left(rT\frac{\partial s}{\partial r}\right)=S\frac{\partial s}{\partial t}, r_0 \le r \le \infty, 0 \le t \le \infty\,, \tag{2.19}$$

where the symbols stand for aquifer transmissivity (T), storage coefficient (S), drawdown (s), time (t) and radial coordinate (r). In fact, Eq.(2.19) is the same as Jacob and Lohman's (Eq.(2.14)). The boundary conditions in Eq.(2.15) need to be modified and complemented as follows

$$\begin{aligned} s(r_w,t) &= s_w \\ \frac{\partial s}{\partial r}(R(t),t) &= 0 \\ s(R(t),t) &= 0\,. \end{aligned} \tag{2.20}$$

In the tunnel case, r_0 is the tunnel radius and the boundary conditions are

$$\begin{aligned} s(r_0,t) &= H_0 \\ \frac{\partial s}{\partial r}(R(t),t) &= -\frac{\partial h}{\partial r}(R(t),t) = 0 \\ s(R(t),t) &= 0\,. \end{aligned} \tag{2.21}$$

The difference between Eq.(2.20) and Eq.(2.15) for the boundary condition is that in Perrochet's assumption the boundary conditions are imposed at the finite radius R(t) rather than at infinity as in Jacob's and Lohman's model.

Derivation and solution:

According to assumption B, one can simply replace the right-hand side of Eq.(2.19) with a uniform time-dependent source term, i(t), and consider the following equation

$$\frac{1}{r}\frac{\partial}{\partial r}\left(rT\frac{\partial s}{\partial r}\right)=i(t), r_0 \le r < R(t)\,. \tag{2.22}$$

Accounting for the three boundary conditions in Eq.(2.20), the solution of Eq.(2.22) is

$$s(r,t)=s_0\left(1-\frac{2R(t)^2\ln(r/r_0)-r^2+{r_0}^2}{2R(t)^2\ln(R(t)/r_0)-R(t)^2+{r_0}^2}\right). \tag{2.23}$$

After complicated substitutions, re-arrangements and integrations, Perrochet (2005a) finds an implicit relationship between the radius R(t) and time t:

$$\frac{Tt}{Sr_0^2} = \int_1^x \frac{\frac{u^2+1}{u^2-1}\ln u - 1}{4\frac{u^2}{u^2-1}\ln u - 2} u du \,, \tag{2.24}$$

where $x = R(t)/r_0$. This equation could not be integrated in closed form, but, by polynomial analysis, the following approximation was found to be excellent:

$$\frac{Tt}{Sr_0^2} \cong \frac{1}{\pi e}\left(x^{\frac{x^2}{x^2-1}} - \sqrt{e} \right)^2 \tag{2.25}$$

For a given time t, Eq.(2.25) is solved for $x = R(t)/r_0$, and the value for R(t) is substituted into Eq.(2.23) to yield the drawdown s(r,t).

Integrating Eq.(2.19) between r_0 and R(t) yields the global time-dependent quantities

$$Q(t) = \frac{\partial}{\partial t}\int_{r_0}^{R(t)} 2\pi r Ss(r,t)\, dr = \frac{\partial V(t)}{\partial t}, \tag{2.26}$$

where Q(t) is the flow rate into the tunnel and V(t) is the cumulative volume of extracted water.

By substituting Eq.(2.23) into Eq.(2.26), Perrochet obtained

$$Q = 2\pi T s_0 \cdot G(\alpha), \tag{2.27}$$

$$\text{where } G(\alpha) \cong \frac{1}{\ln\left(1+\sqrt{\pi\alpha}\right)} \text{ and } \alpha = \frac{Tt}{Sr_0^2}.$$

Discussion:

Perrochet (2005a) compares Eq.(2.27) and Eq.(2.16). The agreement with the solution of Jacob and Lohman (1952) is excellent throughout the range of dimensionless time, and the relative errors of dimensionless discharge ($Q/(2\pi T s_0)$ or $G(\alpha)$) are maximum in the range $10^1 < \alpha < 10^2$, where they reach about 5×10^{-3}. The errors vanish

for very small and very large times. Eq.(2.27) may, therefore, replace Eq.(2.16) to predict transient discharge rates at a well or a tunnel under confined conditions and constant drawdown.

Because this solution uses only a logarithmic function, it may be used with great computational benefits in practice, as well as when further mathematical manipulations, such as differentiation or integration, are required.

Eq.(2.27) or Eq.(2.16) may be used to predict transient discharge rates, as long as the no-flow moving boundary at the distance R(t) from the well or the tunnel has not reached any system boundary. When $R(t) >> r_0$, the time required for the no-flow moving boundary to reach the nearest boundary at $R_{\max}$, can be evaluated as follows:

$$t = \frac{Sr_0^{\,2}}{\pi T}\left(\frac{R_{\max}}{r_0\sqrt{e}} - 1\right)^2 \cong \frac{SR_{\max}^{\,2}}{\pi e T}, \tag{2.28}$$

For larger times, Eq.(2.27) or Eq.(2.16) can no longer be used because their assumptions are no longer satisfied. Discharge rates should then be predicted by other means, such as the image-based analytical method or numerical simulation.

2.3.2.1.3 Application of Perrochet solution

Because of the simplified analytical expression of the specific discharge in Eq.(2.27), Perrochet (2005b) does further mathematical manipulations to evaluate transient, excavation speed-dependent discharge rates into a tunnel gradually excavated in a homogenous infinite aquifer. Consider the progressive excavation of a permeable zone at an average drilling speed, v, as illustrated in Figure 2.15.

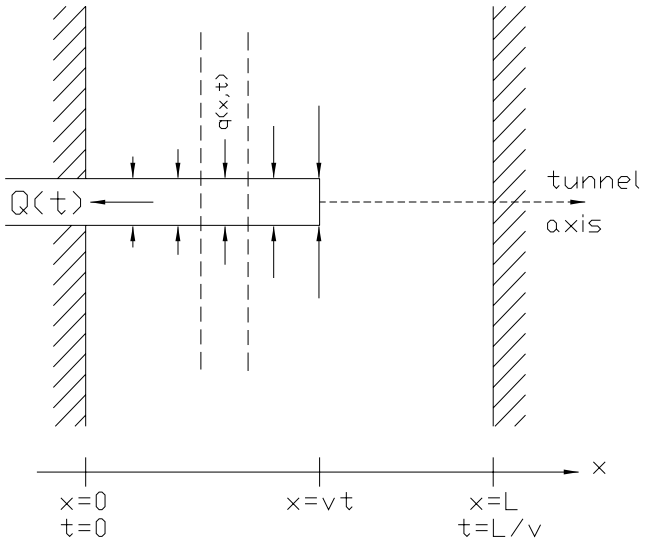

Figure 2.15 Nonuniform specific discharge resulting from progressive excavation

Assuming now that perfect radial symmetry of the flow is preserved at all times and that the aquifer is not significantly perturbed beyond the tunnel face, the specific discharge at any location x<vt along the tunnel axis can be expressed from Eq.(2.27) by

$$q(x,t)=\frac{2\pi K s_t}{\ln\left(1+\sqrt{\frac{\pi K}{S r_0^{\,2}}\left(t-\frac{x}{v}\right)}\right)},\quad t-\frac{x}{v}>0, \tag{2.29}$$

indicating gradually increasing inflows from the entry point of the permeable zone (x=0) to the vicinity of the drilling front (x=vt). From Eq.(2.29), if x approaches vt (i.e., close to the face), the flow rate, $q(x,t)$, approaches infinity. The above two assumptions may hold particularly well when subvertical zones of relatively high permeability intersecting the tunnel at a high angle or when a reasonably constant advance rate is maintained.

The total discharge into the tunnel during and after excavation through the permeable zone may then be expressed as

$$Q(t)=\int_0^{vt}\frac{2\pi K s_t H(L-x)}{\ln\left(1+\sqrt{\frac{\pi K}{Sr_0^{\,2}}\left(t-\frac{x}{v}\right)}\right)}dx\,, \tag{2.30}$$

where the Heaviside step function H(L-x) (see Appendix A) has been introduced to account for the finite size of the permeable zone and for the assumption that the specific discharge vanishes at the tunnel face.

The time during which Eq.(2.30) may hold can be taken as $t_{\lim}=\frac{1}{\pi e}\frac{SR_{\max}^{\,2}}{K}$. Beyond this limiting time, the specific discharge at location $x<v(t-t_{\lim})$ starts to be influenced, gradually, by possible boundary effects at the distance R from the tunnel axis. Defining the dimensionless parameters

$$\alpha_d=\frac{K}{Sr_0^{\,2}}\frac{L}{v},\quad u=\frac{K}{Sr_0^{\,2}}\frac{x}{v}=\alpha_d\frac{x}{L},\quad \alpha_{\lim}=\frac{Kt_{\lim}}{Sr_0^{\,2}}=\frac{1}{\pi e}\frac{R^2}{r_0^{\,2}},$$

where α_d is the dimensionless excavation time, u is the dimensionless time at which the location x is reached, and $\alpha_{\lim}$ is the dimensionless limiting time. Substituting these definitions in Eq.(2.30) yields the dimensionless discharge rate

$$Q^*(\alpha)=\frac{Q(\alpha)}{2\pi KLs_t}=\frac{1}{\alpha_d}\int_0^{\alpha}\frac{H(\alpha_d-u)}{\ln\left(1+\sqrt{\pi(\alpha-u)}\right)}du \tag{2.31}$$

as a convolution of the production function $G(\alpha)$ and the Heaviside step function (see Appendix A). Integration of the right-hand side of Eq.(2.31) results in

$$Q^*(\alpha)=\begin{cases}\dfrac{F(\alpha)}{\alpha_d}, & \alpha<\alpha_d\\[2ex] \dfrac{F(\alpha)}{\alpha_d}-\dfrac{F(\alpha-\alpha_d)}{\alpha_d}, & \alpha>\alpha_d\end{cases} \tag{2.32}$$

$$F(\alpha)=\int_0^{\alpha}G(u)du=\frac{2}{\pi}\left[E_i\left(2\ln\left(1+\sqrt{\pi\alpha}\right)\right)-E_i\left(\ln\left(1+\sqrt{\pi\alpha}\right)\right)-\ln(2)\right],$$

where $E_i(\cdot)$ is the exponential integral function, which is expressed as $E_i(x)=\int_{-\infty}^{x}\frac{e^s}{s}ds$ (s is the integral variable). Typical curves are provided in Figure 2.16 for a range of

dimensionless excavation times. Notice that tunneling is complete when $\alpha = \alpha_d$: at this time, groundwater inflow is maximum.

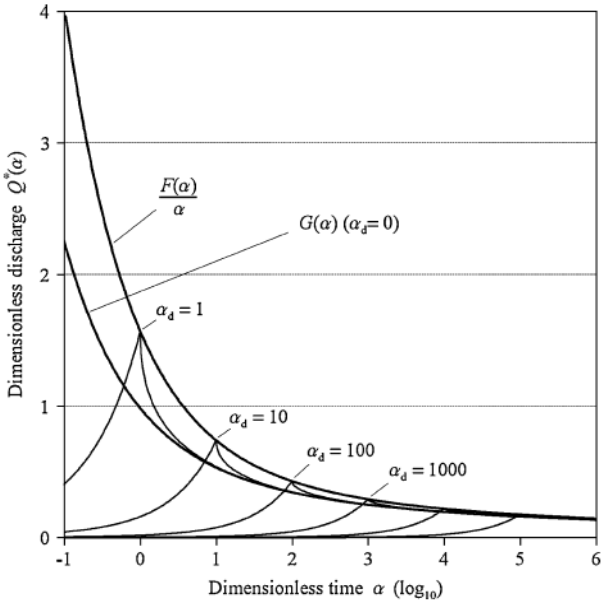

Figure 2.16 Dimensionless curves for estimating transient and maximum discharge into a tunnel for various drilling times α_d (From Perrochet, 2005b)

Notwithstanding the relatively crude additional assumptions enforced in Eq.(2.29), the curves in Figure 2.16 indicate transient discharge rates that are more realistic than those obtained with the classical instantaneous-excavation approach. At the outset of tunnel excavation, the length of the tunnel is zero, so the discharge rate is zero. This contrasts with the results obtained from the classical instantaneous-excavation approach seen in Eq.(2.16), (2.17) and (2.18), which predicts infinite initial discharge. The progressive-excavation solution in Eq.(2.32) generates values that increase more or less rapidly, depending on the penetration rate, as would be expected.

After about four-fifths of the excavation time ($\alpha / \alpha_d \approx 4/5$), discharge rates start to exceed the value predicted by using the classical Jacob method (Eq.(2.16), (2.17) and (2.18)) at the same dimensionless time value. When excavation is complete ($\alpha = \alpha_d$),

this excess is about one-third at short advance rates and decreases gradually for larger advance rates. Hence, the flow rates predicted by the classical Jacob approach using time values corresponding to the expected duration of tunnel excavation are underestimated during excavation of the last fifth of the tunnel length and thereafter.

2.3.2.1.4 Application of Perrochet solution to heterogeneous ground

Perrochet and Dematteis (2007) combine the approach of Perrochet (2005b) with the superposition principle and extend the analysis to tunnels gradually drilled through heterogeneous formations. Consider N consecutive sectors as schematized in Figure 2.17, each of them characterized by specific parameters.

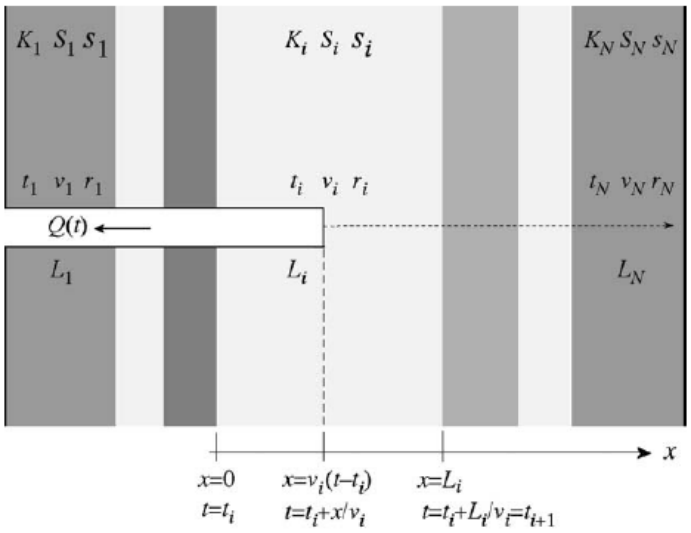

Figure 2.17 Schematic of a tunnel progressively excavated through a subvertical multilayered system. Sector parameters and local drilling coordinates (From Perrochet and Dematteis, 2007)

Summing up the transient contribution of each sector, the result can be expressed as follows:

$$Q(\alpha) = 2\pi \sum_{i=1}^{N} H(t-t_i) \times \int_{0}^{v_i(t-t_i)} \frac{K_i s_i H(L_i - x)}{\ln\left[1+\sqrt{\frac{\pi K_i}{S_i r_i^2}\left(t-t_i-\frac{x}{v_i}\right)}\right]} dx, \qquad (2.33)$$

where $t_i = \sum_{j=1}^{i-1} \frac{L_j}{v_j}$, $t_1 = 0$, and t_{N+1} = total excavation time.

2.3.2.1.5 A "combined" solution for a tunnel in the presence of constant infinite linear head boundary in an ideal confined aquifer

Renard (2005) considers the case of a constant drawdown in a well or tunnel in the presence of a constant infinite linear total head boundary in an ideal confined aquifer. By applying the convolution method and the Laplace transform to the solution of the discharge in the tunnel, the author combines two stages (early stage transient flow and late stage steady-state flow), and gives an approximate solution as a weighted average of the two stages asymptotes plus a correction term as follows:

$$\frac{Q(t)}{2\pi T s_w} \cong \frac{A}{\ln\left(1+\sqrt{\frac{\pi T t}{r_w{}^2 S}}\right)} + \frac{B}{\ln\left(\frac{2R}{r_w}-1\right)} + C \tag{2.34}$$

$$A = \frac{2}{\pi}\arctan\left[\frac{(2R/r_w-2)^2}{\pi T t/(r_w{}^2 S)}\right]$$

$$B = \frac{2}{\pi}\arctan\left[\frac{\pi T t/(r_w{}^2 S)}{(2R/r_w-2)^2}\right]$$

$$C = \frac{AB}{2}\frac{\ln\left[(2R/r_w-1)\left(\sqrt{2}R/r_w-\sqrt{2}+1\right)\right]}{\left[\ln(2R/r_w-1)\right]^2 \ln\left(\sqrt{2}R/r_w-\sqrt{2}+1\right)},$$

where R [L] is the shortest distance between the well/tunnel axis and the constant total head boundary. The other symbols have the same meaning as before.

In fact, for the early stage, and/or for a large distance to the boundary, $A \to 1$, $B \to 0$, $C \to 0$,

$$\frac{Q(t)}{2\pi T s_w} \cong \frac{1}{\ln\left(1+\sqrt{\frac{\pi T t}{r_w{}^2 S}}\right)},$$

which is the approximate solution of Jacob and Lohman (1952) (in Eq.(2.27)) obtained by Perrochet (2005a). For the late stage, and/or small distance to the boundary, $A \to 0$, $B \to 1$, $C \to 0$,

$$\frac{Q(t)}{2\pi T s_w} \cong \frac{1}{\ln\left(\frac{2R}{r_w} - 1\right)},$$

which is the approximate solution of Goodman (1965), shown in the following as Eq.(2.49). C is a correction term for the mid-term transition time.

According to Renard's analysis, the relative error between the exact solution (the numerical inversion of a Laplace transform solution) and the approximate discharge is always < 2% during the whole time period and the maximum relative error occurs during the transient.

2.3.2.2 Early linear flow model (water table drawdown)

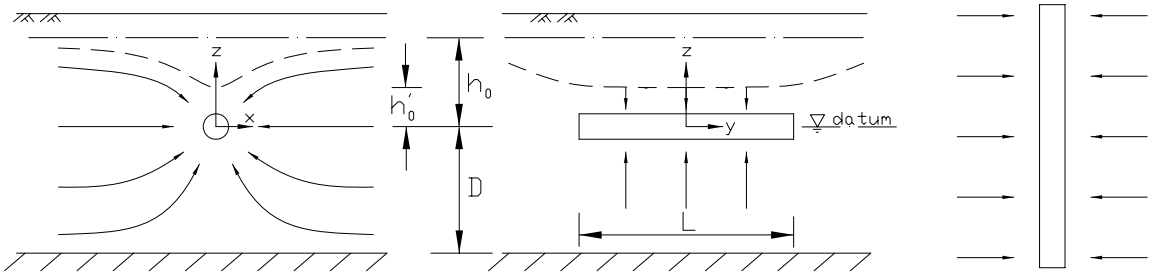

(a) tunnel end view (b) tunnel side view (c) tunnel plan view

Figure 2.18 Early linear flow model

Löw (2002) analyzes and summarizes the solution by Goode and Thambynayagam (1987), Odeh and Babu (1990) and Kawecki (2000). As shown in Figure 2.18, the water total head will start to decline as soon as the pressure drop from the draining tunnel reaches the water table (when Phase 1, early radial flow, ends). First order estimations of water table drawdown and tunnel inflow rate can be made for the

case in which the flow pattern can be approximated by superposing the linear horizontal flow with the vertical flow to the tunnel. Kawecki (2000) has developed a set of equations for this case that are based on approximations derived for horizontal oil wells in confined aquifers:

$$h_0 - h_t = \frac{1}{\sqrt{\pi}} \cdot \frac{2Q}{LK_x\left(h_0'+h_0+2D\right)} \cdot \sqrt{\frac{\left(h_0'+h_0+2D\right)K_x t}{2S_y}} + \frac{Q}{2\pi L\sqrt{K_x K_z}} \cdot \sigma_z , \qquad (2.35)$$

where, $\sigma_z = \ln\left(\frac{h_0'+D}{2\pi r_0}\right) + 0.25 \cdot \ln\left(\frac{K_x}{K_z}\right) - \ln\left(\sin\frac{180^0 D}{h_0'+D}\right)$, and

$$h_0' = h_t + \frac{Q}{2\pi L\sqrt{K_x K_z}} \cdot \sigma_z .$$

h_0' is the approximately uniform saturated thickness of the aquifer above the tunnel crown (or the water table elevation at the tunnel at time t). D is the vertical height of the tunnel above the base of the aquifer. h_0 and h_t are the total heads of the undisturbed formation and at the tunnel side walls (referenced to the axis of tunnel). K_x is the horizontal hydraulic conductivity. K_z is the vertical hydraulic conductivity, and S_y is specific yield (the volume of water that a saturated porous medium can yield by gravity drainage per unit volume of the porous medium). σ_z is a skin factor (dimensionless) that accounts for the pressure loss due to the vertical flow.

Discussion:

In this author's opinion, Kawecki's method is an approximate one for the tunnel flow, because, usually, the pressure head at the tunnel wall is constant (zero pressure head), whereas in horizontal oil wells the discharge rate is a constant.

Eq.(2.35) is composed of two flow components to the tunnel. The first part describes unconfined flow as to a fully penetrating channel driven by the drawdown $\left(h_0 - h_t\right)$. The second part describes vertical flow to a tunnel in an aquifer of thickness

$(h_0'+D)$. If the tunnel drawdown $(h_0 - h_t)$ is given, Eq.(2.35) can be solved iteratively for $Q(t)$ (notice that h_0' is a function of $Q(t)$ and σ_z is a function of $h_0'(Q(t))$).

Eq.(2.35) can be used to analyze drawdown and inflow when the closer aquifer boundary begins to have a significant effect on the flow. Strictly, however, these equations apply only when D represents the distance to the further aquifer boundary. The end of early linear tunnel flow is the time when flow through the end faces of the draining tunnel becomes significant, as shown in Figure 2.19—to be compared with Figure 2.18 C.

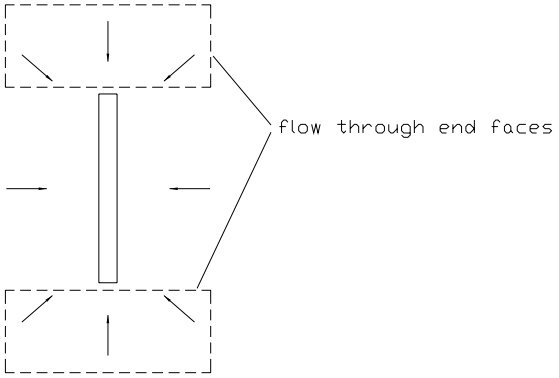

Figure 2.19 Plan view of post-linear-flow pattern

However, this situation is rare for classical tunnel configurations, where the aquifer ends at the portals of the tunnel. On the other hand, it could be important for underground structures of limited extent, such as caverns, or for partially sealed tunnels. The end of the early linear flow period can be estimated from the following equation (Kawecki, 2000):

$$t = \frac{0.084 L^2 S_y}{K_y (h_0'+h_0 + D)}. \tag{2.36}$$

As Löw (2002) mentions, Eq.(2.35) does not include vertical groundwater recharge, which can be an important factor for the location of a free water table above a draining tunnel. Therefore, the equations overestimate water table drawdown and underestimate

tunnel inflow, as long as there is groundwater recharge from the surface (either diffuse through precipitation or localized through infiltrating creeks or rivers).

2.3.2.3 Steady flow models

2.3.2.3.1 Goodman's constant total head model (inflow through tunnel walls without drawdown)

2.3.2.3.1.1 Classical method solution

Based on the Polubarinova-Kochina (1962) solution, which is stated in terms of an infinite line sink and a source, Goodman et al. (1965) set up the model shown in Figure 2.20.

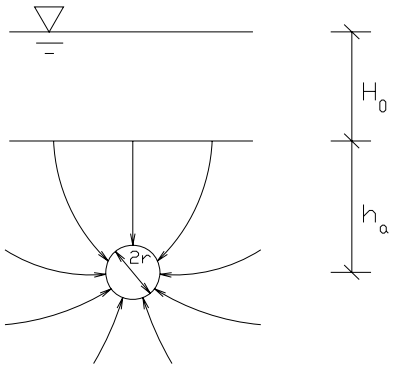

Figure 2.20 Schematic diagram of Goodman's model

Assumptions:

A. The tunnel completely penetrates the water zone (two-dimentional flow);

B. There is so much water supplied that drawdown cannot occur. This leads to a horizontal constant pressure boundary at the surface (e.g., a lake or a large aquifer);

C. Tunnel radius, r, is much smaller than the depth of the tunnel below water table (H_0+h_a), so the line sink can be considered to be located at the tunnel's centerline;

D. The water occupies a semi-infinite plane;

E. Ground is homogenous and isotropic, and its permeability can be treated as uniform.

Derivation and solution:

(1) Fundamental solution:

We consider a unit thickness, horizontally infinite, confined aquifer, as Figure 2.21 shows, where Q is the flow rate into the well and q_r is the radial velocity.

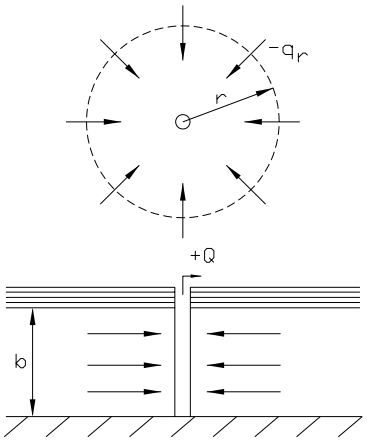

Figure 2.21 A well in a horizontally infinite confined aquifer

The equation of continuity is:

$$Q = -2\pi r b q_r \tag{2.37}$$

Darcy's law states that:

$$q_r = -K\frac{dh}{dr}. \tag{2.38}$$

After integrating Eq.(2.38) into Eq.(2.37), we can obtain the solution for this problem:

$$h = \frac{Q}{2\pi K b}\ln r + C, \tag{2.39}$$

where C is a constant of integration. Let h_R be the total head at the well's wall. By imposing this boundary condition, one obtains:

$$h = \frac{Q}{2\pi K b}\ln\frac{r}{R} + h_R. \tag{2.40}$$

This equation is known as the Thiem equation (Thiem, 1906).

(2) The superposition principle and the method of images (Strack, 1989):

The superposition principle states that if two different functions, say Φ_1 and Φ_2, are the solution of Laplace's equation, then the function

$$\Phi(x,y) = C_1\Phi_1(x,y) + C_2\Phi_2(x,y) \tag{2.41}$$

is a solution of Laplace's equation as well. The method of images consists of combined use of the superposition principle and symmetry. The superposition principle and the method of images can be used to solve the problem of a well near a straight river, where the total head is constant, or a straight impervious boundary.

As for our particular concern, however, there is constant total head boundary and the distance between the discharge well and boundary is h. An image recharge well and the half image aquifer can be added symmetrically to the boundary, as indicated in Figure 2.22.

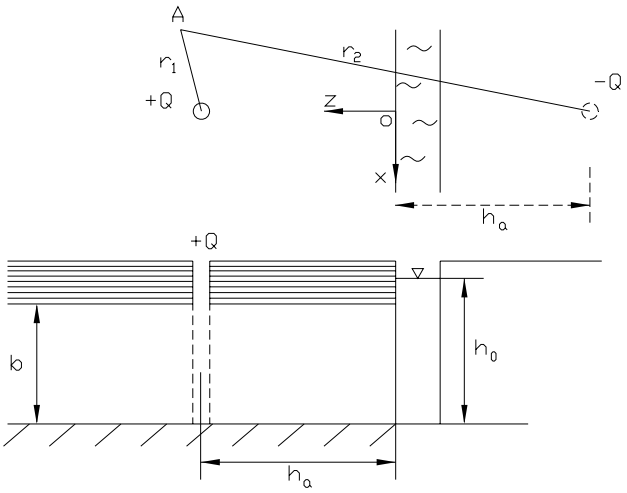

Figure 2.22 Schematic diagram of usage superposition principle and the method of images

For the discharge well, $h_1 = \dfrac{Q}{2\pi Kb}\ln r_1 + C_1$.

For the recharge well, $h_2 = -\dfrac{Q}{2\pi Kb}\ln r_2 + C_2$.

According to the superposition principle,

$$h = h_1 + h_2 = \frac{Q}{2\pi Kb}\ln r_1 - \frac{Q}{2\pi Kb}\ln r_2 + C_1 + C_2 = \frac{Q}{2\pi Kb}\ln\frac{r_1}{r_2} + C\,.$$

Using the boundary condition $h\Big|_{r_1=r_2} = h_0$, we can get $C = h_0$.

If a Cartesian coordinate system is chosen, as indicated in Figure 2.22, the solution becomes:

$$h = \frac{Q}{2\pi Kb}\ln\frac{\sqrt{x^2 + (z - h_a)^2}}{\sqrt{x^2 + (z + h_a)^2}} + h_0\,. \tag{2.42}$$

Then we set $x = 0$, $z = h_a$ (i.e., the center of the well) into Eq.(2.42),

$$h_w = \frac{Q}{2\pi Kb}\ln\frac{r_w}{\sqrt{r_w^{\,2} + 4h_a^{\,2}}} + h_0\,. \tag{2.43}$$

If we consider the assumption in the well case similar to the assumption C of the tunnel case, the radius of the well is much smaller than the distance between the well and the constant total head boundary (i.e., $r_w << h_a$), we have

$$h_w \approx \frac{Q}{2\pi Kb}\ln\frac{r_w}{2h_a} + h_0$$

$$\text{or,}\quad s_w = h_0 - h_w \approx \frac{Q}{2\pi Kb}\ln\frac{2h_a}{r_w}, \tag{2.44}$$

where s_w is the drawdown of the well, h_w is the total head in the well.

Thus, the flow rate can be expressed as:

$$Q = \frac{2\pi Kb(h_0 - h_w)}{\ln(2h_a / r_w)}. \tag{2.45}$$

(3) Transfer the well case to the tunnel case:

If the model in Figure 2.22 is rotated 90 degrees, we can get the transformation from the well to the tunnel. This method is valid, if both well case and tunnel case share the same governing equation and boundary condition, as Figure 2.23 shows.

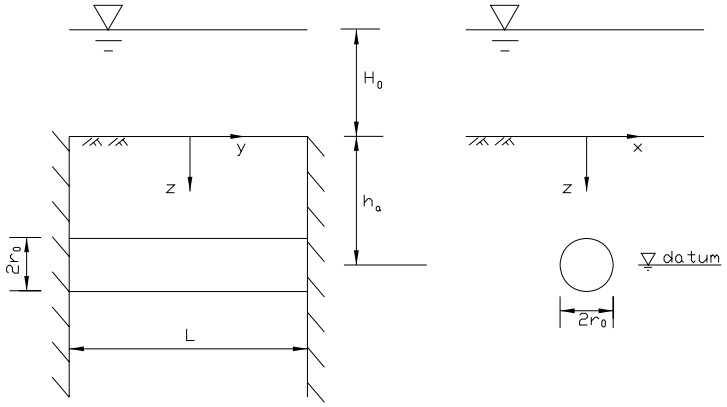

tunnel side view tunnel cross-section

Figure 2.23 Transformation from well to tunnel

Set the radius of well r_w as the radius of tunnel r_0, aquifer thickness b as the full aquifer length L along the tunnel, the initial total head h_0 as $(H_0 + h_a)$, h_w as h_t, then the Eqs.(2.42), (2.44) and (2.45) become, respectively:

$$h = \frac{Q}{2\pi KL} \ln \frac{\sqrt{x^2 + (z - h_a)^2}}{\sqrt{x^2 + (z + h_a)^2}} + H_0 + h_a \tag{2.46}$$

$$h_t = \frac{Q}{2\pi KL} \ln \frac{r_0}{\sqrt{r_0^2 + 4h_a^2}} + H_0 + h_a \approx \frac{Q}{2\pi KL} \ln \frac{r_0}{2h_a} + H_0 + h_a \tag{2.47}$$

$$Q = \frac{2\pi KL(H_0 + h_a - h_t)}{\ln(2h_a / r_0)}. \tag{2.48}$$

Although it is common that the perimeter of a tunnel is a constant pressure head boundary, we can consider that it is a constant total head boundary if assumption C applies (the tunnel radius is much smaller than the tunnel depth below the groundwater table). The total head at the tunnel wall, h_t, is then equal to the elevation head, which is zero in the datum configuration of Figure 2.23.

Thus, Eq.(2.48) for the flow rate into the tunnel is:

$$Q = \frac{2\pi KL(H_0 + h_a)}{\ln(2h_a / r_0)}, \tag{2.49}$$

where K [LT^{-1}] is the effective hydraulic conductivity in the (vertical) plane of flow; H_0 [L] is the depth of the standing water above the ground surface; r_0 [L] is the tunnel's radius; h_a [L] is the distance from the tunnel central line to the top of the ground; and L [L] is the length of the aquifer in which the tunnel is fully penetrated.

Discussion:

If the water table is below the ground surface (Figure 2.24), we can use the following formula, instead of Eq.(2.49):

$$Q = \frac{2\pi KLh'}{\ln\left(2h'/r\right)}, \tag{2.50}$$

where h' [L] is the vertical distance from the tunnel central line to the ground water table. Note: This formula can be used only if the water table remains steady horizontally.

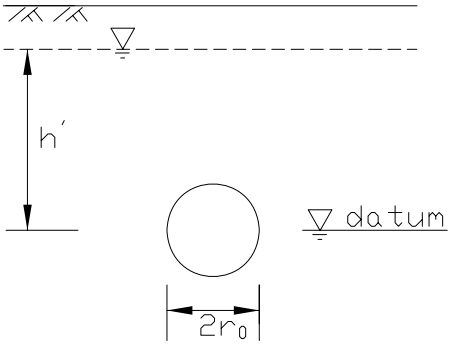

Figure 2.24 Constant groundwater table lower than the ground surface

2.3.2.3.1.2 Green's function solution method (El Tani, 1999)

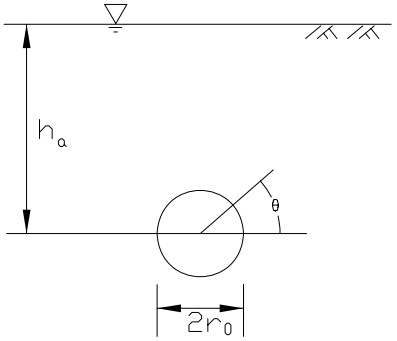

Figure 2.25 Sketch of Green's function method (From El Tani, 1999)

El Tani (1999) uses the same model as Goodman's, except that the water table is just at the ground surface and applies the same assumptions as in Section 2.3.2.3.1.1. Let $\mathbf{K}$ be the hydraulic conductivity tensor, $\boldsymbol{\gamma}_w$ the vector unit weight of water, p the pressure (not total) head, $\nabla\cdot$ the divergence operator (see Appendix D), ∇ the gradient operator (see Appendix D), and $\mathbf{v}$ the groundwater velocity. By substituting Darcy's law $\mathbf{v}=\mathbf{K}\nabla h$ into the continuity equation $\nabla\cdot\mathbf{v}=\mathbf{0}$, one obtains the equation for stationary flow in an aquifer (Eq.(2.5) in terms of pressure head):

$$\nabla\cdot\mathbf{K}\left(-\nabla p+\boldsymbol{\gamma}_w\right)=\mathbf{0}, \tag{2.51}$$

The Green's function $g(\mathbf{x},\mathbf{y})$ of the aquifer is a function which satisfies Eq.(2.51) in an infinite aquifer and for a point source at $\mathbf{y}$:

$$\nabla\cdot\mathbf{K}\nabla g(\mathbf{x},\mathbf{y})=\delta(\mathbf{x}-\mathbf{y}), \tag{2.52}$$

where δ is the Dirac delta (See Appendix A) and $\mathbf{x}$ and $\mathbf{y}$ are position vectors.

First, we need to find the Green's function of the aquifer, $g(\mathbf{x},\mathbf{y})$**:** several Green's functions are listed in Table 2.4. Then, we can obtain the integral solution of Eq.(2.51) according to the Green's 3rd identity (Kellogg, 1953 (p 219 No III)):

$$p(\mathbf{y})=\boldsymbol{\gamma}\cdot\mathbf{y}+\int_C\phi(\mathbf{x})g(\mathbf{x},\mathbf{y})ds(\mathbf{x}), \tag{2.53}$$

where $\boldsymbol{\gamma}\cdot\mathbf{y}$ is the scalar product of the unit weight vector and the position vector; C is the tunnel boundary; $\int_C\phi(\mathbf{x})g(\mathbf{x},\mathbf{y})ds(\mathbf{x})$ is the so-called single-layer potential (for the Laplace equation) (more details are in Wolfgang (1995, p268); and $\phi(\mathbf{x})$ is called the density of the single-layer potential.

Table 2.4 Green's function for 2D aquifers with a horizontal water table

(From El Tani, 1999)

Aquifer	Green's function
Anisotropic and homogeneous. Horizontal permeability k_H. Vertical permeability k_V.	$g(\mathbf{x},\mathbf{y}) = \frac{1}{2\pi\sqrt{k_H k_V}} \ln \sqrt{\frac{k_V(x_1-y_1)^2 + k_H(x_2-y_2)^2}{k_V(x_1-y_1)^2 + k_H(x_2+y_2)^2}}$ 1)
Isotropic and homogeneous. Permeability k. Impervious horizontal base at a depth H from water table.	$g(\mathbf{x},\mathbf{y}) = \frac{1}{2\pi k}\sum_{n=-\infty}^{\infty} \ln \sqrt{\frac{(x_1-y_1)^2 + (4nH + x_2 - y_2)^2}{(x_1-y_1)^2 + (4nH + x_2 + y_2)^2}}$ $+ \frac{1}{2\pi k}\sum_{n=-\infty}^{\infty} \ln \sqrt{\frac{(x_1-y_1)^2 + (2(2n+1)H + x_2 + y_2)^2}{(x_1-y_1)^2 + (2(2n+1)H + x_2 - y_2)^2}}$
Isotropic and non-homogeneous. Permeability $ke^{-2\alpha z}$. z is the depth beneath the water table. α is the intensity of the non-homogeneity.	$g(\mathbf{x},\mathbf{y}) = -\frac{1}{2\pi k} K_0\left(\alpha\sqrt{(x_1-y_1)^2 + (x_2-y_2)^2}\right)$ $+ \frac{1}{2\pi k} K_0\left(\alpha\sqrt{(x_1-y_1)^2 + (x_2+y_2)^2}\right)$ 2)

1) x_1 and x_2 are the horizontal and vertical components of $\mathbf{x}$. y_1 and y_2 are the components of $\mathbf{y}$. The origin is at the water table. The vertical axis is directed upwards. 2) K_0 is a modified Bessel function of the second kind and order zero (See Appendix C).

The amount of water per second and per unit tunnel length that flows into the tunnel is termed Q and is given by the following integral:

$$Q = -\int_C \mathbf{K}\left(-\nabla p + \gamma\right)\cdot \mathbf{n} ds\,, \tag{2.54}$$

where $\mathbf{n}$ is the outward normal to the tunnel perimeter. By substituting Eq.(2.53) into Eq.(2.54), using divergence theory (Kellogg, 1953, p 84) and using Eq.(2.52), we obtain

$$Q = \int_C \phi(\mathbf{y})\, ds(\mathbf{y})\,. \tag{2.55}$$

This means the inflow rate per unit tunnel length is merely the product of the tunnel perimeter and the average value of the single layer potential over the tunnel perimeter.

The single layer potential of a circular tunnel in a semi-infinite, homogeneous and isotropic aquifer may be expressed in an analytical form. $\phi(\mathbf{x})$ is estimated by a Fourier series with N+1 terms and is written in the form:

$$\varphi = \varphi_0 + \varphi_1 \sin\theta + \varphi_2 \cos 2\theta + \ldots, \tag{2.56}$$

where θ is the angle between the radius and the horizontal (positive anti-clockwise).

We insert the Fourier Series Eq.(2.56) and the first Green's function in Table 2.4 into Eq.(2.53), which is then integrated over the edge of the tunnel where the pressure is

zero. The N+1 unknown coefficients of the Fourier Series can be obtained by resolving the following linear set of equations:

$$\sum_{j=0}^{N} A_{ij}\varphi_j = b_i\,,\quad i = 0,1,...,N\,, \tag{2.57}$$

where A_{ij} is the i-j-th entry of a symmetric matrix, and the components of $\boldsymbol{A}$ and $\boldsymbol{b}$ are

$$\begin{aligned}
&A_{0,0} = 4\ln\varepsilon \\
&A_{0,2m} = \frac{(-1)^m}{m}\varepsilon^{2m},\quad m \geq 1 \\
&A_{0,2m+1} = \frac{2(-1)^m}{2m+1}\varepsilon^{2m+1},\quad m \geq 0 \\
&A_{2m,2n} = \frac{(-1)^{m+n}(2m+2n-1)!}{(2m)!(2n)!}\varepsilon^{2(m+n)} - \frac{\delta_{m,n}}{2m},\quad m,n \geq 1 \\
&A_{2m+1,2n} = \frac{(-1)^{m+n}(2m+2n)!}{(2m+1)!(2n)!}\varepsilon^{2(m+n)+1},\quad m \geq 0, n \geq 1 \\
&A_{2m+1,2n+1} = \frac{(-1)^{m+n}(2m+2n+1)!}{(2m+1)!(2n+1)!}\varepsilon^{2(m+n+1)} - \frac{\delta_{m,n}}{2m+1},\quad m,n \geq 0 \\
&b_0 = -\frac{2k}{\varepsilon},\quad b_1 = 2k\,,\quad b_n = 0 \quad n > 1\,,
\end{aligned} \tag{2.58}$$

where $\varepsilon = r_0/2h_a$; r_0 and h_a are shown in Figure 2.25, and

$\delta_{m,n}$ is Kronecker delta, $\delta_{m,n} = \begin{cases} 1, if\ m = n \\ 0, if\ m \neq n \end{cases}$.

The inflow rate for a tunnel is the product of the perimeter and the average potential value. For a circular tunnel, the inflow rate is written

$$q = 2\pi r\varphi_0\,,$$

where φ_0 is the average value of the single layer potential and also the first coefficient of the Fourier Series in Eq.(2.56) and can be obtained by the resolution of the system of equations (2.57) and (2.58).

The precision with which φ_0 is calculated depends on the number of terms in the Fourier series. If the Fourier series is reduced to 1, 2 or 3 terms, the average value φ_0 may be calculated by hand. Otherwise, it is preferable to use a numerical method.

If the Fourier series is truncated and reduced to one term, the inflow rate is

$$q_0 = 2\pi K \frac{h_a}{\ln \frac{2h_a}{r_0}}, \tag{2.59}$$

where h_a is the distance between ground surface and center of the tunnel and the groundwater table is just at the ground surface. r_0 is the radius of the tunnel. This result is the same form as Goodman's (1965) Eq.(2.49):

$$Q = \frac{2\pi KL(H_0 + h_a)}{\ln(2h_a / r_0)}.$$

If H_0 is equal to zero (the condition in this case) and the flow rate per tunnel length is considered, these two solution are exactly the same.

If the Fourier series is reduced to two terms, the inflow rate is

$$q_1 = 2\pi K \frac{1 - 3\left(\frac{r_0}{2h_a}\right)^2}{\left[1 - \left(\frac{r_0}{2h_a}\right)^2\right] \ln \frac{2h_a}{r_0} - \left(\frac{r_0}{2h_a}\right)^2}. \tag{2.60}$$

The approximation q_0 overestimates the inflow rate by less than 2 percent for a ratio r_0/h_a of 20 percent and by less than 7 percent for a ratio r_0/h_a of 40 percent. The approximation q_1 underestimates the inflow rate by less than 1 percent for a ratio r_0/h_a of 70 percent.

By using the Green's Function method, I obtained additional solutions, as shown in Table 2.5.

Table 2.5 Infiltration into tunnels beneath a horizontal water table (From El Tani, 1999)

Tunnel section and aquifer properties	Permeability	Water inflow [1]
Tunnel of square section. c : side length. h : centre depth. [2] Isotropic and homogeneous aquifer. [3]	k [4]	$Q = \frac{2\pi k\, h_r}{\frac{6-\pi}{4} + \ln\frac{2^{3/4}h}{c}}$ [5]
Tunnel of elliptical section. a and b : horizontal and vertical semi-axis. h : centre depth.	k	$Q = \frac{2\pi k\, h_r}{\ln\frac{4h}{a+b}\sqrt{1+\frac{a^2-b^2}{4h^2}}}$ [6]
Two circular identical tunnels. r : radius. h : depth of centres. 2d : distance of centres. [7]	k	$Q = \frac{2\pi k\, h_r}{\ln\frac{2h}{r}\frac{\sqrt{d^2+h^2}}{d}}$
Two circular identical tunnels. r : radius. h : depth of centres. 2d : distance of centres. H : depth of an impervious layer. [8]	k	$Q = \frac{2\pi k\, h_r}{\ln\frac{4}{\pi}\frac{H}{r}\frac{\mathrm{tg}(\pi h/2H)}{\mathrm{th}(\pi d/2H)}\sqrt{\frac{\mathrm{ch}(\pi d/H)-\cos(\pi h/H)}{\mathrm{ch}(\pi d/H)+\cos(\pi h/H)}}}$
Tunnel of circular section. r : radius. h : centre depth. Anisotropic aquifer.	k_H k_V [9]	$Q = \frac{2\pi\sqrt{k_H k_V}\, h_r}{\ln\frac{4h}{r}\frac{\sqrt{k_H}}{\sqrt{k_H}+\sqrt{k_V}}\sqrt{1+\frac{k_V-k_H}{k_H}\frac{r^2}{4h^2}}}$ [10]
Tunnel of circular section. r : radius. h : centre depth. Non-homogeneous aquifer.	$ke^{-2\alpha z}$ [11]	$Q = 2\pi k e^{-2\alpha h}\frac{h_r I_0(\alpha r) - r I_1(\alpha r)}{K_0(\alpha r) - I_0(\alpha r)K_0(2\alpha h)}$ [12]

[1] The quantity of water that flows into the tunnel is Q and is in (m^3/s/meter of tunnel) and per tunnel if there is more than one. It is transformed into (l/s/km of tunnel) when it is multiplied by 10^6.

[2] h is the depth of the centre of the tunnel below the water table or sea bottom for undersea tunnels.

[3] Aquifers in the following are isotropic unless the contrary is mentioned and homogeneous unless the contrary is mentioned.

[4] k (m/s).

[5] Resultant head is $h_r = h - p_T/\gamma$ (m). p_T is the mean pressure on the tunnel edge and γ the specific weight of water. p_T is zero for a drained tunnel and different from zero for a partially drained tunnel.
For undersea tunnels, sea depth is added to the resultant head which becomes $h_r = h + h_s - p_T/\gamma$ where h_s is sea depth.

[6] Approximated integration with $(a^2 - b^2)/h^2 < 1$.

[7] $2d > 2r$.

[8] H is the depth of an impervious base below the water table or sea bottom for an undersea tunnel.
$H > h + r$ and $2d > 2r$.

[9] k_H is the horizontal permeability and k_V is the vertical permeability.

[10] Approximated integration with $(k_V - k_H)r^2/k_H h^2 < 1$.

[11] α (m^{-1}) is the intensity of the non-homogeneity. z is the depth below the water table or sea bottom for an undersea tunnel.

[12] $I_0(x)$, $I_1(x)$ and $K_0(x)$ are modified Bessel functions of the first kind of order zero and one and the second kind of order zero.

2.3.2.3.1.3 Another method to resolve the problem (Lei, 1999; Lei, 2000)

Lei (1999) makes similar assumptions to Goodman's model (Section 2.3.2.3.1.1). The schematic diagram is shown in Figure 2.26.

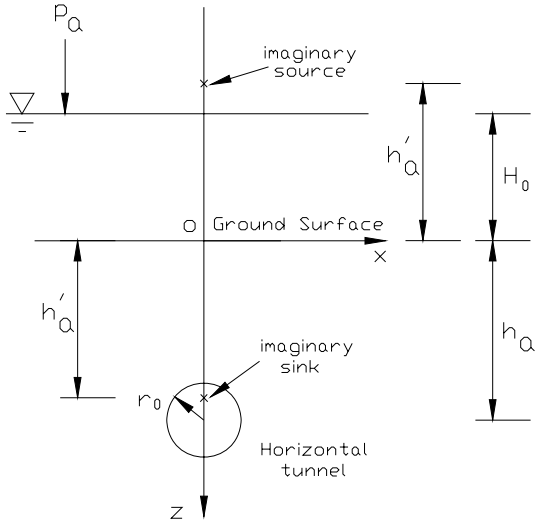

Figure 2.26 Schematic diagram of water inflow (after Lei,1999)

Assumptions:

A. The tunnel is horizontal with a circular cross section and is located in a fully saturated, homogeneous, isotropic, and semi-infinite porous aquifer;

B. The flow is in steady-state;

C. The fluid is incompressible;

D. The total head at the ground surface and that at the tunnel perimeter are both constant.

Equations and boundary conditions:

The two-dimensional flow around the tunnel can be described by the following Laplacian equation (Eq.(2.61)) and boundary conditions:

$$\frac{\partial^2 h}{\partial x^2} + \frac{\partial^2 h}{\partial z^2} = 0 \tag{2.61}$$

$$h\big|_{z=0} = H_0 + p_a / \gamma_w \tag{2.62}$$

$$h\Big|_{x^2+(z-h_a)^2=r_0^2} = h_t\,, \tag{2.63}$$

where h [L] is the total head and p_a/γ_w [L] is the atmospheric pressure head (usually $p_a/\gamma_w \equiv 0$).

Derivation and solutions:

To find the solution to Eq.(2.61) that satisfies the boundary conditions Eq.(2.62) and Eq.(2.63), consider a flow field created by superposition of an imaginary line sink at (0, h'$_a$) with discharge q, and an imaginary line source at (0, -h'$_a$) with recharge q, where h'$_a$ is a parameter to be determined from the boundary condition. The approximations of Goodman's model are that the line sink is locked at the tunnel's centerline. However, here the line sink should not be located at the tunnel's centerline in order for the boundary condition at the tunnel perimeter to be met.

From the total head solution for radial flow (sink) (Strack, 1989)

$$h = \frac{q}{2\pi K}\ln(r) + C \tag{2.64}$$

and the superposition principle, Lei obtains the analytical solution of this model in which the total head at the perimeter of the tunnel is a constant h_t:

$$Q = \frac{2\pi KL\left(H_0 - h_t + p_a/\gamma_w\right)}{\ln\left[h_a/r_0 + \sqrt{\left(h_a/r_0\right)^2 - 1}\right]}\,. \tag{2.65}$$

The solution of Goodman (1965) can be considered an approximation to Eq.(2.65) with $h_t = p_a/\gamma_w + \left(-h_a\right)$ and $h_a >> r_0$ ($\left(h_a/r_0\right)^2 - 1 \approx h_a/r_0$). Compared with this result, Goodman's solution underestimates the inflow rates. For $h_a/r_0 = 2$, the relative error is about -5 percent and the error becomes more significant as h_a/r_0 gets smaller.

Lei (2000) also gives the exact analytical solution of this model with a constant pressure head of p_t at the tunnel wall. In this case, the author sets a constant pressure head everywhere in the flow field, before the tunnel exists; that is, there is a steady linear

vertical downward flow in the aquifer before the tunnel exists. By setting this flow field, it is easy to solve this problem. However, in practice this condition seldom occurs. The author uses the same method as Lei (1999) to get the result

$$Q = \frac{2\pi KL\left(H_0 - p_t/\gamma_w + p_a/\gamma_w\right)}{\ln\left[h_a/r_0 + \sqrt{\left(h_a/r_0\right)^2 - 1}\right]}, \tag{2.66}$$

where the definitions of Q, K, L, H_0, h_a, r_0 are the same as Eq.(2.65), p_t/γ_w [L] is the pressure head at the perimeter of the tunnel, and p_a/γ_w [L] is the atmospheric pressure head.

2.3.2.3.1.4 Heuer's empirical method

Heuer (1995, 2005) gives a semi-empirical method for estimating possible water inflow based on borehole water pressure test results by using the radial flow equation (Goodman's model) with a reduction factor (1/8) to account for many of the idealizations associated with the use of this equation. Some of these factors are depletion of storage, fracture flow (rather than flow in porous media), and changes in the boundary conditions. The method provides an estimate of percentages of tunnel length that will experience different intensities of long term steady-state inflow. It also provides an estimate of possible initial heading inflow by steady-state inflow per unit tunnel length times a heading inflow factor. This method is widely used in the industry, including the Devil's slide tunnel Geohydrologic Study (2004).

The first step in application of this approach is to develop a histogram of the hydraulic conductivity test results from the water pressure testing of the drill holes. If the entire tunnel is in one rock formation, or in formation of similar nature, all test data from the entire tunnel length is plotted on one histogram. If significantly different rock formations are expected along the tunnel length, different histograms are determined for the different tunnel lengths in each formation. Calculations of steady state inflow and the

estimated heading inflow are carried out using the tabular format (see following Figure 2.27, Figure 2.28, Figure 2.29, and Figure 2.30). As noted, the inflows calculated by this method do not consider discrete flows from faults zones.

The specific correlations for steady state inflow (obtained from Goodman's solution divided by 8) and heading inflow factor, F_h, summarized on Figure 2.27 and Figure 2.28, are based upon the author's experience to date for a variety of tunnel projects in a variety of geologic settings. However, these specific correlations may not be universally valid, as the author has stated Heuer, 1995.

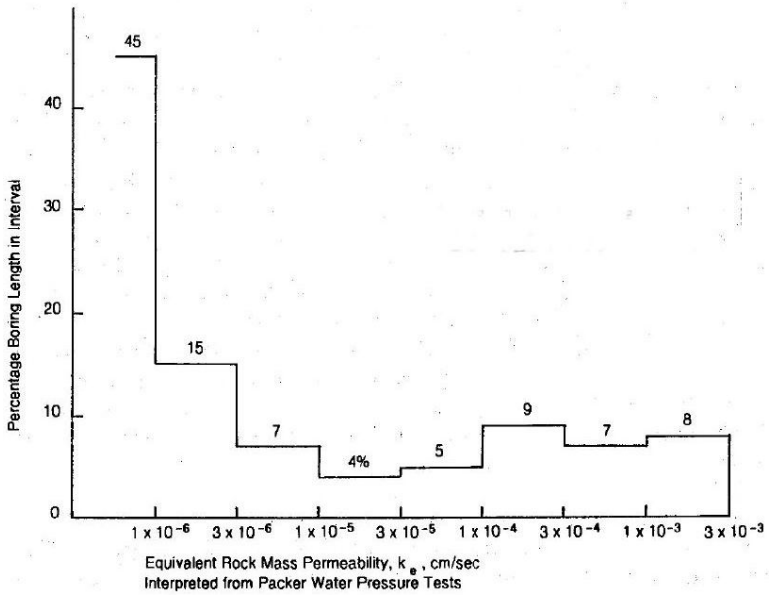

Figure 2.27 Histogram of Hypothetical Tunnel Exploratory Boring Test Results (From Heuer, 1995, Figure 3A)

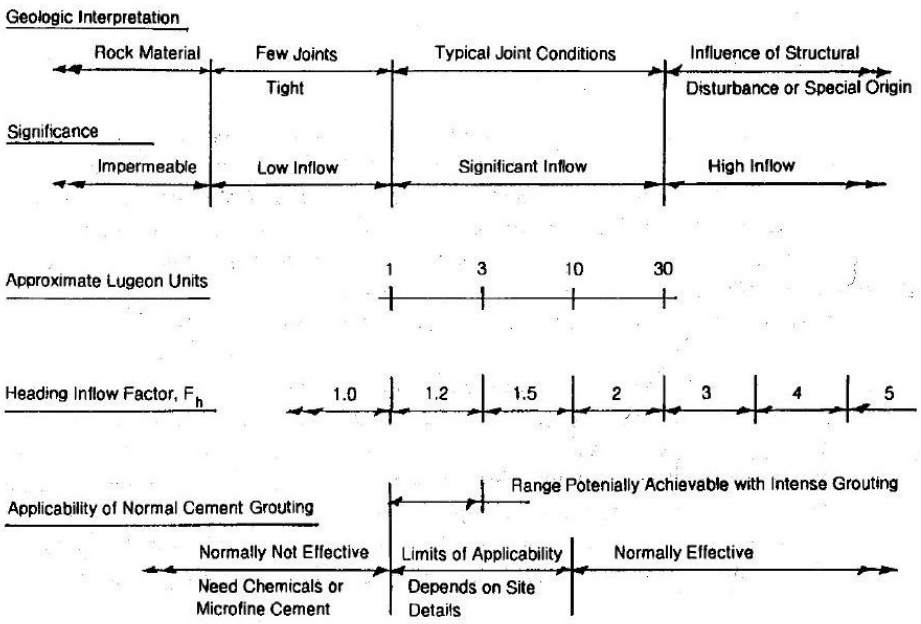

Figure 2.28 Interpretation – Relative Significance (From Heuer, 1995, Figure 3B)

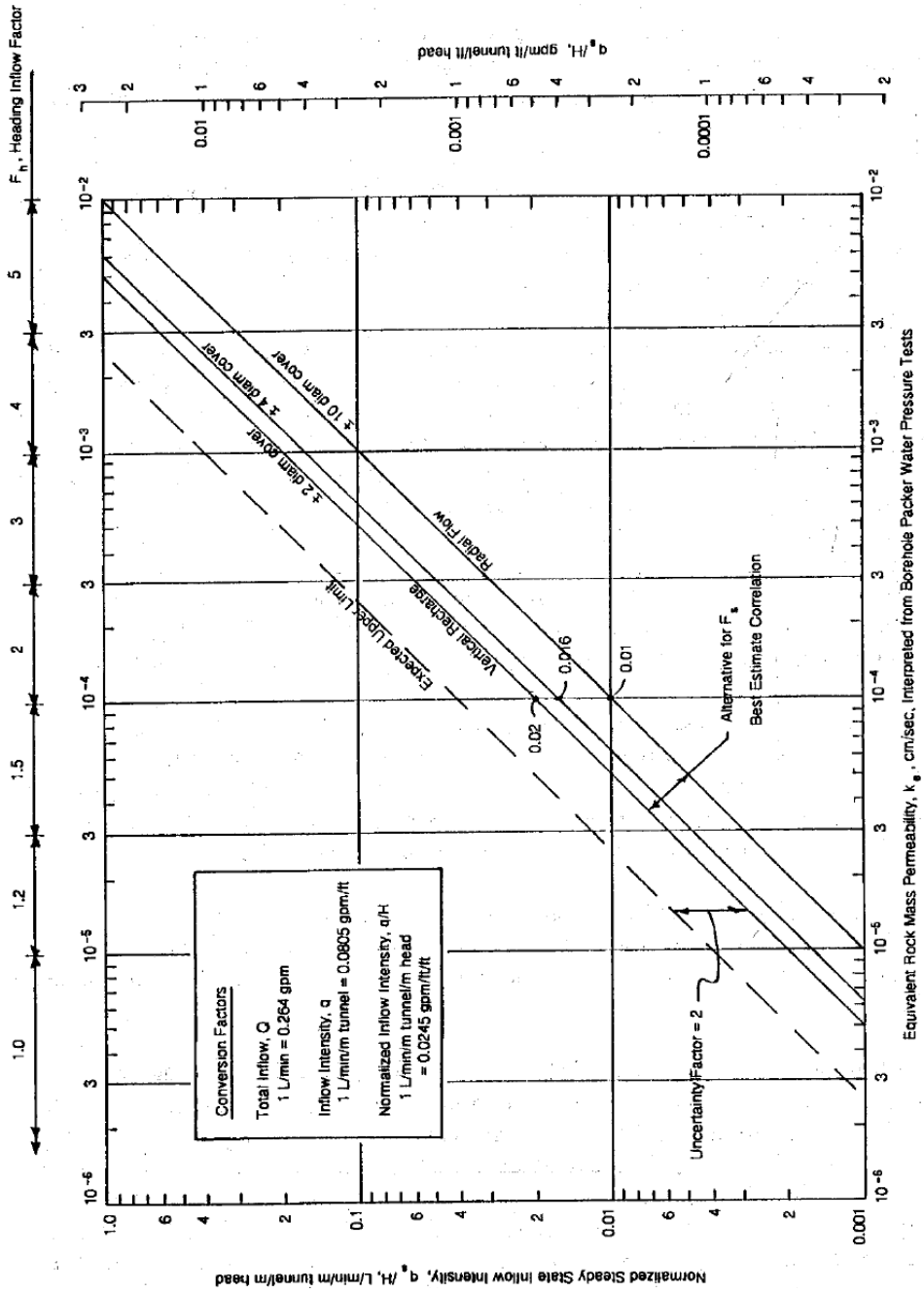

Figure 2.29 Relationship between state inflow and equivalent permeability (From Heuer, 1995, Figure 4)

Note: “Fig. 3A, Fig. 3B and Fig. 4” mentioned in the above figure are Figure 2.27, Figure 2.28, Figure 2.29 respectively.

Figure 2.30 Example analysis (From Heuer, 1995, Figure 6)

2.3.2.3.1.5 Goodman’s augmented solution assuming a hydraulic conductivity gradient

Zhang and Franklin (1993) extended Goodman's steady-state model by taking into account the commonly observed hydraulic conductivity gradient, which is assumed to satisfy the exponential form as the following expression, in which parameter A is linearly composed of two parts to account for the stress-dependent and stress-independent factors.

$$K = K_s \exp(-Ah) = K_s \exp[-C\sigma' - a_3 z], \tag{2.67}$$

where A is the hydraulic conductivity gradient, C and a_3 are coefficients, σ' is the effective stress in the rock mass, z is the depth (z axis is positive downwards with origin at the ground surface, see Figure 2.31).

If we assume a tunnel of circular cross-section driven beneath a sea or lakebed, or into a inexhaustible aquifer, a continuous isotropic semi-infinite medium, isotropic hydraulic conductivity and isotropic stress, then the governing equation and boundary conditions describing the problem of water inflow can be established as follows (the flow model is shown in Figure 2.31):

$$\frac{\partial}{\partial x}\left(K\frac{\partial h}{\partial x}\right) + \frac{\partial}{\partial z}\left(K\frac{\partial h}{\partial z}\right) - q\,\delta(x-0)\delta(z-h_a) = 0 \tag{2.68}$$

$$\begin{aligned} h(x,z)\big|_{z=0} &= H_0 \\ h(x,z)\big|_{z\to\infty} &= H_0 \\ h(x,z)\big|_{x\to\pm\infty} &= H_0, \end{aligned} \tag{2.69}$$

where h is the total head at any given depth (which is equal to the pressure head plus the elevation head $h_a - z$); H_0 is the constant total head (refer to the elevation of tunnel center line as the datum); q is the inflow per unit of tunnel length; h_a is the rock cover (depth of the tunnel below ground surface); d is tunnel diameter; $\delta(t)$ is Dirac delta; and

$$\delta(t) = \begin{cases} 1, \text{if } t = 0 \\ 0, \text{if } t \neq 0 \end{cases}.$$

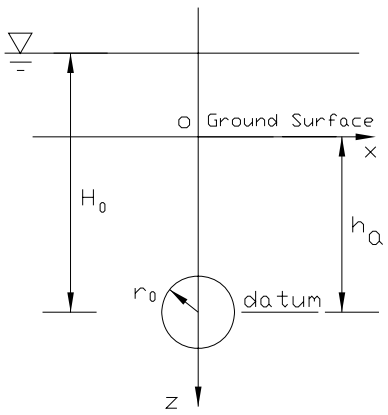

Figure 2.31 Schematic diagram of water inflow (after Zhang and Franklin, 1993)

The hydraulic conductivity K in Eq.(2.68) is a function of depth and water pressure. For steady-state tunnel inflow under conditions (2.69) the water pressure in the x-z coordinates can be determined as:

$$u = \gamma_w (h - h_a + z)$$

and the effective stress term becomes

$$\sigma' = \gamma_m z - \gamma_w (h - h_a + z) = (\gamma_m - \gamma_w) z - \gamma_w h + \gamma_w h_a , \tag{2.70}$$

substituting Eq.(2.70) into Eq.(2.67), we obtain the hydraulic conductivity expression for this particular problem:

$$K = K_s \exp(-a_1 h_a) \exp(-Az) \exp(a_1 h), \tag{2.71}$$

where $a_1 = \dfrac{\gamma_w}{\gamma_m - \gamma_w}(A - a_3)$. a_3 is a stress-independent factor that lies between 0 and A and may be estimated as about 0.25A, for the usual situation, where hydraulic conductivity is proportional to the cube of joint aperture and inversely proportional to joint spacing and both aperture and spacing are decreasing exponentially with depth (Manev and Avramova, 1970; Snow, 1968).

The constant K_s in Eq.(2.73) is the surface intercept of the exponential conductivity gradient, not the actual hydraulic conductivity at surface. The way to obtain

K and A are obtained by least-squares fitting a straight line to a set of hydraulic conductivity measurements at different depths plotted on a $\log_{10}(K)$ versus depth graph. The negative slope of the line divided by $\log_{10}(e)$ is the conductivity gradient A, and the intercept of the line on the $\log_{10}(K)$ axis is K_s.

The Fourier transform has been used by the authors to solve the problem in Eqs.(2.68), (2.69) and (2.71) and the water inflow rate Q is obtained as:

$$Q = \frac{2LK_s \exp(-a_1 h_a)\pi\left[\exp(a_1 H_0)-1\right]\exp(-Ah_a)}{a_1\left[Y_0\left(\frac{A}{2}r_0\right)-Y_0\left(\frac{A}{2}\sqrt{r_0^2+4h_a^2}\right)\right]}, \tag{2.72}$$

where $Y_0(\cdot)$ is Bessel's function of the second kind and zero order, which is defined in Appendix A and whose values may be found in mathematical handbooks (Luke, 1962).

If the tunnel size is very small compared with its depth (i.e., $r_0/h_a<<1$), then the solution can be further simplified as follows:

$$Q = \frac{2LK_s\pi \exp\left[-(A+a_1)h_a\right]\left[\exp(a_1 H_0)-1\right]}{a_1\left[Y_0\left(\frac{A}{2}r_0\right)-Y_0(Ah_a)\right]}. \tag{2.73}$$

Inflow prediction should be based on the hydraulic conductivity measured at the tunnel depth plus the gradient A measured within several diameters above and below this depth. The parameter K_s in Eq.(2.73) can be replaced by the measured hydraulic conductivity K_0 (measured hydraulic conductivity) to obtain

$$Q = \frac{2LK_0\pi \exp\left[-(A+a_1)h_a\right]\cdot\left[\exp(a_1 H_0)-1\right]}{a_1\left[Y_0\left(\frac{A}{2}r_0\right)-Y_0(Ah_a)\right]}. \tag{2.74}$$

If the hydraulic conductivity gradient A=0 (i.e., if the hydraulic conductivity does not change with depth), then Eq.(2.73) reduces to Goodman's solution

$$Q = \frac{2\pi K_s L H_0}{\ln(2h_a/r_0)}. \tag{2.75}$$

2.3.2.3.2 Dupuit horizontal flow model (inflow through tunnel walls with drawdown)

The excavation of an underground opening often changes the ground water regime of a locality. The distribution of water, the direction and velocity of its movement, and the rate of its fluctuation with time may be affected. As Goodman (1965) states, there are two methods to solve this problem. One approach is to treat this unsteady flow as a sequence of steady states, using the results with a rule for unwatering the uppermost rock units that generates an assumed shape for the drawdown surface at any time. A second approach is to improve a simple formula known to be inadequate (usually in two dimensions) by the use of empirical coefficients whose values are determined in model studies.

Using Dupuit horizontal flow model, Goodman et al. (1965) give semi-empirical solutions for transient flow and steady-state flow, if there is enough recharge to keep the water table constant with time. Perrochet and Musy (1992) solve these two cases by assuming that the shape of the water table is elliptical, and Raymer (2005) develops a similar lateral model.

2.3.2.3.2.1 The initial solution in groundwater mechanics (Strack, 1989)

First, we consider the approximately one-dimensional flow that is shown in Figure 2.32. The infiltration flow rate that enters the system vertically is W [LT^{-1}]. The resistance to flow in the vertical direction is neglected in accordance with the Dupuit assumption.

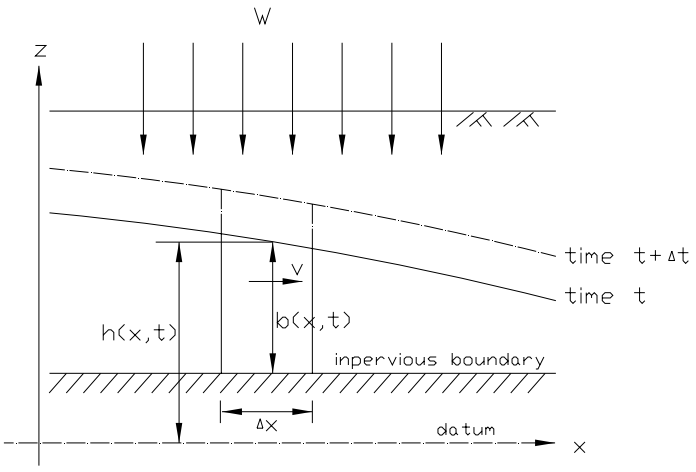

Figure 2.32 Unsteady water flow in the unconfined aquifer

According to the principle of mass conservation, during the time interval, Δt, the inflow into the volume with sides Δx, b and unit width, minus the outflow, plus the infiltration will be equal to the storage change. That is,

$$Q_x\left(x-\frac{1}{2}\Delta x\right)-Q_x\left(x+\frac{1}{2}\Delta x\right)+Q_w=\Delta Q_s; \tag{2.76}$$

And because $$Q_x\left(x-\frac{1}{2}\Delta x\right)=v\left(x-\frac{1}{2}\Delta x\right)\cdot b\left(x-\frac{1}{2}\Delta x\right)\cdot\Delta t$$

$$Q_x\left(x+\frac{1}{2}\Delta x\right)=v\left(x+\frac{1}{2}\Delta x\right)\cdot b\left(x+\frac{1}{2}\Delta x\right)\cdot\Delta t,$$

one obtains:

$$Q_x\left(x-\frac{1}{2}\Delta x\right)-Q_x\left(x+\frac{1}{2}\Delta x\right)=\left[v\left(x-\frac{1}{2}\Delta x\right)\cdot b\left(x-\frac{1}{2}\Delta x\right)-v\left(x+\frac{1}{2}\Delta x\right)\cdot b\left(x+\frac{1}{2}\Delta x\right)\right]\cdot\Delta t$$

$$=\frac{\partial}{\partial x}\left[v(x,t)b(x,t)\right]\cdot\Delta x\cdot\Delta t,$$

Consequently Eq.(2.76) becomes:

$$-\frac{\partial(vb)}{\partial x}\cdot\Delta x\cdot\Delta t+W\cdot\Delta x\cdot\Delta t=S_y\cdot\frac{\partial h}{\partial t}\cdot\Delta x\cdot\Delta t, \tag{2.77}$$

where $v(x,t)$ is the horizontal velocity of flow (the vertical velocity is neglected because of the Dupuit assumption); $b(x,t)$ is the thickness of the aquifer; and S_y is the specific yield of the aquifer, i.e., the amount of water that a portion of an aquifer releases from storage (per unit mass or volume of aquifer and per unit change in hydraulic head) while remaining fully saturated.

Furthermore, according to Darcy's law, $v(x)$ is equal to $-K\frac{\partial h}{\partial x}$, which gives:

$$\frac{\partial}{\partial x}\left(Kb\frac{\partial h}{\partial x}\right)+W=S_y\cdot\frac{\partial h}{\partial t} \quad . \tag{2.78}$$

This equation is known as the unconfined unsteady (one dimensional) flow (Boussinesq) equation (see Eq.(2.5)).

Then, we consider an unconfined aquifer bounded by two long, parallel rivers (constant hydraulic boundary conditions); there is no infiltration and no water table change (steady flow). A cross-section through the aquifer is given in Figure 2.33.

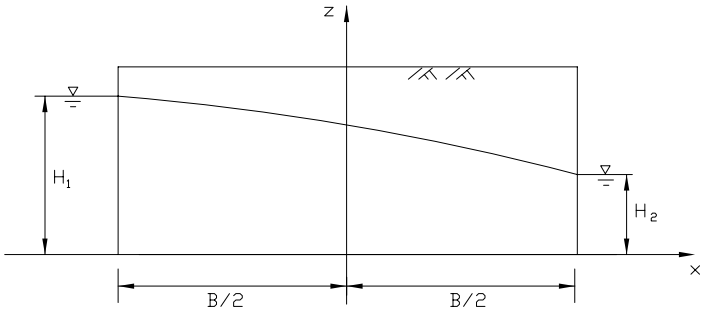

Figure 2.33 One-dimensional flow in an unconfined aquifer

In this situation, the basic Eq.(2.78) becomes

$$\frac{\partial}{\partial x}\left(Kb\frac{\partial h}{\partial x}\right)=0\,. \tag{2.79}$$

If the impervious base is horizontal, the datum is located at the impervious base, and $b=h$, Eq.(2.79) can be rearranged as

$$\frac{\partial^2\left(\frac{1}{2}Kh^2\right)}{\partial x^2} = \frac{\partial^2 \Phi}{\partial x^2} = 0\,, \tag{2.80}$$

where we define $\Phi = \frac{1}{2}Kh^2 + C_u$ as the discharge potential.

This equation has the general solution:

$$\Phi = C_1 x + C_2\,.$$

The boundary conditions are

$$h\big|_{x=-B/2} = H_1 \quad \text{or} \quad \Phi\big|_{x=-B/2} = \Phi_1 = \frac{1}{2}KH_1{}^2$$

$$h\big|_{x=B/2} = H_2 \quad \text{or} \quad \Phi\big|_{x=B/2} = \Phi_2 = \frac{1}{2}KH_2{}^2\,.$$

Application of the boundary conditions yields

$$\Phi = \frac{\Phi_2 - \Phi_1}{B}x + \frac{\Phi_1 + \Phi_2}{2}\,.$$

The discharge q_x is found from $q_x = -\frac{\partial \Phi}{\partial x}$,

$$q_x = \frac{\Phi_1 - \Phi_2}{B} \quad \text{or} \quad q_x = \frac{K\left(H_1{}^2 - H_2{}^2\right)}{2B}\,. \tag{2.81}$$

This result is known as the Dupuit formula.

An expression for the total head h is obtained as

$$h = \sqrt{\frac{1}{2}\left(H_1{}^2 + H_2{}^2\right) - \frac{H_1{}^2 - H_2{}^2}{B}x}\,. \tag{2.82}$$

This equation represents a parabola, known as the Dupuit parabola.

2.3.2.3.2.2 Semi-empirical solution (Goodman et al., 1965)

Assumptions:

A. The flow in the vertical direction is neglected (Dupuit assumptions);

B. The tunnel completely penetrates a water bearing zone;

C. The line of drawdown is a parabola fixed at the center of the tunnel;

D. The flow is steady from time t to time t+ Δ t (Dupuit formula can be used)

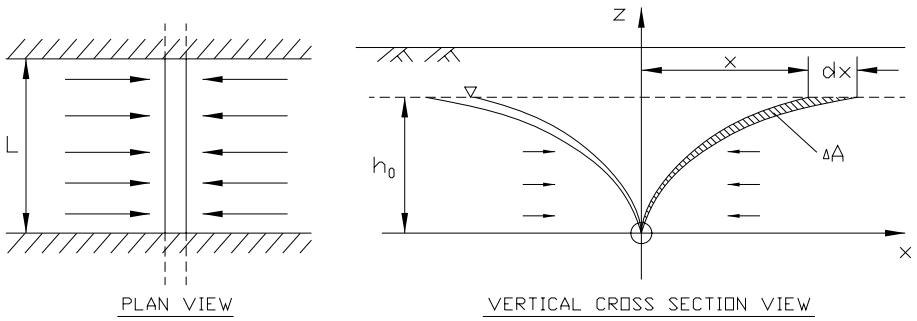

Figure 2.34 Goodman's unsteady flow model in water bearing zone

Derivation and solution:

Consider one half side aquifer. Goodman et al. (1965) use assumption D, and let H_1 in Eq.(2.82) be equal to h_0 (the initial total head, if the tunnel axis is the datum), H_2 be equal to zero and B be equal to x in Eq.(2.81). Then, using the Dupuit formula, the flow in the time interval dt is

$$dQ = q \cdot L \cdot dt = \frac{KLh_0^{\,2}}{2x} \cdot dt\,, \tag{2.83}$$

where K [LT^{-1}] is the hydraulic conductivity of the aquifer, drawdown h_0 [L] is the difference between the total head inside the tunnel, and the total head beyond the area of influence of the tunnel (this could also be taken as the initial total head above the tunnel horizon before tunneling begins).

To provide flexibility, Goodman introduced the coefficient C, so that

$$dQ = \frac{KLh_0^{\,2}}{Cx} \cdot dt\,. \tag{2.84}$$

Because the drawdown shape has been assumed parabolic, the total amount of water drained in time t is

$$Q = \frac{1}{3} \cdot x \cdot L \cdot h_0 \cdot S_y\,. \tag{2.85}$$

In the time interval dt it is equal to

$$dQ = \frac{1}{3} \cdot dx \cdot h_0 \cdot L \cdot S_y , \tag{2.86}$$

where S_y is the specific yield.

Combining Eqs.(2.84) and (2.86) gives

$$\frac{KLh_0^{\,2}}{Cx} \cdot dt = \frac{1}{3} \cdot dx \cdot h_0 \cdot L \cdot S_y . \tag{2.87}$$

This can be separated and integrated directly, which leads to the following formula for x, where x=0 when t=0:

$$x = \sqrt{\frac{6Kh_0 t}{CS_y}} . \tag{2.88}$$

Substituting Eq.(2.88) into Eq.(2.85) yields the following formula for the cumulative discharge through two side walls of a tunnel completely penetrating an infinitely wide unrercharged aquifer:

$$Q = \sqrt{\frac{8KL^2 h_0^{\,3} S_y t}{3C}} . \tag{2.89}$$

Discussion:

By using model tests, Goodman et al. (1965) obtained a value of C=1.36 (instead of 2) in Eq.(2.89) for full penetration. For partial penetration into the pervious zone, by calculating the C values giving best agreement between this expression and the model test data, it was found that a linear relationship exists as follows:

$$C = 0.12 + 1.24D , \tag{2.90}$$

where D is the fraction of the width of the water bearing zone penetrated by the tunnel.

2.3.2.3.2.3 Lateral model (Raymer, 2005)

Assumptions:

A. The layer is homogenous, isotropic and uncompressible;

B. The flow in the vertical direction is neglected (Dupuit assumptions);

C. The tunnel completely penetrates a water bearing zone;

D. Groundwater table is depressed to the tunnel centerline. Then, the inflow into the tunnel can be given by Dupuit lateral flow to both sides of an open trench.

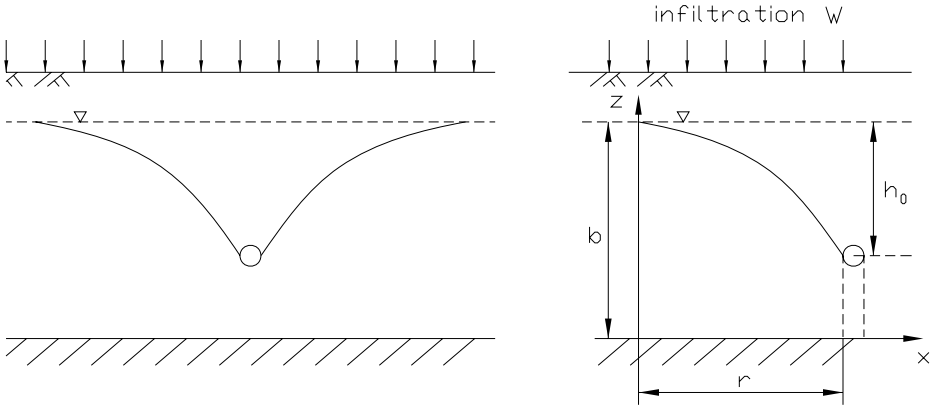

Figure 2.35 Raymer's lateral flow model

As Figure 2.35 shows, the governing equation (See Eq.(2.78) with $S_y = 0$) and the boundary conditions are, respectively:

$$\frac{\partial}{\partial x}\left(Kh\frac{\partial h}{\partial x} \right) + W = 0$$

$$h\big|_{x=0} = b \tag{2.91}$$

$$h\big|_{x=r} = b - h_0$$

$$q\big|_{x=0} = Kh\frac{\partial h}{\partial x}\big|_{x=0} = 0$$

where r is the lateral distance over which drawdown has spread to one side of the tunnel. Before steady state, r, changes with respect to time. W is the recharge rate.

By solving Eq.(2.91), the solutions are:

$$r = \sqrt{\frac{K\left(2bh_0 - h_0^{\,2}\right)}{W}}$$

$$q_x = Wx \tag{2.92}$$

$$h = \sqrt{b^2 - \frac{W}{K}x^2}$$

We can find that the water surface is no longer a parabola (Dupuit parabola Eq.(2.82)), but rather an ellipse because of the infiltration recharge.

If we let x be equal to r (maximum drawdown), we let L be the tunnel length and we consider the flow at both sides, the total flow rate into the tunnel should be:

$$2Lq_x\big|_{x=r} = 2LWr = 2L\sqrt{KW\left(2bh_0 - h_0^{\,2}\right)} = 2L\sqrt{2TWh_0^{'}} \qquad (2.93)$$

where T is equal to the transmissivity Kb. h_0' is the "corrected drawdown," which is equal to $h_0 - \left(h_0^{\,2}/2b\right)$.

From the above Eq.(2.93), once only the infiltration recharge is considered, the flow is no longer directly proportional to the permeability, it is a function of both recharge and permeability and it varies with the square-root of the permeability. Because the lateral model assumes that the two tunnel side walls extend vertically all the way to the base of the flow system, which is not realistic, then it is necessary to place a limit on the thickness of the flow system to avoid overestimating the inflow. For practical purposes, Raymer suggests that the thickness of the flow system be limited to

$$b \le 1.5h_0 . \qquad (2.94)$$

However, Raymer (2005) made a mistake in his derivation, in that the factor "2" under the square root was missing in Eq.(2.93). Therefore, in turn, the calculated inflow rate in Table 2.6 and Figure 2.36 needs to be corrected. The revised table and figure can be seen in Table 2.7 and Figure 2.37.

Table 2.6 Actual and estimated inflows using different models (from Raymer, 2005)

	Chattahoochee		Nancy Creek		Clear Creek	
K_{avg}	3.0×10^{-5} cm/s		6.7×10^{-5} cm/s		7.9×10^{-4} cm/s	
	L/s	gpm	L/s	gpm	L/s	gpm
Actual	90	1,430	88	1,400	Not completed	
Lateral	89	1,403	92	1,457	155	2,451
Heuer	63	1,005	96	1,523	644	10,210

Table 2.7 Actual and estimated inflows using different models (Revised)

	Chattahoochee		Nancy Creek		Clear Creek	
Kavg	3.0 x 10-5 cm/s		6.7 x 10-5 cm/s		7.9 x 10-4 cm/s	
	L/s	gpm	L/s	gpm	L/s	gpm
Actual	90	1,430	88	1,400	Completed but no data	
Lateral	126	1,984	130	2,060	219	3466
Heuer	63	1,005	96	1,523	644	10,210

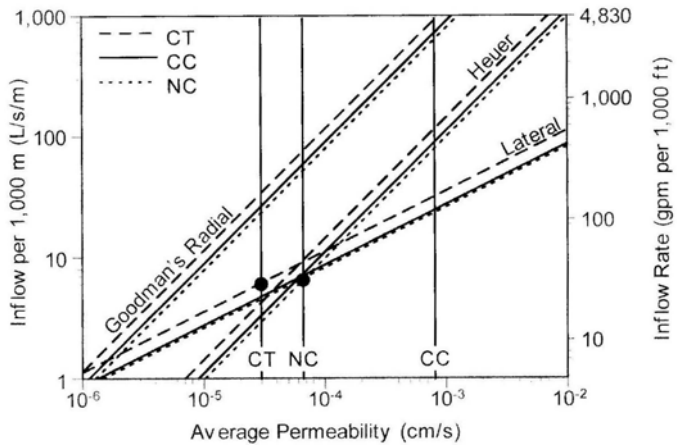

Figure 2.36 Inflow versus permeability for lateral, radial, and Heuer models (from Raymer, 2005)

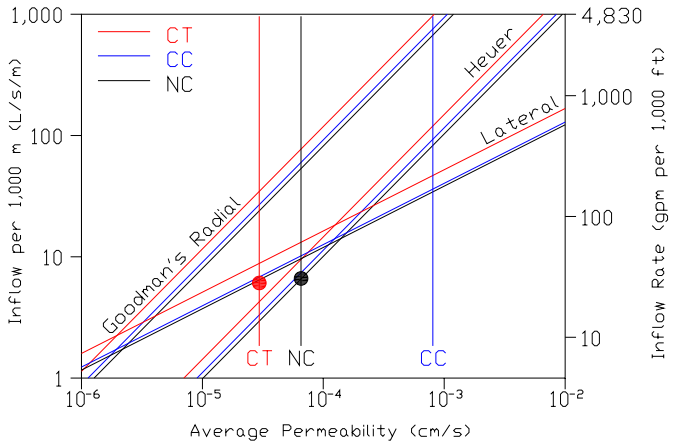

Figure 2.37 Inflow versus permeability for lateral, radial, and Heuer models (Revised)

2.3.2.3.2.4 Elliptical water table solution

Perrochet and Musy (1992) present a formulation based on the classical Dupuit-Forchheimer hypothesis (Strack, 1989) and shape of the water table as follows.

Assumptions:

A. Applicability of Darcy's law

B. Horizontal flow

C. Homogenous, isotropic and uncompressible layer

D. Infiltrated rainfall directly recharge the water table

E. Evapotranspiration is neglected

F. The water table has an elliptical shape

Two cases are considered: the tunnel is located either at the edge of the impervious boundary or at the interface of two layers.

If Eq.(2.78) is integrated over x, one obtains:

$$q(t) = Wr - \frac{\partial V}{\partial t}, \tag{2.95}$$

where q is the linear flow into the tunnel; W is the constant intensity of the infiltrated rainfall during a given time period; and V is the quantity of gravity water (i.e., water that can be yielded by gravity) stored in the aquifer.

For case 1: drain or tunnel lying on an impervious layer

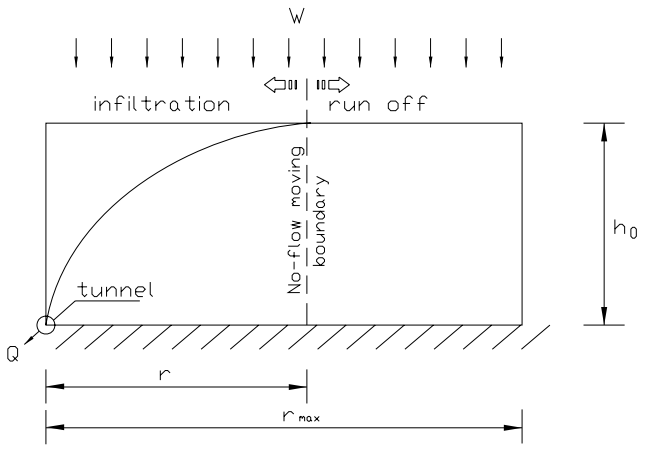

Figure 2.38 Perrochet and Musy's lateral flow model (case 1)

As Figure 2.38 shows, applying Dupuit's formula Eq.(2.81) and the given assumptions, $q(t)$ and $V(t)$ can be expressed as

$$q(t) = \frac{Kh_0^{\,2}}{r} \tag{2.96}$$

$$V(t) = S_y \frac{\pi}{4} h_0 r + S_y h_0 (R_{\max} - r), \tag{2.97}$$

where K is the saturated hydraulic conductivity and S_y is the specific yield/drainable porosity. $V(t)$ is obtained by computing the water volume that can be yielded by gravity below the water surface (a quarter of an ellipse and a rectangle). $R_{\max}$ is the maximum width considered in the model.

Differentiating Eq.(2.97) and substituting it into Eq.(2.95) together with Eq.(2.96) yields the differential equation:

$$S_y\left(1-\frac{\pi}{4}\right)h_0 r\frac{\partial r}{\partial t}+Wr^2=Kh_0{}^2 \tag{2.98}$$

to be solved with the initial boundary condition:

$$r\big|_{t=0}=R_0\,,$$

where R_0 is the initial "no-flow moving boundary" location.

Eq.(2.98) can be integrated as follows:

$$r(t)=\sqrt{\left(R_0{}^2-\frac{Kh_0{}^2}{W}\right)\exp\left[-\left(\frac{8W}{S_y(4-\pi)h_0}\right)^t\right]+\frac{Kh_0{}^2}{W}}\,, \tag{2.99}$$

where R_0 is the initial width of the depression zone, when the constant infiltration W over the period t takes place, and $r(t)$ is the width of the depression zone at the end of this time period.

From Eq.(2.99), where the flow reaches steady state ($t\to\infty$),

$$\exp\left[-\left(\frac{8W}{S_y(4-\pi)h_0}\right)^t\right]\to 0$$

thus,
$$r(\infty)=h_0\sqrt{\frac{K}{W}} \tag{2.100}$$

Also from Eq.(2.99), we can find that for, an extended drought period (W=0):

$$\left(R_0{}^2-\frac{Kh_0{}^2}{W}\right)\exp\left[-\left(\frac{8W}{S_y(4-\pi)h_0}\right)^t\right]\to\frac{8Kh_0}{S_y(4-\pi)}t \quad \text{(using de l'Hospital Rule)}$$

thus,
$$r(t)\big|_{w\to 0}=\sqrt{\frac{8Kh_0}{S_y(4-\pi)}t+R_0{}^2} \tag{2.101}$$

As noted, Eqs. (2.82) and (2.83) are valid as long as $r\le R_{\max}$.

For case 2: drain or tunnel lying above an impervious layer

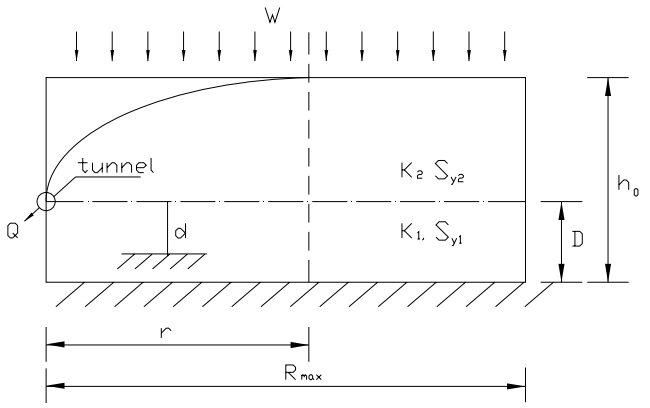

Figure 2.39 Perrochet and Musy's lateral flow model (case 2)

As shown in Figure 2.39, consider a tunnel located at the boundary between the horizontal layers of different hydraulic conductivity and storativity. Call d the equivalent depth of an impervious base that takes into account the different hydraulic conductivities; d is equal to D if $K_1 = K_2$.

As Figure 2.39 shows, the flow into the tunnel $q(t)$ may be calculated as (Perrochet and Musy, 1992):

$$q(t) = \frac{[2K_2 d + K_1(h_0 - D)](h_0 - D)}{r}, \tag{2.102}$$

where the equivalent depth d may vary in time and is a function of the distance r:

$$d(t) = \frac{\pi D r}{4D\ln(D/u) + \pi r}, \quad r > 2D \tag{2.103}$$

$$d(t) = \frac{\pi r}{4\ln(2r/u)}, \quad r < 2D, \tag{2.104}$$

where u is the wetted perimeter of the tunnel.

From Figure 2.40, the volume V of gravity water (i.e., water that can be yielded by gravity) stored in the aquifer can be written as the sum of three parts:

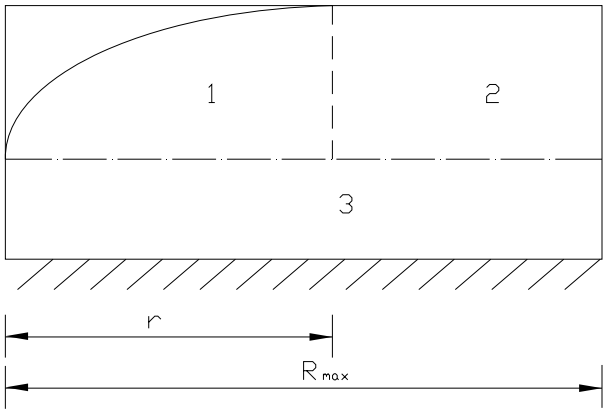

Figure 2.40 Sketch for calculating the water volume within the watertable

$$V(t) = S_{y1}\left[\frac{\pi}{4}(h_0 - D)r + (h_0 - D)(R_{\max} - r)\right] + S_{y2}DR_{\max}. \tag{2.105}$$

Differentiating Eq.(2.105) and substituting it and Eq.(2.102) into Eq.(2.95) yields the differential equation:

$$S_{y1}\left(1 - \frac{\pi}{4}\right)(h_0 - D)r\frac{\partial r}{\partial t} + Wr^2 = [2K_2 d + K_1(h_0 - D)](h_0 - D) \tag{2.106}$$

to be solved with the initial boundary condition:

$$r|_{t=0} = R_0$$

where R_0 is the initial "no-flow moving boundary" location. Eq.(2.106) can be integrated only when d is assumed to be constant in time:

$$r(t) = \sqrt{\left(R_0{}^2 - \frac{[2K_2 d + K_1(h_0 - D)](h_0 - D)}{W}\right)\exp\left[-\left(\frac{8W}{S_{y1}(4-\pi)(h_0 - D)}\right)t\right] + \frac{[2K_2 d + K_1(h_0 - D)](h_0 - D)}{W}}. \tag{2.107}$$

Eq.(2.107) may be used to analyze the cases of steady state flow ($t \to \infty$) and of an extended drought period (W=0).

$$r(\infty) = \sqrt{\frac{[2K_2 d + K_1(h_0 - D)](h_0 - D)}{W}} \tag{2.108}$$

$$r(t)|_{W\to 0} = \sqrt{\frac{8[2K_2 d + K_1(h_0 - D)]}{S_{y1}(4-\pi)}t + R_0{}^2} \tag{2.109}$$

As noted, Eq.(2.108) and Eq.(2.109) are valid as long as $r \le R_{\max}$.

Since Eq.(2.107) contains d, which is a function of r, an iterative procedure must be adopted: an initial approximate value of d or its limit cases Eq.(2.108) and Eq.(2.109) is inserted in Eq.(2.107); a first estimate of *r* is then obtained which, after substitution in Eq.(2.103) or Eq.(2.104), will give an improved value of *d*. This iterative procedure is carried out until convergence is reached.

2.3.2.3.3 Other classical steady state flow models

2.3.2.3.3.1 Steady state flow into tunnel face (point-sink flow)

If a tunnel is drilled from an impermeable stratum into a permeable stratum and the tunnel face just meets with the permeable stratum, we can use the point-sink flow solution to simulate this case. As shown in Figure 2.41, the tunnel model is obtained by rotating the well model 90 degrees. The rotation is valid when both cases share the same governing equation and boundary conditions. If the depth of the tunnel H_0 and the distance from the tunnel to the lower impervious base are much larger than the tunnel diameter, and if the groundwater surface is constant, then the boundary conditions in the tunnel case can be considered the same as in the well case. However, the flow field around the tunnel is not strictly radial because of gravity.

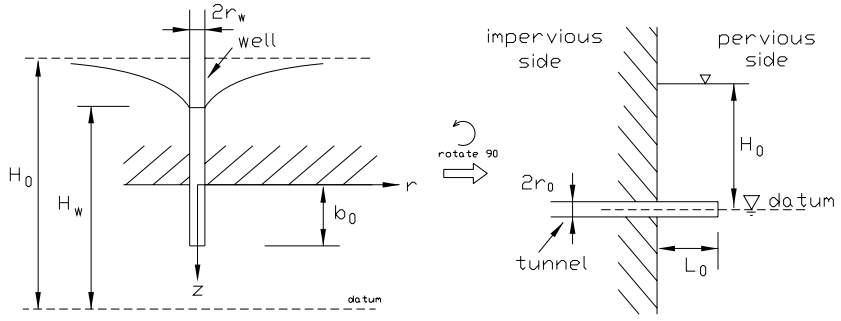

well flow tunnel face flow

Figure 2.41 Tunnel face steady state inflow

Assumptions:

A. The tunnel is horizontal with a circular cross section and is located in a fully saturated, homogeneous, isotropic, and semi-infinite porous aquifer;

B. The groundwater table is constant;

C. The total head at the tunnel perimeter is constant, which is reasonable as the radius of the tunnel is much smaller than its pressure head;

D. The fluid is incompressible;

E. The flow is in steady state and Darcy's law can be applied

Equation and boundary conditions:

First, we can consider a flow toward a point-sink in an infinite aquifer by using the continuity equation and Darcy's law (in spherical coordinate system) as follows:

$$q_r = -K \cdot \frac{dh}{dr} \cdot 4\pi r^2 \tag{2.110}$$

$$h\Big|_{r \to r_w} = H_w \tag{2.111}$$

$$h\Big|_{r \to R} = H_0, \tag{2.112}$$

where H_w and H_0 are the total head at the well and at the distance *R*.

Solution:

$$Q = \frac{4\pi K\left(H_0 - H_w\right)}{\frac{1}{r_w} - \frac{1}{R}} \tag{2.113}$$

If we use this solution to calculate the tunnel face inflow in a semi-infinite porous aquifer, then $H_w = 0$ and $R >> r_0$ (in tunnel case R= H_0), and we can obtain

$$Q = 2\pi K r_0 H_0 . \tag{2.114}$$

Comments and notes:

A. Eq.(2.114) is based on the assumption of steady-state flow; the initial water inflow may be larger;

B. Steady-state implies recharge at a boundary. If the reservoir is limited, inflow rate will reduce as the total head is reduced.

C. This solution is different from the expression given by the Underground Technology Research Council (UTRC), 1996, which is

$$Q = 4\pi K r_0 H_0 \tag{2.115}$$

2.3.2.3.3.2 Steady state flow into partially penetrated tunnel

When the tunnel is partially bored into an aquifer, we can use the solution of partially penetrated well flow in a semi-infinite confined aquifer or finite confined aquifer (Figure 2.42 and Figure 2.43).

1) Semi-infinite confined aquifer

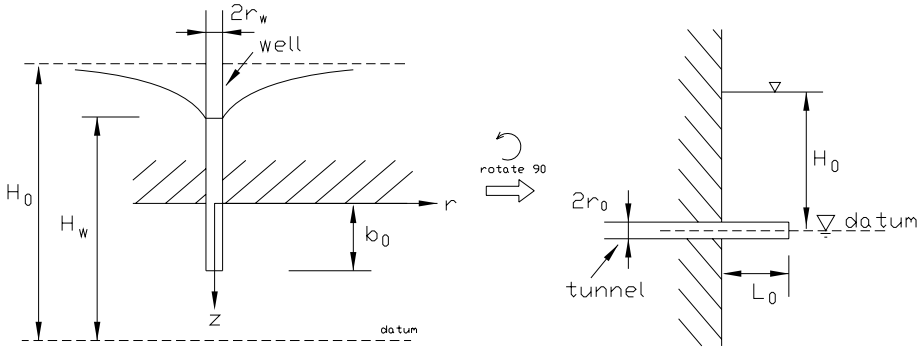

(a) well flow (b) tunnel flow

Figure 2.42 Steady state inflow into partially penetrated well/tunnel (semi-infinite confined aquifer)

Assumptions:

The assumptions are the same as those in steady state flow into tunnel face case (Section 2.3.2.3.3.1).

Solutions:

First, we can consider the partially penetrated well as an infinite number of point-sinks in a semi-infinite aquifer or as a line-sink. By using the image method and integrating along the well length (Xue, 1986, p 230), we can get the total head :

$$H_0 - h = \frac{Q}{4\pi K b_0}\left(Arsh\frac{b_0 + z}{r} + Arsh\frac{b_0 - z}{r} \right), \tag{2.116}$$

where z and r are the coordinates in the cylindrical system of Figure 2.42; h is the total head at (z, r); and $Arsh(\alpha) = \ln\left(\alpha + \sqrt{\alpha^2 + 1}\right)$.

According to numerous experiments by В. Д. Бабушкин (Xue, 1986), z can be set as $0.75b_0$ at the perimeter of the well ($r = r_w$), with the aim of making the amount of actual flow equal to the flow rate obtained with Eq.(2.116). That is because the side wall of the well is not a real equipotential line:

$$Q = \frac{4\pi K b_0 (H_0 - H_w)}{Arsh\frac{0.25b_0}{r_w} + Arsh\frac{1.75b_0}{r_w}}, \tag{2.117}$$

where H_w is the total head at the well and H_0 is the total head for the well. This is called the В. Д. Бабушкин formula.

Similarly, we can transfer Eq.(2.117) into the tunnel case as (Figure 2.42 b)

$$Q = \frac{4\pi K L_0 H_0}{Arsh\frac{0.25L_0}{r_0} + Arsh\frac{1.75L_0}{r_0}}, \tag{2.118}$$

where L_0 is the tunnel length in the stratum, and r_0 is the radius of the tunnel.

The validity of the rotating operation is mentioned in the steady-state flow into tunnel face case (Section 2.3.2.3.3.1).

Comments and notes:

A. Eq.(2.118) is based on the assumption of steady-state flow; initial water inflow may be larger;

B. Steady-state implies recharge at a boundary. If the reservoir is limited, the inflow rate will decrease as the total head decreases.

C. If we set a very small value for L_0 ($L_0 < r_0$), the result of Eq.(2.118) is approximately equal to that of Eq.(2.114). It is consistent with the physical meaning. Thus, we can just use Eq.(2.114), when $L_0 < r_0$.

D. If L is relatively large ($L_0 > 10r_0$), we can use $Arsh(\alpha) = \ln\left(\alpha + \sqrt{\alpha^2 + 1}\right)$ $\cong \ln 2\alpha$ (when $\alpha >> 1$) to simplify Eq.(2.118) as

$$Q = \frac{2\pi K L_0 H_0}{\ln \dfrac{1.32 L_0}{r_0}}. \tag{2.119}$$

E. This solution is different from the expression given by the Underground Technology Research Council (UTRC, 1996), which is

$$Q = \frac{2\pi K L_0 H_0}{Arsh \dfrac{L_0}{2r_0}}, \tag{2.120}$$

where $Arsh\left(\dfrac{L_0}{2r_0}\right) = \ln\left(\dfrac{L_0}{r_0}\right)$, for $L_0 > 10r_0$. $Arsh\left(\dfrac{L_0}{2r_0}\right) = \dfrac{L_0}{2r_0}$, for $L_0 < r_0$.

2) Finite confined aquifer

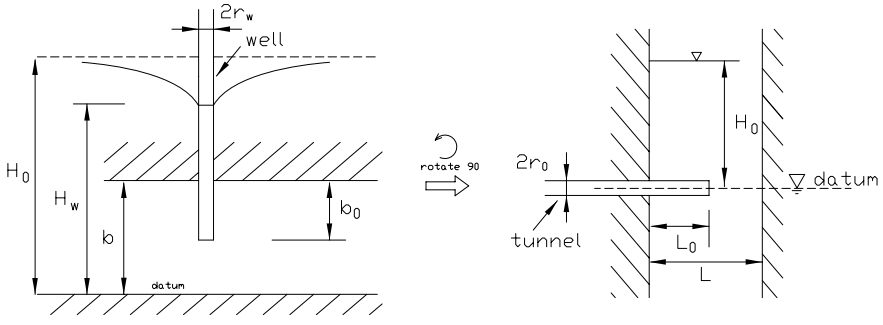

well flow tunnel flow

Figure 2.43 Steady-state inflow into partially penetrated well/tunnel (finite confined aquifer)

Based on the line-sink solution (Case 2), Muskat (1932) applied the image method to obtain the solution of steady-state inflow into a partially penetrated well in a finite confined aquifer as

$$Q = \frac{4\pi K b_0 (H_0 - H_w)}{2\ln\frac{4b}{r_w} - f(\alpha) - 2\alpha\ln\frac{4b}{R}}, \tag{2.121}$$

where $\alpha = b_0 / b$, $f(\alpha) = \ln\frac{\Gamma(0.875\alpha)\Gamma(0.125\alpha)}{\Gamma(1-0.875\alpha)\Gamma(1-0.125\alpha)}$, $\Gamma(z)$ is the Gamma function $\Gamma(z) = \int_0^\infty t^{z-1}e^{-t}dt$, R is the influence radius.

Kozeny (1933) summarized Muskat's analysis using a somewhat simpler empirical expression that is sufficiently accurate for most practical cases:

$$Q = \frac{2\pi K b_0 (H_0 - H_w)}{\ln\frac{R}{r_w}}\left[1 + 7\sqrt{\frac{r_w}{2b_0}}\cdot\cos\left(\frac{\pi b_0}{2b}\right)\right] = Q_f \cdot C, \tag{2.122}$$

where $Q_f = \frac{2\pi K b (H_0 - H_w)}{\ln\frac{R}{r_w}}$ is the flow rate of a fully penetrated well

and $C = \frac{b_0}{b}\left[1 + 7\sqrt{\frac{r_w}{2b_0}}\cdot\cos\left(\frac{\pi b_0}{2b}\right)\right]$ is the correction coefficient or the ratio between the flow rate of a partially penetrated well to that of a fully penetrated well.

Similarly, we can transfer Eqs.(2.121) and (2.122) into the tunnel case as

$$Q = \frac{4\pi K L_0 H_0}{2\ln\frac{4L}{r_0} - f(\alpha) - 2\alpha\ln\frac{4L}{R}} \tag{2.123}$$

$$Q = \frac{2\pi K L_0 H_0}{\ln\frac{R}{r_0}}\left[1 + 7\sqrt{\frac{r_0}{2L_0}}\cdot\cos\left(\frac{\pi L_0}{2L}\right)\right], \tag{2.124}$$

where L_0 is the tunnel length in the stratum; r_0 is the radius of the tunnel; and R is the influence radius (approximately, we can set $R = 2H_0$ for tunnel), $\alpha = L_0 / L$.

Comments and notes:

A. In this case, the model is the same as Perrochet's (2005b), except that the flow phase is different. Perrochet's model (Section 2.3.2.1.3) considers the transient flow that occurs when the tunnel is driven into the stratum. However, the model mentioned here considers steady-state flow when the tunnel is partially penetrated.

B. Eq.(2.123) and Eq.(2.124) are based on the assumption of steady-state flow; initial water inflow may be larger.

C. Steady-state implies recharge at a boundary. If the reservoir is limited, the inflow rate will decrease as the total head decreases.

D. If we set $\alpha = L_0 / L = 1$ in Eq.(2.123), then $f(\alpha) = 0$, and we can get the solution for the fully penetrating tunnel:

$$Q = \frac{2\pi KLH_0}{\ln \frac{R}{r_0}} = \frac{2\pi KLH_0}{\ln \frac{2H_0}{r_0}}. \tag{2.125}$$

Similarly, if we set $L_0 = L$ in Eq. (2.118), we can get the same solution for full penetration as Eq.(2.124), which is the same as the Goodman's solution Eq.(2.50), when the water table is lower than the ground surface.

2.3.2.4 Others solutions

Hwang and Lu (2007) proposed another semi-analytical approach for analyzing the problem of tunnel water inflow by using the convolution-deconvolution method; the time-variant inflow problem is transformed to a constant flow problem. Next, the groundwater problem in a finite domain is transformed to a problem in an infinite domain by the image method and the superposition principle.

For the constant flow and variable drawdown problem of sources and sinks, the governing equation can be written as

$$s(r,t) = Q \cdot F(P,r,t), \tag{2.126}$$

where *s* is the water level drawdown; Q is the rate of inflow; Q(0) is the initial inflow; F is mathematical function of drawdown; P is the parameter vector that gathers all the relevant hydro-geological parameters (including permeability, coefficient of storage, thickness of aquifer and distance to the boundary); r is distance to the location of water inflow; and t is the time after the beginning of the water inflow.

Based on the principle of convolution (Sneddon, 1976), the corresponding variable flow solution is

$$s(r,t) = Q(0) \cdot F(P,r,t) + \int_0^t F(P,r,t-\tau)\frac{\partial Q}{\partial t}\Big|_{t=\tau} d\tau, \tag{2.127}$$

where τ is a time variable in [0, t].

To perform the numerical integration to solve the problem, the time domain is discretized and the flow rate is stepwise approximated. Then, Eq.(2.126) can be written as

$$\begin{aligned} s(r,t_i) &= \sum_{j=1}^{i}(Q_j - Q_{j-1}) \cdot F(P,r,t_j - t_{j-1}) \\ &= (Q_1 - Q_0)F(P,r,t_1 - t_0) + (Q_2 - Q_1)F(P,r,t_2 - t_1) \end{aligned}, \tag{2.128}$$

where $s(r,t_i)$ is the drawdown at the time of t_i and $Q_0 = 0$ when $t_0 = 0$.

Because the tunnel water inflow is unknown and the drawdown at the tunnel heading is known ($r = r_0$, r_0 is the radius of the tunnel), we can transform Eq.(2.128) into

$$Q(t_i) = Q(t_{i-1}) + \frac{s_h - \sum_{j=1}^{i-1}[Q(t_j) - Q(t_{j-1})]F(P,r_0,t_i - t_{j-1})}{F(P,r_0,t_i - t_{i-1})}, \tag{2.129}$$

where Q is the inflow at the tunnel heading or from the tunnel sidewall and s_h is the drawdown at the tunnel heading, a constant value.

The instantaneous inflow $Q(t_1)$ at the initial moment is

$$Q(t_1) = \frac{s_h}{F(P, r_0, t_1)}. \tag{2.130}$$

In Eq.(2.129), the F function is the primary controlling factor and different hydro-geological conditions have different forms of the F function. The F functions for different boundary conditions can be derived from two basic formulae: the point sink solution for constant flow in infinite domain (simulating the inflow at the heading) and the link sink solution for constant flow in infinite domain (simulating the inflow from the tunnel sidewall). The image method and superposition principle can be used to solve the real finite domain problem according to various hydro-geological boundary conditions. One example of F function can be found in the initial paper (Hwang and Lu, 2007).

2.3.3 NUMERICAL METHODS

Analytical solutions are typically based on many assumptions, such as a homogeneous and isotropic media, a linear water table configuration, and specific flow domain. However, for many problems, the assumpations that must be made to obtain an analytical solution will not be realistic. In these cases, we must resort to approximate methods using mumerical techniques to solve the mathematical model. Numerical methods do not require some restrictive assumptions. For example, it is possible to obtain numerical solutions for the case of anisotropic and nonhomogeneous aquifer properties and for problems with complex and time-dependent boundary conditions.

In this section, the numerical methods for groundwater flow in continous Darcian media are briefly summarized, including problems types and different numerical methods. Governing equations can be found in Section 2.2.3.

2.3.3.1 Problem types

2.3.3.1.1 Boundary value problems

Mathematical models of groundwater flow based on Eqs.(2.8), (2.9) or (2.10) are classified as boundary value problems. In boundary value problems, we can specify the value of the unknown quantity or field variable (i.e., hydraulic head or pressure head) along portions of the aquifer boundaries. Derivatives of the field variable (i.e., rate of groundwater flow) also can be specified along portions of the aquifer boundaries (e.g., to represent groundwater recharge) or at special points within the aquifer called point sources or sinks. These specified values are collectively referred to as boundary conditions and when they are combined with Eqs.(2.8), (2.9) or (2.10), the result is a mathematical model that can be solved for values of the field variable at any point within the aquifer. In boundary value problems, boundary conditions and computed values of the field variable do not change with time and the minimum and maximum values of the field variable always occur on the boundaries of the aquifer or at point sources or sinks.

2.3.3.1.2 Initial value problems

Mathematical models of groundwater flow based on Eqs.(2.5), (2.6) or (2.7) are classified as initial boundary value problems. Boundary conditions, i.e., specified values of the field variable (hydraulic head or pressure head) and its derivative (rate of groundwater flow), are specified in the same way as for boundary value problems. In addition, values of the field variable must be specified at all points within the aquifer at some initial time t_0 and these specified values are collectively referred to as initial conditions. When the boundary conditions and initial conditions are combined with Eqs.(2.5), (2.6) or (2.7), the result is a mathematical model that can be solved for values of the field variable at any point in the aquifer at any time $t > t_0$. In initial value problems, boundary conditions and computed values of the field variable can change with time and

the minimum and maximum values of the field variable at time t can occur at any point within the aquifer.

2.3.3.2 Numerical methods

When using numerical methods, we seek a discrete approximation for the solution (i.e., computed values of the field variable at a set of specified points within the aquifer at a set of specified times; the number and location of the points and the number and choice of times is determined in advance by the analyst). The accuracy of the solutions obtained by numerical methods can be very good (exact in some cases) but depends on several factors including: the type of numerical method used, the complexity of the boundary and initial conditions, and the computational precision of the computer used to implement the method. In general, it is easier to obtain high-accuracy numerical solutions for steady-state groundwater flow problems than for transient groundwater flow.

Several types of numerical methods have been used to solve groundwater flow problem, the two principal ones being the finite difference method and the finite element method.

To the best of the author's knowledge, the finite difference method was first applied to problems of groundwater flow in the mid-1960s (Istok, 1989). The method has a number of advantages that contribute to its continued widespread use and popularity: (1) for simple problems (e.g., one-dimensional, steady-state groundwater flow in an isotropic and homogeneous aquifer) the mathematical formulation and computer implementation are easily understood; (2) efficient numerical algorithms have been developed for implementing the finite difference method on computers; (3) well-documented computer programs for solving problems of groundwater flow are widely available at little or no cost; and (4) the accuracy of solutions to steady-state and transient groundwater flow problems is generally quite good. However, the finite difference method also has disadvantages: the method works best for rectangular or prismatic

aquifers of uniform composition; it is difficult to incorporate irregular or curved aquifer boundaries, anisotropic and heterogeneous aquifer properties, or sloping soil and rock layers into the numerical model without introducing numerous mathematical and computer programming complexities.

The finite element method was first used to solve groundwater flow in the early 1970s (Istok, 1989). The method has several advantages compared to the finite difference method: (1) irregular or curved aquifer boundaries, anisotropic and heterogeneous aquifer properties, and sloping soil and rock layers can be easily incorporated into the numerical model; (2) the accuracy of solutions to groundwater flow is very good (exact in some cases) (Istok, 1989); and (3) the finite element method lends itself to modular computer programming wherein a wide variety of types of problems can be solved using a small set of identical computer procedures.

Because these two methods will not be used in this research, the details of the finite difference method and the finite element method are not introduced in the dissertation. Many references (Istok, 1989, Wang and Anderson, 1982, etc.) are available for the reader's interest.

2.4 Models and methods for discrete fracture network

Discrete fracture network (DFN) models are based on the premise that groundwater flow and transport in crystalline rocks occur primarily within fractures. Thus, this approach simulates individual fractures in the rock, then solves for the flow in the interconnected fracture system. This section summarizes several conceptual models for discrete fracture networks (DFN), which have been devised to represent fracture networks.

At various levels of sophistication, these models attempt to account for geometrical experimental observations. Mechanical models are not considered here; they generate fracture networks by modeling the deformation and failure of rock, and the subsequent nucleation and propagation of fractures. Most existing models derive from a few basic ones, which were reviewed by Dershowitz and Einstein (1988) and Chiles (1988).

In the earliest models (e.g., Snow, 1969), the fracture network was represented by three orthogonal families of infinite planes, with constant or random spacings (one fracture set is shown in Figure 2.44).

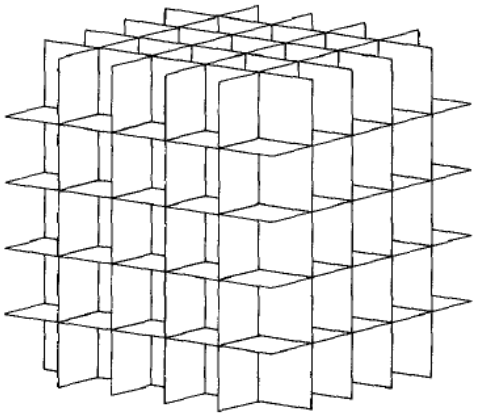

Figure 2.44 Three dimensional orthogonal model (From Dershowitz and Einstein, 1988)

In the Poisson plane (or Poisson line, in two dimensions) models, which Priest and Hudson (1976) were among the first to use, the distance of an infinite fracture plane from an arbitrary origin is a Poisson process and its orientation is also random, possibly with an anisotropic distribution (Figure 2.45). Such a model was used by Andersson et al. (1984) and Andersson and Thunvik (1986), among others. The fractures are of infinite extension, which makes the network density size-dependent.

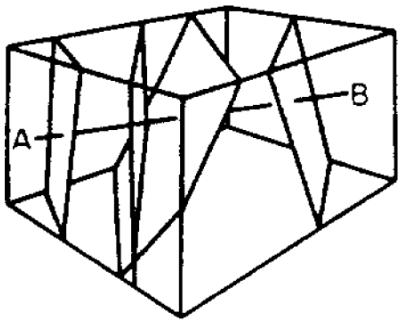

Figure 2.45 Infinite fracture plane with random spacing and orientation (From Priest and Hudson, 1976)

Networks of finite fractures can be generated by using variants of the Poisson plane model (Dershowitz and Einstein, 1988). This Dershowitz model is generated by two processes (Figure 2.46). The first process is the definition of joint planes by a Poisson plane process of uniformly distributed locations and by orientations following a specified distribution. The intersections between these planes define lines on each joint plane, which divide each plane into polygons. The second process consists of identifying the persistent portions of polygons on each plane as joints, and the remainder as intact rock. Joint edges are defined by joint plane intersections; as a result, all joint intersections occur at joint edges.

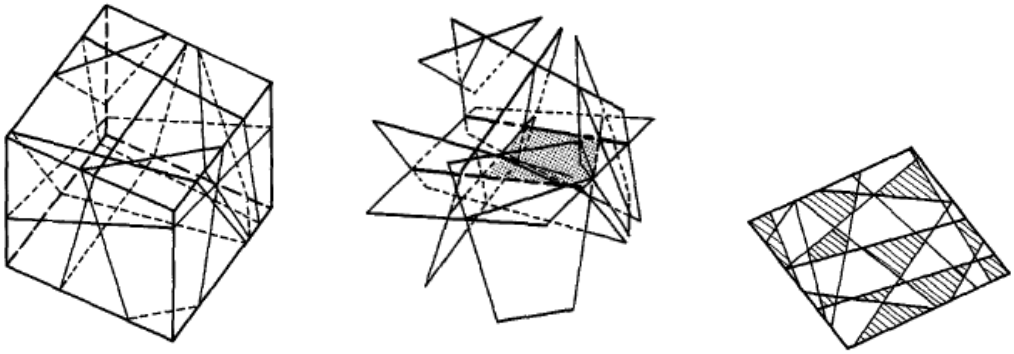

a) 3D Poisson plane process b) Poisson line process c) Marking of polygonal joints

Figure 2.46 Generation of Dershowitz joint system model (From Dershowitz and Einstein, 1988)

The so-called Boolean model, which is also made up of finite fractures, was first used to simulate fracture networks by Beacher et al. (1977) and it is currently by far the most widely used. Fractures, generally disk-shaped, characterized by their diameter and orientation, are thrown at random in space, according to a Poisson process. Since the individual fracture characteristics are input parameters of the model (which was not the case in the variants of the Poisson plane model above), their distribution can easily be fitted to match field data. Other applications of the Boolean disk model can be found in Long et al. (1985) and Andersson and Dverstorp (1987).

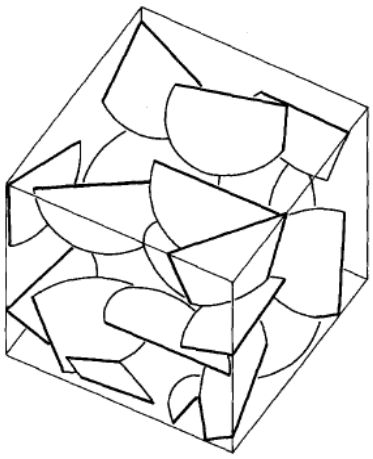

Figure 2.47 Baecher model (Boolean model) (From Dershowitz and Einstein, 1988)

Huseby et al. (1997) extended the Baecher model to regular or random polygonal fracture shapes (Figure 2.48). The two-dimensional counterpart of the disk model consists of segments in the plane, which mimic a trace map.

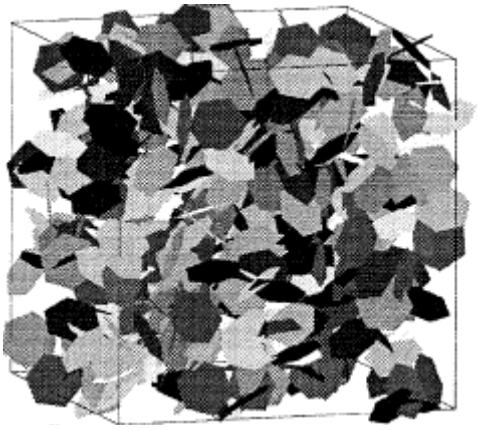

Figure 2.48 Extended Baecher model (From Huseby et al., 1997)

In the Boolean models above, the fracture sizes, orientations and locations are independent and spatially stationary random functions. It is conceptually easy to introduce correlations or spatial heterogeneity. Long and Billaux (1987) introduced fracture density variations in a two-dimensional fracture network to reproduce experimental density variograms (see Chapter 3). Billaux et al. (1989) devised a two-step generation procedure, the so-called parent-daughter process. A first set of Poisson points (seeds, or parents) is generated, possibly with a spatially heterogeneous density. Disk-shaped fractures (daughters) are then randomly distributed in swarms around each of the seed points (Figure 2.49).

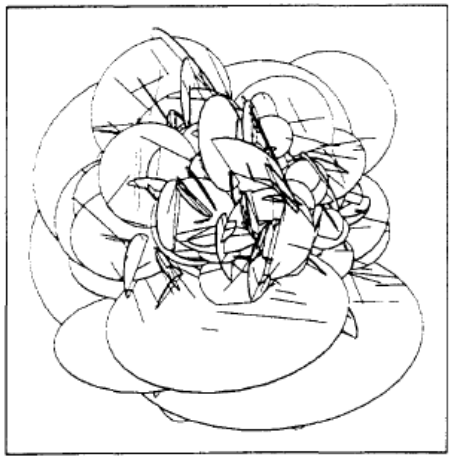

Figure 2.49 Parent-daughter model (From Billaux et al., 1989)

FracMan is a software package developed by Golder Associates, Inc., to model the geometry of discrete features. The software provides a tool for the stochastic simulation of rock fracture systems. Some other conceptual models of the geometry of the rock fracture systems are incorporated in FracMan, such as an enhanced Baecher model, the Levy-Lee clustering model, the nearest neighbor model, the war zone model,

the Poisson rectangle model, and the non-planar zone model, which are shown in Figure 2.50.

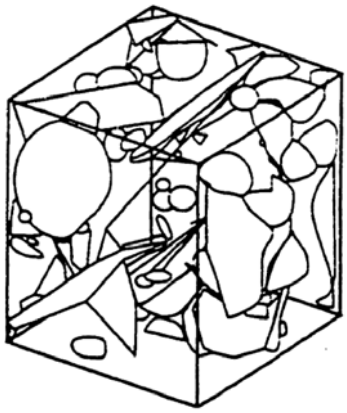

a) Enhanced Baecher Model

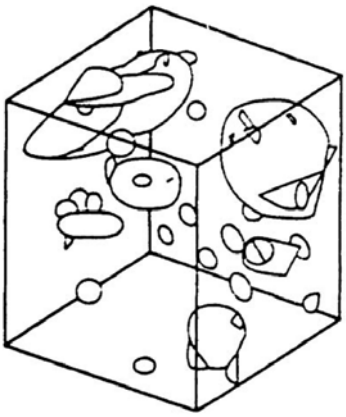

b) Nearest Neighbor Model

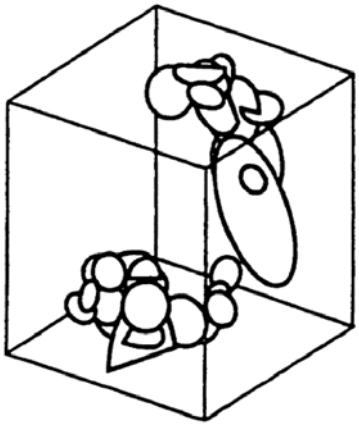

c) Levy-Lee Fractal Model

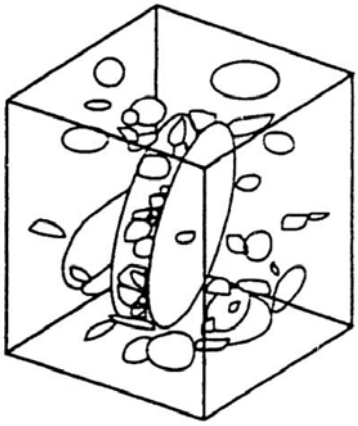

d) War Zone Model

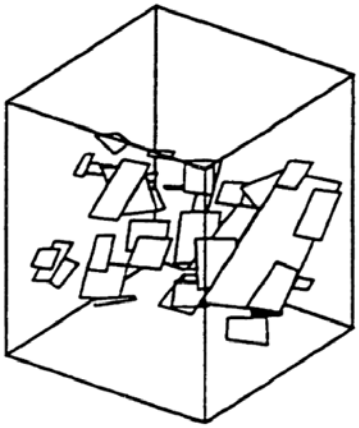

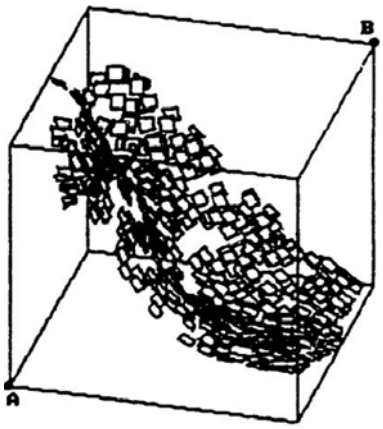

d) Poisson Rectangle Model b) Non-planar Zone Model

Figure 2.50 Some conceptual models in FracMan (From FracMan manual)

The enhanced Baecher model, an extension of the Baecher model, provides for the termination of fractures at intersections with pre-existing fractures; the Levy-Lee clustering model is a stochastic model that uses a fractal process to produce clusters of smaller fractures around widely scattered larger fractures; the nearest neighbor model, a semi-stochastic, pattern-based model, simulates the tendency of fractures to be clustered around major joints and faults by preferentially producing new fractures in the vicinity of earlier fractures; the war zone model, a semi-stochastic, pattern-based model, models the geometry of shear zones by preferentially producing fractures in the regions between subparallel and neighboring fractures; and the Poisson rectangle model is a simple version of the enhanced Baecher model and simulates fractures represented by rectangles with prescribed length and width, rather than as polygonal disks.

In this research, a new conceptional model will be used. All fractures are assumed to be disc-shaped, the same as in the Baecher model. However, geostatistics will be used to reproduce the spatical clustering of fractures. To the best of the author's knowledge, the aspects in this research attempt to advance the state-of-the-art with respect to FracMan:

1) Using disc-shape fractures allows for the use of analytical solutions in each fracture. As a consequence, the unknowns are the total heads and the flow rates at each intersection, whereas, in FracMan, all fractures need to be discreted into finite elements and the unknowns are the total heads and flow amounts at each element node, which means that much more computer memory and computing time are required;

2) Geostatistical tools (semi-variogram and indicator Gaussian sequential simulation, Chapter 3) will be used to characterize and reproduce the fracture clustering;

this is a better measure than fractal, nearest neighbor model, or war zone models in FracMan;

3) In this research, the fracture aperture-trace length relationship will be used;

4) The observed phenomenon that bigger fractures tend to occur in higher fracture intensity zones can be reproduced.

It is worth mentioning that there is an approach that may be considered intermediate between continuous method and discontinuous method: the Oda approach (Oda, 1985), which calculates Equivalent Porous Media (EPM) properties from DFN fractures. More details can be found in the original publication (Oda, 1985).

2.5 Notation

α factor of $G(\alpha)$ well function ($\frac{Tt}{Sr_w^2}$)

Φ the discharge potential [L^3T^{-1}], $\Phi = Kbh + C$ for confined flow, $\Phi = \frac{1}{2}Kh^2 + C$ for unconfined flow

γ kinematic viscosity [$L^2\ T^{-1}$]

γ_w the specific weight of water [$ML^{-2}T^{-2}$]

δ the Dirac singularity

σ' effective stress

b layer thickness [L]

b_0 the well length over which a permeable zone is penetrated partially [L]

c the compressibility of the system (rock + water) [LT^2M^{-1}]

D the vertical height of the tunnel above the base of the aquifer

e the base of the natural logarithm

E_i ( ) the exponential integral function

F_h heading inflow factor (a number between about 1 and 5) [-]

$G(\alpha)$ the well function of the solution of Jacob and Lohman (constant drawdown test)

g acceleration of gravity [LT^{-2}]

H( ) the Heaviside step function (See Appendix A)

H_0 the distance between water table and ground surface [L]

H_1, H_2 the boundary condition of 1-D flow

h total head [L]

h_a the distance between ground surface and center of the tunnel [L]

h_0 initial total head; or the distance between water table and datum [L]

h_0' the approximately uniform saturated thickness of the aquifer above the tunnel (or the water table elevation at the tunnel at time t in the early linear flow model) [L]

h_R the total head of the formation where the distance with the well is R [L]

h_t the total head of the tunnel referenced to the datum [L]

$J_0(x)$ Bessel functions of zero order of the first kinds

K hydraulic conductivity [LT^{-1}]

$\underline{K}$ the tensor of the hydraulic conductivity

K_x the horizontal hydraulic conductivity [LT^{-1}]

K_z the vertical hydraulic conductivity [LT^{-1}]

k intrinsic permeability [L^2] or [darcy, 1da=9.8697E-3 cm^2]

k_e equivalent permeability []

L tunnel length over which a permeable zone is penetrated fully [L]

L_0 tunnel length over which a permeable zone is penetrated partially [L]

p the pressure head [$ML^{-1}T^{-2}$]

p_a the atmospheric pressure [$ML^{-1}T^{-2}$]

p_t water pressure at the tunnel wall [$ML^{-1}T^{-2}$]

Q( ) the discharge/total inflow of the well/tunnel [$L^3\ T^{-1}$]

q_h the heading inflow [LT^{-1}]

q_s the steady state inflow per unit tunnel length (through tunnel wall) [LT^{-1}]

$R_{\max}$ the distance from the axis of well or tunnel to the nearest boundary

r the distance from the well [L]

r_0 the radius of the tunnel [L]

r_w the radius of the well [L]

S the storage coefficient of the aquifer

S_y specific yield (drainage porosity)

s_0 specified drawdown at the tunnel [L]

s_h the drawdown at the tunnel heading [L]

s_w the drawdown of the water table in the well case [L]

s_t the drawdown of the water table in the tunnel case[L]

s(r, t) the drawdown function [L]

T the transmissibility of the aquifer [$L^2\ T^{-1}$] (typically, T=Kb)

t time [T]

V(t) the cumulative volume of extracted water [L^3]

v the average drilling speed or the flow velocity [LT^{-1}]

$W(\ )$ the well function, $W(x)=\int_x^\infty \frac{e^{-s}}{s}ds$, (s is integral variable)

$Y_0(x)$ Bessel functions of zero order of second kinds

z_t the vertical height of the tunnel above the base of the aquifer [L]

CHAPTER 3: FRACTURE SIMULATION

Simulating flow and transport in fractured media is an important topic in many fields (water resource, petroleum, civil, hazardous waste disposal, etc.). In general, there are two ways to model the fractured rock masses: continuum model and discrete model. Sometimes, fracture systems behave more like continuous porous media. However, in many cases and at a certain scale, fractured media cannot be considered a continuum. Clustering is a significant property of rock fractures, which is implied by Raymer (2005): "[In hard rock tunnels], *most of the inflow occurs in a few places, some of the inflow occurs in many places, and much of the tunnel is dry.*" Therefore, in the fractured media modeling, the fracture spatial arrangement will be very important because it directly affects the permeability of the fractured media.

To the best of my knowledge, the stochastic modelling of fracture networks originated in percolation studies (Robinson, 1983) and its wider application to rock engineering was promoted in the 1980s by the work of several research groups (e.g., Long et al., 1982; Baecher, 1983; Andersson et al., 1984; Dershowitz and Einstein, 1988; Xu and Dowd, 2010). The general approach is to treat locations, size, orientation and other properties of the fractures as random variables with inferred probability distributions. To reduce the complexity of the problem, simple geometry is assumed for fractures with the most common geometries being straight lines for two-dimensional fractures and ellipses or circular disc for three-dimensional fractures, although infinite two-dimensional planes are also used (Dershowitz and Einstein, 1988).

The first step of the modelling process is to collect discontinuity data for statistical analysis. The most common measurement technique is by scanlines, or window survey, of rock outcrops or excavated rock surfaces. If drill cores are available, scanlines and/or window surveys can also be applied to core samples. Additional data can be

obtained along the borehole using either a down-the-borehole camera or wireline geophysical, logging. Data thus collected, however, are essentially one- or two-dimensional and are, therefore, biased samples of the complete, but inaccessible, three-dimensional fracture networks that are being sampled. The biases, due to sample truncation, censoring and edge effects (Section 1.3.6), require correction before the two-dimensional data can be used for three-dimensional modelling (e.g., Einstein and Baecher, 1983; Villaescusa and Brown, 1992; La Pointe, 2002; Fouche and Diebolt, 2004).

The second step in fracture modelling consists of dividing the fractures into sub-sets according to fracture orientations. This is based on the belief that fractures formed by the same geological activity will have similar properties, including similar preferential orientations. Classification of sub-sets is aided by fracture orientation rose diagrams in two-dimensional applications and hemispherical projections in three-dimensional applications. Each set is modelled separately and the final simulation is the combination of all independently simulated sub-sets. If sets are correlated, the correlations can be modelled either by a hierarchical model (Lee et al., 1990) or by a plurigaussian simulation (Dowd et al., 2007).

Thirdly, spatial arrangement is the first distribution parameter to be simulated in fracture networks. There is some research in the fracture spatial arrangement that is different from the research in fracture spacing. Spatial analysis can be implemented in terms of location, orientation, intensity, trace length, aperture, or other strength or hydraulic properties. La Pointe (La Pointe, 1993) summarized two major methods to analyze fracture patterns: stochastic-geometric methods and stochastic-mechanistic methods, in which geostatistical methods and fractals are widely used, as described in Chapter 1 Section 1.4.1. Multiple-point statistics and a combination of geostatistics for fracture density and object-based modelling for fracture geometry have been recently used to simulate fractures (Dowd et al., 2007). Dowd et al. (2007) summarize these

methods and propose a new approach based on pluri-Gaussian structural simulation. This approach incorporates into the simulation the spatial correlation between different sets of fractures. However, this method simulates fractures using digital pixels, which is not of much use in large-scale three-dimensional fracture simulation. In geostatistical modelling (Young, 1987; Chiles, 1988; Billaux et al., 1989; Viruete et al., 2003), the variable modelled is usually the fracture density, N(X), or the number of fracture representation points within a unit area (for two dimensions) or a unit volume (for three dimensions). For a given dataset, the variable is derived from a specified grid system in which N(X) for each cell can be calculated and the spatial correlations of N(X) can be modelled. In simulations, for each grid cell, N(X) is simulated on the basis of the geostatistical model and then the N(X) points are distributed within the cell according to a Poisson rule.

The fourth and final step is the simulation of the geometry of individual fractures. Fracture size (diameter or aperture) and orientation are generally modelled by Monte Carlo sampling from the corresponding probability distribution functions (PDF). Additional fracture properties (e.g., roughness, permeability) can be included in the model if required.

In the third step, software FracMan performs fracture arrangement simulation by using geostatistical methods; fractal methods (La Pointe, 1993); the parent-daughter model (Long and Billaux, 1987); and Levy-Lee clustering, nearest neighbor or war zone model (Sectioin 2.4). The fractal model may not be extensively used because self-similarity is only valid over a limited range of scales (Korvin, 1989) and because it is difficult to condition with respect to the measured data. The Levy-Lee clustering model inherently still belongs to fractal models (Ivanova, 1995). The parent-daughter model and nearest neighbor model are actually geostatistical models; however, simulations documented in most previous research are based on the assumption of Gaussian distribution for the simulated variables, which is typically not true for rock fracture intensity because rock fractures are typically clustered (Marrett et al., 2005, Manuscript).

Therefore, in this section a new method is developed to reproduce the clustering property of fractures by using a geostatistical tool called Sequential Indicator Simulation (SIS). SIS is used to reproduce the local intensity of fractures along the scanline, then one fracture size (diameter or aperture) is sampled from its distribution, and then the diameter-aperture relationship is used to simulate the other fracture size (aperture or diameter). After spatially distributing all fractures with their properties (size and orientation), the whole fracture set is simulated in the domain. The sequential indicator simulation is validated to be an effective method for fracture spatial simulation. In this section, each fracture is assumed to have a circular disc shape with a constant aperture; the aperture of one fracture may be different from the aperture of another fracture. The center of each fracture along the scanline (normal to the fracture plane) is on the scanline.

In this chapter, theoretical background of geostaticscal techniques used in this research will be introduced in Section 3.1. Then all steps of fracture simulation implemented in this research will be given in Section 3.2. In Section 3.3, two fracture simulation cases will be studied.

3.1 Theoretical background

In this section, all theoretical background is introduced, including variogram, kriging, sequential simulation, sequential indicator simulation, intensity-aperture relationship and length-aperture relationship.

3.1.1 GEOSTATISTICS

3.1.1.1 Definitions

The definitions that follow may be found in Chiles and Delfiner (1999) and Journel and Huijbregts (1978).

3.1.1.1.1 Random function (RF)

Given a domain, $D \subset \mathbf{R}^n$, with a positive volume, and a probability space, (Ω, A, P), a random function, (RF), is a function of two variables, $Z(\mathbf{x}, \omega)$, such that for each $\mathbf{x} \in D$ the section $Z(\mathbf{x}, \cdot)$ is a random variable on (Ω, A, P). Each of the function $Z(\cdot, \omega)$ defined on D as the section of the RF at $\omega \in \Omega$ is a realization of RF. For clarity, the RF is simply denoted by $Z(\mathbf{x})$, and a realization by the lowercase $z(\mathbf{x})$.

For the k-dimensional space, random function is the joint variability of k Random Variables $Z(\mathbf{u}_1), Z(\mathbf{u}_2), ..., Z(\mathbf{u}_k)$. Since each RV is characterized by a distribution $F_Z(z)$, the RF is characterized by a multivariate joint distribution: $F_{Z_1, Z_1, .., Z_K}(z_1, z_2, .., z_K)$ for all finite values of k.

3.1.1.1.2 Stationarity

Stationarity: Pattern of spatial variability remains invariant with location and is characterized only by the lag **h** defining the pattern. Stationarity is statistical homogeneity.

Strict Stationarity. RF such that its entire spatial law remains invariant under an arbitrary translation of the points by a vector **h**:

$$\Pr\{Z(\mathbf{x_1}) < z_1, ..., Z(\mathbf{x_k}) < z_k\} = \Pr\{Z(\mathbf{x_1} + \mathbf{h}) < z_1, ..., Z(\mathbf{x_k} + \mathbf{h}) < z_k\} \qquad (3.1)$$

Physically this means that the phenomenon is homogeneous in space and so repeats itself in the whole space.

Second-order Stationarity: A slightly reduced requirement is that only the first two moments remain invariant under translation:

$$\begin{aligned} &E\{Z(\mathbf{u})\} = m \quad \forall\ \mathbf{u} \\ &E\{[Z(\mathbf{u}) - m] \cdot [Z(\mathbf{u} + \mathbf{h}) - m]\} = C(\mathbf{h}) \quad \forall\ \mathbf{u} \end{aligned}, \qquad (3.2)$$

where $E\{\cdot\}$ is the expectation. A second-order stationary random function (SRF) is isotropic if its covariance only depends on the length $|h|$ of the vector **h** and not on its orientation.

3.1.1.1.3 Intrinsic Random Function

If a milder hypothesis is to assume that for every vector, **h,** the increment, $Y_h(\mathbf{x}) = Z(\mathbf{x}+\mathbf{h}) - Z(\mathbf{x})$, is a second-order stationary random function (SRF) in **x**, then $Z(\mathbf{x})$ is called an intrinsic random function (IRF).

3.1.1.2 Covariance of a Stationary Random Function

A stationary random function (SRF) $Z(\mathbf{x})$ is characterized by its mean $m = E\{Z(\mathbf{x})\}$ and its covariance $C(\mathbf{h}) = E\{[Z(\mathbf{x})-m][Z(\mathbf{x}+\mathbf{h})-m]\}$. The covariance shows how the correlation between $Z(\mathbf{x})$ and $Z(\mathbf{x}+\mathbf{h})$ evolves with the separation, or lag, **h**. $C(\mathbf{h})$ depends on the length of **h**, which is the distance between **x** and **x+h**, and on its direction. It is said to be isotropic when the covariance depends only on distance. A covariance is an even function and is bounded by its value at the origin: $C(\mathbf{h}) = C(-\mathbf{h}), |C(\mathbf{h})| \le C(\mathbf{0})$. Here $C(\mathbf{0})$ actually is the variance of SRF.

3.1.1.3 Variogram (Semivariogram) of an Intrinsic Random Function

An intrinsic random function (IRF) is a random function whose increments are second-order stationary. It is characterized by its linear drift

$$m(\mathbf{h}) = E\{Z(\mathbf{x}+\mathbf{h}) - Z(\mathbf{x})\} = \langle \mathbf{a}, \mathbf{h} \rangle \tag{3.3}$$

and its semi-variogram

$$\gamma(\mathbf{h}) = \frac{1}{2} Var\{Z(\mathbf{x}+\mathbf{h}) - Z(\mathbf{x})\}, \quad (3.4)$$

where $m(\mathbf{h})$ is a linear function of the vector $\mathbf{h} = (h_1, ..., h_n)$, namely $m(\mathbf{h}) = \langle \mathbf{a}, \mathbf{h} \rangle = a_1 h_1 + ... + a_n h_n$ for some gradient vector $\mathbf{a} = (a_1, ..., a_n)$. Unless explicitly stated otherwise, we will assume that the IRF has no drift, or $m(\mathbf{h}) \equiv 0$.

The semi-variogram shows how the dissimilarity between $Z(\mathbf{x})$ and $Z(\mathbf{x}+\mathbf{h})$ evolves with separation **h**. The semi-variogram is in general anisotropic. It is an even, nonnegative function valued 0 at $\mathbf{h} = \mathbf{0}$. $-\gamma(\mathbf{h})$ must be a conditionally positive definite function (Guichardet, 1972). The semi-variogram $\gamma(\mathbf{h})$ is sometimes called "theoretical" because it is a construct involving neither a particular realization nor a particular region.

An SRF is obviously also an IRF and therefore has a semi-variogram. In that case, the semi-variogram is linked to the covariance by the relation:

$$\gamma(\mathbf{h}) = C(\mathbf{0}) - C(\mathbf{h}). \quad (3.5)$$

Thus the semi-variogram of an SRF is bounded by $C(\mathbf{0})$. If the covariance is known, the variogram is also known. In practice, the semi-variogram is typically normalized by the variance $C(\mathbf{0})$ (i.e., the normalized semi-variogram is typically bounded by 0 and 1) if the maximum of $C(\mathbf{h})$ is the variance.

3.1.1.3.1 Terms

1. Sill and range

The rate of the semi-variogram increase reflects the degree of dissimilarity of ever more distant samples. The semi-variogram can increase indefinitely if the variability of the phenomenon has no limit at large distances. If, conversely, the semi-variogram

reaches a limiting value, called the sill, it means that there is a distance beyond which Z(x) and Z(x+h) are uncorrelated. This distance is called the range (see Figure 3.1). Such behavior characterizes what is called a transition phenomenon because it is often observed in the case of phemomeana where discontinuities delimit compartments at the boundaries of which the variability is high. The range then has the same order of magnitude as the compartments. More generally, the range gives an exact sense of the conventional concept of area of influence for a sample.

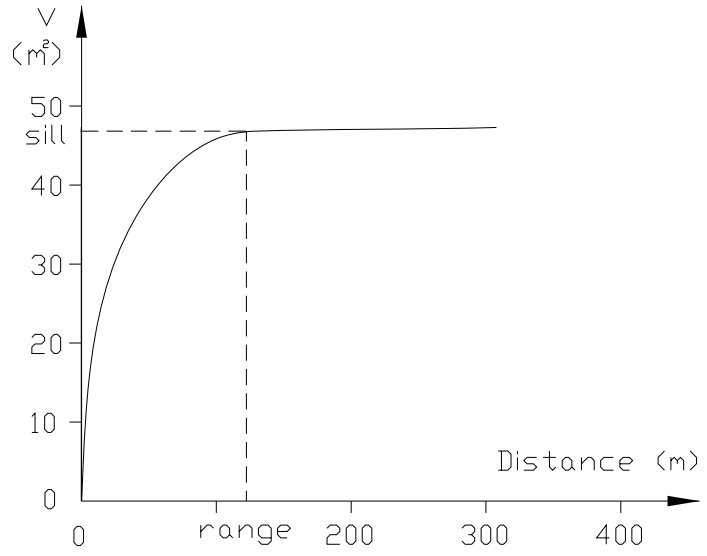

Figure 3.1 Sill and range on the variogram

2. Nugget effect

If a semi-variogram does not tend toward zero when h → 0, the regionalized variable is generally not continous and is thus very irregular. The origin of this denomination is as follows: gold commonly occurs as nuggets of pure metal that are much smaller than the size of a sample. By extension, the term "nugget effect" (in the wide sense) is applied to all discontinuities at the origin, even if their cause is different (see Figure 3.2). In general, the nugget effect is due to:

- A microstructure or "geological noise," namely a component of the phenomenon with a range shorter than the sampling support (true nugget effect);

- A structure with a range shorter than the smallest interpoint distance; and/or
- Measurement or positioning errors.

In the absence of close sampling points, it is impossible to tell from the variogram itself which cause is applicable; moreover, they can be mixed. Knowledge about the physics of the problem is essential for modeling the variogram.

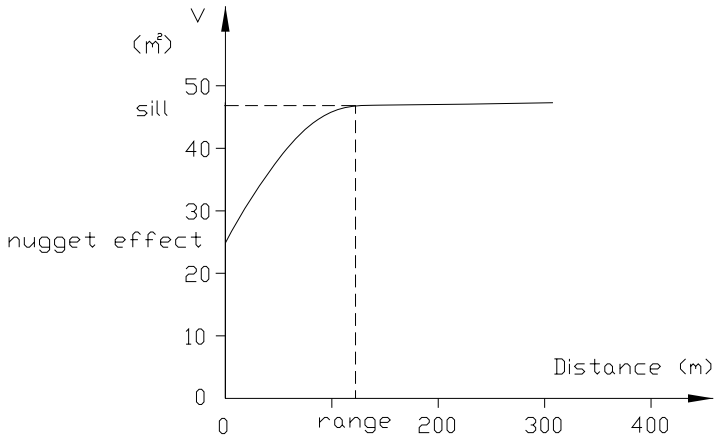

Figure 3.2 Nugget effect on the variogram

3.1.1.3.2 Isotropic models

Since data available to model a semi-variogram is sparse, semi-variogram inference is possible only for few lags h. However, during estimation, semi-variogram is needed for arbitrary lag h. Therefore, we need to model a continuous semi-variogram function that yields a semi-variogram value for all lags. Some common normalized models are given below.

1. Pure nugget effect model

$$\gamma(\mathbf{h}) = \begin{cases} 0 \text{ if } \mathbf{h} = 0 \\ 1 \text{ otherwise} \end{cases} \tag{3.6}$$

2. Spherical family models and derived models

Family of spherical models in $\mathbf{R}^n$ expressed as a function of $r = |\mathbf{h}|$;

$$\gamma_n(r) = \begin{cases} 1 - a^n v_{n-1} \int_{r/a}^{1} \left(1-u^2\right)^{\frac{n-1}{2}} du & \text{if } r \le a \\ 1 & \text{if } r \ge a \end{cases} , \tag{3.7}$$

where a is the range and v_n is the volume of a unit diameter ball in $\mathbf{R}^n$:

$$v_n = \frac{\pi^{n/2}}{2^{n-1} n \Gamma\left(n/2\right)} , \tag{3.8}$$

where $\Gamma(\cdot)$ is the Gamma function defined in Eq.(1.19).

- If n=1, triangle model, valid in $\mathbf{R}^1$:

$$\gamma_1(r) = \begin{cases} \frac{r}{a} & \text{if } r \le a \\ 1 & \text{if } r \ge a \end{cases} \tag{3.9}$$

- If n=2, circular model in $\mathbf{R}^2$:

$$\gamma_2(r) = \begin{cases} 1 - \frac{2}{\pi}\left[\arccos\left(\frac{r}{a}\right) - \frac{r}{a}\sqrt{1-\frac{r^2}{a^2}} \right] & \text{if } r \le a \\ 1 & \text{if } r \ge a \end{cases} \tag{3.10}$$

- If n=3, spherical model in $\mathbf{R}^3$:

$$\gamma_3(r) = \begin{cases} \frac{3}{2}\frac{r}{a} - \frac{1}{2}\frac{r^3}{a^3} & \text{if } r \le a \\ 1 & \text{if } r \ge a \end{cases} \tag{3.11}$$

When we speak of a spherical model without specifying n, we are of course referring to the model $\gamma_3(r)$. Because of its validity in $\mathbf{R}^n$ for n=1,2, or 3, its well-marked range, and its ease of calculation, it is very widely used.

Two derived models:

- Cubic model (corresponds to the Radon transform (Deans, 1983) of order 2 of the spherical covariogram of $\mathbf{R}^5$):

$$\gamma_c(r) = \begin{cases} 7\frac{r^2}{a^2} - \frac{35}{4}\frac{r^3}{a^3} + \frac{7}{2}\frac{r^5}{a^5} - \frac{3}{4}\frac{r^7}{a^7} & \text{if } r \le a \\ 1 & \text{if } r \ge a \end{cases} \tag{3.12}$$

- Pentamodel (corresponds to the Radon transform of order 4 of the spherical covariogram of $\mathbf{R}^7$):

$$\gamma_p(r) = \begin{cases} \frac{22}{3}\frac{r^2}{a^2} - 33\frac{r^4}{a^4} + \frac{77}{2}\frac{r^5}{a^5} - \frac{33}{2}\frac{r^7}{a^7} + \frac{11}{2}\frac{r^9}{a^9} - \frac{5}{6}\frac{r^{11}}{a^{11}} & \text{if } r \le a \\ 1 & \text{if } r \ge a \end{cases} \tag{3.13}$$

3. Exponential model

$$\gamma(\mathbf{h}) = 1 - e^{-\frac{3|\mathbf{h}|}{a}} \tag{3.14}$$

Practical range is a (i.e., the distance at which the variogram reaches 95 percent of sill).

4. Linear model

$$\gamma(|\mathbf{h}|) = h, \quad h \ge 0 \tag{3.15}$$

5. Linear-with-sill model

$$\gamma(|\mathbf{h}|) = \begin{cases} h, & 0 \le h \le a \\ 1, & h > a \end{cases} \tag{3.16}$$

6. Gaussian model

$$\gamma(\mathbf{h}) = 1 - e^{-3\cdot\left(\frac{|\mathbf{h}|}{a}\right)^2} \tag{3.17}$$

Practical range is *a* (i.e., the distance at which variogram reaches 95 percent of sill).

7. Bessel model

$$\gamma(\mathbf{h}) = 1 - \frac{h}{a} K_1\left(\frac{h}{a}\right), \ h \ge 0 \quad , \tag{3.18}$$

where $K_1[.]$ is the modified Bessel function of the first order and the second kind (Arfken and Weber, 2001).

8. Logarithmic model

$$\gamma(\mathbf{h}) = \begin{cases} \log(h+a), & h > 0 \\ 0, & h = 0 \end{cases} \tag{3.19}$$

9. Power-law models

$$\gamma(\mathbf{h}) = |\mathbf{h}|^{\omega}, \quad 0 < \omega < 2, \quad h \geq 0 \tag{3.20}$$

Power-law variogram represents self-similar phenomena (i.e., phenomena for which a characteristic scale cannot be defined), which is fractal property.

10. Hole effect model (Periodic model)

A positive definite model in three dimensions is given as:

$$\gamma(\mathbf{h}) = 1 - \frac{a}{\mathbf{h}} \cdot Sin\left(\frac{h}{a}\right) \quad , \tag{3.21}$$

where h is the length of $\mathbf{h}$.

3.1.1.3.3 Anisotropic models

1. Geometric anisotropy

In this case, the range is different in different directions, and the sill is the same in all directions (see Figure 3.3).

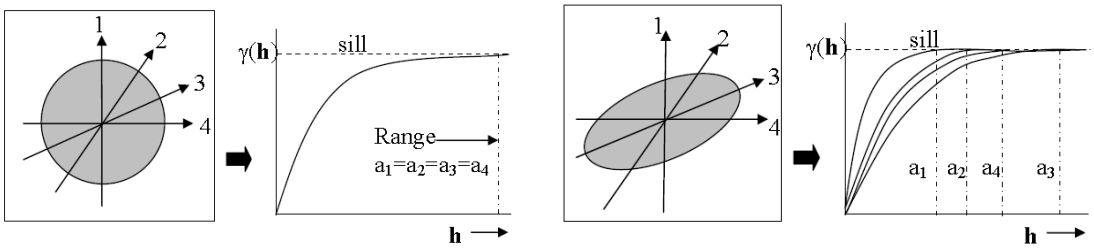

Figure 3.3 (a) Isotropic variogram (b) Anisotropic variogram

Anisotropic models in three dimensions can be modeled by transforming any vector $\mathbf{h}$ in the original cartesian space to an equivalent vector $\mathbf{h}'$ relative to the direction of anisotropy. If the phenomenon we are interested in has maximum continuity (longest range) along azimuth angle θ and dip angle φ, the original cartesian xyz coordinates can be rotated so that x becomes parallel to the direction of the major range, y is parallel to the direction of the middle range, and z is parallel to the direction of the minor range. See Appendix E for details of coordinates' rotation. If the rotation matrix is $\mathbf{R}_{\theta,\varphi}$, after two step rotation, the equivalent vector $\mathbf{h}'$ relative to the direction of anisotropy becomes $\mathbf{R}_{\theta,\varphi} \cdot \mathbf{h}$. In order to transform $\mathbf{h}'$ to an isotropic set of axes, define:

$$\lambda_1 = \frac{a_{\text{minor}}}{a_{\text{major}}} \quad \text{and} \quad \lambda_2 = \frac{a_{\text{minor}}}{a_{\text{vertical}}} \tag{3.22}$$

So the resultant vector is

$$\mathbf{h}'' = \begin{bmatrix} \lambda_1 & 0 & 0 \\ 0 & 1 & 0 \\ 0 & 0 & \lambda_2 \end{bmatrix} \mathbf{R}_{\theta,\varphi} \cdot \mathbf{h} = \mathbf{D}_{\lambda} \cdot \mathbf{R}_{\theta,\varphi} \cdot \mathbf{h} \quad , \tag{3.23}$$

which is isotropic with range a_{minor}.

2. Zonal anisotropy

Phenomena that exhibit different sills in different directions are said to exhibit zonal anisotropy (see Figure 3.4).

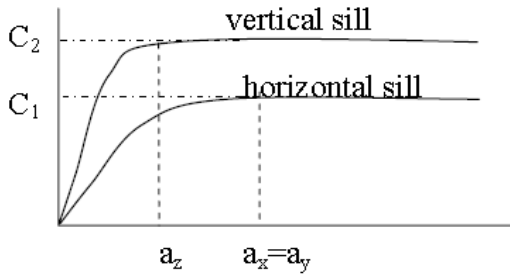

Figure 3.4 Zonal anisotropy

If a particular variogram structure has infinite range in a particular direction, then that structure does not contribute any value to the sill.

3. Nested structure

Modeling can proceed with nested structures (i.e., a nested sum of K+1 isotropic basic models).

$$\gamma(\mathbf{h}) = C_0 + \sum_{k=1}^{K} C_k \cdot \gamma_k \left(\left| \mathbf{h}_k " \right| \right) \quad , \tag{3.24}$$

where C_k is the contribution of the k[th] structure to the total sill and C_o is the nugget effect. Generally, $\sum_{k=0}^{K} C_k = C(\mathbf{0})$ (i.e., the covariance for $\mathbf{h} = \mathbf{0}$) (Section 3.1.2). Anisotropy of each structure may be different, $\mathbf{h}_k " = \mathbf{A}_k(\theta_k, \varphi_k, \lambda_k) \cdot \mathbf{h}$, where $\mathbf{A}_k(\theta_k, \varphi_k, \lambda_k) = \mathbf{D}_{\lambda}^{k} \cdot \mathbf{R}_{\theta,\varphi}^{k} \cdot \mathbf{h}$, as shown in Eq.(3.23).

In three dimensions, if $\lambda^k{}_1 = \lambda^k{}_2 = 1$, the model is isotropic; if $\lambda^k{}_1 \cdot \lambda^k{}_2 \neq 0$, the model is geometrically anisotropic; and if $\lambda^k{}_1 \cdot \lambda^k{}_2 = 0$, the model is zonal anisotropic (e.g., the structure appears to be missing in a particular direction).

3.1.1.4 Estimation and Kriging

A central problem in geostatistics is the reconstruction of a phenomenon over a domain based on values observed at a limited number of points. Mathematically this can be regarded as an interpolation, or approximation problem. In the classic approach, the unknown function is approximated by a parametric function whose form is postulated in advance, either explicitly or implicitly. The parameters are selected so as to optimize some criterion of best fit at the data points, which can be statistical or deterministic. Once

the approximating function is determined, it is a simple matter to evaluate it wherever needed.

Kriging is a method named by G. Matheron in 1963 in honor of D. G. Krige. The main difference is that kriging starts from a statistical model of nature rather than a model of the interpolating function. Kriging (generalized regression) provides a minimum error variance unbiased estimate for the random function $Z(\mathbf{u})$. All kriging estimators are but variants of the basic linear regression n estimator Z*(u) defined as:

$$Z^*(\mathbf{u}) - m(\mathbf{u}) = \sum_{\alpha=1}^{n} \lambda_\alpha(\mathbf{u})\left[Z(\mathbf{u}_\alpha) - m(\mathbf{u}_\alpha)\right] \quad , \tag{3.25}$$

where

$\mathbf{u}, \mathbf{u}_\alpha$: location vectors for estimation points and one of the neighboring data points, indexed by α;

n: the number of data points in local neighborhood used for estimation of $Z^*(\mathbf{u})$;

$m(\mathbf{u}), m(\mathbf{u}_\alpha)$: expected values (means) of $Z(\mathbf{u})$ and $Z(\mathbf{u}_\alpha)$; and

λ_α: kriging weight assigned to datum $Z(\mathbf{u}_\alpha)$ for estimation location **u**; same datum will receive different weight for different estimation location.

$Z(\mathbf{u})$ is treated as a random field with a trend component, $m(\mathbf{u})$, and a residual component, R(**u**)= Z(**u**)- m(**u**). Kriging estimates residual at **u** as the weighted sum of residuals at surrounding data points. Kriging weights, λ_α, are derived from covariance function or semivariogram, which should characterize residual component.

The goal is to determine weights, λ_α, that minimize the variance of the estimator

$$\sigma_E^2(\mathbf{u}) = Var\left\{Z^*(\mathbf{u}) - Z(\mathbf{u})\right\} \tag{3.26}$$

under the unbiasedness constraint $E\left\{Z^*(\mathbf{u}) - Z(\mathbf{u})\right\} = 0$.

The random field (RF) Z(**u**) is decomposed into residual and trend components, Z(**u**) = R(**u**) + m(**u**), with the residual component treated as an RF with a stationary mean of 0 and a stationary covariance (a function of lag, **h**, but not of position, **u**):

$$E\left\{R(\mathbf{u})\right\} = 0 \tag{3.27}$$

$$Cov\left\{R(\mathbf{u}), R(\mathbf{u}+\mathbf{h})\right\} = E\left\{R(\mathbf{u}) \cdot R(\mathbf{u}+\mathbf{h})\right\} = C_R(\mathbf{h}) \tag{3.28}$$

The residual covariance function is generally derived from the input semivariogram model, $C_R(\mathbf{h}) = C_R(\mathbf{0}) - \gamma(\mathbf{h}) = Sill - \gamma(\mathbf{h})$. Thus the semivariogram we feed to a kriging program should represent the residual component of the variable.

Figure 3.5 summarizes the three main forms of kriging and their underlying models.

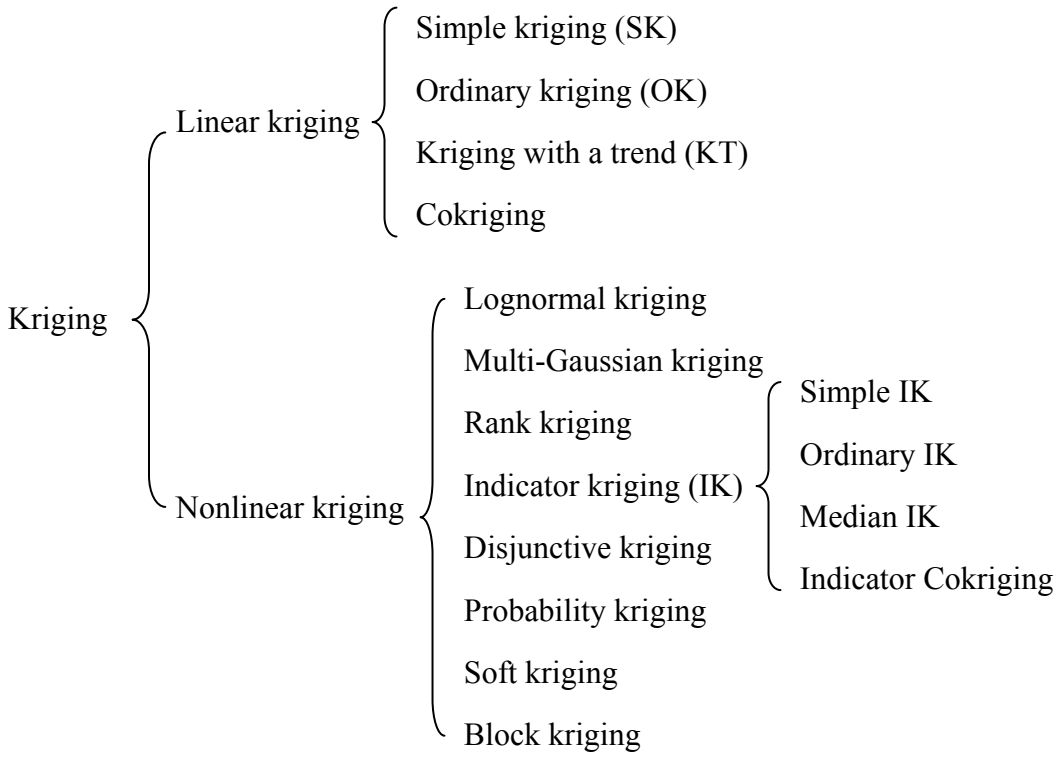

Figure 3.5 Main forms of Kriging

In the remaining part of Section 3.1.1.4, simple kring, ordinary kriging and indicator kriging are briefly introduced. Indicator kriging will be used in the sequential indicator simulation in Section 3.1.1.5.5. More details on different krigings can be found in many references, such as Journel and Huijbregts (1978) and Chiles and Delfiner (1999).

Most krigings (except for indicator kriging) start with a prior distribution over functions. This prior takes the form of a Gaussian process: N samples from a function will be normally distributed, where the covariance between any two samples is the covariance function of the Gaussian process evaluated at the spatial location of two points. A set of values is then observed, each value associated with a spatial location. Now, a new value can be predicted at any new spatial location, by combining the Gaussian prior with a Gaussian likelihood function for each of the observed values. The resulting posterior distribution is also Gaussian, with a mean and covariance that can be simply computed from the observed values and their variance (Williams, 1998).

3.1.1.4.1 Simple Kriging

The practical assumptions for the application of simple kriging are:

1) Intrinsic stationarity of the field;

2) The mean E[Z(x)] = m is constant and known;

3) The variable is normally distributed, and its covariance function C(**h**) is known.

For simple kriging, we assume that the trend component is a constant and known mean, m(**u**) = m, so that

$$Z_{SK}^{*}\left(\mathbf{u}\right)=m+\sum_{\alpha=1}^{n}\lambda_{\alpha}\left(\mathbf{u}\right)\left[Z\left(\mathbf{u}_{\alpha}\right)-m\right] \tag{3.29}$$

This estimate is automatically unbiased, since $E\left\{Z\left(\mathbf{u}_{\alpha}\right)-m\right\}=0$, so that $E\left\{Z_{SK}^{*}\left(\mathbf{u}\right)\right\}=m=E\left\{Z\left(\mathbf{u}_{\alpha}\right)\right\}$. The estimation error $Z_{SK}^{*}\left(\mathbf{u}\right)-Z\left(\mathbf{u}\right)$ is a linear

combination of random variables representing residuals at the data points, $\mathbf{u}_\alpha$, and the estimation point, $\mathbf{u}$:

$$Z^*_{SK}(\mathbf{u}) - Z(\mathbf{u}) = \left[Z^*_{SK}(\mathbf{u}) - m\right] - \left[Z(\mathbf{u}) - m\right]$$

$$= \sum_{\alpha=1}^{n} \lambda_\alpha(\mathbf{u}) R(\mathbf{u}_\alpha) - R(\mathbf{u}) = R^*_{SK}(\mathbf{u}) - R(\mathbf{u}) \tag{3.30}$$

Using rules for the variance of a linear combination of random variables, the error variance is then given by:

$$\sigma^2_E(\mathbf{u}) = Var\left\{R^*_{SK}(\mathbf{u})\right\} + Var\left\{R_{SK}(\mathbf{u})\right\} - 2Cov\left\{R^*_{SK}(\mathbf{u}), R_{SK}(\mathbf{u})\right\}$$

$$= \sum_{\alpha=1}^{n}\sum_{\beta=1}^{n} \lambda_\alpha(\mathbf{u})\lambda_\beta(\mathbf{u}) C_R(\mathbf{u}_\alpha - \mathbf{u}_\beta) + C_R(\mathbf{0}) - 2\sum_{\alpha=1}^{n} \lambda_\alpha(\mathbf{u}) C_R(\mathbf{u}_\alpha - \mathbf{u}) \tag{3.31}$$

To minimize the error variance, we take the derivative of the above expression (Eq.(3.31)) with respect to each of the kriging weights and set each derivative to zero. This leads to the following system of equations:

$$\sum_{\beta=1}^{n} \lambda_\beta(\mathbf{u}) C_R(\mathbf{u}_\alpha - \mathbf{u}_\beta) = C_R(\mathbf{u}_\alpha - \mathbf{u}) \quad \alpha = 1,...,n \tag{3.32}$$

Because of the constant mean, the covariance function for Z(**u**) is the same as that for the residual component, $C(\mathbf{h}) = C_R(\mathbf{h})$, so that we can write the simple kriging system directly in terms of C(**h**):

$$\sum_{\beta=1}^{n} \lambda_\beta(\mathbf{u}) C(\mathbf{u}_\alpha - \mathbf{u}_\beta) = C(\mathbf{u}_\alpha - \mathbf{u}), \quad \alpha = 1,...,n \tag{3.33}$$

This can be written in matrix form as

$$\mathbf{K}\boldsymbol{\lambda}_{SK}(\mathbf{u}) = \mathbf{k}, \tag{3.34}$$

where $\mathbf{K}_{SK}$ is the matrix of covariances between data points, with elements $\mathbf{K}_{i,j} = C(\mathbf{u}_i - \mathbf{u}_j)$; $\mathbf{k}$ is the vector of covariances between the data points and the estimation point, with elements given by $\mathbf{k}_i = C(\mathbf{u}_i - \mathbf{u})$; and $\boldsymbol{\lambda}_{SK}(\mathbf{u})$ is the vector

of simple kriging weights for the surrounding data points. If the covariance model is licit (meaning the underlying semivariogram model is licit) and no two data points are colocated, then the data covariance matrix is positive definite and we can solve for the kriging weights using

$$\boldsymbol{\lambda}_{SK} = \mathbf{K}^{-1}\mathbf{k} \tag{3.35}$$

Once we have the kriging weights, we can compute both the kriging estimate and the kriging variance, which is given by

$$\sigma^2_{SK}(\mathbf{u}) = C(\mathbf{0}) - \boldsymbol{\lambda}^T{}_{SK}(\mathbf{u})\mathbf{k} = C(\mathbf{0}) - \sum_{\alpha=1}^{n}\lambda_\alpha(\mathbf{u})C(\mathbf{u}_\alpha - \mathbf{u}) \tag{3.36}$$

The simple kriging is based on the assumption that the mean is constant and known over the entire domain. The Ordinary Kriging (OK) algorithm, however, might be considered if enough data are available to re-estimate locally the normal score mean.

3.1.1.4.2 Ordinary Kriging

Similar to SK, the practical assumptions for the application of ordinary kriging are:

1) Intrinsic stationarity of the field;

2) The mean E[Z(x)] = μ(x) is unknown but constant in the local neighborhood of each estimation point;

3) The variable is normally distributed, and its covariance function C(**h**) is known. However, assumption 2 is different from SK.

In this case, the kriging estimator can be written

$$\begin{aligned} Z^*(\mathbf{u}) &= m(\mathbf{u}) + \sum_{\alpha=1}^{n}\lambda_\alpha(\mathbf{u})\left[Z(\mathbf{u}_\alpha) - m(\mathbf{u})\right] \\ &= \sum_{\alpha=1}^{n}\lambda_\alpha(\mathbf{u})Z(\mathbf{u}_\alpha) + \left[1 - \sum_{\alpha=1}^{n}\lambda_\alpha(\mathbf{u})\right]m(\mathbf{u}) \end{aligned} \tag{3.37}$$

And we filter the unknown local mean from the SK estimator by requiring that the kriging weights sum to one. This results in the following ordinary kriging estimator:

$$Z_{OK}^{*}(\mathbf{u}) = \sum_{\alpha=1}^{n} \lambda_{\alpha}(\mathbf{u}) Z(\mathbf{u}_{\alpha}) \quad \text{with} \quad \sum_{\alpha=1}^{n} \lambda_{\alpha}(\mathbf{u}) = 1 \tag{3.38}$$

In order to minimize the error variance subject to the unit-sum constraint on the weights, we actually set up the system minimize the error variance plus an additional term involving a Lagrange parameter, $\mu(\mathbf{u})$ m :

$$L = \sigma_{E}^{2}(\mathbf{u}) + 2\mu(\mathbf{u})\left[1 - \sum_{\alpha=1}^{n} \lambda_{\alpha}(\mathbf{u})\right] \ , \tag{3.39}$$

so that minimization with respect to the Lagrange parameter forces the constraint to be obeyed:

$$\frac{1}{2}\frac{\partial L}{\partial \mu} = 1 - \sum_{\alpha=1}^{n} \lambda_{\alpha}(\mathbf{u}) = 0 \, . \tag{3.40}$$

In this case, the system of equations for the kriging weights turns out to be

$$\begin{cases} \sum_{\beta=1}^{n} \lambda_{\beta}(\mathbf{u}) C(\mathbf{u}_{\beta} - \mathbf{u}_{\alpha}) + \mu(\mathbf{u}) = C(\mathbf{u} - \mathbf{u}_{\alpha}), \alpha = 1, ..., n \\ \sum_{\beta=1}^{n} \lambda_{\beta}(\mathbf{u}) = 1 \end{cases} , \tag{3.41}$$

where the $\lambda_{\alpha}(\mathbf{u})$'s are the OK weights and $C_{R}(\mathbf{h})$ is the covariance function for the residual component of the variable. In simple kriging, we could equate $C_{R}(\mathbf{h})$ and $C(\mathbf{h})$, the covariance function for the variable itself, due to the assumption of a constant mean. That equality does not hold here, but in practice the substitution is often made anyway, on the assumption that the semivariogram, from which C(**h**) is derived, effectively filters the influence of large-scale trends in the mean.

In fact, the unit-sum constraint on the weights allows the ordinary kriging system to be stated directly in terms of the semivariogram (in place of the $C_{R}(\mathbf{h})$ values

above). In a sense, ordinary kriging is the interpolation approach that follows naturally from a semivariogram analysis, since both tools tend to filter trends in the mean.

Once the kriging weights (and Lagrange parameter) are obtained, the ordinary kriging error variance is given by

$$\sigma^2_{OK}(\mathbf{u}) = C(\mathbf{0}) - \sum_{\alpha=1}^{n} \lambda_\alpha(\mathbf{u}) C(\mathbf{u}_\alpha - \mathbf{u}) - \mu(\mathbf{u}) \tag{3.42}$$

Note that the SK weights are different from the OK weights. In fact, OK amounts to re-estimating, at each new location, $\mathbf{u}$, the mean m by using the SK algorithm (Eq.(3.33)). Since OK is most often applied within moving search neighborhoods (i.e., using different data sets for different locations $\mathbf{u}$) the implicit re-estimated mean denoted $m^*(\mathbf{u})$ depends on the location, $\mathbf{u}$. Thus the OK estimator is a simple kriging, where the constrant mean value m is replaced by the location-dependent estimate $m^*(\mathbf{u})$.

OK as applied within moving data neighborhoods is already a nonstationary algorithm, in the sense that it corresponds to a nonstationary RF model with varying mean but stationary covariance. This ability to rescale locally the RF model $Z(\mathbf{u})$ to a different mean value $m^*(\mathbf{u})$ explains the extreme robustness of the OK algorithm.

When simulating fractures, one has to keep in mind that the distributions of fracture intensity (Section 1.1.1.3) often violate the assumption of normality (Section 3.1.1.4) required by most forms of Kriging, such as SK and OK. Fracture intensity is consistently discrete and positively valued, and consequently, right skewed. One way to circumvent this problem is to transform the fracture intensity distribution into a normal distribution. However, in sequential Gaussian simulation (Section 3.1.1.5.4) the data has to be transformed into Gaussian space, hence the sequential Gaussian simulation reproduces only the normal score variogram, not the original space variogram. However one non-parametric Kriging technique, the Indicator Kriging, does not assume that the

data to be interpolated are normally distributed, and therefore it will be used in the future fracture simulation.

3.1.1.4.3 Indicator Kriging

Indicator kriging (IK) makes no assumption of normality and is essentially a non-parametric kriging. Instead of assuming a normal distribution at each estimate location, IK builds the cumulative distribution function (CDF) of simulated variable at each point **u** based on the behavior and correlation structure of indicator transformed data points in the neighborhood of **u**.

Indicator transformed data points are constructed as follows. A series of threshold values are established between the smallest and largest data values in the set. These threshold values, referred to here as IK cutoffs, are used to numerically build the CDF of the estimation point. For each IK cutoff z_k, data in the neighborhood of **u** are transformed into 0s and 1s: 0s if the data are greater than the threshold and 1s if they are smaller. By this transformation, the binary indicator RF $I(\mathbf{u};z_k)$ is obtained. IK then estimates the probability that the estimation point is less than the threshold value by using one of indicator krigings (next section), given this neighborhood of transformed data and a model of the IK cutoff correlation structure (variogram). By performing this operation for each cutoff (z_k, k=1,…,K) across the range of data approximates the CDF at the estimation point, which represents a probabilistic model for the uncertainty about the unsampled value $z(\mathbf{u})$. The estimated value at this point can be obtained by indicator back-transforming the expectation of this CDF.

If $z(\mathbf{u})$ is itself a binary categorical variable, e.g., set to 1 if a specific rock type prevails at **u**, to 0 otherwise, then the direct kriging of $z(\mathbf{u})$ provides a model for the probability that $z(\mathbf{u})$ be one, i.e., for that rock type to prevail at location **u**.

If $z(\mathbf{u})$ is a continuous variable, then the correct selection of the cutoff values z_k is essential: too many cutoff values and the inference and computation become needlessly tedious and expensive; too few, and the details of the distribution are lost.

3.1.1.4.3.1 Simple Indicator Kriging (SIK)

Like SK, the assumptions for the application of simple indicator kriging are:

1) Intrinsic stationarity of the field;

2) The mean $E[I(\mathbf{u};z_k)]$ is constant and known; and

3) Known covariance function $C_I(\mathbf{h};z_k)$.

Indeed, the constant mean of the binary indicator RF $I(\mathbf{u};z_k)$ is the cumulative distribution function (cdf) of the RF $Z(\mathbf{u})$ itself, i.e.:

$$E\left\{I\left(\mathbf{u};z_k\right)\right\}=1\cdot\Pr\left\{Z\left(\mathbf{u}\right)\le z_k\right\}+0\cdot\Pr\left\{Z\left(\mathbf{u}\right)>z_k\right\}=\Pr\left\{Z\left(\mathbf{u}\right)\le z_k\right\}=F\left(z_k\right) \quad (3.43)$$

By using SK algorithm, the SK estimate of the indicator transform $i(\mathbf{u};z_k)$ is thus written as:

$$\left[i\left(\mathbf{u};z_k\right)\right]^*_{SIK}=\sum_{\alpha=1}^{n}\lambda_\alpha\left(\mathbf{u};z_k\right)i\left(\mathbf{u}_\alpha;z_k\right)+\left[1-\sum_{\alpha=1}^{n}\lambda_\alpha\left(\mathbf{u};z_k\right)\right]F\left(z_k\right) \quad , \qquad (3.44)$$

where the $\lambda_\alpha\left(\mathbf{u};z_k\right)$s are the SK weights corresponding to cutoff z_k. These weights are obtained by solving a SK system:

$$\sum_{\beta=1}^{n}\lambda_\beta\left(\mathbf{u};z_k\right)C_I\left(\mathbf{u}_\beta-\mathbf{u}_\alpha;z_k\right)=C_I\left(\mathbf{u}-\mathbf{u}_\alpha;z_k\right),\quad \alpha=1,...,n \quad , \qquad (3.45)$$

where $C_I\left(\mathbf{h};z_k\right)=Cov\left\{I\left(\mathbf{u};z_k\right),I\left(\mathbf{u}+\mathbf{h};z_k\right)\right\}$ is the indicator covariance at cutoff z_k. If K cutoff values z_k are used, simple IK requires K indicator covariances $C_I\left(\mathbf{h};z_k\right)$ in addition to the K cdf values $F(z_k)$.

3.1.1.4.3.2 Ordinary Indicator Kriging (OIK)

Like OK, the assumptions for the application of ordinary indicator kriging are:

1) intrinsic stationarity of the field;

2) the mean E[I($\mathbf{u}$;z_k)] is constant but unknown; and

3) known covariance function $C_I(\mathbf{h};z_k)$.

Like simple kriging, SIK depends on the CDF values $F(z_k)$, interpreted as mean indicator values. However, if the CDF values $F(z_k)$ are constant but unknown, by using OK algorithm, the OIK estimate of the indicator transform, and $i(\mathbf{u};z_k)$ is thus written as:

$$\left[i\left(\mathbf{u};z_k\right)\right]^*_{OIK} = \sum_{\alpha=1}^{n} \lambda_\alpha\left(\mathbf{u};z_k\right) i\left(\mathbf{u}_\alpha;z_k\right) \quad , \tag{3.46}$$

where the $\lambda_\alpha\left(\mathbf{u};z_k\right)$s are the OIK weights corresponding to cutoff z_k. These weights are obtained by solving the OIK system:

$$\begin{cases} \sum_{\beta=1}^{n} \lambda_\beta\left(\mathbf{u};z_k\right) C_I\left(\mathbf{u}_\beta - \mathbf{u}_\alpha;z_k\right) + \mu\left(\mathbf{u};z_k\right) = C\left(\mathbf{u} - \mathbf{u}_\alpha;z_k\right), \alpha = 1,...,n \\ \sum_{\beta=1}^{n} \lambda_\beta\left(\mathbf{u};z_k\right) = 1 \end{cases} , \tag{3.47}$$

where $C_I\left(\mathbf{h};z_k\right) = Cov\left\{I\left(\mathbf{u};z_k\right), I\left(\mathbf{u}+\mathbf{h};z_k\right)\right\}$ is the indicator covariance at cutoff z_k; and $\mu\left(\mathbf{u};z_k\right)$ is the Lagrange parameter associated with the constraint $\sum_{\beta=1}^{n} \lambda_\beta\left(\mathbf{u};z_k\right) = 1$.

Note that the SIK weights are different from the OIK weights. In fact, OIK amounts to re-estimating, at each new location, $\mathbf{u}$, and the mean F(z) is used in SIK. Since OK is most often applied within moving search neighborhoods (i.e., using different data sets for different locations $\mathbf{u}$), the implicit re-estimated mean denoted $F^*\left(\mathbf{u};z\right)$ depends on the location $\mathbf{u}$. Thus the OIK estimator is a simple indicator kriging, where the constant mean valve F(z) is replaced by the location-dependent estimate $F^*\left(\mathbf{u};z\right)$.

An example of indicator kriging can be found in Appendix F.

3.1.1.5 Simulation

A (conditional or nonconditional) simulation of the random function $\{Z(x): x \in \mathbf{R}^n\}$ is simply a realization of Z(x), randomly selected in the set of all possible realization.

3.1.1.5.1 Why we need simulation

Let us consider the simplified problem proposed by Alfaro (1979) and illustrated in Figure 3.6: a submarine cable is to be laid between two cities on both sides of an ocean, and we want to predict the length of the cable. Measurements of the depth of the sea floor are available every 100m. An easy solution is to estimate the depth by kriging at every point along the profile and to compute the length of this kriged curve. The length obtained for the profile is L=945m. But this result is not quite convincing, since the actual seafloor is far more complex than the kriged one (kriging has a smoothing effect). As a result, the length computed from the kriged profile certainly underestimates the actual length.

To get the exact solution, we need a continuous, or at least very dense survey of depth. In the present case a survey with samples taken every 10m gives a length L=1182. Is there a way of avoiding the costs of the second survey? Based on the fractal theory, the length of a curve depends on the scale of investigation. If the investigation interval is infinitesimal, the length of the seafloor along the profile will be infinite. However, a cable has some rigidity, and if we admit that it can hang above the sea bottom over distances of about 10m, then the goal becomes an estimation of the length for an interval is 10m.

The idea of conditional simulations is to build a representation of the phenomenon that is consistent with the data observed at the 100m sampling interval, as kriging is, and yet reproduces the local fluctuations at the scale of 10m. A conditional simulation is not a reality but only a possible version of it, among myriad others. The conditional simulation differs from the real seafloor, often more than kriging does, but has the same character.

The cable measured on this simulation with a sampling interval of 10m is very close to the true length: L=1154 instead of L=1182.

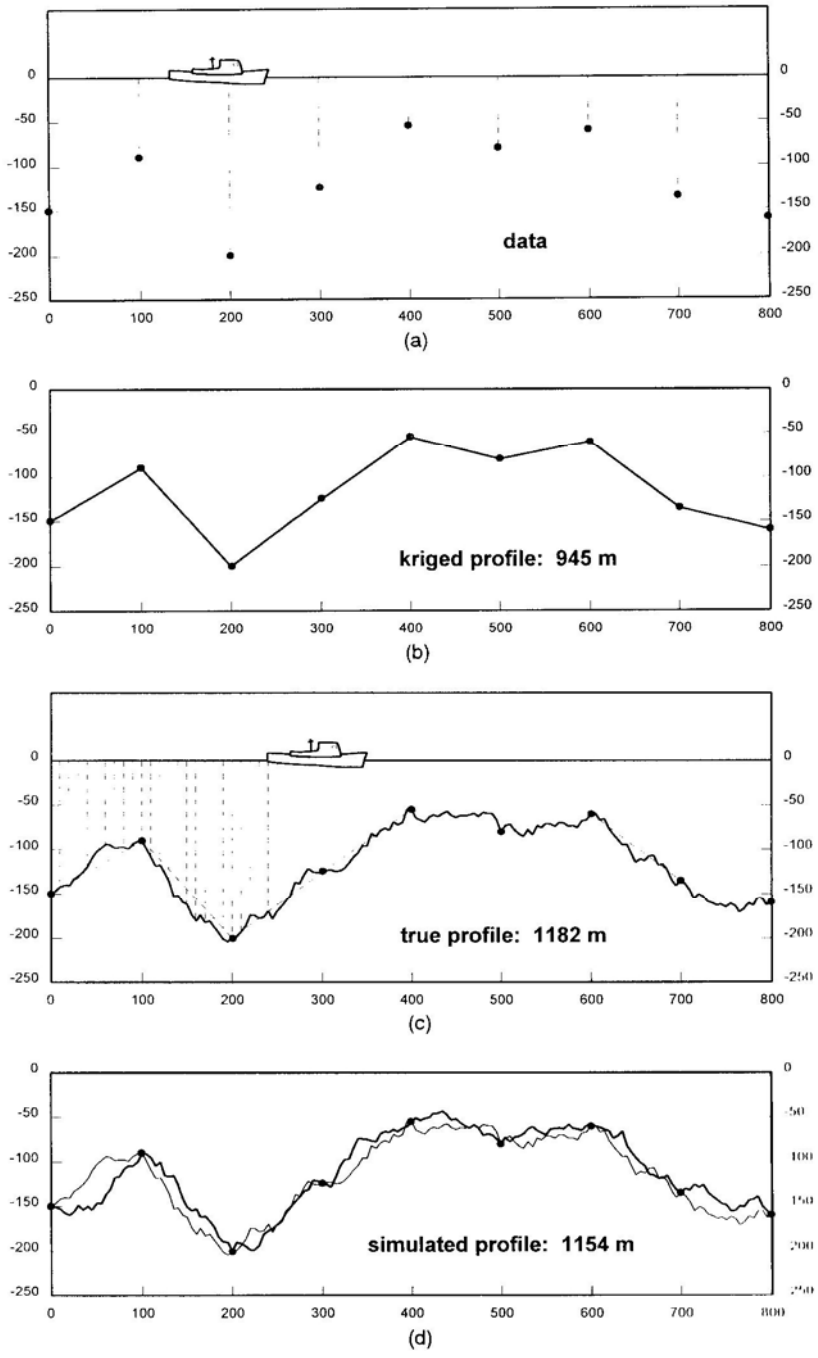

Figure 3.6 Submarine cable: (a) seafloor survey with 100m spacing; (b) kriging estimate of the seafloor; (c) continuous survey (true profile); (d) conditional simulation based on the 100m data, and true profile. From Alfaro (1979)

3.1.1.5.2 Limitations of Kriging

Although kriging provides viable means to interpolate and extrapolate data, it suffers from some drawbacks:

1. Kriging is a statement of the reproduction of covariance between the data and the unknown expressed as a weighted linear combination of the covariance between the data, because weights λ_α are found by solving system of equations linear in covariance matrix terms. However, reproduction of covariance between any two estimated values is not assured (i.e., the covariance between two estimates does not match the covariance model).

2. Even though the RF Z(u) is assumed to have unit variance (normalized to the variance, Section 3.1.1.3), the kriged values do not reproduce that variance. In fact, the variance of the kriged map is less ($1-\sigma_K^2$ instead of 1), which means that kriged maps are smooth, deterministic and less reflective of variability. Here σ_K^2 is the minimum error variance in kriging,

$$\sigma_K^2 = 1 - \sum_{\alpha=1}^{n} \lambda_\alpha(\mathbf{u})\rho(\mathbf{u}-\mathbf{u}_\alpha), \tag{3.48}$$

where $\rho(\mathbf{u}-\mathbf{u}_\alpha)$ is the correlation coefficient between simulated value Z(**u**) and the known value $Z(\mathbf{u}_\alpha)$.

3.1.1.5.3 Stochastic Simulation

The two problems with kriging (too smooth and incorrect texture) may be remedied by adding a residual $R(\mathbf{u})$ to the kriged estimate $Z^*(\mathbf{u})$:

$$Z_S(\mathbf{u}) = Z^*(\mathbf{u}) + R(\mathbf{u}) \tag{3.49}$$

Since one of the drawbacks of kriging $Z^*(\mathbf{u})$ is that it is deterministic, we can make the residue $R(\mathbf{u})$ stochastic, and so $Z_S(\mathbf{u})$ becomes stochastic.

Since $Z^*(\mathbf{u})$ is an unbiased estimate of $Z(\mathbf{u})$, for $Z_S(\mathbf{u})$ to be unbiased, we need $E\{R(\mathbf{u})\}=0$. We also require:

$$Var\{Z_S(\mathbf{u})\}=Var\{Z^*(\mathbf{u})+R(\mathbf{u})\}=Var\{Z(\mathbf{u})\}=1 \tag{3.50}$$

If we assume $Cov\{Z^*(\mathbf{u}),R(\mathbf{u})\}=0$, the requirement becomes $Var\{R(\mathbf{u})\}=\sigma_K^2$.

In sum, the residual $R(\mathbf{u})$ added to the kriged values should satisfy

$$\begin{cases} E\{R(\mathbf{u})\}=0 \\ Var\{R(\mathbf{u})\}=\sigma_K^2 \end{cases} \tag{3.51}$$

to remedy the two limitations of kriging mentioned above. Also it can be proven that, if the residual is the estimation error ($R(\mathbf{u})=Z(\mathbf{u})-Z^*(\mathbf{u})$), then $R(\mathbf{u})$ is orthogonal to the kriging estimate, i.e., $Cov\{Z^*(\mathbf{u}),R(\mathbf{u})\}=0$ (Chiles and Delfiner, 1999).

Based on the above derivation, several simulation methods came into being and are summaried in Table 3.1.

Table 3.1 Main characteristics of the various simulation methods (From Chiles and Delfiner, 1999)

Method	Covariance	$\mathbb{R}^n$	Model Type	Ergodic	Conditioning	Systematic Grid Required	N_S	Exact Covariance
Sequential Gaussian	All C	All n	Gaussian	Yes	Direct	No	$< 10^3$ $> 10^3$	Yes No
Matrix decomposition	All C	All n	Gaussian	Yes	Direct	No	$< 10^3$	Yes
Turning bands	All C, γ, K	$n > 1$	*	No, if single direction	Kriging	No	All N_S	*
Autoregressive	Damped exponential and sinusoidal	$n = 1,2$	Gaussian	Yes	Kriging	Yes	All N_S	Yes
Moving average	Most C with short range	$n = 1,2$ $n > 2$	Gaussian	Yes	Direct Kriging	Yes	All N_S	Yes
Dilution	Most C, γ	All n	Jump	Yes	Kriging	No	All N_S	Yes
Continuous spectral	All C, γ	All n	Gaussian (Periodic)	No	Kriging	No	All N_S	Yes
Discrete spectral	Most $C, \gamma = \lvert h \rvert^\alpha$, polynomial K All C finite range	$n = 1$ $n > 1$	Gaussian	Yes	Kriging	Yes	All N_S	Yes
Poisson hyperplanes	Linear	All n	Jump	No	Kriging	No	All N_S	Yes
Integration	Polynomial or spline K	$n = 1$	Apparent drift	—	Kriging	No	All N_S	*
Sequential indicators	All valid C	All n	Discrete	Yes	Direct	No	All N_S	*
Truncated Gaussian	C of a particular family	All n	Discrete	*	Iterative	*	*	*
Voronoi	Specific C	All n	Mosaic	Yes	Not known	No	All N_S	Yes
Poisson polyhedra	Exponential	All n	Mosaic	Yes	Not known	No	All N_S	Yes
Substitution	Particular C	All n	—	*	Kriging	*	*	*
Boolean	Specific C	All n	Binary	Yes	Iterative	No	All N_S	Yes
Simulated annealing	—	All n	Not known	Yes	Iterative	Yes	All N_S	No

Note: C, γ and K indicate the possibility of simulating covariances, variograms and generalized covariances; n: dimension of the space; N_S: number of points simulated; for methods that are coupled with another method, * indicates a property that depends on the associated method, — means not applicable or unknown. Many variants exist, notably as regards the model type.

3.1.1.5.4 Sequential Simulation

Sequential simulation has grown to be one of the most popular and computationally efficient tools for obtaining simulations that reproduce a certain histogram and a certain type of variogram(s), which have been obtained from the data. Bayes' theorem (1) is the basic theorem behind the sequential simulation.

$$P(A,B) = P(A|B) \cdot P(B) \tag{3.52}$$

If z_1 and z_2 are two outcomes at locations $\mathbf{u_1}$ and $\mathbf{u_2}$, and there are n condition data, then from Bayes' theorem we have:

$$F\left(z_1, z_2 \middle| (n)\right) = F\left(z_2 \middle| z_1, (n)\right) \cdot F\left(z_1 \middle| (n)\right) \tag{3.53}$$

Generalizing the above expression to N points,

$$\begin{aligned} & F\left(z_1, z_2, .., z_N \middle| (n)\right) \\ & = F\left(z_N \middle| z_1, z_2, .., z_{N-1}, (n)\right) \cdot F\left(z_1, z_2, .., z_{N-1} \middle| (n)\right) \\ & = F\left(z_N \middle| z_1, z_2, .., z_{N-1}, (n)\right) \cdot F\left(z_{N-1} \middle| z_1, z_2, .., z_{N-2}, (n)\right) \cdot F\left(z_1, z_2, .., z_{N-2} \middle| (n)\right) \\ & = ... \\ & = F\left(z_N \middle| z_1, z_2, .., z_{N-1}, (n)\right) \cdot F\left(z_{N-1} \middle| z_1, z_2, .., z_{N-2}, (n)\right) \cdot ... \cdot F\left(z_2 \middle| z_1, (n)\right) \cdot F\left(z_1 \middle| (n)\right), \end{aligned} \tag{3.54}$$

where $F\left(z_N \middle| z_1, z_2, .., z_{N-1}, (n)\right)$ implies conditioning using the (n) original data and the (N-1) previously simulated values.

The decomposition above implies the following steps to carry out sequential simulation:

- ✓ model the CDF at the first location, $\mathbf{u_1}$, conditioned to the n-original data;
- ✓ draw an outcome, z_1, from that CDF, and add that simulated value to the conditioning data set for the next node;
- ✓ model CDF at i^{th} node given the n-original data and all the (i-1) previously simulated values; draw an outcome z_i from that CDF; and
- ✓ repeat procedure until all the nodes are visited; obtain one realization of the RF $Z(\mathbf{u})$.

There are two ways to obtain CDF $F^*\left(\mathbf{u}; z_k \middle| (n)\right)$ at each location $\mathbf{u}$. One is the parametric or multi-Gaussian approach, which uses traditional kriging as the engine. A

normal score transformation of the original data into Gaussian space is needed before the sequential Gaussian simulation. After simulation in the Gaussian space, a back transformation to identify the target histogram needs to be performed, which ensures reproduction of the target distribution deemed relevant for the field of observation. Therefore, the sequential Gaussian simulation reproduces only the normal score variogram, not the original space variogram. The other is a non-parametric or indicator approach, which uses indicator kriging as the engine and is introduced as follows.

3.1.1.5.5 Sequential Indicator Simulation (SIS)

In mathematical terms, the most convenient method for simulation is sequential Gaussian simulation (SGS) (Deutsch and Journel, 1998) because all conditional distributions from which simulated values are drawn are Gaussian with parameters determined by the solution of a traditional kriging system. However, at least two limitations can be attributed to SGS:

1) It relies on the assumption of multi-variate Gaussianity, an assumption that can never be fully checked in practice yet always seems to be taken for granted. Multi-Gaussianity leads to simulated realizations that have maximally disconnected extremes (maximum entropy, Journel and Deutsch, 1993), a property that often conflicts with geological reality (Goovaerts, 1997; Caers, web resource).

2) It reproduces, in theory, only the normal score variogram, not the original variogram model. Usually, reproduction of the normal score variogram entails the reproduction of the original data variogram if the data histogram is not too skewed. However, in the case of high skewness, the reproduction of the variogram model after back-transformation is not guaranteed at all (Caers, web resource). This will be shown in Section 3.3 through a case study.

Because of these two limitations, Sequential Indicator Simulation (SIS) was developed. This simulation uses indicator kriging (IK) as the simulation engine. The

basic background of IK is the Luenberger Theorem, which is stated in Appendix G. From this theorem, the following implications can be obtained: the estimate of binary indicator RF I($\mathbf{u}$;z_k) $I^*(\mathbf{u};z_k)=\sum_{\alpha=1}^{n}\lambda_\alpha(\mathbf{u};z_k)i(\mathbf{u}_\alpha;z_k)$ (Eq.(3.46)) is the best estimate in a minimum norm (error variance) sense; $I^*(\mathbf{u};z_k)$ is also an estimator for $I(\mathbf{u};z_k)\big|(n)$ i.e. $I^*(\mathbf{u};z_k)=E\{I(\mathbf{u};z_k)\big|(n)\}$.

To process SIS in a way that each node be simulated along the random path (a path formed by randomly picking one unsimulated location each time), IK provides a CCDF model through the K probability estimates (Section 3.1.1.4.3, Eqs. (3.44) and (3.46)):

$$I^*(\mathbf{u};z_k\big|(n))=\Pr^*\{Z(\mathbf{u})\le z_k\big|(n)\},\quad k=1,...,K \tag{3.55}$$

Within-class interpolation provides the continuum for all threshold values. The Monte Carlo simulation of a realization is obtained by drawing a uniform random number $p\in[0,1]$ and retrieving the CCDF p quantile $z(\mathbf{u})=F^{*-1}(\mathbf{u};p\big|(n))$ such that $F^*(\mathbf{u};z(\mathbf{u})\big|(n))=p$. According to Eq.(3.54), the simulated value $z(\mathbf{u})$ is added into the indicator data set and the next location along the random path is simulated conditioning to the updated data set.

3.1.2 INTENSITY-APERTURE RELATIONSHIP

Marrett et al. (2005, Manuscript) state that large-aperture fractures are more strongly partitioned into clusters than are small-aperture fractures. The spatial organization and size organization might be coupled, which causes the largest fractures to grow in the midst of the largest clusters; alternatively, the largest clusters might represent process zones around the largest fractures. I demonstrate this phenomenon by using Marrett et al.'s data. The data set is from a scanline perpendicular to calcite-filled veins in

the Marble Falls Limestone at Pedernales Falls State Park in Texas (Gomez and Marrett, in review). The data set represents 916 fractures along 59m of a layer-parallel outcrop. The scanline is discretized by 1m intervals. For each interval, the intensities (number of fracture/interval length) and maximum apertures are plotted in Figure 3.7, which shows the relationship between frequency and local maximum aperture. We can find that the larger maximum apertures tend to happen in fracture cluster zones where the frequency is higher.

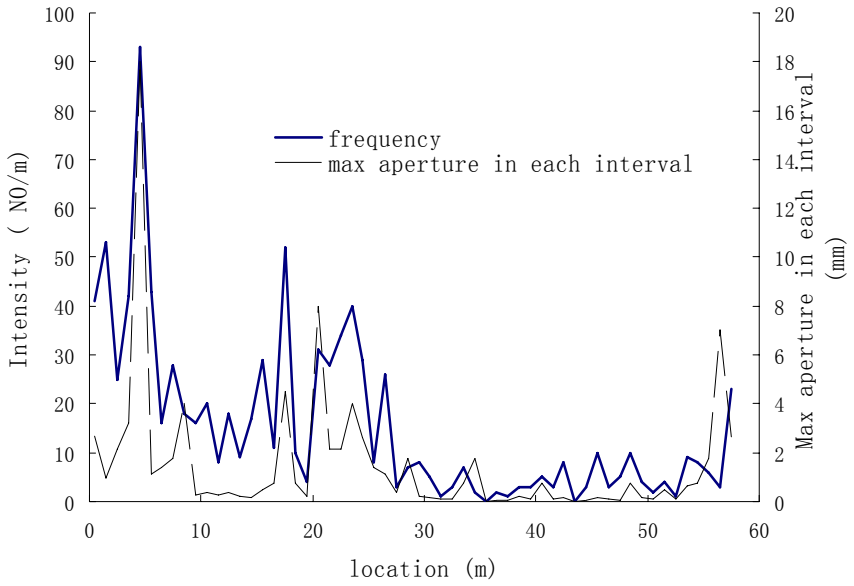

Figure 3.7 An example of frequency and aperture relationship

This property provides a hint to fracture aperture sampling from its CDF. The author uses the same data as above to build one aperture CDF. The minimum value of aperture measured was 0.05mm while the largest was 18.0mm. As shown in Figure 3.8, the CDF of the aperture is typically very steep in the small aperture range and very flat in the large aperture range.

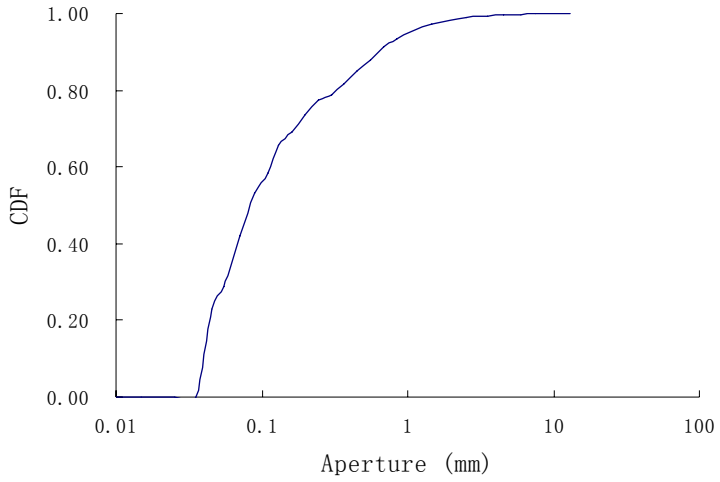

Figure 3.8 A typical CDF of fracture aperture (data from Marrett et al., 2005 Manuscript)

When sampling from the aperture CDF, it is very unlikely that a large aperture be selected unless a large number of samples are drawn, as is the case in fracture clusters. It is thus reasonable to expect that the larger fractures tend to occur in the more intense fracture zones when using the Monte Carlo sampling from the aperture CDF. This will be confirmed in the case history of Section 3.3.

3.1.3 TRACE LENGTH-APERTURE RELATIONSHIP

Based on the literature review, many researchers proposed different relationships between trace length and aperture. More details can be seen in Section 1.3.4. As described in Chapter 1, almost all data sets of length and displacement or aperture relationship show considerable scatter, part of which may reflect sampling limitations (e.g., measurement along chords of fracture surfaces) and differences in fracture linkage host layer thickness and host rock strength.

From the author's point of view, it is best if the specific trace length-aperture relationship can be obtained for one specific research case by mearsuring trace length and aperture. However, it is sometimes hard or impossible to get one of these quantities. For

example, aperture data was not collected by geologists in the real case study presented in Chapter 5. In this case, the best I can do is use a reasonable published trace length-aperture relationship. As shown in Figure 3.9 (the same as Figure 1.5), Marrett et al. (1997) summarize most previous research data and collect data from microfractures in low-porosity sandstones using the SEM-CL technique. This data set covers more data and a wider range (0.0005mm ~ >1m for aperture) than other data sets. In addition, for civil engineering (tunnel inflow in this research), the aperture size we are interested in is in the range of 0.01mm to 1mm, which is covered by this data set rather than the others.

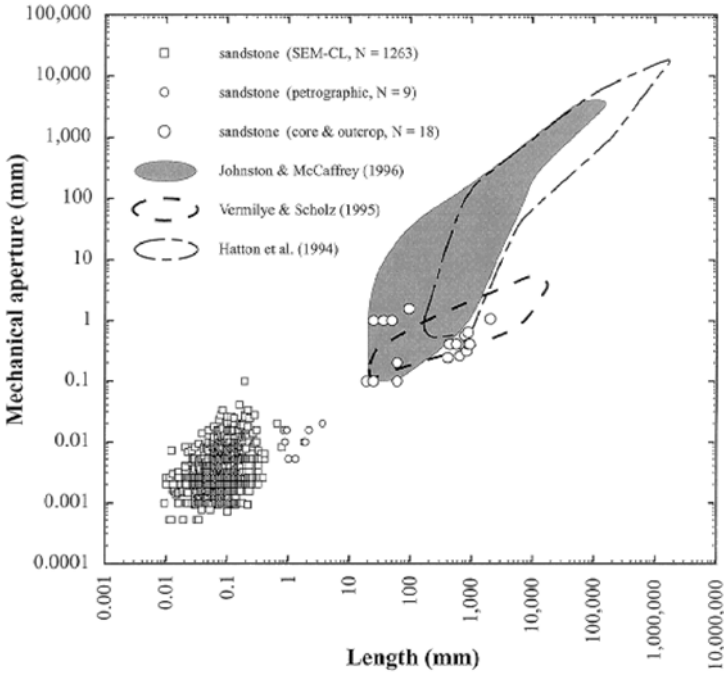

Figure 3.9 Mechanical aperture vs length for extension fractures (From Marrett and Laubach, 1997) (same as Figure 1.5)

I found the following relationship between length and mechanical aperture based on the above data sets.

$$L = kT^a , \tag{3.56}$$

where, L (mm) is the fracture trace length; T (mm) is the fracture mechanical aperture; and a and k are constants, a=1.3, k=100 [mm/ $mm^{1.3}$].

This relationship will be used in the fracture simulation as the first estimation. The final trace length-aperture relationship can be calibrated based on the total flow measurements at the beginning of tunnel excavation. Once the apertures (diameters) are simulated, the diameters (apertures) can be obtained based on this relation. It is worthy to note that if diameters are simulated first, the above relationship is between trace length and aperture, not diameter and aperture. From a statistical point of view, it is reasonable to convert the diameter to the trace length by

$$L_i = d_i \frac{\overline{L}}{\overline{d}}, \tag{3.57}$$

where L_i is the fracture trace length needed in the trace length-aperture relationship; d_i is the fracture diameter simulated before; $\overline{L}$ is the average trace length; and $\overline{d}$ is the average diameter. If the trace length or diameter distribution is known, existing closed-form formulas can be used to obtain $\overline{L}$ and $\overline{d}$. For several different distributions and corresponding closed-form formulas can be found in Tonon and Chen (2007). If apertures are simulated first, the trace length L_i can be obtained from Eq.(3.56). Then, by using the same idea, one can get the diameter by

$$d_i = L_i \frac{\overline{d}}{\overline{L}} \tag{3.58}$$

3.1.4 DIFFERENCE BETWEEN MECHANICAL AND HYDRAULIC APERTURE

The hydraulilc aperture controls the flow in a fracture rather than the mechanical aperture. Even though mechanical apertures are obtained from diameter-aperture relationship, there are at least three other items that must be considered.

First, the flow through a fractured rock mass depends on: (a) the aperture of the fractures, which in turn depends on (b) the normal stress acting across the fractures,

which in turn depends on (c) the *in situ* stress. When the fracture is subjected to a compressive normal stress, its aperture reduces. An increasing normal stress is required to continue reducing the aperture. The mechanical aperture is the amount by which the fracture opens when it is unloaded from a normal stress value equal to the intact rock compressive strength to zero. Thus, the hydraulic aperture and the mechanical aperture are governed by different aspects of the geometry in three dimensions: the hydraulic aperture is governed by the channels of aperture spaces and the mechanical aperture by the regions where there is connecting rock, i.e., where the aperture has zero values (John and Hudson, 2000, page 146).

Second, fractures' surfaces are not smooth, but rough. When the fracture surfaces are rough, the geometrical aperture will vary all along the fracture. In two dimensions, the hydraulic aperture will be less than the mean geometrical aperture because the flow will be controlled by regions of smaller aperture, which act as a bottleneck to the flow. In three dimensions, it may be different because water flow will occur, along and across the fracture aperture, in the higher-aperture channels formed between the fracture surfaces. Thus, an equivalent hydraulic fracture aperture will be less than the mean geometrical aperture in two dimensions, but could be greater in three dimensions.

Third, in the geological history, some fractures are filled with gouge, clay, calcite, or gypsum, and tend to transmit groundwater poorly, and some fractures are eroded to be wider if there is appropriate hydraulic condition.

There have been many attempts to relate the mechanical and hydraulic properties of a fractured rock (e.g., Barton et al., 1985, Bayuk and Chesnokov, 1998; Renshaw, 1995, Rasolofosaon and Zinszner, 2002; Lee et al., 2001; Liu, 2005).

Lee et al. (2001) implemented hydraulic tests under normal and shear loads. As shown in Figure 3.10, the ratio between the hydraulic aperture and mechanical aperture was about 0.20 for granite joints under 2MPa normal pressure, and it was about 0.22 for marble joints under 1MPa normal pressure.

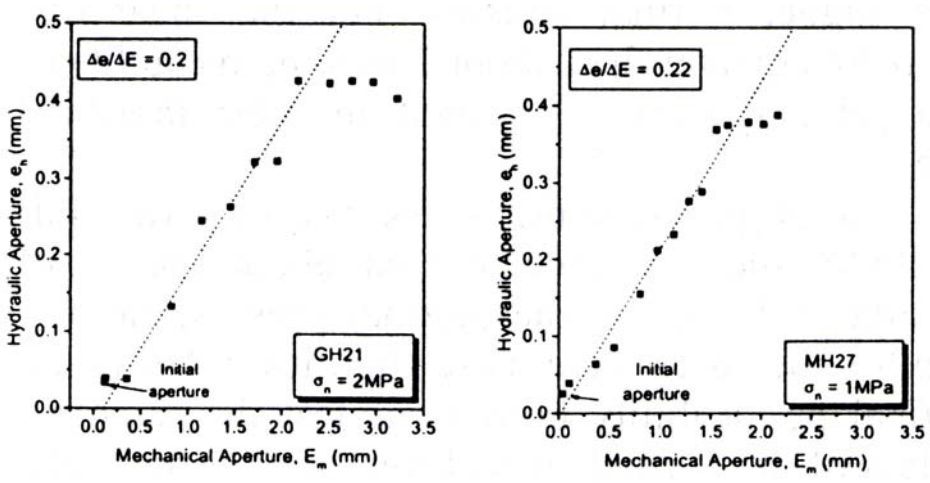

Figure 3.10 Typical relation between mechanical aperture and hydraulic aperture (From Lee et al., 2001)

Laubach (2003) uses practical approaches to identifying sealed and open fractures. He shows how the characterization challenge presented by sparse fracture sampling can be overcome by measuring a surrogate, the abundance of rock-mass cement that precipitated after fractures ceased opening. Sampling limitations are overcome because the surrogate is readily measured in small rock samples, including sidewall cores and cuttings. A diverse core database shows that this surrogate correctly predicts where large fractures are sealed. Information on the timing of the fracture opening relative to the cement sequence can be obtained in two ways. First, evidence of fracture-movement history and cement sequences in sparse large fractures can be extrapolated to areas having only cement data. Alternately, evidence of fracture timing can be acquired from sealed, micrometer-scale fractures. Distribution of porosity-reducing cement is commonly heterogeneous (from bed to bed and location to location) in siliciclastic and carbonate rocks. However, because patterns of sealed or open fractures cannot be delineated using fracture observations alone, surrogates have practical value for identifying open fractures.

This technology was not used in this research because there is no rock core available for the real tunnel project case study (Chapter 5). However, this technology definitely can be used in the next research cycle.

3.2 Simulation implementation

In this section, all simulation steps are introduced, including locations (using sequential indicator simulation), aperture (or diameter) (using its CDF), and diameter (or aperture) (using length-aperture relationship).

The flow chart of this simulation is shown in Figure 3.11.

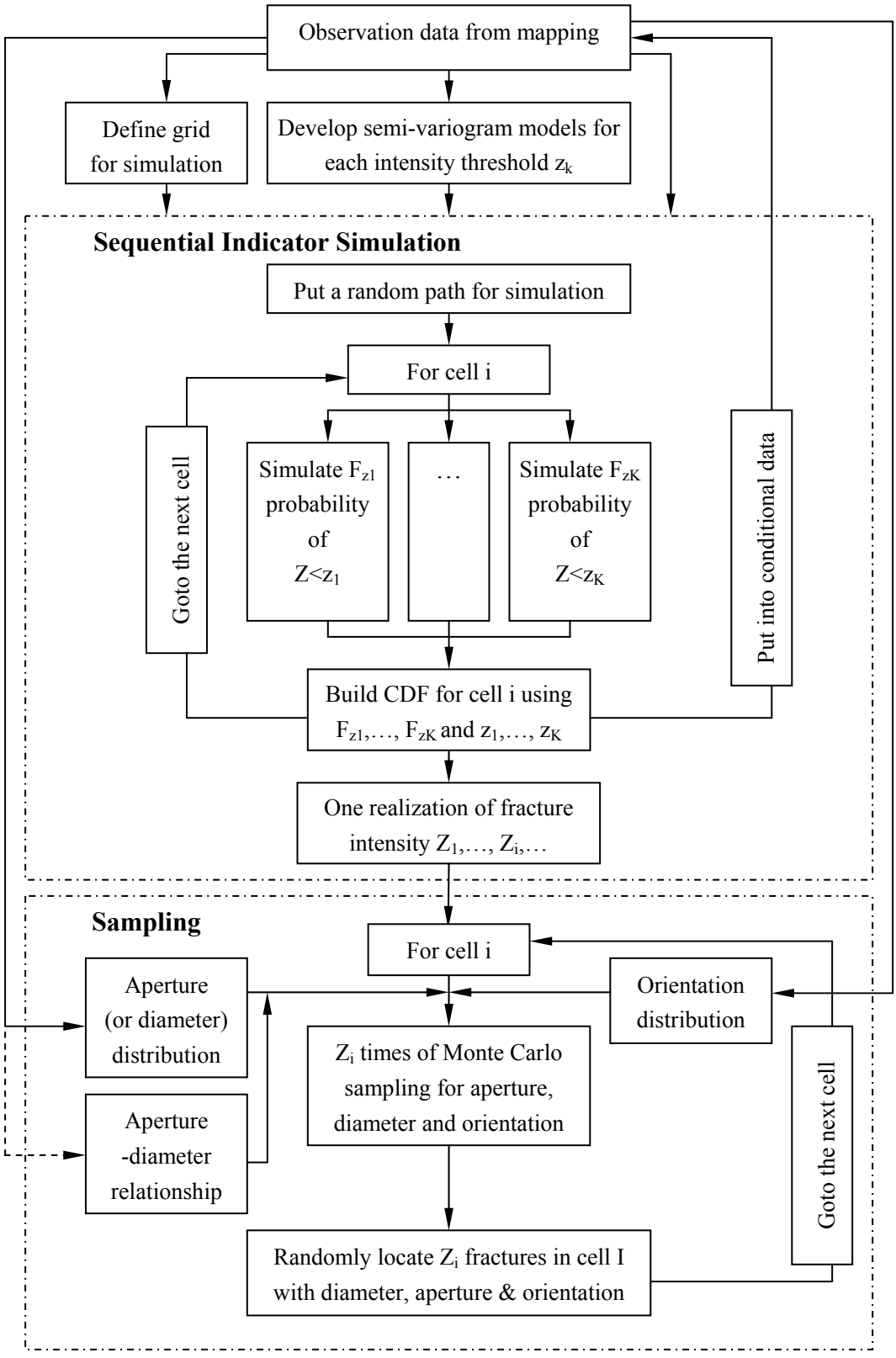

Figure 3.11 Flow Chart of Simulation

3.2.1 OBSERVATION DATA

3.2.1.1 Investigate *S (s=1,…S)* fracture sets and determine the fracture orientation and geology history (if possible).

3.2.1.2 For each fracture set *s*, set up several scanlines. Along each scanline, record all fracture locations, apertures (and/or trace lengths). Here scanlines can be drawn on the outcrop, or along a borehole, or on a tunnel wall. Scanlines do not have to be perpendicular to the fracture set. However, the angle θ between the scanline and fracture normal needs to be recorded, because the fracture intensity along the scanline should be corrected by this angle (Section 1.1.1.3) if the simulated scanlines (decribed later) do not have the same direction as this scanline.

For each fracture set:

3.2.2 SIMULATE THE FRACTURE INTENSITY

3.2.2.1 Define a grid in the simulation domain

3.2.2.1.1 2D simulation grid

The simulation domain can be built as a vertical rectangle (L*B) with coordinate system as shown in Figure 3.12, where x is parallel to the observed scanline.

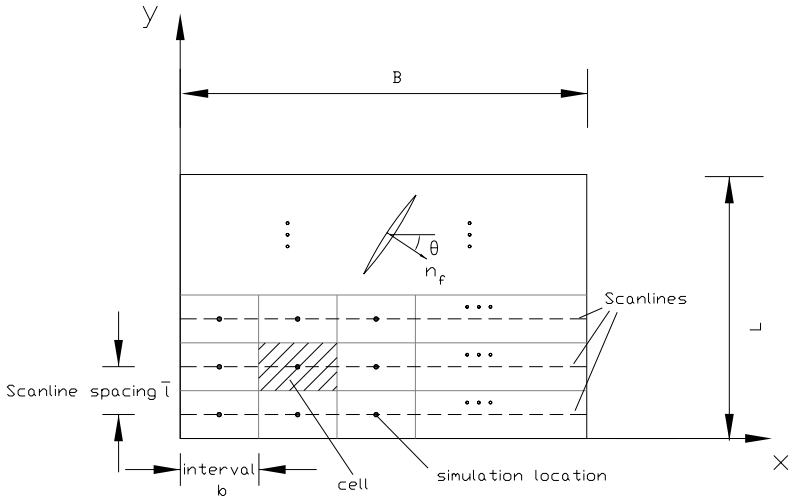

Figure 3.12 Simulation grid in 2D fracture simulation

Simulation scanline spacing is a very important parameter, which will affect the overall fracture density. If the simulation scanline spacing is set too small, there will be too many simulated fractures. If it is too large, the simulated fracture density will be too low. The relationship between measure P10 and P21 (Section 1.3.5) is

$$P21 = P10 \times C_{P2}, \tag{3.59}$$

where P21 is the total length of fracture traces per area of exposure [L^{-1}]; P10 is the number of fractures per length of scanline [L^{-1}]; and C_{P2} is the coefficient shown in Figure 1.7.

If we consider any simulation cell with the dimension $b \times \bar{l}$, then the expected number of fractures in this cell is $P10 \times b$. Therefore, the total fracture trace length in this cell is $P10 \times b \times \overline{L}$ if the average trace length is $\overline{L}$. From the definition of P21, the expected fracture trace length in this cell is $P21 \times b \times \bar{l}$. Therefore we obtain

$$P10 \times b \times \overline{L} = P21 \times b \times \bar{l} \tag{3.60}$$

By substituting Eq.(3.59) into Eq.(3.60), one obtains,

$$\bar{l} = \overline{L} / C_{P2} \tag{3.61}$$

Eq.(3.61) provides an exstimation for the simulated scanline spacing. From Figure 1.7, if the angle θ between the scanline and fracture normal is less than 45-degree, $C_{P2} \approx 1$ and $\bar{l} = \overline{L}$ is a good approximation. If θ is greater than 45-degree, the simulated scanline spacing can be calculated from Eq.(3.61) by using the corresponding C_{P2} value obtained from Figure 1.7.

As for interval length *b*, there is no restrictive requirement for b. However, b should be a reasonable value less than the semi-variogram range. Because in each cell of length b there is only one value (located at the center of the cell) to represent the property of the cell, if the cell is too large (compared to the semi-variogram range), the spatial

pattern will not be validly represented during the simulation. On the other hand, if b is too short, there will be a large number of cells, which will influence the simulation time. A good value for b can be 0.1 to 0.3 times the shortest range.

3.2.2.1.2 3D simulation grid

Typically, the simulation domain is selected around the researching object, which is a tunnel in our research. Let α and β be the azimuth and plunge of the fracture normal. Let α_t be the trend of the tunnel axis (assumed horizontal). The X', Y', Z' coordinate system used in the simulation domain is set as follows: Y' is horizontal and parallel to the tunnel axis, X' is orthogonal to Y' in the horizontal plane, Z' points upwards, and the origin is located at the tunnel center. Therefore, all fractures projections onto the tunnel cross section are ellipses, as shown in Figure 3.13.

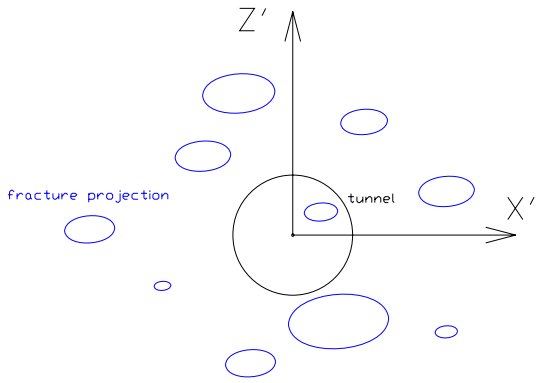

Figure 3.13 Fracture projections to tunnel cross section

Recall that, in two dimensions, the simulation scanline spacing is equal to $\overline{L}/C_{P2}$. In three dimensions, consider a circular fracture whose diameter is equal to the fracture (Figure 3.14). Consider a square whose area is equivalent to the circular fracture. When the square is projected onto the cross section plane, the length of the two sides of the projected square divided by C_{P2} can be used as the scanline spacings in the two

directions. Therefore, the coordinate system should be rotated about Y' and let X' and Z' overlap the major axis and minor axis of ellipses to get a new coordinate system $X''\text{-}Y''\text{-}Z''$ for building simulation grid. It can be seen in Figure 3.14.

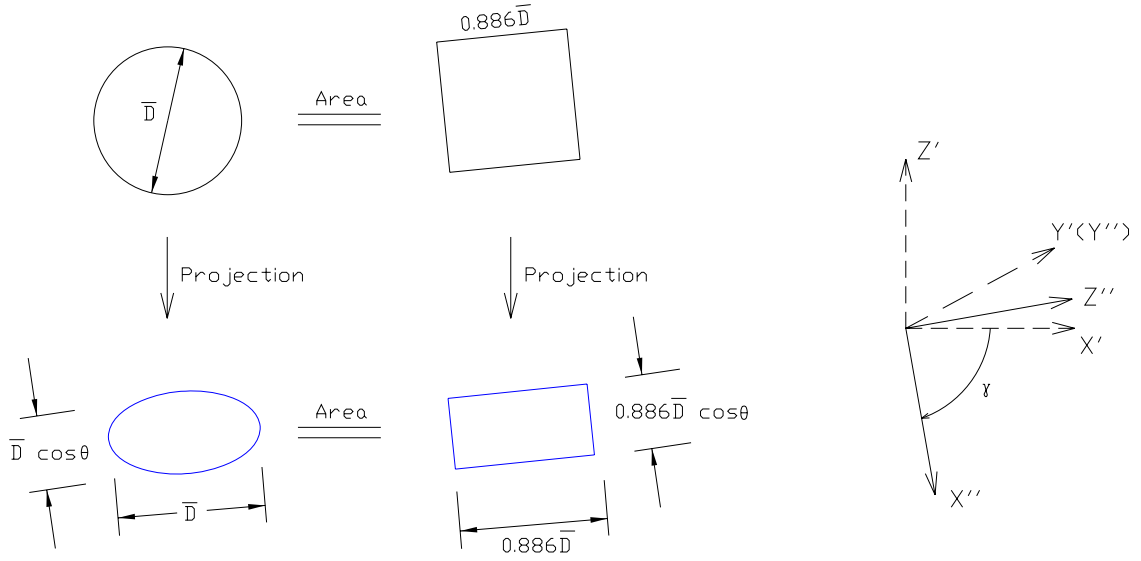

Figure 3.14 Sketch of scanline spacing determination and system rotation

Let α and β be the azimuth and plunge of the fracture normal. Let α_t be the trend of the tunnel axis (assumed horizontal). Then the direction cosines of the fracture normal in the $X'\text{-}Y'\text{-}Z'$ system can be expressed as:

$$\left\{n_{x'}, n_{y'}, n_{z'}\right\} = \left\{\cos\beta \cdot \sin\left(\alpha - \alpha_t\right), \cos\beta \cdot \cos\left(\alpha - \alpha_t\right), -\sin\beta\right\} \tag{3.62}$$

The rotation angle γ from $X'\text{-}Y'\text{-}Z'$ to the simulation grid coordinate system $X''\text{-}Y''\text{-}Z''$ (Figure 3.14) can be determined by:

$$\gamma = arc\tan\left(\frac{n_{z'}}{n_{x'}}\right) = arc\tan\left(-\frac{\tan\beta}{\sin\left(\alpha - \alpha_t\right)}\right) \tag{3.63}$$

Here, a negative value denotes clockwise rotation and a positive value denotes anti-clockwise rotation). Recall that angle θ is the angle between fracture normal and the tunnel axis. When a fracture projects onto the tunnel cross-section plane, the minor axis of the ellipse is equal to the diameter of the fracture times $\cos\theta$. From Eq.(3.61),

Simulation scanlines are located with the regular spacing in X'' and Z'' directions: $l_{x''} = \overline{L_{x''}} / C_{P2} = 0.866\bar{D} \cdot \cos\theta / C_{P2}$ and $l_{z''} = \overline{L_{z''}} / C_{P2} = 0.866\bar{D} / C_{P2}$ ($\bar{D}$ is the average fracture diameter). In the Y'' direction, they are subdivided into intervals of length b (Section 3.2.2.1.1). The whole simulation grid can be seen in Figure 3.15.

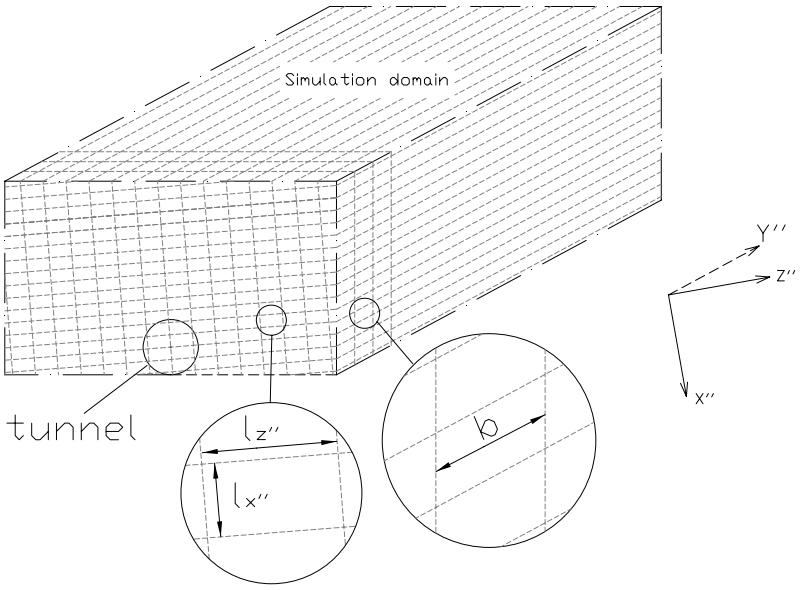

Figure 3.15 Simulation grid in 3D fracture simulation

3.2.2.2 Insert the observed scanlines in the simulation grid and obtain observed fracture intensities.

3.2.2.3 Count all observed fractures n_p in each cell that intersects on observed scanlines and calculate the fracture intensity ($Z_p = n_p / b$) in each cell. Notice that here the fracture number is divided by b, the width of the cell. However, it is valid when observation scanlines have the same direction as the simulation scanline. If they have a different direction, the fracture intensity needs to be converted into the simulation scanline direction, because the P10 measure is orientation-dependent (Section 1.3.5). Later simulated results are intensities along the simulation scanlines, not the observation scanlines.

3.2.2.4 Determine SIS cutoff values for fracture intensity (Section 3.1.1.5.5), compute the semi-variograms for each threshold in the X' and Y' directions for the two-dimensional case (in X'', Y'' and Z'' directions for the 3D case) by using GAM.exe (Deutsch and Journel, 1998), and fit the experimental points using appropriate models (Section 3.1.1.3).

3.2.2.5 Simulate the fracture intensity using the sequential indicator simulation (SIS) by using SISIM.exe (Deutsch and Journel, 1998) as detailed in Section 3.1.1.5.5. During the simulation, the observed data are kept in the simulated domain as conditional data in order to make the simulation results as close to the reality as possible.

3.2.3 SAMPLE FRACTURE PROPERTIES AND LOCATE FRACTURES IN EACH CELL

Simulate the fracture properties (aperture or diameter, and orientation) by using Monte Carlo sampling from aperture (or diameter) distribution and orientation distribution. Compute the diameter (or aperture) according to sampled aperture (or diameter) value and trace length - aperture relationship. Then Poisson locate each fracture in each cell. A sketch of this algorithm can be seen in Figure 3.16.

If the trace length-aperture relationship is experiential, it may be used for the first estimation of aperture (or diameter), and the parameters of this relationship could be calibrated by comparing the simulated flow results with the measured flow data.

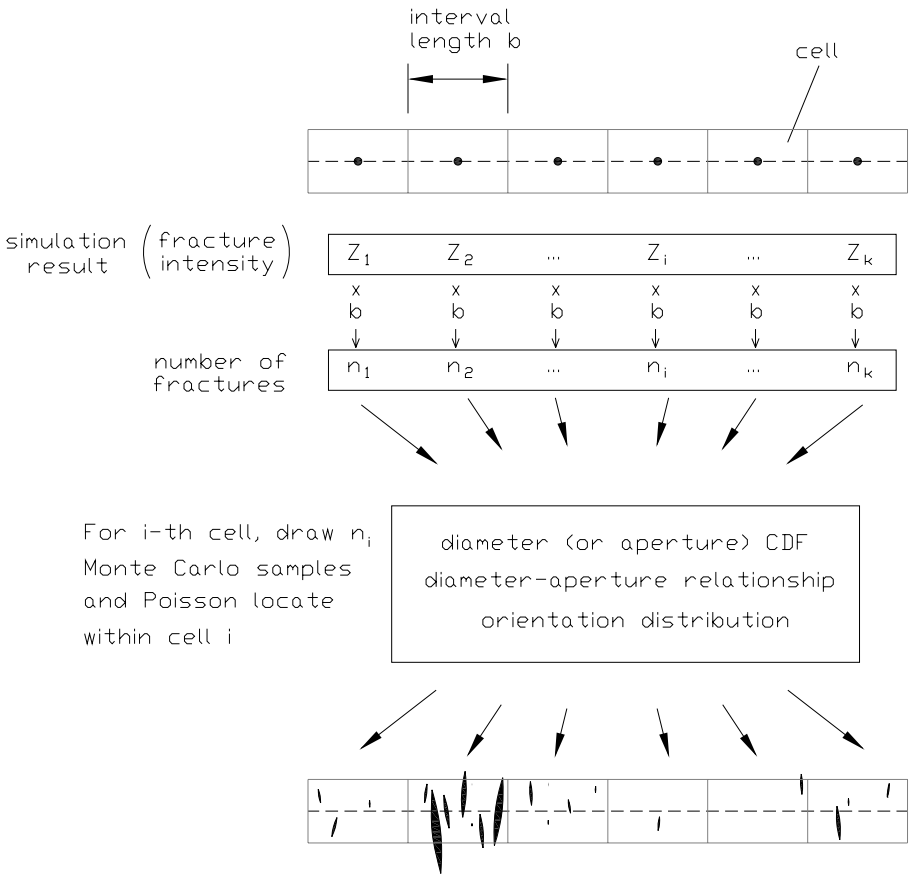

Figure 3.16 Sketch of Monte Carlo sampling for fracture properties

3.2.4 REPEAT STEP 2 AND 3 FOR ALL OTHER SETS OF FRACTURES

3.2.5 ASSEMBLE ALL FRACTURE SETS TOGETHER

A fracture network is generated by using the algorithm presented in Chapter 4.

3.3 Case study

In this section, two case studies are given to show the application of the simulation method described in Section 3.2. One case deals with fracture simulation in a two-dimensional domain based on only one scanline observation where fracture intensity and aperture were collected. The other case study deals with fracture simulation in a two-dimensional domain based on two scanline observations where fracture intensity and trace length were observed.

3.3.1 PEDERNALES FALLS STATE PARK FRACTURE SET

3.3.1.1 Fracture intensity simulation and aperture sampling

The author uses the data set from a scanline perpendicular to calcite-filled veins in the Marble Falls Limestone at Pedernales Falls State Park, Texas (Gomez and Marrett, in review). The data set represents 916 fractures along 59m of a layer-parallel outcrop. All data can be found in Appendix H-1.

A fracture intensity spatial pattern will be simulated in a 100m x 100m two-dimensional domain.

The whole scanline is subdivided into 59 one-meter intervals (b = 1m). For each interval, the number of fractures, n_p, is recorded (intensity = number/1m). The intensities along the scanline can be seen in Figure 3.17 (data can be found in Appendix H-2).

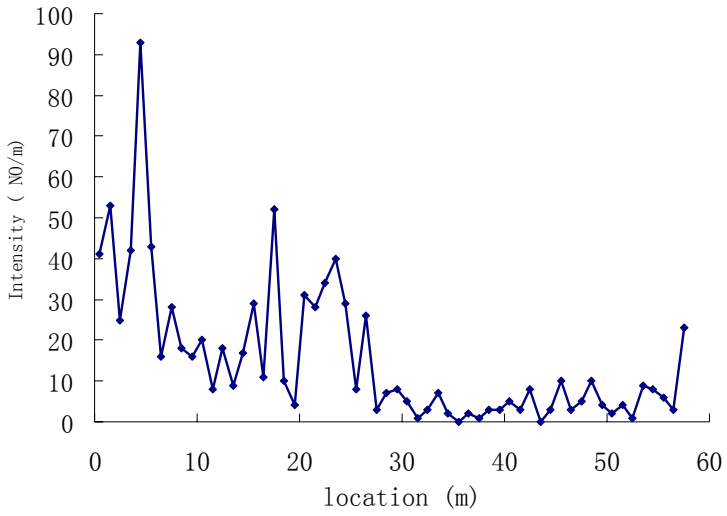

Figure 3.17 Intensity distribution along the scanline

I recommend that the intensity thresholds equally subdivide the intensity CDF. Based on my experience, this strategy can reproduce simulation results and spatial pattern closer to reality (input). Also, any important value (for example, a censoring value for aperture) should be selected as threshold because these values will control the eventual physical phenomenon. In this case study, five intensity thresholds are picked as 3, 5, 8, 15 and 30 fractures/m. For example, 3 fractures/m is at 16 percent, 5 fractures/m are at 35 percent, 8 fractures/m are at 45 percent, 15 fractures/m are at 64 percent, and 30 fractures/m are at 85 percent. Based on these 59 intensity data, the experimental indicator semivariograms are calculated using the routine GAM.exe in GSLIB (1998) and fit by spherical models with different nugget effect values for different thresholds as shown in Figure 3.18 and Table 3.2 (data can be found in Appendix H-3).

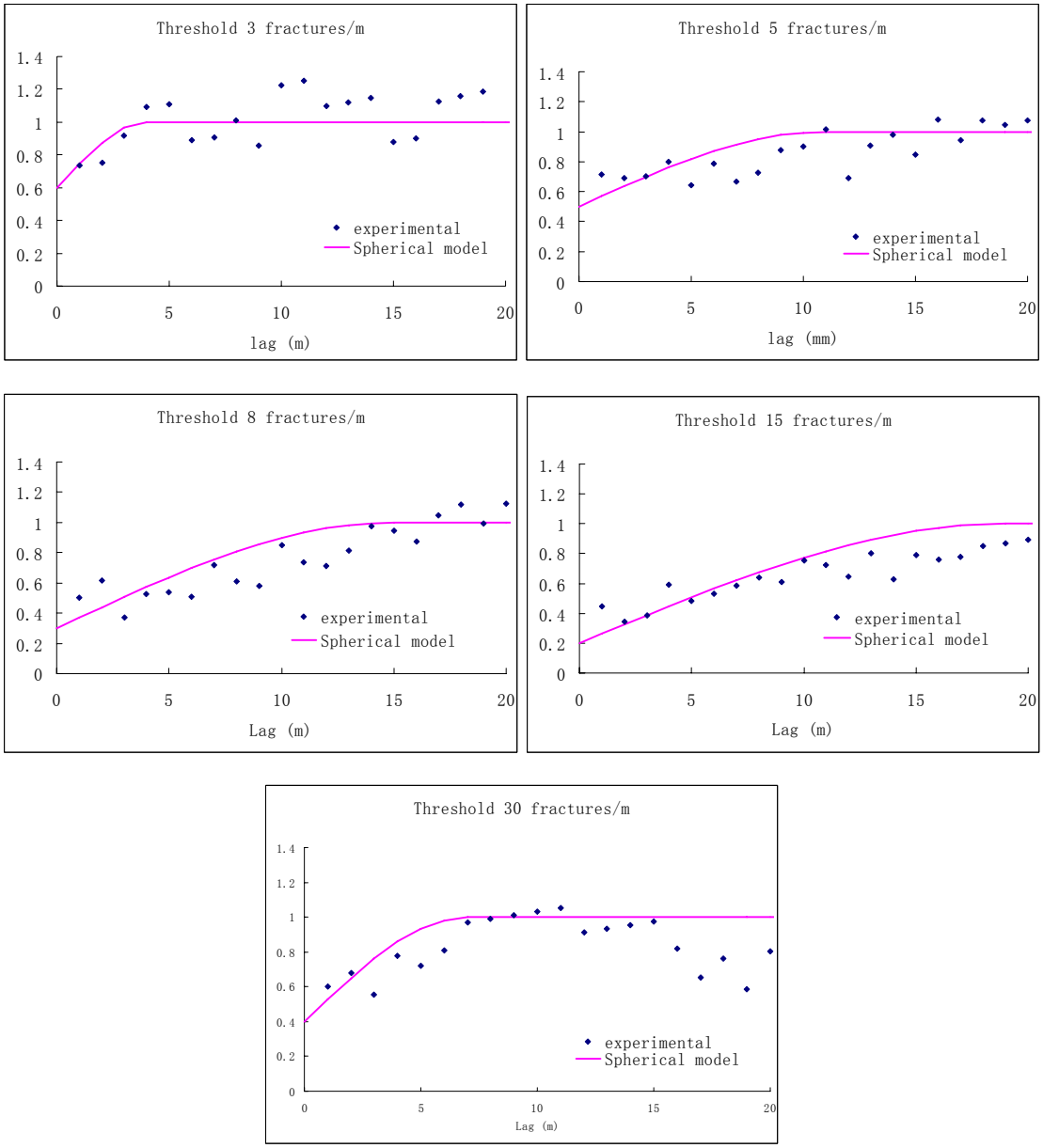

Figure 3.18 Experimental indicator semi-variograms and corresponding models in the scanline direction

Table 3.2 Parameters for indicator semivariogram models

Thresholds	Minor Range (m)	Major Rang (m)	Nugget Effect	CDF
3 fractures/m	4	100	0.6	0.155
5 fractures/m	11	100	0.5	0.345
8 fractures/m	15	100	0.3	0.448
15 fractures/m	19	100	0.2	0.638
30 fractures/m	7	100	0.4	0.845

In this case study, a 100m x 100m two-dimensional domain will be simulated. The average fracture length is assumed to be 1m and scanlines are perpendicular to fractures, which means the cell size can be set as 1m x 1m (Section 3.2.2.1.1). The direction of the *x*-axis is the normal direction of the fractures, and also the direction of the minor ranges (Section 3.1.3.3) for all indicator semivariogram models. The conditional (observed) data start from the origin in the first row (y=0) and occupy the first 59m. Based on the geological evidence that fractures tend to propagate much longer in the plane of the fracture than normal to it, the major ranges (Section 3.1.3.3) for all thresholds are set as the dimension of the simulated domain (100m). Since the minimum and maximum observed intensities are 0 and 93 fractures per meter, respectively, the minimum and maximum simulated data values are set as 0 and 100 fractures per meter in this simulation.

Once the intensity (i.e., the number of fractures) is simulated in each cell, fractures can be Poisson located in each cell.

The aperture of each fracture can be sampled from the probability distribution of its population. Based on the observed fracture data along the scanline, the aperture distribution follows a power-law of the kind:

$$f = kb_i^a \ or \ \log(f) = a\left(\log b_i\right) + \log k \tag{3.64}$$

The frequency is computed as

$$f = n / L\,, \tag{3.65}$$

where n is the number of fractures whose apertures are larger than b_i (mm) and L is the total length of scanline (mm).

Combining Eqs.(3.64) and (3.65), the cumulative distribution function (CDF) is obtained as:

$$F\left(b_i\right) = 1 - \frac{n}{N} = 1 - \frac{fL}{N} = 1 - \frac{kb_i^a L}{N}, \tag{3.66}$$

where N is the total number of fractures along the scanline.

In this case study, k=0.000786, a=-1.148904, L=59020mm, and N=916. The minimum value of aperture measured is 0.05mm while the largest is 18.0mm. The aperture distribution (power-law) and its CDF are shown in Figure 3.19.

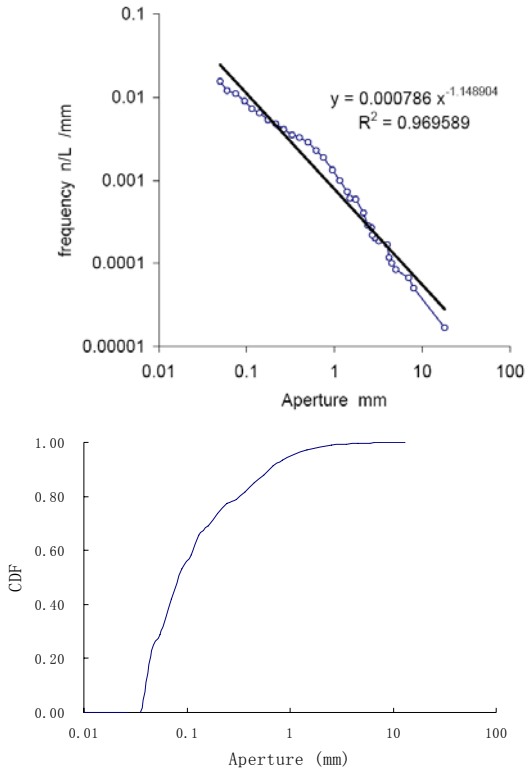

Figure 3.19 Aperture power-law distribution and its CDF

In this case study, after the fracture intensity simulation, only aperture is sampled from its CDF by using Monte Carlo sampling to verify that the sampling strategy can reproduce the phenomenon that the larger fractures tend to occur in the more intense fracture zone. Additionally, in this case study, the maximum aperture is set as 30mm to avoid sampling unreasonably large aperture values because of the power expression for the aperture distribution.

3.3.1.2 Results

Based on the parameters in Table 3.2 for the indicator semi-variogram models, the simulation is implemented by using the routine "SISIM.exe" in GSLIB (1998). One simulated realization of the intensity distribution in a 100m x 100m domain is shown in Figure 3.20. Each cell in Figure 3.20 represents a 1m x 1m square. The number of fractures/cell has been given a different color: the light color zones indicate highly fractured zones, whereas dark blue zones indicate the continuously intact rock. Since fractures are assumed to propagate in the *y*-direction, from a geological point of view, it is easier to develop continuous fracture zones in the *y*-direction than in the *x*-direction.

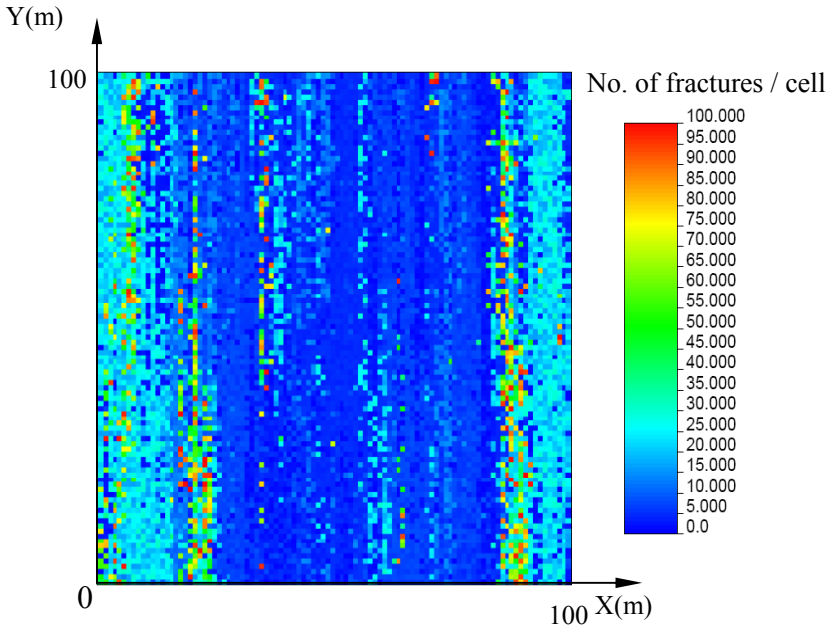

Figure 3.20 Simulated intensity distribution in the 100m x 100m domain

3.3.1.3 Comparison studies

As shown in Figure 3.21, a 100m-long control scanline in the simulated domain is randomly picked normal to the fracture plane. It is subdivided into 1-meter intervals, which are the same as the original data set. The intensity and the maximum aperture in each interval along this scanline are computed based on the simulated fractures encountered along this control scanline. Indicator semivariograms of the intensity for

several thresholds were computed together with intensity-maximum aperture relationship and aperture CDF. All these simulated results are compared with the original data, as shown in Figure 3.22, Figure 3.23, Figure 3.24, and Table 3.3. From this comparison, we can find that semivariograms are well reproduced, although there is a slight deviation from the input models, which is typical of any simulation. The intensity-max aperture relationship and the aperture power-law distribution are well reproduced as well, and confirm that large aperture fractures are likely to be located in fracture clusters.

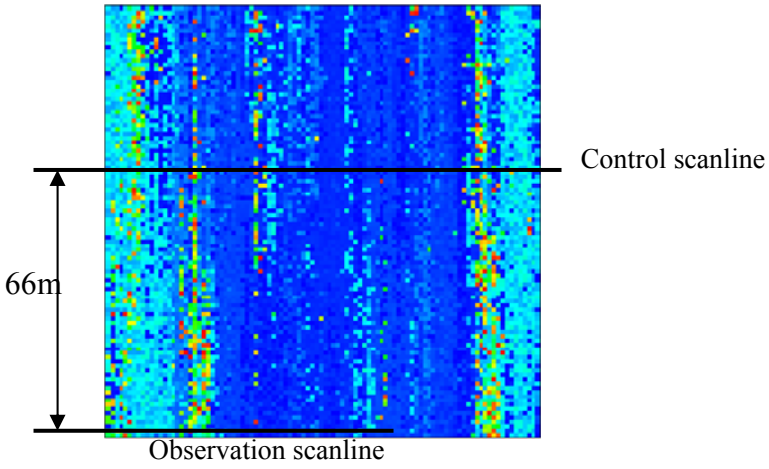

Figure 3.21 Scanline at a random simulated location and original data scanline

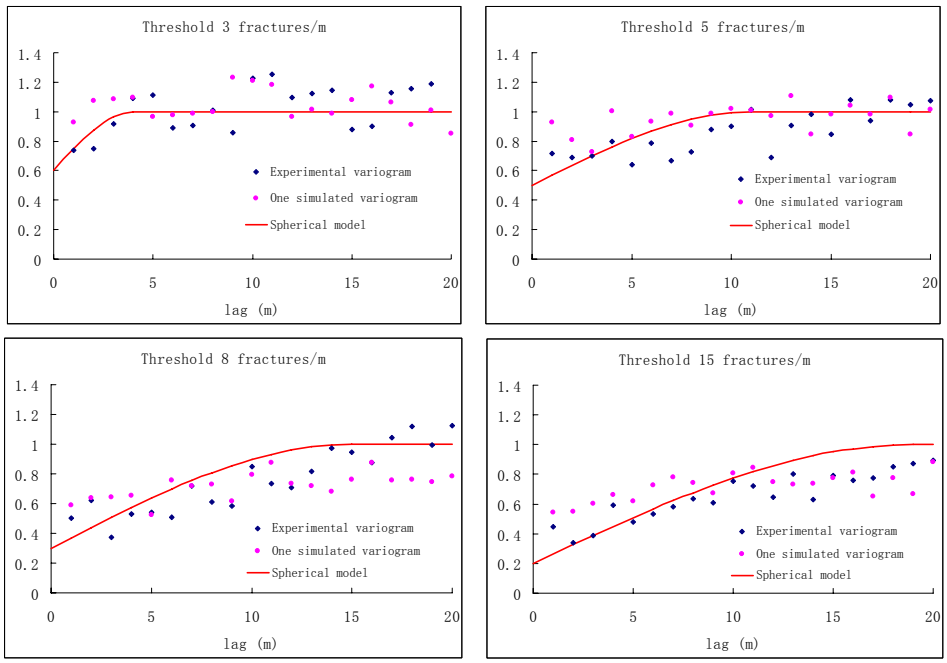

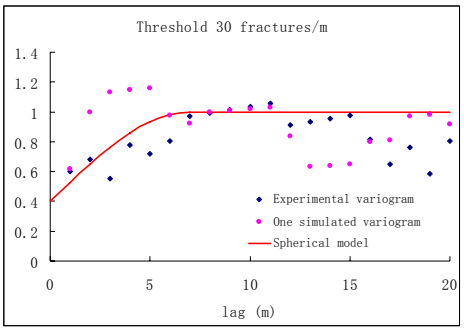

Figure 3.22 Experimental, simulated and modeled semi-variograms in the x-direction

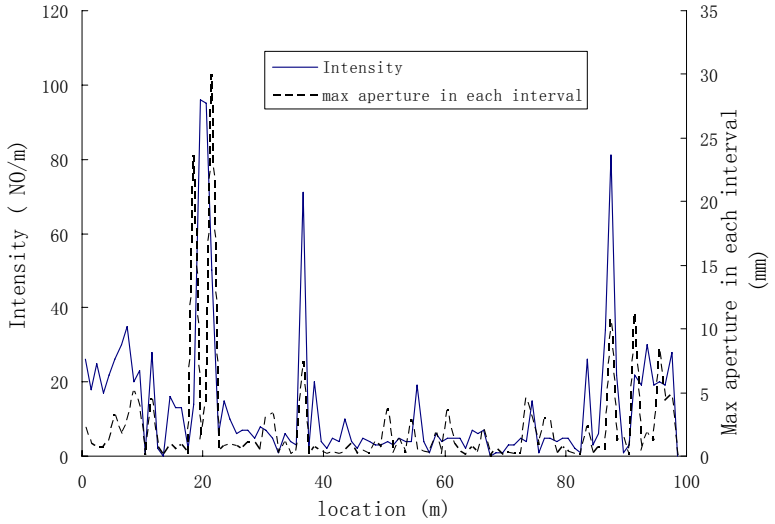

Figure 3.23 Simulated intensity-max aperture relation

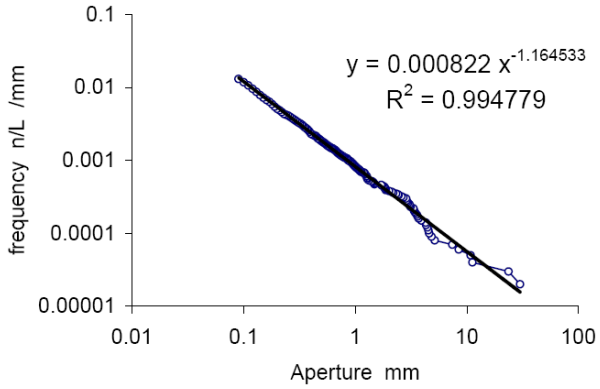

Figure 3.24 Simulated aperture CDF(original data in Figure 3.19)

Table 3.3 Comparison between Original and Simulated Data Sets

Data Set	Scanline Length (m)	Fracture NO.	Max Aperture (mm)	Min Aperture (mm)	Aperture Distribution Para.
Original	59	916	18	0.05	k = 0.000786 a = -1.149
Simulated	100	1303	30	0.09	k = 0.000822 a = -1.165

It is worth mentioning that, after the trial of using Gaussian sequential simulation, the author found that the simulation result could not reproduce the original semi-variogram model, which indicates that for the skewed distribution random function (like fracture intensity), the indicator sequential simulation is better than the Gaussian sequential simulation. The procedure of the trial is described as follows.

1) Normal score transform the original data (in Appendix H-2) by using transformation routine NSCORE.EXE (Deutsch and Journel, 1998);

2) Analyze the transformed data to get semi-variogram and fit with a model;

3) Run Gaussian sequential simulation in the simulation domain (Section 3.3.1.1) by using routine SGSIM.EXE (Deutsch and Journel, 1998) conditioned with the transformed data; and

4) Normal score back transform the simulation results by using BACKTR.EXE (Deutsch and Journel, 1998).

As shown in Figure 3.25, the semi-variogram of the final simulation results cannot reproduce the input model very well. Actually, this situation is even worse if the original data is more skewed. For example, in the real tunnel case study (Section 5.2), for fracture Set 1, 86.7 percent intensities are 0s (Table 5.14). The spatial correlation is likely to be lost when the simulation results (normal sorces) are transformed back to the original distribution. The spatial correlation of the simulated result is weaker than the model when the lag is less than around 10m, and stronger when the lag is greater than 10m. The range of the simulated results is longer than the model.

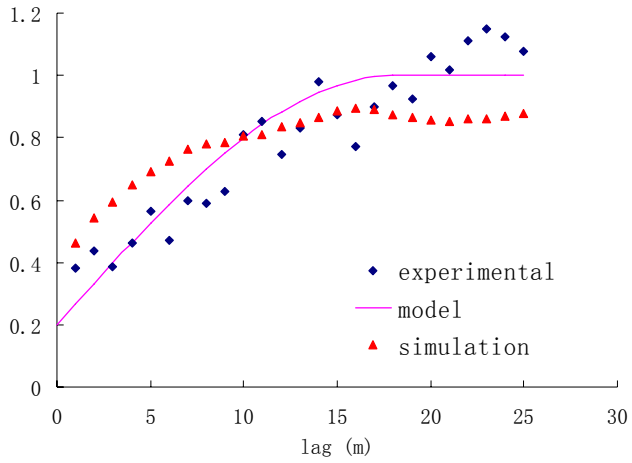

Figure 3.25 Experimental, simulated and modeled semi-variograms in the x-direction (Gaussian sequential simulation)

3.3.1.4 Summary

Fracture spatial arrangement has been simulated by using the conditional sequential indicator simulation based on observation fracture data. The following conclusions can be drawn:

1) The fracture intensity in each cell along a scanline could be studied as a simulation variable instead of the fracture aperture itself because fractures are commonly distributed in a clustered pattern.

2) Sequential Gaussian Simulation (SGS) is a common technique to implement simulation. However, because SGS needs the assumption of multi-variate Gaussianity and reproduces only the normal score variogram instead of the original one in skewed data cases, Sequential Indicator Simulation (SIS) is a better technique in this case.

3) Larger fractures tend to occur in the more intense fracture zones. Monte Carlo sampling could be used to reproduce this property because the CDF of the aperture is very steep in the small aperture range and very flat in the large aperture range.

4) If fractures in each cell are just randomly located during the simulation, the spatial correlation between fractures in each cell is not reproduced, but there is no effect on the global spatial arrangement, and in turn on the fluid flow in the medium.

5) To the contrary, clustering is an important property of rock fractures. The precision of simulating flow and transport in fractured media largely depends on the representation of this clustering property, which could be well reproduced with the proposed algorithm.

3.3.2 BARTON AND LARSON (1985) TRACE MAP FROM PA100 AT YUCCA MOUNTAIN

3.3.2.1 Fracture intensity simulation and length sampling

This case study uses a published two-dimensional dataset comprising mapped fractures from the Yucca Mountain nuclear waste disposal project mapped by Barton and described by Barton and Larson (1985). As shown in Figure 3.26, this data set represents a fracture-trace map of pavement PA100 with 214 m^2 area. A straight-segment idealization of the trace pattern is shown in Figure 3.27.

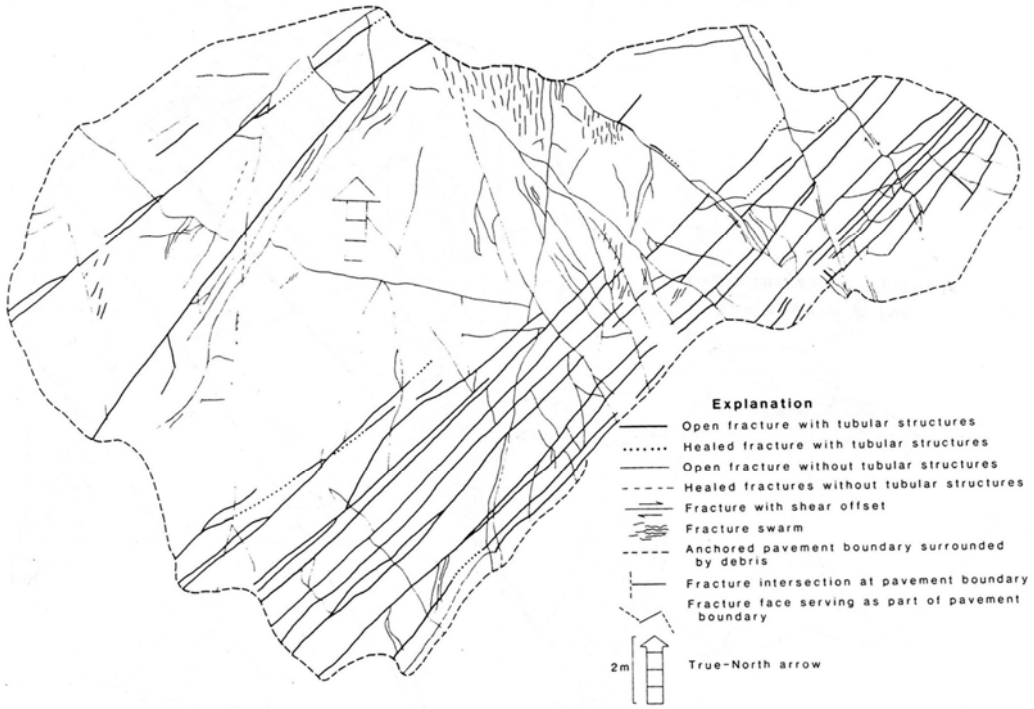

Figure 3.26 Fracture trace map of PA 100 at Yucca Mountain (From Barton and Larson, 1985)

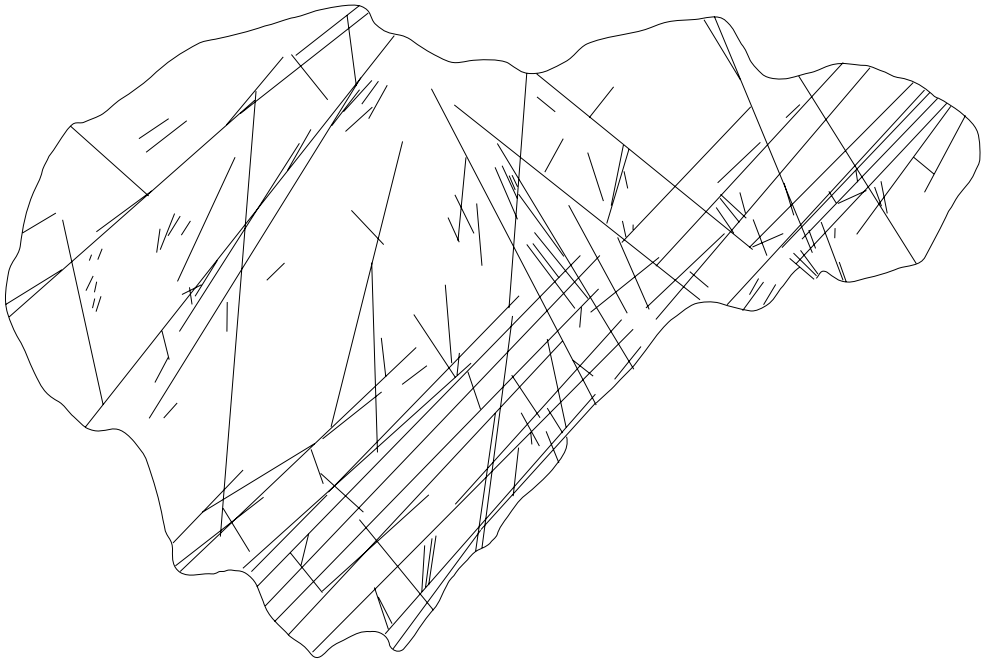

Figure 3.27 Digitized fracture trace map of PA 100

As shown in Figure 3.28, the author ploted the rose diagram for all fractures, in which Sets 1 and 2 are major fracture sets. In this case study, Set 1 will be simulated. Only fractures that belong to set 1 are shown in Figure 3.29.

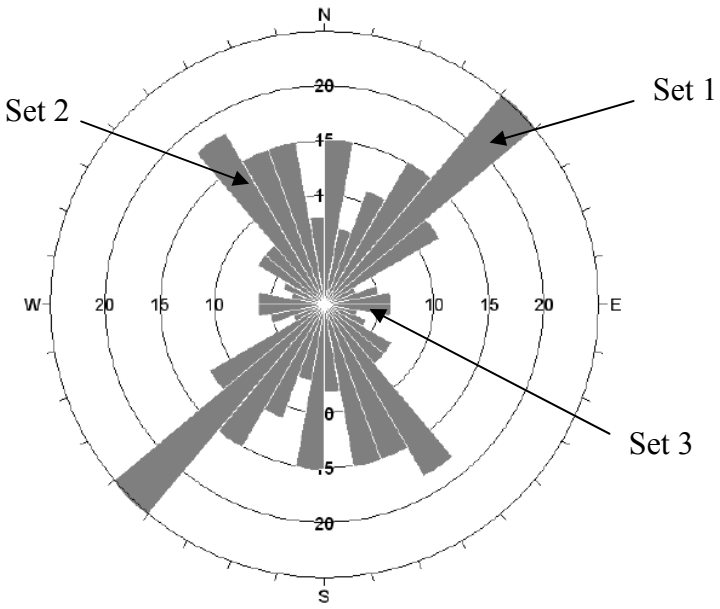

Figure 3.28 Rose diagram for all fractures in PA100 map

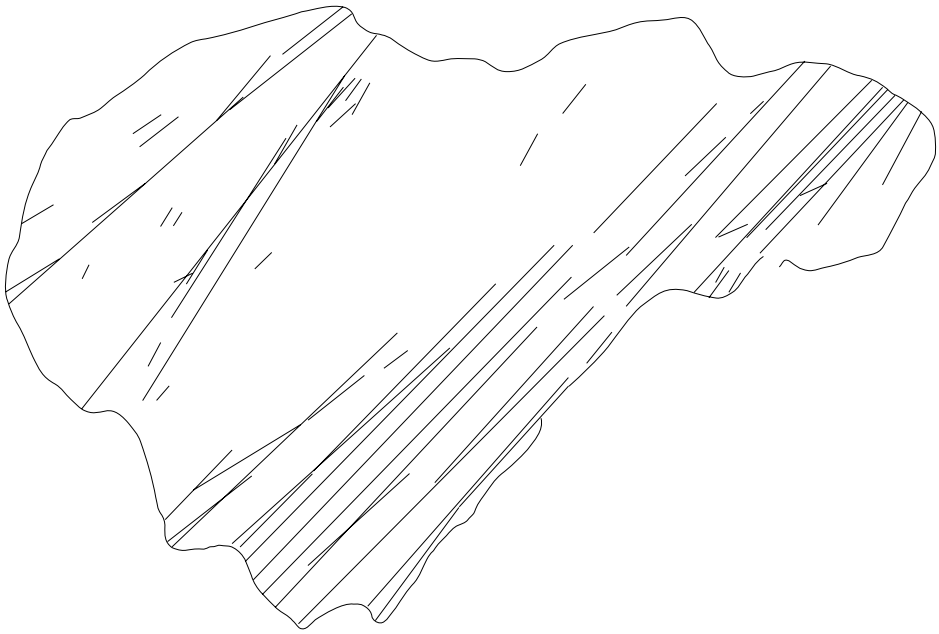

Figure 3.29 Fracture set 1 trace map

By sampling all fracture length and orientation in Figure 3.29, correcting sampling bias and analyzing the data set, the author found that the trace length follows a negative exponential distribution (Figure 3.30) and the orientation follows a normal

distribution (Figure 3.31). The average trance length is 4.66m. In Figure 3.31, the orientation is defined by the angle clockwise from North to fracture trace.

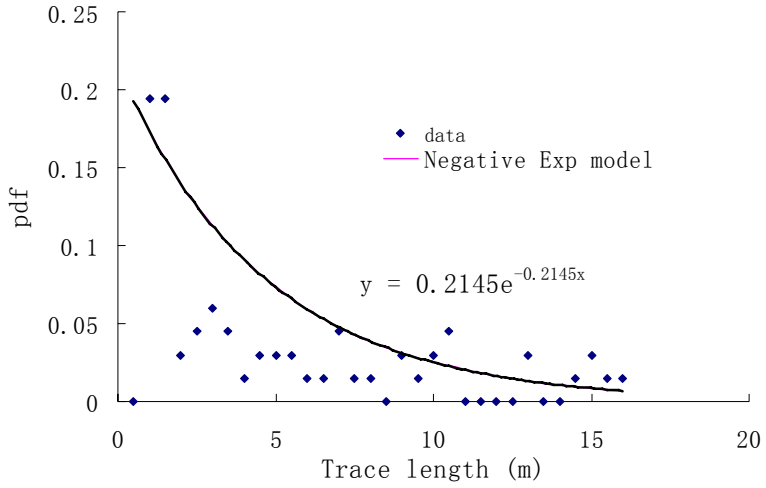

Figure 3.30 Trace length distribution and fitting model

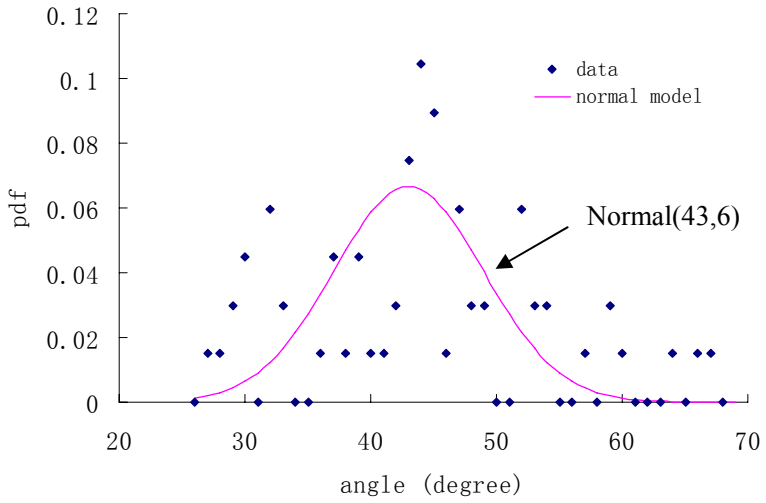

Figure 3.31 Orientation distribution and fitting model

If we draw simulation scanlines perpendicular to the fracture average direction (43 degree azimuth), the simulation scanline spacing can be selected as the average trace length 4.66m (Section 3.2.2.1.1). Here the cell width b is selected as 2.5m. The simulation grid is set as shown in Figure 3.32.

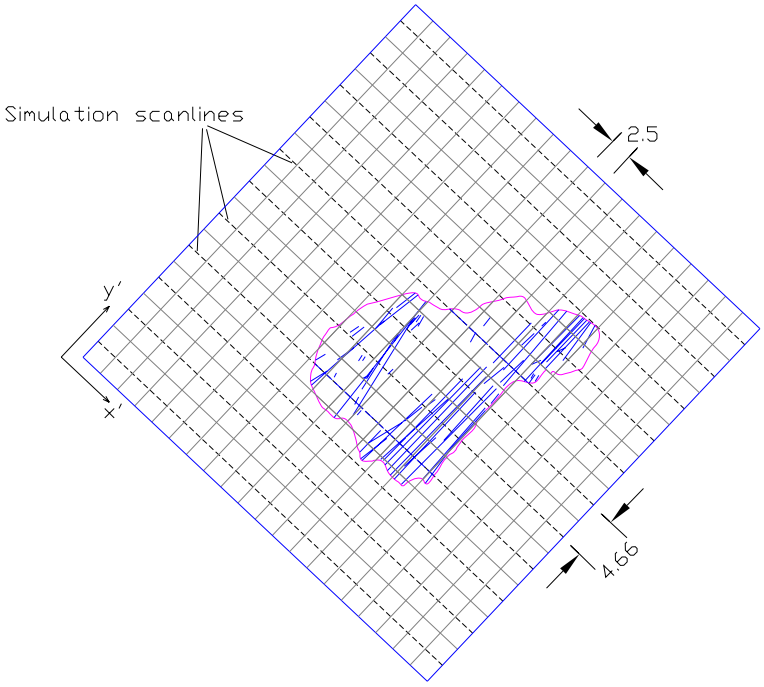

Figure 3.32 Simulation grid (50mX51m)

In order to get fracture intensity data, two scanlines are drawn on the PA100 domain. For convenience, these two scanlines match the simulation grid (Figure 3.33), although it is not necessary to do so.

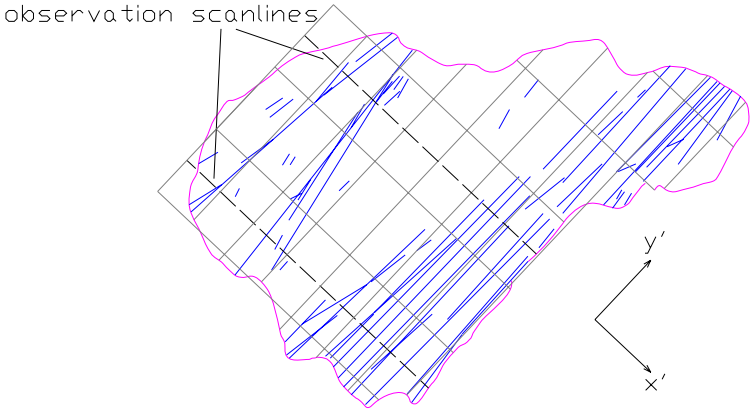

Figure 3.33 Observation scanlines

The observed intensities are shown in Table 3.4. Its CDF is shown in Figure 3.34.

Table 3.4 Observed fracture intensity (No. / 2.5 m)

Location (m)	1.25	3.75	6.25	8.76	11.25	13.75	16.25
Scanline 1	2	0	3	0	2	5	4
Scanline 2	0	2	2	0	0	4	3

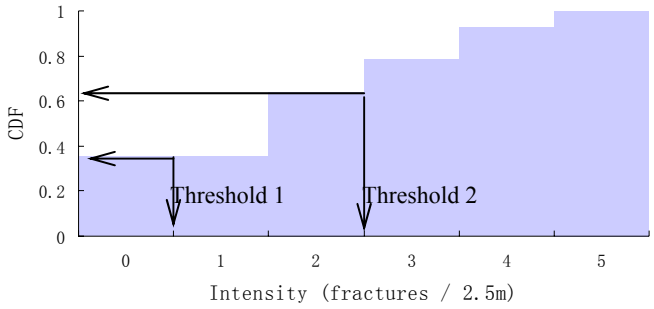

Figure 3.34 Observed intensity CDF

From Table 3.4 and Figure 3.34, because 35.7 percent of the data are less than 0.5 (0s) and 64.3 percent of the data are less than 2.5 (0s and 2s), two intensity thresholds (equally divide intensity CDF) are picked as 0.5 and 2.5 fractures/2.5m. This is similar to Case study 1 (Section 3.3.1.1). Based on the observed intensity data, the experimental indicator semivariograms are calculated using the routine GAM.exe in GSLIB (1998) and fit by spherical models with different nugget effect values for different thresholds shown in Figure 3.37 and Table 3.5.

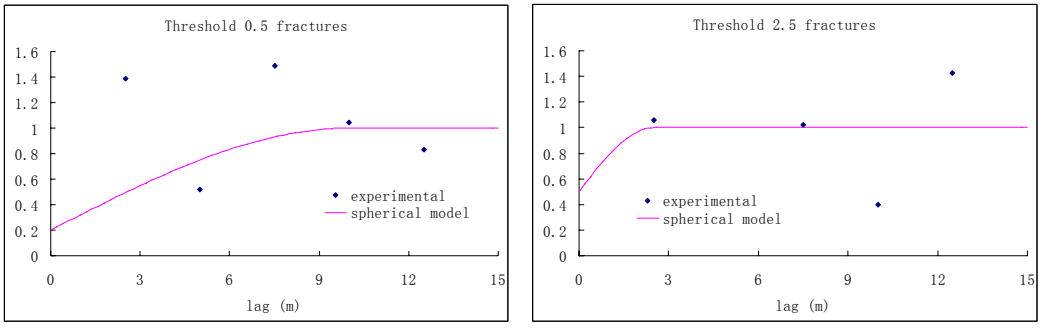

Figure 3.35 Experimental indicator semi-variograms and corresponding models

Table 3.5 Parameters for indicator semivariogram models

Thresholds	Range (m) in X'	Rang (m) in Y'	Nugget Effect	CDF
0.5 fractures/2.5m	10.0	40	0.2	0.4
2.5 fractures/2.5m	2.5	40	0.5	0.7

The conditional data are included during the simulation to improve the results. The minimum and maximum observed intensities are 0 and 5 fractures per 2.5m, so the minimum and maximum simulated data values are set as 0 and 6 fractures per 2.5m during simulation. Once the intensity for each cell is simulated, the length and orientation of each fracture can be sampled from their distributions (Figure 3.30 and Figure 3.31). There is also the other sampling strategy. Simulated variables are sampled from its experimental CDF rather than from the fitting model, if we believe all observed data can represent the population very well or no model can fit the observed data. This time, the experimental CDF for the trace length is used rather than the fitting models in Figure 3.30. The experimental CDF for the trace length is shown in Figure 3.36. Fractures are Poisson located in each cell.

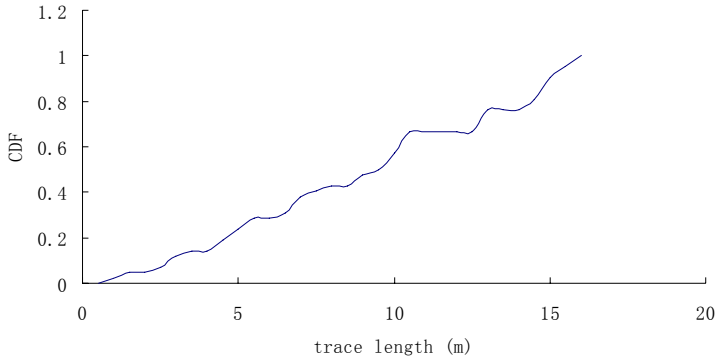

Figure 3.36 Experimental CDF for the trace length

3.3.2.2 Simulation results

Based on the parameters in Table 3.5 for the indicator semi-variogram models, the simulation is implemented by using the routine "SISIM.exe" in GSLIB (1998). One simulated realization of the intensity distribution in the simulated domain is shown in

Figure 3.37, from which we can find that the cluster pattern is well reproduced not only in the original region, but also everywhere in the domain.

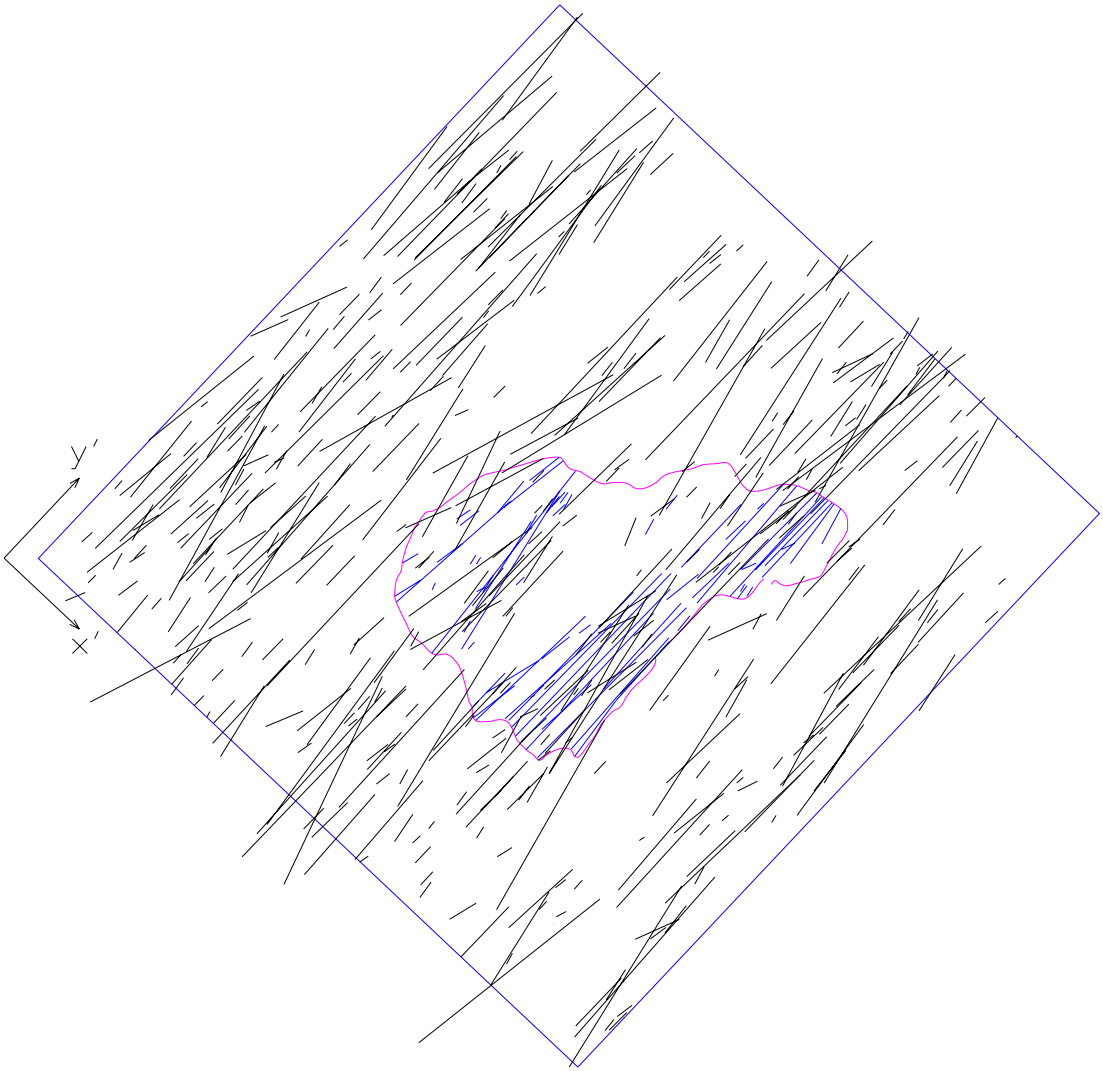

Figure 3.37 Simulated fracture distribution in the simulated domain (blue lines are original traces)

3.3.2.3 Analysis of the results

As shown in Figure 3.38, four 50m-long control scanlines in the simulated domain are randomly picked normal to the fracture plane. They are subdivided into 2.5-meter intervals, which is the same as the original data set. Indicator semi-variograms of the intensity for two thresholds (0.5 and 2.5 fractures/2.5 m) were computed. They well

reproduced the semi-variogram models, although there is a slight deviation from the input models (Figure 3.39), as in Case study 1. The length distribution is well reproduced as well, as shown in Figure 3.40.

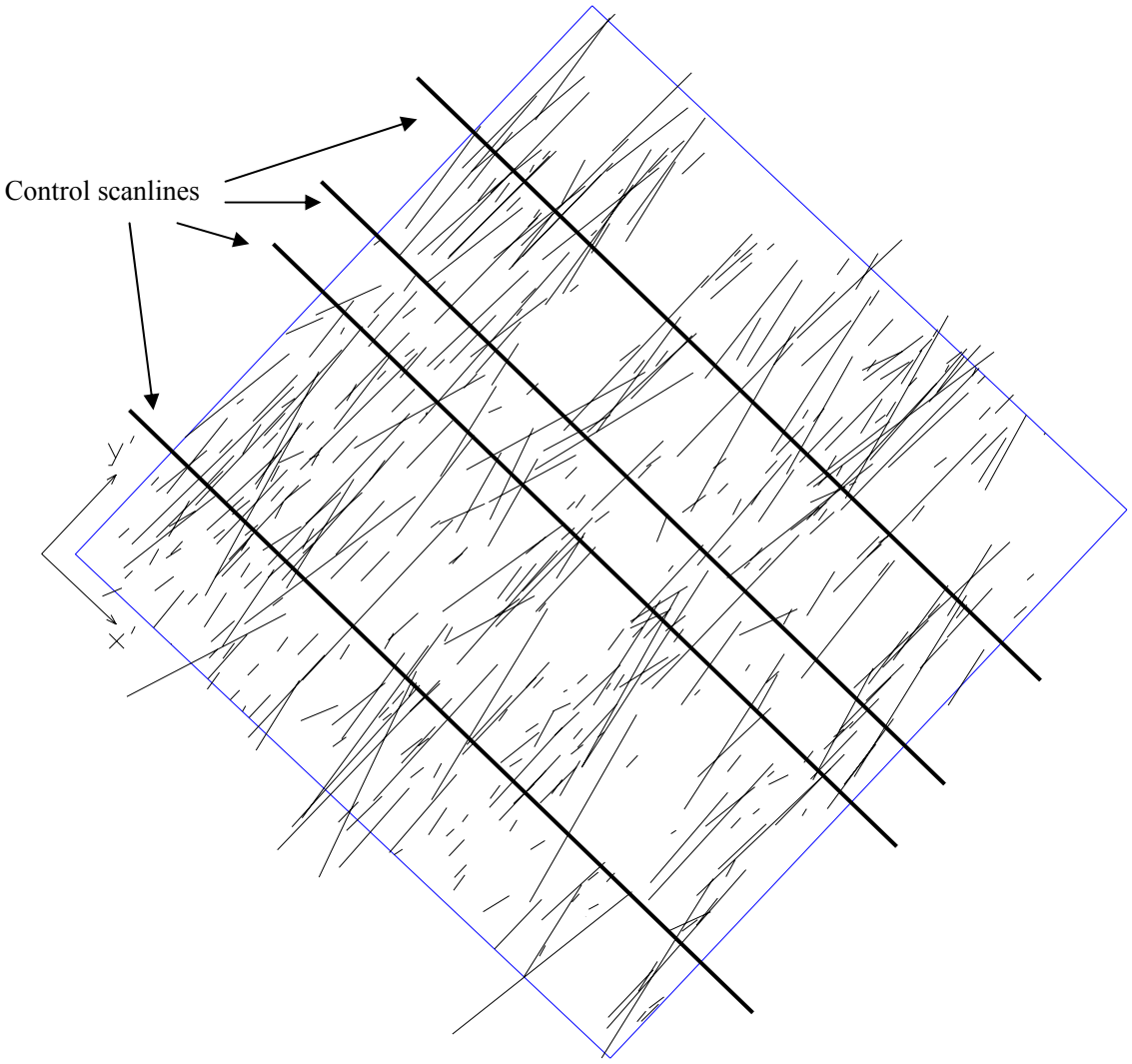

Figure 3.38 Control scanlines at a random simulated location

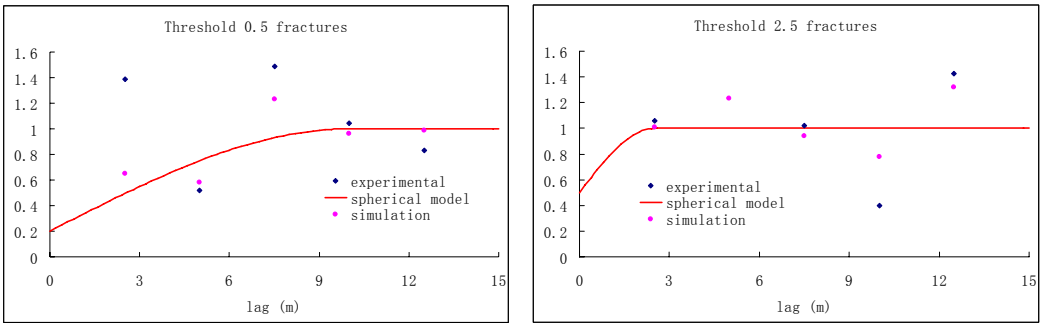

Figure 3.39 Experimental, simulated and modeled semi-variograms

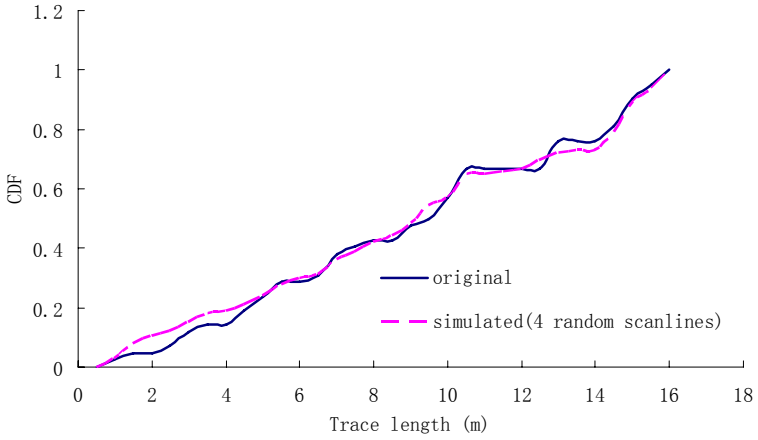

Figure 3.40 Simulated and original fracture trace length distribution

Lee et al. (1990) use the Ripley's K function (Dixon, 2002) to test the simulation results. Ripley's K function is expressed as:

$$K_{ij}(t) = \lambda_j^{-1} \cdot E[\text{number of fractures in set j within distance } t \text{ of a randomly chosen fracture in set i}], \quad (3.67)$$

where λ_j is the intensity of fracture set j, $E[.]$ is the expectation.

For an unbounded region and a homogeneous Poisson process of one event i, $K_{ii}(t) = \pi t^2$, i.e. $K_{ii}(t) - \pi t^2 = 0$. Here the Ripley's K function is used to test the simulation results for fractures of PA 100 at the Yucca Mountain. Since there is only one fracture set, i = j in Eq.(3.67). As shown in Figure 3.41, for the original fracture set,

function $K_{ii}(t)-\pi t^2$ is positive when t is less than 7m, which means that the range of the spatial correlation for the original data is around 7m, beyond which there is no spatial correlation. The average function $K_{ii}(t)-\pi t^2$ for ten simulations has almost the same range as the original one, which means that simulations reproduced the spatial arrangement well. The maximum value of function $K_{ii}(t)-\pi t^2$ for the simulations is slightly lower than the original one, because in each simulated cell, fractures are Poisson located, which causes the function $K_{ii}(t)-\pi t^2$ to slightly tend to the random case ($K_{ii}(t)-\pi t^2=0$), as shown in Figure 3.41. However, the global spatial arrangement is reproduced quite well.

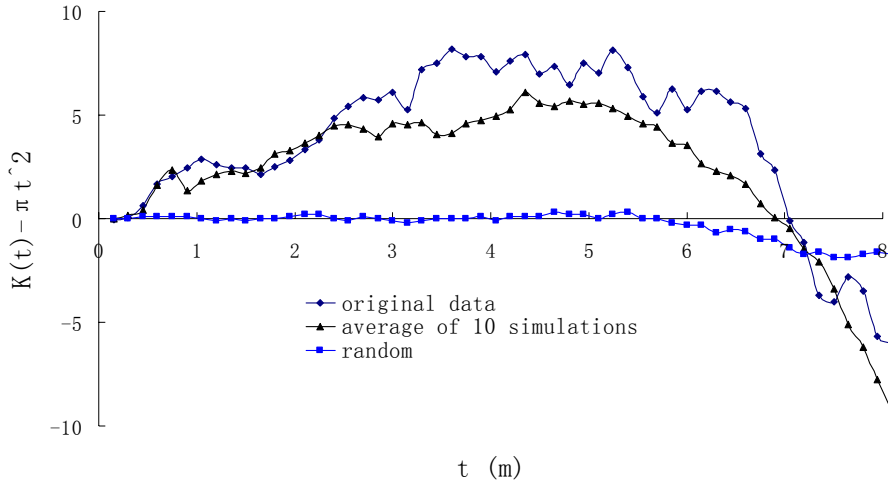

Figure 3.41 Simulated and original Ripley's K functions

CHAPTER 4: FRACTURE NETWORK GENERATION AND FLOW ANALYSIS

In this section, the fracture network is generated provided the simulated fracture sets. After the generation of the fracture network, the simplification is implemented in order to save computer storage and speed the calculation. Once the simplified fracture network is generated, water flow is simulated in the fracture network based on the work of Long et al. (1985). Some improvements are processed during the reproduction of this flow simulation. The sketch of the flow chart is shown in Figure 4.1.

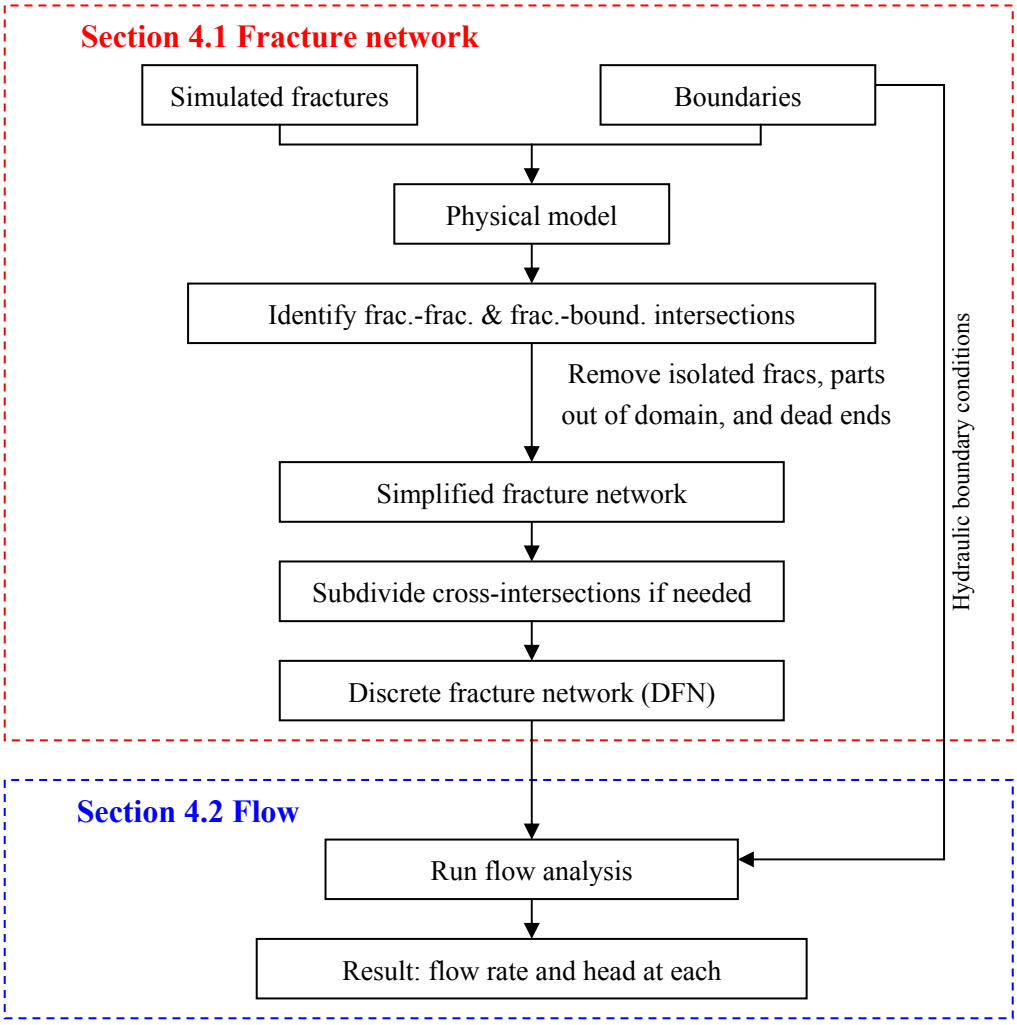

Figure 4.1 Flow chart of fracture network generation and flow analysis

4.1 Fracture network generation and post-processing

In this section, the conceptual model of fracture network is given. All the algorithms of fracture network generation are introduced, including the network simplification. A flow chart in this section is given as the follow chart (Figure 4.2).

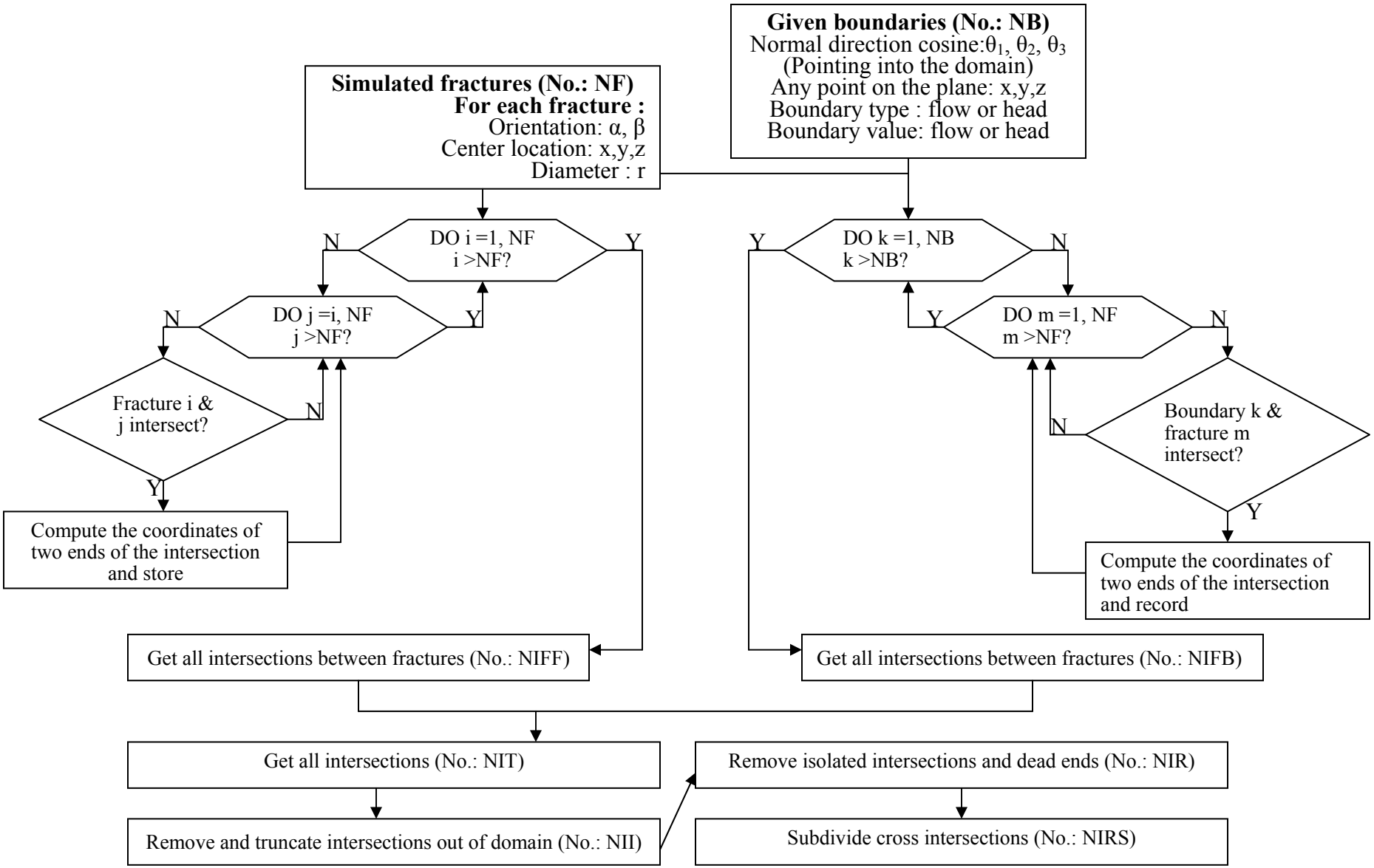

Figure 4.2 Flow chart of fracture network generation

4.1.1 FRACTURE NETWORK GENERATION

4.1.1.1 Conceptual model

Based on the analysis of trace data and examination of fracture surfaces, several studies have reported that fractures are likely to be roughly elliptical or circular (Baecher et al., 1978; Pollard, 1976). In this three-dimensional model, all fractures are assumed to be circular because the circular shape simplifies the flow calculation (Section 4.2). In Chapter 3 (fracture simulation), fractures with a disk shape are simulated, which is based on this conceptual model.

4.1.1.2 Algorithms of fracture network generation

If the fracture information (sets, location, orientation, diameter and aperture) is known or simulated, all possible intersections between any two fractures can be determined.

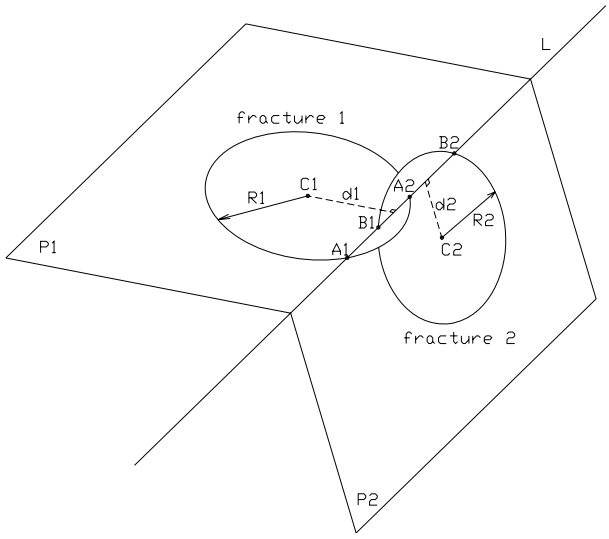

Figure 4.3 Sketch of intersection detection between two fractures

As shown in Figure 4.3, if fracture 1 is in plane 1 and fracture 2 is in plane 2, then call L the intersection of planes 1 and 2. If the distance from the center of fracture 1 to the line L – d1 is greater than its radius R1 or the distance from the center of fracture 2 to the line L – d2 is greater than its radius R2, then there is no intersection between fracture 1 and 2.

Under the condition of d1<R1 and d2<R2, if A1 (or A2, or both) is in the segment B1-B2, or B1 (or B2, or both) is in the segment A1-A2, fractures 1 and 2 must intersect with each other. Otherwise there is no intersection. The intersection could be B1A2, A1A2, B1B2, or A1B2, depending on the relationship between these four points and the length of two intersections.

As for the intersections between fracture and boundary, the sketch can be seen in Figure 4.4.

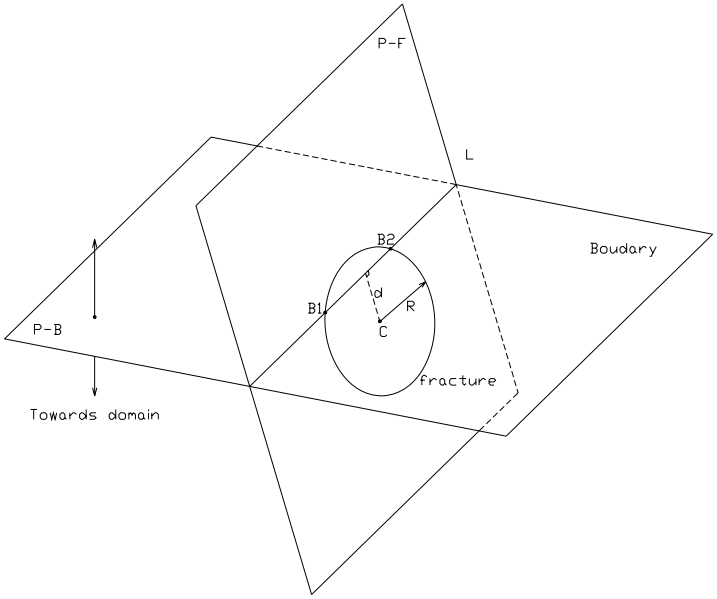

Figure 4.4 Sketch of intersection detection between a fracture and a boundary plane

If the fracture is in plane P-F and the boundary is in plane P-B, then call L the intersection of these two planes. If the distance d from the center of the fracture to the

line L is greater than the fracture radius R, then there is no intersection between the fracture and the boundary.

Based on the above two steps, all possible intersections can be obtained. The next step is to remove the fractures located outside the domain. For each possible intersection, two endpoints can be inside or outside the domain, as shown in Figure 4.5. Here only convex domains are considered because the algorithm for concave domain is more complicated, and it may be added in the future.

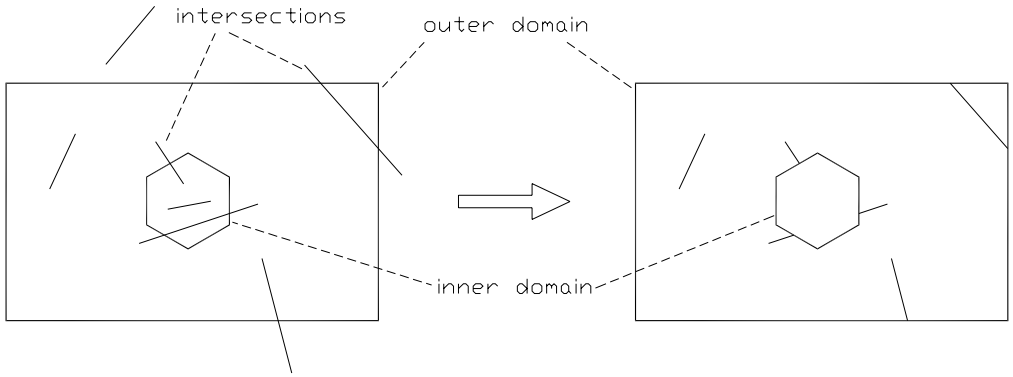

Figure 4.5 Sketch of intersection removal outside the domain

Because large numbers of fractures often are needed to represent fractured rock adequately, after the removal of fractures outside the domain and truncating the intersections out of domain, the minimization of required computer time and memory is crucial. For steady-state fow, any portion of the mesh linked to the rest of the mesh by only one point is a deadend and does not contribute to water flow. The removal of such deadend clusters simplifies the mesh and therefore speeds up computation, without changing its response. An algorithm for removing these dead ends is described by Billaux and Fuller (1989).

The last step of fracture network generation is to subdivide cross-intersections, as shown in Figure 4.6.

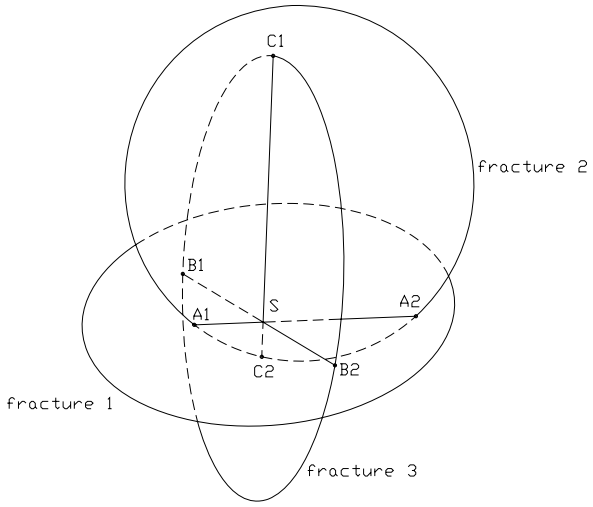

Figure 4.6 Three fractures intersect mutually

In the flow analysis (Section 4.2), the total head at each intersection is assumed to be constant, which means that the total head at the common point of three segments (point S, in Figure 4.6) may be different (A1A2, B1B2 and C1C2). In order to avoid the head discontinuity at the common point, the three segments are subdivided into six segments (A1S, A2S, B1S, B2S, C1S and C2S), as shown in Figure 4.7. More accurate flow rate and total head results should be obtained than without subdivision. Actually, further infinitesimal subdivision should lead to the exact solution. However, further subdivision would entail more computer memory and will not achieve more accurate results (Long et al., 1985). In this research, if the segment is too short, it will not be subdivided. This value can be set in the routine.

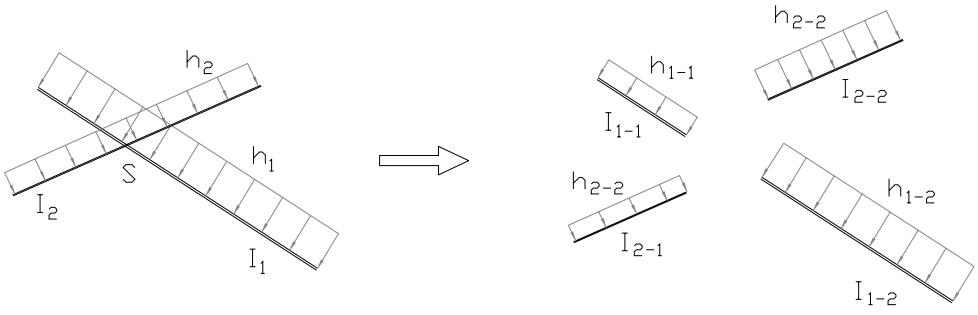

Figure 4.7 Sketch of cross-intersecion subdivision

4.2 Flow analysis

In this section, based on the work of Long et al. (1985), flow simulation is reproduced with some improvements. All theoretical background and algorithms are given in this section. Some base case studies are given to verify the algorithms and code in Section 5.1.

4.2.1 INTRODUCTION

Long et. al (1985) developed a model for steady fluid flow in three-dimensional, random networks of fractures. In this model, the fractures are disc-shaped discontinuities in an impermeable matrix. Where the disc model is appropriate, it is possible to calculate flow through fracture networks. After the boundary conditions and the desired fractures are specified, the intersections (nodes) between these discs (elements) are identified. Then steady flow through the network can be calculated using a mixed analytical-numerical technique. In each fracture, analytic equations for flow into or out of each node as a function of the average head at each node are developed. The equations are based on image theory and the assumption that each node is a source (or sink) of uniform strength. A set of mass balance equations is constructed that equate flow into a node from one of its associated fractures to flow out of the node into the other associated fracture. These equations are solved for the average head at each node, and flux between fractures can then be calculated by substituting the average head values back into the analytical equations.

I adopt Long et al.'s model in this research with at least four improvements as follows: (1) a double numerical integral is used to calculate the potential in the disc plane due to the line source, instead of the combination of a very complicated analytic expression and a single numerical integral; (2) the cross-intersections are considered

(Section 4.1.1.2); (3) the anisotropic spatial correlation of fracture intensity is considered, instead of the isotropic correlation model (Section 3.2); (4) the relationship between fracture intensity and fracture size (aperture or diameter) is taken into account (Section 3.2), instead of being simulated separately.

4.2.2 CONCEPTUAL MODEL

It is assumed that the two fracture walls are parallel and that a parallel plate model for flow is appropriate. The model cannot account directly for channeling within the fracture planes. Head loss across the intersections between fractures and flow along the intersections are assumed to be negligible.

The arrangement and size distribution of fractures in the model can be completely arbitrary. Several workers have contributed conceptual models for the arrangement of fractures in rock. La Pointe and Hudson (1981), Veneziano (1979), Baecher and Lanney (1978), and Dershowitz (1984) have developed such conceptual models. The arrangement and size distribution of fractures in the model can also follow some distributions. Long et. al (1985) use the model in which circular fractures have log-normally distributed radii and are randomly located in space.

However, fractures may be spatially correlated. The presence of one fracture may increase the likelihood of there being another of the same set close by. The author uses a new model that can reproduce this clustering property by using the knowledge of geostatistics. The details are shown in Chapter 3.

A variety of fracture orientation distributions is possible and, in general, these distributions can be determined from field data. Arnold's hemispherical normal, Bringham's, Fisher's, and uniform distributions have all been used by various authors.

A simple example of such a random fracture network is shown in Figure 4.8. In this case, three orthogonal sets of fractures have been drawn to simplify the illustration; in general, any orientation distribution is possible.

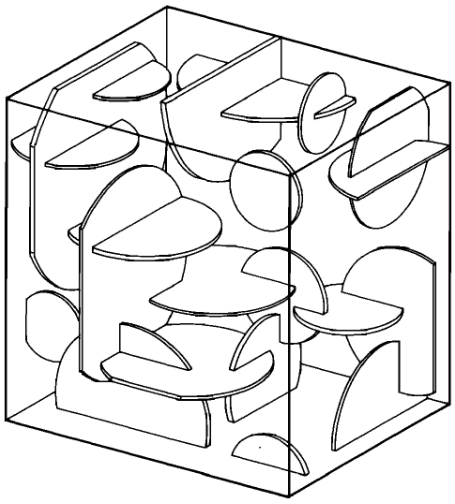

Figure 4.8 A Simple Example of the Conceptual Model (From Long et. al, 1985)

4.2.3 FLOW CHART

The flow chart of this flow model is shown as Figure 4.9.

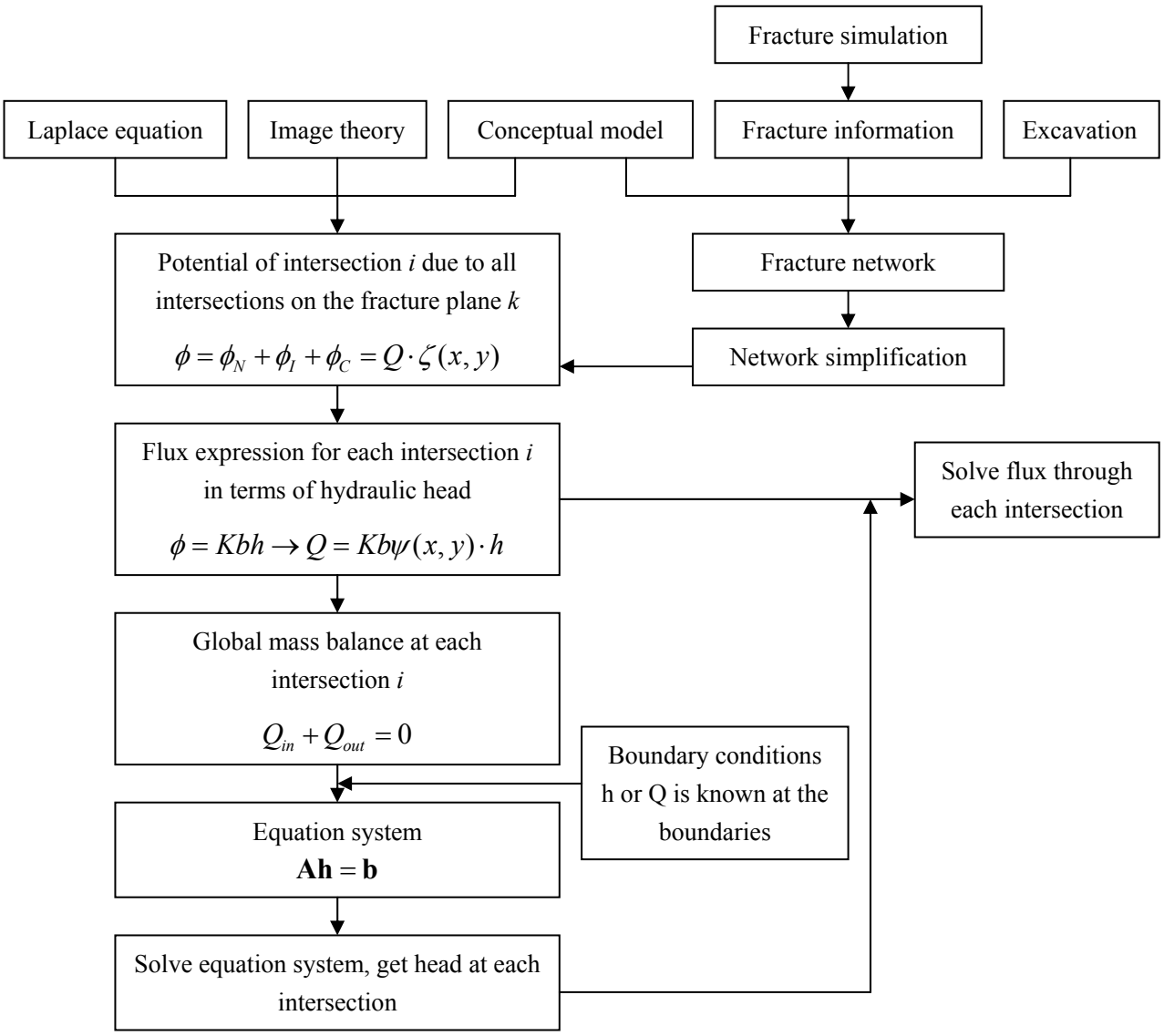

Figure 4.9 Flow Chart of the Flow Simulation

4.2.4 IMAGE THEORY APPLICATION

The solution of the problem of flow in a fracture disc uses image sources and sinks to account for the impermeable boundaries. In fact, the simplicity of the image system for a source or sink within a circle is a major advantage of assuming fractures are circular. The head distribution within a disc with impermeable boundaries containing an

arbitrary number of line sources and sinks is based on the solution for a point source within a circular flow region. Consider a disc that contains a point source of strength +m at B as shown in Figure 4.10.

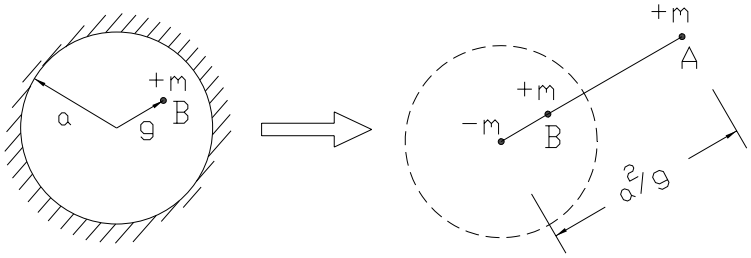

Figure 4.10 Image System for a Point Source in a Circle (After Long et. al, 1985)

For steady state conditions Milne-Thomson (1968, p.222) gives an image system that accounts for the impermeable circular boundary with radius a. If the source is located in the circle at B, which has the distance g to the disc center, then there is an image source of strength +m on the same ray at A which has the distance a^2/g to the disc center and an image sink of strength -m at the disc center. The potential at any point in the fracture can be found by accumulating the potential contributions of the source and the two images, as shown in Eq.(4.1):

$$\phi_{m@r=g\,(with\ IBC)} = \phi_{m@r=g} + \phi_{m@r=a^2/g} + \phi_{-m@center} = \phi_N + \phi_I + \phi_C \qquad (4.1)$$

where $\phi_{m@r=g\,(with\ IBC)}$ is the potential due to a source with the strength of m at location g (distance to the center) in the circular domain with the radius of a and the impervious boundary; $\phi_{m@r=g}$ or ϕ_N is the potential due to a source with the strength of m at location g (distance to the previous center) in the infinite domain; $\phi_{m@r=a^2/g}$ or ϕ_I is the potential due to a source with the strength of m at location a^2/g (distance to the previous center) in the infinite domain; $\phi_{-m@center}$ or ϕ_C is the potential due to a source with the strength of -m at the previous center in the infinite domain.

Because the total flow into the fracture equals the total flow out of the fracture, the total strength of all sources must be equal and opposite to the total strength of all sinks. Therefore, because the total strength of all required images at r=0 is always zero, the third term in Eq.(4.1) will always be zero.

We can distribute point sources along a line segment formed by the intersection of two fractures in the circle, such that the strength per unit line length is constant. Next, the locus of the distributed images needs to be found, followed by the expression for the potential at any point in the fracture disc due to the sources along the intersection and the image. A non-radial line segment source will have an arc-shaped image constructed. A radial source will have a radial segment image. Figure 4.11 shows these two cases. The equations for the locus of the arc and radial images are derived as shown in Appendix I.

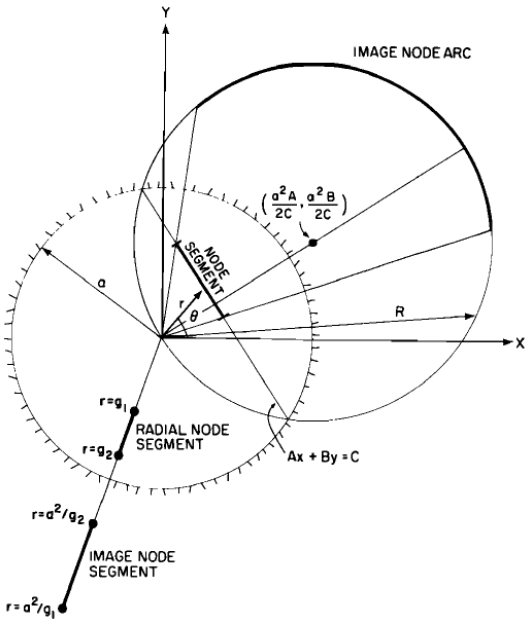

Figure 4.11 Image of a Line Segment (From Long et. al, 1985)

4.2.5 SOLUTION OF THE LAPLACE EQUATION IN EACH FRACTURE

The fundamental solution of the Laplace equation for the potential due to a point source in an infinite plane of transmissivity Kb is

$$\phi = Kbh = -\frac{Q}{2\pi}(\ln r), \tag{4.2}$$

where Q is the strength of the source, r is the distance from the source, and h is the hydraulic head. In this research, K and b are considered to be two separate parameters instead of one parameter Kb (transmissivity), although field tests typically yield transmissivity values. In this research, two parameters, K and b, are used because the aperture b of fractures can be measured in the field and simulated as described in the procedure of Section 3.2 when there is no *in situ* flow test data. For laminar flow in parallel plates, the conductivity K can also be computed by

$$K = \frac{g \cdot b^2}{12\nu}, \tag{4.3}$$

where g is the gravity acceleration, [L/T^2], ν is the kinematic viscosity of water [L^2/T], and b is the opening of two parallel plates or hydraulic aperture [L].

If point sources are distributed over a line segment in the plane of length *l*, the potential in the plane due to the line source is given by the average of Eq.(4.2) over the segment:

$$\phi_N = Kbh = -\frac{Q}{2\pi l}\int_0^l \ln r_p(\xi)\, d\xi, \tag{4.4}$$

where Q/l is the constant strength per unit line length, Q is the total strength of the line source, and r_p is the distance to any point in the plane. For each node we must specify $r_p(\xi)$ and evaluate the integral.

To find the potential contribution of the images, a similar integration is performed along the image of the node. In this case, however the strength per unit line length is not constant. For each infinitesimal length along the intersection, $d\xi$, the corresponding infinitesimal piece of image is ds. Now the strength per unit line length on the image is $(Qd\xi)/(lds)$. So the potential due to the image is given by

$$\phi_I = Kbh = -\frac{Q}{2\pi l}\int_{S_1}^{S_2} \frac{d\xi}{ds} \ln r_p(s)\, ds \,. \tag{4.5}$$

To evaluate this integral we must specify both $r_p(s)$ and $d\xi/ds$, or find $r_p(\xi)$ and change the limits of integration to $\xi(S_1)$ and $\xi(S_2)$. When the appropriate integrals have been evaluated (Section 4.2.6) for each node i in the k-th fracture, we have an expression for potential of the form

$$\phi_i^k = \phi_{iN}{}^k + \phi_{iI}{}^k = Q_i f_{iN}{}^k + Q_i f_{iI}{}^k = Q_i F_i^k \,. \tag{4.6}$$

The F_i^k in Eq.(4.6) represents shape functions for the total head distribution over the entire fracture due to the presence of the *i*th intersection.

4.2.6 POTENTIAL DISTRIBUTION

We need to evaluate the potential distribution in the disc due to both the sources distributed along the intersection itself and the sources distributed on the image arc or radial segment. In the following, $\phi_{iN}{}^k$ will be the potential due to the sources distributed along the intersection *i* in fracture *k*; $\phi_{iI}{}^k$ will be the potential due to the sources distributed along the image. Thus the potential due to the presence of intersection *i* is $\phi_i^k = \phi_{iN}{}^k + \phi_{iI}{}^k$.

By superposition, the total potential due to all the intersections in the circle will be given by

$$\phi^k = \Sigma_i \phi_i^k + C^k K^k b^k \,, \tag{4.7}$$

where C^k is the datum head, which is constant for each fracture and will be eliminated during derivation; b^k is the aperture of the fracture *k*; and K^k is the fracture hydraulic conductivity, defined in Eq.(4.3).

To be precise, using Eq.(4.7) to find ${\phi_{iN}}^k$ allows one to calculate the potential distribution due to the source node *i* at any point on the fracture except on the line itself, where the potential is undefined. However, for the global mass balance equations, the only potentials we need are the average potentials at the intersections (i.e., $\overline{\phi}_i^k$). Thus, we avoid this problem by assuming that the potential distribution at any point (not on the line intersection itself) can be calculated by assuming that the intersections are line sources with no thickness. However when computing the potential contribution at node *i* due to node *i*, integration will be singular if the node *i* is still assumed to have no thickness. Appendix J gives the calculation of the average potential near the node due to the sources on the node. The average potential due to the fracture node *i* itself is:

$$\overline{\phi}_{iN} = -\frac{Q}{4\pi l^2}\left(l^2 \ln l^2 - 3l^2\right), \tag{4.8}$$

where Q is the flow into or out of the fracture *i* through this intersection; *l* is the length of this intersection.

4.2.7 TOTAL POTENTIAL FIELD IN THE FRACTURE

In Eq.(4.1), the third potential term, ϕ_{iC}, associated with intersection *i* is the potential due to an image of strength, $-Q_i$, at the center of the fracture. However, as previously explained, the total strength of all such images at the center is zero, so no head is contributed from the sum of the images at the center.

The total potential in fracture *k* is given by

$$\phi^k = \sum_{i=1}^{n} \phi_i^k + C^k K^k b^k = \sum_{i=1}^{n} \left({\phi_{iN}}^k + {\phi_{iI}}^k\right) + C^k K^k b^k = \sum_{i=1}^{n} Q_i F_i^k + C^k K^k b^k \tag{4.9}$$

The average potential at each intersection *j* of fracture *k* due to the presence of all intersections in fracture *k* is

$$\bar{\phi}_j^{\,k} = \frac{1}{l_j}\int_{l_j}\left(\sum_{i=1}^{n}\phi_i^{\,k}\right)dl_j + C^k K^k b^k = \frac{1}{l_j}\int_{l_j}\left(\sum_{i=1}^{n} Q_i F_i^{\,k}\right)dl_j + C^k K^k b^k$$

$$= \sum_{i=1}^{n} Q_i\left(\frac{1}{l_j}\int_{l_j} F_i^{\,k}\,dl_j\right) + C^k K^k b^k = \sum_{i=1}^{n} Q_i \Psi_{ij}^{\;k} + C^k K^k b^k, \qquad (4.10)$$

where $\Psi_{ij}^{\;k} = \frac{1}{l_j}\int_{l_j} F_i^{\,k}\,dl_j$ is the shape function for the average head on intersection *j* in fracture *k* due to the intersection *i* also on fracture *k*. The value of $\Psi_{ij}^{\;k}$ maybe difficult to obtain analytically, but it can be easily approximated by double numerical integration (5-point Gaussian Quadrature):

$$\Psi_{ij}^{\;k} = \frac{1}{l_j}\int_{l_j} F_i^{\,k}\,dl_j = \frac{1}{l_j}\int_{l_j}\left(f_{iN}^{\;k} + f_{iI}^{\;k}\right)dl_j$$

$$= \frac{1}{l_j}\int_{l_j}\left(\frac{-1}{2\pi l_i}\int_{l_i}\ln r_p(\xi)\,d\xi + \frac{-1}{2\pi l_i}\int_{S_i}\frac{d\xi}{ds}\ln r_p(s)\,ds\right)dl_j$$

$$= -\frac{1}{2\pi l_i l_j}\int_{l_j}\left(\int_{l_i}\ln r_p(\xi)\,d\xi + \int_{S_i}\frac{d\xi}{ds}\ln r_p(s)\,ds\right)dl_j \qquad (4.11)$$

4.2.8 SOLUTION OF THE FLOW EQUATIONS

Eq.(4.10) provides the potential distribution in each fracture as a function of the flux into or out of each node. In order to satisfy mass balance locally, we note that the sum of the fluxes in a fracture element must be zero. Thus for *n* nodes on a fracture, there are n-1 independent values of Q_i. Using this fact, we invert Eq.(4.10) to obtain expressions for Q_i in terms of the $\bar{\phi}_j^{\,k}$. When this is done for every fracture in the network, there are two independent expressions for each Q_i, since node *i* exists on both fractures forming intersection *i*. By equating each of these pairs, we guarantee mass balance through the network. The set of equations equating flow into each intersection to flow out of each intersection can be solved for the h_j. We solve for h_j rather than $\bar{\phi}_j^{\,k}$

because the average potential, $\overline{\phi}_j^{\,k}$, will have a different value in each of the two intersecting fractures if the transmissivity of the two fractures is different. The average total head at the node, h_j, however, will be the same in both fractures. Values of Q_i can be found by substituting the h_j into the analytical solutions for Q_i developed for each of the fractures that intersect at i. The details of this technique are given below.

In the fracture *k*, for the intersection *j*, since

$$\overline{\phi}_j^{\,k} = \overline{h}_j^k K^k b^k . \tag{4.12}$$

From Eq.(4.10), one gets

$$\overline{h}_j^k = \sum_{i=1}^{n} \frac{Q_i}{K^k b^k} \Psi_{ij}^{\;k} + C^k \tag{4.13}$$

For mass conservation we have $\sum_{i=1}^{n} Q_i = 0$ or $Q_n = -\sum_{i=1}^{n-1} Q_i$. Based on these, we have

$$\overline{h}_j^k = \sum_{i=1}^{n-1} \frac{Q_i}{K^k b^k} \Psi_{ij}^{\;k} + \frac{Q_n}{K^k b^k} \Psi_{nj}^{\;k} + C^k$$

$$= \sum_{i=1}^{n-1} \frac{Q_i}{K^k b^k} \Psi_{ij}^{\;k} - \sum_{i=1}^{n-1} \frac{Q_i}{K^k b^k} \Psi_{nj}^{\;k} + C^k = \sum_{i=1}^{n-1} \frac{Q_i}{K^k b^k} \left(\Psi_{ij}^{\;k} - \Psi_{nj}^{\;k} \right) + C^k \text{, j=1, n-1} \tag{4.14}$$

These are (n-1) equations.

To eliminate the constant C^k, we subtract $\overline{h}_{j+1}$ from $\overline{h}_j$:

$$\overline{h}_j - \overline{h}_{j+1} = \sum_{i=1}^{n-1} \frac{Q_i}{K^k b^k} \left(\Psi_{ij}^{\;k} - \Psi_{nj}^{\;k} \right) - \sum_{i=1}^{n-1} \frac{Q_i}{K^k b^k} \left(\Psi_{i(j+1)}^{\;k} - \Psi_{n(j+1)}^{\;k} \right)$$

$$= \sum_{i=1}^{n-1} \frac{Q_i}{K^k b^k} \left[\left(\Psi_{ij}^{\;k} - \Psi_{nj}^{\;k} \right) - \left(\Psi_{i(j+1)}^{\;k} - \Psi_{n(j+1)}^{\;k} \right) \right] = \sum_{i=1}^{n-1} \frac{Q_i}{K^k b^k} \zeta_{ij}^{\;k} \tag{4.15}$$

Eq.(4.15) can be written in a matrix form:

$$\begin{bmatrix} \bar{h}_1 - \bar{h}_2 \\ \bar{h}_2 - \bar{h}_3 \\ \dots \\ \bar{h}_{n-1} - \bar{h}_n \end{bmatrix} = \frac{1}{K^k b^k} \begin{bmatrix} \zeta_{11}^k & \zeta_{12}^k & \cdots & \zeta_{1(n-1)}^k \\ \zeta_{21}^k & \zeta_{22}^k & \cdots & \zeta_{2(n-1)}^k \\ \dots & \dots & \dots & \dots \\ \zeta_{(n-1)1}^k & \zeta_{(n-1)2}^k & \cdots & \zeta_{(n-1)(n-1)}^k \end{bmatrix} \begin{bmatrix} Q_1 \\ Q_2 \\ \dots \\ Q_{n-1} \end{bmatrix} \tag{4.16}$$

Then we have,

$$Q_i = \sum_{j=1}^{n-1} \left(\zeta_{ij}^{\ k} \right)^{-1} K^k b^k \left(\bar{h}_j - \bar{h}_{j+1} \right) = K^k b^k \sum_{j=1}^{n-1} \psi_{ij}^{\ k} \left(\bar{h}_j - \bar{h}_{j+1} \right) \quad \text{(i=1, n-1)} \tag{4.17}$$

$$Q_n = -\sum_{i=1}^{n-1} Q_i = -K^k b^k \sum_{i=1}^{n-1} \sum_{j=1}^{n-1} \psi_{ij}^{\ k} \left(\bar{h}_j - \bar{h}_{j+1} \right), \tag{4.18}$$

where $\psi_{ij}^{\ k}$ is the inverse of $\zeta_{ij}^{\ k}$.

4.2.9 GLOBAL MASS BALANCE EQUATIONS

Two versions of Eq.(4.17) or Eq.(4.18) are written for each intersection, once for each fracture associated with the intersection. For example, if fracture k and fracture p intersect at i, then the flow enters k from p (or vice versa) through i and can be expressed by

$$K^k b^k \sum_{j=1}^{J-1} \psi_{ij}^{\ k} \left(\bar{h}_j - \bar{h}_{j+1} \right) + K^p b^p \sum_{m=1}^{M-1} \psi_{im}^{\ p} \left(\bar{h}_m - \bar{h}_{m+1} \right) = 0, \tag{4.19}$$

where j and m have global numbers which correspond to local numbering j=(1,J) and m=(1,M), respectively, when there are J nodes on fracture k and M nodes on fracture p. If node *i* is the *M*th node on *p* or the *J*th node on *k*, then we use Eq.(4.18) instead of Eq.(4.17) to form Eq.(4.19). We write one equation, Eq.(4.19) or its equivalent, for each node in the network.

4.2.10 BOUNDARY CONDITIONS

If a fracture intersects a boundary, we can assign a constant head, $\bar{h}_j = H_j$, to the node. Constant flux boundaries can be accommodated by substituting Eq.(4.17) or Eq.(4.18) for Eq.(4.19), where Q_i in this case is the specified flux through the boundary node. When all these equations have been assembled, expanding and collecting terms gives an equation system of the form

$$\mathbf{A}\bar{\mathbf{h}} = \mathbf{b} \tag{4.20}$$

The vector $\mathbf{b}$ is nonzero only for nodes *j*, which are boundary nodes. The matrix $\mathbf{A}$ is symmetric and sparse, and the bandwidth can be minimized by appropriate node numbering. Inversion of $\mathbf{A}$ allows calculation of $\bar{\mathbf{h}}$, which in turn allows calculation of Q_i through Eq.(4.17) and Eq.(4.18) and calculation of C^k through Eq.(4.13).

CHAPTER 5: TUNNEL APPLICATIONS

In this chapter, the fracture simulation and flow model described in Chapter 3 and 4 are applied to tunnel cases. First, some simple ideal tunnel cases are analyzed, followed by a real case history. Based on these cases, the summary and conclusion of this study are drawn. Futher research is also suggested.

5.1 Ideal case studies

Two simple cases and ideal tunnel cases are studied. In order to verify the validity of the code for simulating flow rate and head distribution, single fracture flow is checked first, followed by double fractures flow. Two ideal tunnel cases are considered, one consisting of regular fracture shapes regularly located in space, and the other consisting of two sets of fractures randomly located that form two flow paths. These cases are compared using the commercial software FracMan (by Golder Associates, Inc.).

5.1.1 SIMPLE CASE STUDIES

In order to verify the validity of the Long et al.'s (1985) analytical-numerical method and the code implementation carried out in this research, flow in one fracture and two fractures are studied, some of which are studied in the original work of Long et al. (1985).

5.1.1.1 One fracture case

The fracture has radius R=5m and aperture b=0.01m (assume the laminar flow occurs). As shown in Figure 5.1, the boundaries contain Boundary 1 which has a constant

head H1=1.0m and Boundary 2 which has a constant head H2=0.0m, with distance D=4m between the two boundaries (symmetric with respect to the center of the fracture).

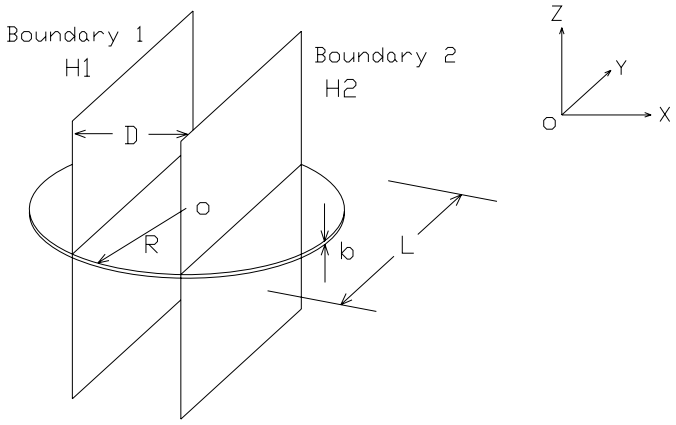

Figure 5.1 One fracture intersecting two parallel boundaries

This physical model is calculated by the code *FractureFlow* (developed by the author for this research). Results are compared with two extreme cases (rectangular parallel plates, Figure 5.2 (a) and (c), which can be computed analytically.

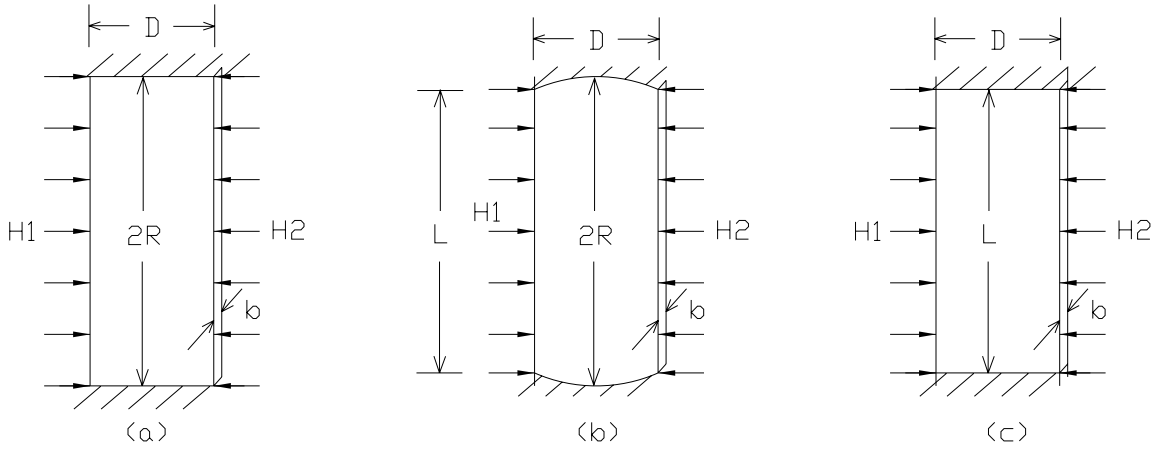

Figure 5.2 (a) Parallel plate model of dimensions D*2R; (b) the model of dimensions in Figure 5.1; (c) parallel plate model of dimensions D*L;

Table 5.1 Flow rate in three cases

Flow rate at the two boundaries (m^3/s)		
Case (a)	Case (b)	Case (c)

(analytical*)	(by *FractureFlow*)	(analytical)
2.042	1.967	1.871

Note * : The analytical solution is based on $Q = k \cdot i \cdot A = k \cdot i \cdot b \cdot l = \frac{gb^3}{12\gamma} \cdot \frac{H_1 - H_2}{D} \cdot l$

Results (Table 5.1) shows that flow rate in Case (b) is between upper limit Case (a) and lower limit Case (c), indicating that the code *FractureFlow* is applicable to the single fracture case.

5.1.1.2 Two fracture case

Consider two fractures with radii R=5m, apertures b=0.01 or 0.02m (assume the laminar flow occurs), and transmissivities T=Kb. They intersect with each other at intersection F1-F2 of length L. As shown in Figure 5.3, there are two boundaries. Boundary 1 has a constant head H1=1.0m intersecting with Fracture 1 at intersection (H1-F1), which is parallel to F1-F2 with distance D1. Boundary 2 has a constant head H2=0.0m intersecting with Fracture 2 at intersection (H2-F2), which is also parallel to F1-F2 with distance D2.

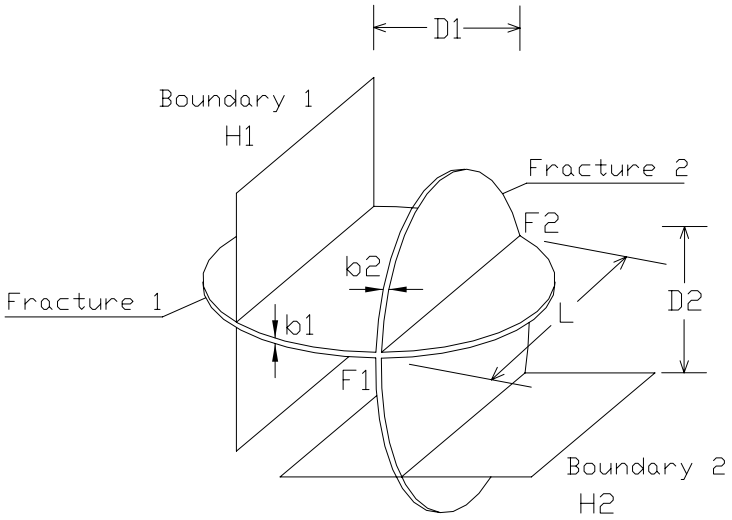

Figure 5.3 Two fracture case with two boundaries

This model (Figure 5.3) is calculated by using the code *FractureFlow*. Results are also compared with two extreme cases (connected rectangular slots, Figure 5.4 (a) and (c)) that can be computed analytically. For these three cases, different apertures for Fractures 1 and 2 and different boundary locations are combined, as shown in Table 5.2.

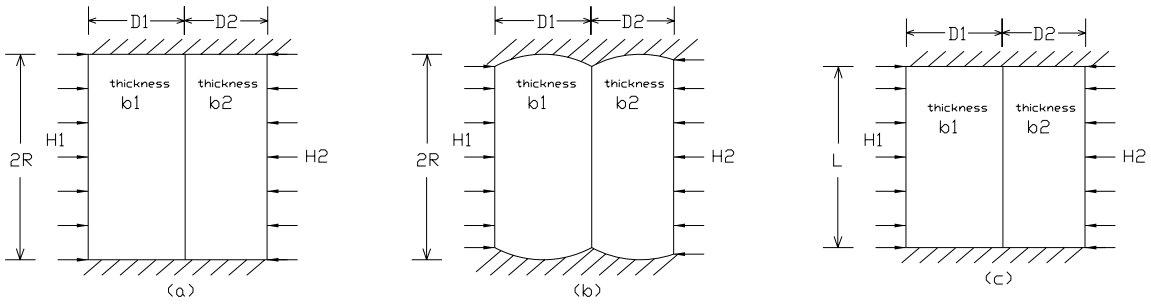

Figure 5.4 (a) the slab model of dimensions (D1+D2)*2R; (b) the model of dimensions in Figure 5.3; (c) the slab model of dimensions (D1+D2)*L;

Table 5.2 Flow rate and head at the intersection in three cases

	Case (a) (analytical*)		Case (b) (by *FractureFlow*)		Case (c) (analytical)	
	Flow rate (L/s)	Head at intersection (m)	Flow rate (L/s)	Head at intersection (m)	Flow rate (L/s)	Head at intersection (m)
D1=D2=4m,b1=b2=0.01m	1.250	0.500	1.205	0.500	1.146	0.500
D1=6m, D2=2m, b1=b2=0.01m	1.250	0.250	1.119	0.258	1.000	0.250
D1=D2=4m, b1=0.02m, b2=0.01m	1.667	0.667	1.606	0.667	1.333	0.667

Note * : The analytical solution is based on $Q = k \cdot i \cdot A = k \cdot i \cdot b \cdot l = \frac{g b^3}{12\gamma} \cdot \frac{H_1 - H_2}{D} \cdot l$.

Here, the series domains need to be taken into account.

Results (Table 5.2) shows that flow rates in Case (b) are alway between the upper limit Case (a) and the lower limit Case (c), and head values at intersection F1-F2 in Case (b) are very close to (or the same as) Case (a) and (c). This indicates that the code *FractureFlow* is applicable to intersecting fractures, at least for the two fracture cases. It is worth mentioning that the head distribution should not always be a constant in Case

(b), because the two-sided no-flow boundaries are curved. Because of the constant head distribution assumption along each intersection in Dr. Long's (1985) analytical-numerical method, the head along each intersection is averaged. However, it does not significantly affect the global head distribution and flow rate as illustrated below (Section 5.1.2).

5.1.2 IDEAL TUNNEL CASES STUDY

Two ideal tunnel cases are studied. One is composed of eight fractures that intersect one by one to form a flow path from the recharge boundary to the tunnel boundary. The other is composed of thirteen quasi-randomly located fractures forming two flow paths that connect the recharge zone and the tunnel.

5.1.2.1 Eight regularly located fractures

The eight fractures have radii of 5m and aperture b (varied in the study). The coordinate system is set as follows: the x-axis is horizontal and parallel to the tunnel axis, the y-axis is orthogonal to the x-axis in the horizontal plane, and the z-axis points upwards. The zero-elevation datum is set at the center of the tunnel (x-axis). The recharge boundary is located at elevation 20m, with a constant head boundary of 30m. The tunnel has a square cross section with side length of 5.0m, and it is excavated from the origin to x=30m. It intersects with three fractures, from which water will flow into the tunnel. A three-dimensional sketch of this model is shown in Figure 5.5. The fracture and boundary input is listed in Table 5.3 and Table 5.4, respectively.

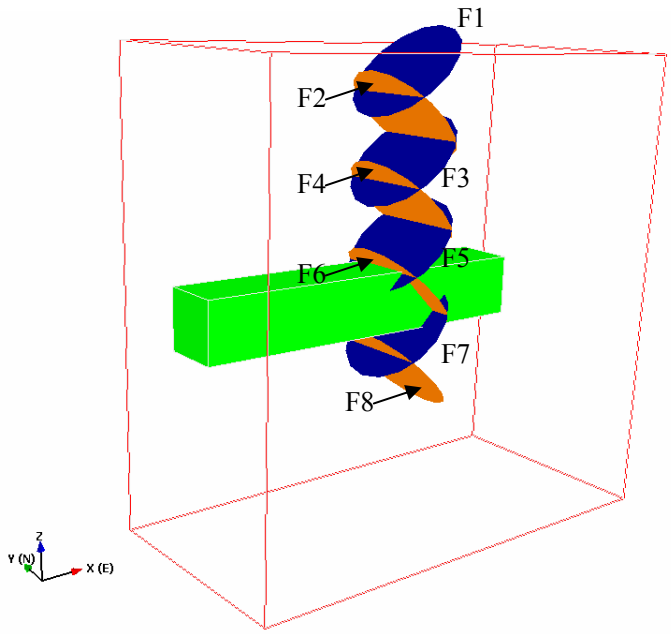

Figure 5.5 3D sketch of eight fracture network

Table 5.3 Input list for the eight fractures

Fracture No.	Fracture center location			Orientation		Radius (m)	Aperture (m)		Hydraulic conductivity (m/s)	
	X (m)	Y (m)	Z (m)	Dip direction	Dip angle		Case1	Case2	Case1	Case2
1	20.00	0.00	18.23	-90.00	45.00	5.00	0.001	0.001	0.817	0.817
2	20.00	0.00	14.70	90.00	45.00	5.00	0.001	0.002	0.817	3.267
3	20.00	0.00	11.16	-90.00	45.00	5.00	0.001	0.003	0.817	7.350
4	20.00	0.00	7.63	90.00	45.00	5.00	0.001	0.004	0.817	13.067
5	20.00	0.00	4.09	-90.00	45.00	5.00	0.001	0.004	0.817	13.067
6	20.00	0.00	0.55	90.00	45.00	5.00	0.001	0.003	0.817	7.350
7	20.00	0.00	-3.01	-90.00	45.00	5.00	0.001	0.002	0.817	3.267
8	20.00	0.00	-6.52	90.00	45.00	5.00	0.001	0.001	0.817	0.817

Table 5.4 Input list for the boundaries

Boundary No.	Boundary Location Type*	Point on the plane			Orientation of normal			Boundary Type†	Boundary value (m or m/s)
		X (m)	Y (m)	Z (m)	nx	ny	nz		
1	1(recharge)	0.00	0.00	20.00	0.00	0.00	-1.00	1	30.00
2	2(tunnel)	0.00	0.00	2.50	0.00	0.00	1.00	1	0.00
3	2(tunnel)	0.00	-2.50	0.00	0.00	-1.00	0.00	1	0.00
4	2(tunnel)	0.00	0.00	-2.50	0.00	0.00	-1.00	1	0.00
5	2(tunnel)	0.00	2.50	0.00	0.00	1.00	0.00	1	0.00
6	2(tunnel)	40.00	0.00	0.00	1.00	0.00	0.00	1	0.00

Note: * 1 indicates outer boundary; 2 indicates inner boundary.

† 1 indicates constant head boundary; 2 indicates constant flow boundary.

This ideal tunnel case (Figure 5.5) is calculated by the code *FractureFlow*. Results are compared with the commercial software Fracman (by Gloder Assoc.), as shown in Table 5.5.

Table 5.5 Results comparison for the eight fracture ideal tunnel case

Intersection No.	Case 1				Case 2			
	Head value at Intersection (m)		Flow rate into tunnel (L/s)		Head value at Intersection (m)		Flow rate into tunnel (L/s)	
	By *FF*	By *FM*	By *FF*	By *FM*	By *FF*	By *FM*	By *FF*	By *FM*
1 (F1-F2)	24.00	23.97	9.21	9.41	4.86	4.85	39.20	38.56
2 (F2-F3)	17.99	17.93			1.72	1.71		
3 (F3-F4)	11.99	11.90			0.79	0.78		
4 (F4-F5)	5.99	5.87			0.40	0.38		

Note: here *FF* indicates *FractureFlow*, which is code produced in this research; *FM* indicates commercial software *FracMan*.

Results (Table 5.5) show that head values at the fracture intersections and total flow rates into the tunnel computed by *FractureFlow* (Solution A) are very close to the results obtained with *FracMan* (Solution B). The good match between these two solutions indicates that the code *FractureFlow* is applicable to more complicated fracture networks besides just one or two fractures. Based on author's knowledge, the slight difference between these two solutions is caused by: (1) the constant head distribution assumption along each intersection in Solution A; and (2) the limited number of sides (16) available in *FracMan* to simulate a circle with a polygon in Solution B. It is hard to tell which reason causes more error in each calculation. Regardless, these two solutions are very close and this difference can be ignored in tunnel industry.

5.1.2.2 Quasi-randomly located fractures

In this part, one slightly more realistic case is studied and compared with *FracMan* as well. Thirteen fractures have radii 3.0~9.0m and aperture from

0.008~0.020m. The coordinate system is set as follows: the x-axis is horizontal and parallel to the tunnel axis; the y-axis is orthogonal to the x-axis in the horizontal plane; and the z-axis points upwards. The zero-elevation datum is set at the center of the tunnel (x-axis). The recharge boundary is located at Elevation 20m, with a constant head boundary of 30m. The tunnel has a square cross section with side length of 5.0m, and it is excavated from the origin to x=50m. It intersects four fractures, from which water will flow into the tunnel. A three-dimensional sketch of this model is shown in Figure 5.6. The fracture and boundary input is listed in Table 5.6 and Table 5.7, respectively.

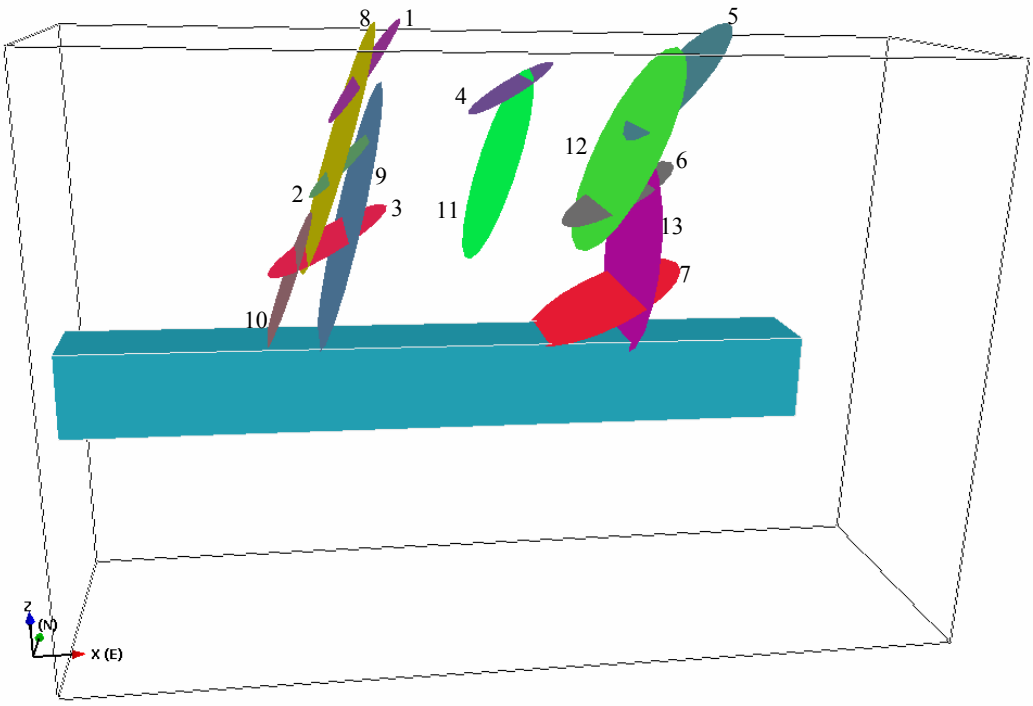

Figure 5.6 3D sketch of thirteen fracture network

Table 5.6 Input list for thirteen fractures

Fracture No.		Fracture center location			Orientation		Radius (m)	Aperture (m)	Hydraulic conductivity (m/s)
		X (m)	Y (m)	Z (m)	Dip direction	Dip angle			
Set 1	1	20.00	0.00	18.00	270.00	55.00	4.00	0.0010	0.817
	2	18.50	0.00	12.00	270.00	45.00	3.00	0.0008	0.523
	3	17.50	0.00	7.00	270.00	30.00	4.50	0.0012	1.176
	4	29.50	0.00	17.00	270.00	32.00	3.20	0.0009	0.662
	5	40.70	0.00	17.50	270.00	50.00	5.00	0.0015	1.838
	6	37.00	0.00	10.00	270.00	30.00	4.20	0.0011	0.988

	7	36.30	0.00	2.50	270.00	27.00	5.80	0.0017	2.360
Set 2	8	18.20	0.00	13.00	270.00	73.00	8.40	0.0020	3.267
	9	18.90	0.00	8.50	270.00	76.00	9.00	0.0019	2.948
	10	14.90	0.00	4.30	270.00	70.00	4.80	0.0013	1.380
	11	28.70	0.00	12.00	270.00	72.00	6.50	0.0018	2.646
	12	37.50	0.00	13.00	270.00	65.00	7.40	0.0018	2.646
	13	38.20	0.00	6.00	270.00	85.00	7.00	0.0017	2.360

Table 5.7 Input list for boundaries

Boundary No.	Boundary Location Type*	Point on the plane			Orientation of normal			Boundary Type†	Boundary value (m or m/s)
		X (m)	Y (m)	Z (m)	nx	ny	nz		
1	1	0.00	0.00	20.00	0.00	0.00	-1.00	1	30.00
2	2	0.00	0.00	2.50	0.00	0.00	1.00	1	0.00
3	2	0.00	-2.50	0.00	0.00	-1.00	0.00	1	0.00
4	2	0.00	0.00	-2.50	0.00	0.00	-1.00	1	0.00
5	2	0.00	2.50	0.00	0.00	1.00	0.00	1	0.00
6	2	50.00	0.00	0.00	1.00	0.00	0.00	1	0.00

Note: * 1 indicates outer boundary; 2 indicates inner boundary.

† 1 indicates constant head boundary; 2 indicates constant flow boundary.

This ideal tunnel case (Figure 5.6) is calculated by the code *FractureFlow*. Results are compared with the commercial software *FracMan* (by Golder Assoc.), as shown in Table 5.8.

Table 5.8 Results comparison of thirteen fracture ideal tunnel case

Intersection No.	Head value at Intersection (m)		Flow rate into tunnel (L/s)	
	By *FractureFlow*	By *Fracman*	By *FractureFlow*	By *Fracman*
1 (F1-F8)	26.42	26.90	124.14	119.81
2 (F2-F8)	19.51	20.80		
3 (F2-F9)	4.88	6.18		
4 (F3-F8)	13.98	16.2		
5 (F3-F9)	4.32	5.47		
6 (F3-F10)	10.86	13.60		
7 (F5-F12)	20.67	20.90		
8 (F6-F12)	17.17	18.10		
9 (F6-F13)	5.71	6.39		
10 (F7-F13)	0.67	1.64		

Results in Table 5.8 show that head values at the intersections and total flow rates into the tunnel computed by *FractureFlow* (Solution A) are close to the results obtained

with *FracMan* (Solution B). The good match between these two solutions indicates that the code *FractureFlow* is applicable to much more complicated fracture networks similar to natural ones. As mentioned in Section 5.1.2.1, the slight difference between these two solutions is caused by: (1) the constant head distribution assumption along each intersection in Solution A; (2) the limited number of sides (16) available in *FracMan* to simulate a circle with a polygon in Solution B. It is hard to tell which reason causes more error in each calculation. The head difference is a little larger than the regularly located fractures case. Fortunately, the flow difference is just around 3.5 percent. In the tunnel industry, what counts is the flow rate rather than the head distribution in the rock mass.

5.2 A real tunnel case study

After verifying *FractureFlow* in simple cases, in this section *FractureFlow* and the fracture simulation algorithm in Chapter 3 are validated by using a real tunnel case. The project will be first introduced including background and geotechnical conditions. Next, details of the simulation procedures will be presented.

5.2.1 INTRODUCTION

In this part, the project background, research scope, and its geological and hydrogeological conditions are described, most of which are from GBR (JJG, 2007) of this project.

5.2.1.1 Project background and study range

The Cobb County Water System (CCWS) provides for the collection and treatment of wastewater for most areas in Cobb County in Georgia. The existing infrastructure providing sewer service to the South Cobb service area basin does not have sufficient capacity to accommodate projected 2040 wastewater flows. The South Cobb

Tunnel Project is designed to provide needed long-term sewer conveyance capacity and to allow Cobb County to eliminate two major pumping stations and about 87,000 linear feet of aging sewer lines and force mains.

The South Cobb Tunnel is one of the largest capital improvement projects in water system history. A $305 million construction contract was awarded to Shea-Traylor J.V. (a joint venture of J.F. Shea Construction and Traylor Brothers) on March 11, 2008. Construction began in July 2008 and will take six years to complete.

The South Cobb Tunnel project entails constructing a six-mile, 27-foot excavated diameter tunnel located in hard rock, with depths ranging from 150 feet to 400 feet. A map of the project is shown in Figure 5.7. The main tunnel alignment is portrayed in red. Most of this main tunnel will be excavated using a 27-foot tunnel boring machine (TBM).

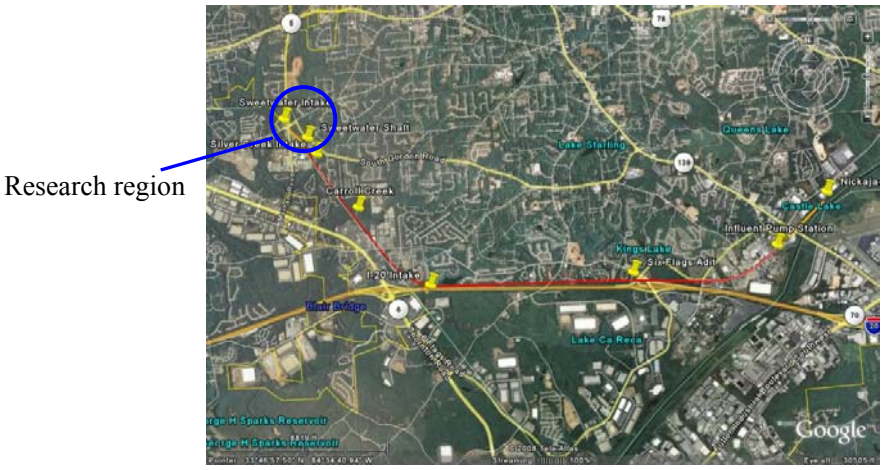

Figure 5.7 Plan view of The South Cobb Tunnel Project (From http://www.southcobbtunnel.org/; tunnel alignment is shown in red)

The whole main tunnel chainage of this project is from 0+00 feet to 290+74 feet, in which Station 290+74 to Station 286+33 is the starter tunnel excavated by a drilling and blasting method. The remainder is excavated using a rock TBM starting from Station 286+33 to Station 0+000. The TBM tunnel from Station 286+00 to 276+00 is chosen as the range of this research (Figure 5.7). The TBM tunnel is still under construction, and is scheduled for completion by the middle of 2011.

5.2.1.2 Geotechnical conditions

1) Rock types and rock units

The tunnel is divided into ten large-scale geologic units (Table 5. 9). The range of this research belongs to Unit 9, in which the predominant rock types are chlorite schist and mica schist.

Table 5. 9 Rock units of this project (From South Cobb Tunnel Project GBR, 2007)

Unit	*Start*	*End*	*Predominant Rock Types*	*Schistose*	*Gneissic*
1	0+00	20+80	mylonite	81%	19%
2	20+80	53+40	granitic gneiss and augen gneiss		100%
3	53+40	96+10	mica schist	95%	5%
4	96+10	130+30	granofels and amphibolite		100%
5	130+30	194+20	mica schist, quartzofeldspathic schist	85%	15%
6	194+20	228+20	granitic gneiss		100%
7	228+20	236+10	interlayered schist and gneiss	83%	17%
8	236+10	261+30	migmatitic gneiss and schist	28%	72%
9	261+30	290+74	chlorite schist and mica schist	100%	
10	*Sweetwater Tunnel*		quartzofeldspathic schist	60%	40%

1. Starting and ending stations based on TBM tunnel. Stations considered accurate to ±200 feet.
2. Percentages of schistose and gneissic rock considered accurate to ±10 percentage points.

2) Geotechnical Profile

Figure 5.8 is a geotechnical profile of the tunnel alignment in the research range. This profile shows approximate interlayers of soil zone, transition zone and bedrock, as well as the approximate ground surface and hydraulic head above the tunnel. The base of the soil zone was obtained from those borings where it was recognized and logged. The base of the transition zone (i.e., a partially weathered zone between soil and bed rock) was obtained from the boring logs and corresponds to the depth (GBR, 2007).

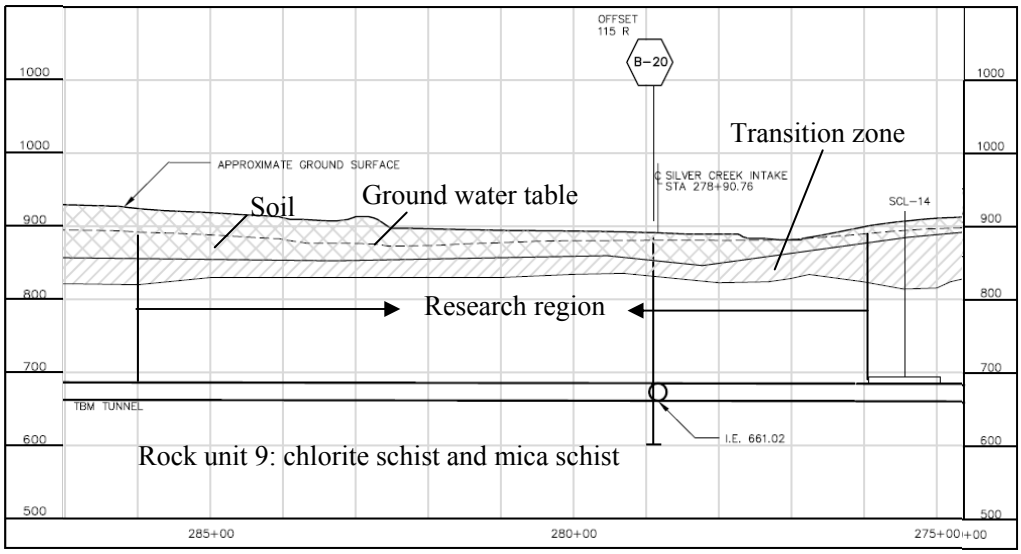

Figure 5.8 Geotechnical profile of the tunnel alignment in the research range (From GBR, 2007)

3) Joint sets

Figure 5.9 shows the most common joint orientations along the tunnel alignment, as measured in the rock cores. This compilation is considered a more statistically representative of the conditions at the tunnel depth than the field mapping data.

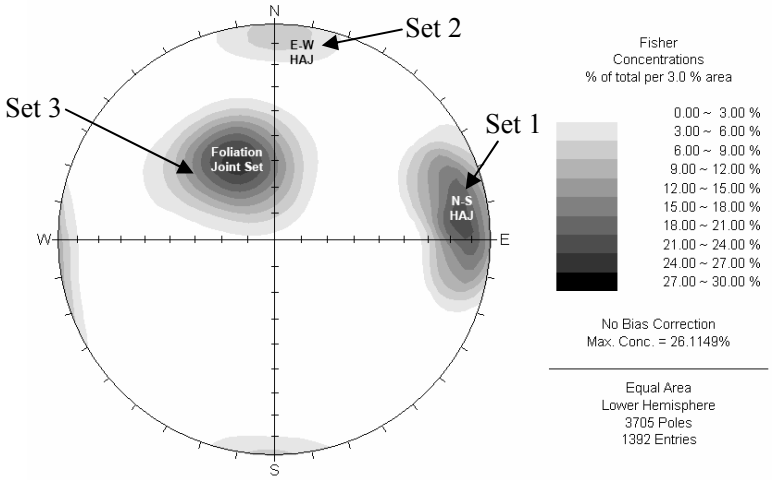

Figure 5.9 Stereoplot of major joint sets (From GBR, 2007)

Three main joint sets are prominent on Figure 5.9: north-south high-angle joints (Set 1); east-west high-angle joints (Set 2); and foliation joints (Set 3).

From GBR (2007), most high-angle joints and some foliation joints are shear fractures. These joints are commonly cemented or filled with gouge, clay, calcite, or gypsum, and tend to transmit groundwater poorly. However, where these fractures are near other water bearing fractures, the calcite and gypsum cements can dissolve out and the gouge or clay can soften and wash out. In these cases, high-angle joints can also yield considerable water. All high-angle joints in the transition zone typically fall into this latter category of open, water-bearing joints.

From GBR (2007), high-angle joints are not evenly spaced. They tend to occur in sets of closely spaced subparallel joints, described as "swarms." Joints on the edge of a swarm tend to be spaced farther apart and joints in the center of the swarm tend to be spaced closer together. The joints on the outer edges of the swarm typically show less offset. The joints in the center of the swarms typically show evidence of greater offset and rock damage, including hydrothermal alteration, mineral cements, and gouge. Larger swarms of high-angle joints form fracture zones and lineaments. This pattern of swarms is too large to observe in core but can be seen clearly in tunnels and shafts.

Most foliation joints are extensional partings along foliation. Some are open and transmit groundwater. Others are incipient joints that are incompletely formed in the ground but then open in response to blasting or mining. Water-bearing foliation joints are commonly weathered with iron staining or fluffed mica. Foliation joints are more commonly open at shallow depth, especially in the transition zone (i.e., a partially weathered zone between soil and bed rock). With increasing depth, foliation joints tend to become tighter. Open foliation joints are expected to be rare (but not absent) where the tunnel is more than 300 feet deep. Where open foliation joints are present at depth, they are likely to yield large amounts of groundwater into the tunnel.

4) Permeability

Permeability in Figure 5.10 was compiled from the packer test data. The scale of the tests is 20 feet along the borehole. Because permeability is a scale-dependent property, the statistical distribution might change considerably if permeability were measured at smaller or larger scales.

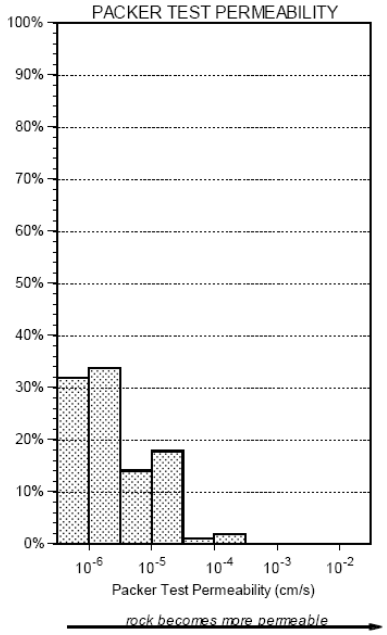

Figure 5.10 Permeability distribution from packer tests (From GBR, 2007)

Rock mass permeability is reported as hydraulic conductivity in centimeters per second. Rock with a permeability $<10^{-6}$ cm/s will be dry or damp in the tunnel. A rock mass with permeability between 10^{-6} and 10^{-5} cm/s will produce seeps and dribbles. Higher permeabilities will produce more significant inflows. As the permeability becomes higher, the quantity of water produced from the rock mass will become controlled by the development of the hydraulic gradient around the tunnel and becomes complicated.

5) Hydrogeology

Groundwater behavior depends on the head of water above the excavation, the supply of water, and the permeability.

The estimated static groundwater head above the tunnel (prior to excavation) is shown on the Geotechnical Profile (Figure 5.8). Recharge comes from infiltrating rainfall over a broad area around the excavation and from large streams near the excavation. The Chattahoochee River and Sweetwater Creek are large enough to act as infinite sources of recharge at the scale of the project.

The permeability of the transition zone is intermediate between soil and bedrock. The bedrock zone has fracture porosity. Water occurs in the fractures and flows through the fractures. The broad-scale permeability of the rock mass depends on the apertures, density, and interconnection of the fractures. The permeability in the bedrock zone is not uniformly distributed. Most of the inflows to the tunnels will occur in a few places, some of the inflows will occur in many places, and large sections of the tunnel will yield negligible inflow.

The foliation joints tend to be the principal pathways for groundwater flow in the bedrock zone. The foliation joints tend to be open and to become more open as they approach the ground surface. Because they dip at about 30 to 70 degrees, the foliation joints are effective at transmitting recharge water from the soil zone and from streams down into the bedrock zone and into the tunnel. High angle joints can also transmit water but are more commonly tight.

The soil zone has dual porosity consisting of both fracture porosity and matrix porosity. The fractures provide a small amount of storage and most of the soil-mass permeability. The soil matrix provides most of the storage and a small portion of the overall permeability. The dual porosity results in delayed yield, which affects dewatering, grouting, and stability.

Delayed yield occurs when water is drained or pumped from the soil. Water travels through the fractures toward the well or excavation. Because the fractures are

more permeable and have less storage than the matrix, drawdown spreads outward quickly. Then the matrix slowly begins to drain into the fractures over the full area of the drawdown. As an example, a pumping test at the Sweetwater Construction Shaft (see GDR, 2007) showed substantial drawdown in the soil fractures more than 50 feet from the pumping well within one hour after pumping began. This same test, based on an assumed specific yield of 15 percent also indicated that it would take about ten days to achieve 50 percent matrix drainage, three months to achieve 80 percent matrix drainage, and four years to fully drain the matrix adjacent to the fractures. (The specific yield is the free-draining porosity of the soil, as opposed to the total porosity.)

Groundwater inflows can wash out joint fillings and destabilize the ground, even after support has been installed. Inflows can also wash the grout out of grouted rock-bolts, making them less effective for initial support and ineffective as permanent support.

5.2.2 SIMULATION

In this section, all simulation procedures proposed in this research are elaborated in detail. This project is used to interpret and illustrate the simulation methods. The steps are as follows:

1) Collect raw fracture data from the geotechnical baseline report (GBR) and fracture maps of the tunnel wall;

2) Analyze fracture data to obtain fracture data sets, orientation distribution parameters and trace length distribution;

3) Specify research domain, define simulation grids, obtain fracture intensity spatial correlation models, and implement the fracture intensity simulation based on the spatial correlation models with conditional data for each fracture set;

4) Sample the fracture diameters from the diameter distribution, which is derived from the observed trace length distribution;

5) Assign mechanical apertures using the published trace length-aperture relationship as the first estimation, and convert to hydraulic apertures (this is because of the shortage of aperture measurements); the final trace length-aperture relationship is calibrated based on the total flow measurements at the beginning of tunnel excavation;

6) Poisson locate fractures into each cell to which they belong;

7) Assign boundary conditions to the flow model according to geotechnical reports and field observations;

8) Combine fractures of all sets, generate the discrete fracture network, remove un-intersected fractures, out-of-domain fractures, and dead-ends in the network, subdivide cross-intersections, and run flow analysis in the fracture network;

9) Analyze and interprete simulation results, then compare with observed flow data.

All of the above procedures are described in detail below:

5.2.2.1 Data collection

There are no fracture locations in boring logs and no fracture observations on outcrops for this project, so the only available source for fracture spatial information is the mapping on the tunnel walls. The fracture mapping is prepared by the project geologist right after the tunnel is excavated. In fracture maps, all visible fractures on the upper part of the tunnel wall are depicted including the description of rock types, major joints, and water inflow properties. These maps give the precise location of all fracture traces that can be used for spatial correlation research and size analysis. Also, the observed inflow data are needed to compare with the simulated inflow, which can be used to calibrate and optimize the simulation models. All fracture maps in the research range are shown in Appendix K.

Unfortunately, fracture orientation is not recorded and fracture maps do not provide the fracture set to which each fracture belongs. However, the overall fracture

orientation distribution and fracture sets are found in the project GBR, which is summarized in Section 5.2.1.2 3). The technique used here to distinguish different fracture sets from fracture maps is described next.

5.2.2.2 Data analysis

In this part, it is shown how to parameterize each orientation distribution, assign a fracture to a fracture set based on its fracture map, and obtain fracture trace length and diameter distribution.

1) Tunnel and fracture orientation

From the plan view drawing of the tunnel alignment it is understood that the tunnel is excavated in the direction of 162° (18° SE). The plunge of the tunnel axis is almost horizontal, which can be assumed as 0° .

There is no direct fracture orientation data in the fracture maps. I used information on orientation from the equal area stereoplot in Figure 5.9. From the stereoplot, the trend and plunge of normals to the three fracture sets can be read, if the average orientation is assumed to be located at the center of the densest contour. If the Fisher model is assumed for the orientation distributions in this project, Eq.(1.1) gives the probability distribution function (PDF). If we integrate $f(\theta)$ from 0 to θ, the cumulative distribution function (CDF) is obtained as:

$$F(\theta) = \int_0^{\theta} f(\theta)\, d\theta = \frac{e^{K} - e^{K\cos\theta}}{e^{K} - e^{-K}}. \tag{5.1}$$

We can solve Eq.(5.1) for K as:

$$K = \frac{\ln\left[1 - F(\theta)\right]}{\cos\theta - 1}, \tag{5.2}$$

where K is the parameter of the Fisher distribution model.

Eq.(5.2) gives the formula to estimate parameter K if a certain angle θ and the probability $F(\theta)$ of the angle (between one fracture and the "true" value) are known. Several θ and $F(\theta)$ values can be obtained from the stereoplot in Figure 5.9 by estimating the area portion in each contour. Therefore, an average K value can be estimated by Eq.(5.2). The results are shown in Table 5.10.

Table 5.10 Orientation distribution parameters

Fracture set	Average normal to fracture		Fisher model parameter K
	Trend °	Plunge °	
Set 1	84	14	20.51
Set 2	2	5	32.92
Set 3	335	57	17.22

2) Assign fractures to fracture sets based on fracture maps

Since fracture traces are mapped without sorting them into sets, it is difficult to determine which fracture belongs to which fracture set if we only know the overall fracture sets as shown in the stereoplot of Figure 5.9.

If one fracture intersects an orientated observation plane, it is not hard to determine the apparent orientation on that plane. However, when the observation surface is curved, which is the case in a tunnel, it is not as easy to determine the fracture orientation because generally the trace is not a straight segment. When a circular fracture intersects a cylinder-shaped tunnel wall, two cases may be distinguished:

- The fracture extends enough to cut all the way through the tunnel wall. In this case, the trace is a sinusoidal shape curve. The orientation of the fracture can be determined from the crest and trough of the sinusoid and the tunnel orientation.

- The fracture has a finite size and partially intersects the tunnel wall. In this case, it is very difficult to determine exactly the orientation of the fracture based only on the trace shape. Here the author uses the geometric results of a disc intersecting a cylinder (Mauldon and Mauldon, 1997; Gupta and Adler, 2006) to simulate fracture traces when fractures are randomly located in space with diameters and orientations that follow a given Fisher distribution with parameter K.

During trace shape simulation, the orientation can be sampled using the Monte Carlo method. If a random number p (0~1) is drawn for $F(\theta)$, by solving Eq.(5.1) for θ, we obtain:

$$\theta = \arccos\left(\frac{\ln\left[e^{K} - p\left(e^{K} - e^{-K}\right)\right]}{K}\right). \tag{5.3}$$

Here, K assumes different values for different fracture sets as given in Table 5.10.

The simulated traces for the three fracture sets are shown in Appendix L. Real fracture maps in Appendix K are then compared with the simulated traces in Appendix L to determine which trace belongs to which fracture set. Sometimes it may be difficult to assign a fracture to a set because its shape looks similar to two simulated traces. Actually, the fracture set should not only be determined by the fracture orientation. Geologic origin, termination relationship, and other factors such as mineral filling are also important clues to determining set distinction.

3) Fracture trace statistics and diameter distributions

After assigning traces to fracture sets, each trace length (curved) was measured in AutoCAD by redrawing traces with a spline to the original scale. Statistics of fracture traces, average trace length, and length distributions are listed in Table 5.11. The CDF of trace length for each fracture set is shown in Figure 5.11.

Table 5.11 Number of traces and length distribution of each fracture set

Set	Number of traces	Average trace length (feet)	Estimated trace length (exponential) distribution (pdf)	Percentage shorter than tunnel diameter
1	49	12.04	$y = 0.08e^{-0.08x}$	93.2%
2	47	18.72	$y = 0.06e^{-0.06x}$	84.5%
3	70	27.06	$y = 0.037e^{-0.037x}$	72.8%

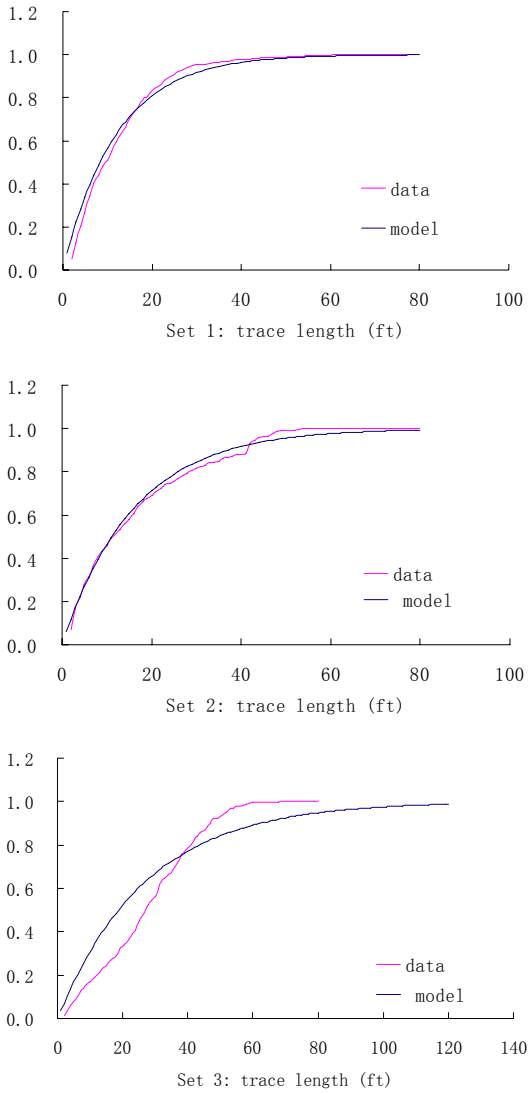

Figure 5.11 Experimental and model CDF of fracture trace length

Gupta and Adler (2006) show that when discs intersect a cylindrical tunnel, "*the distributions of disks can be known from the disk-plane inverse formula when most of the*

trace lengths are less than the gallery diameter." The tunnel diameter of this research is 26.73 feet. Figure 5.11 shows that all fracture sets well satisfy Gupta's and Adler's criterion to consider disc-cylinder intersections as disc-plane intersections, and therefore I can use disc-plane inverse formulas to derive the diameter distribution of discs from the trace length distribution provided by Tonon and Chen (2007). In particular, if the trace length is exponentially distributed, the diameter distribution of the fracture discs is (Tonon and Chen, 2007):

$$f(y) = A\frac{BesselK[1, Ay]}{BesselK[0, Ac]}, \tag{5.4}$$

where A is the parameter of exponential distribution of the trace length $f(x) = Ae^{-Ax}$;

c is the minimum fracture diameter; and *BesselK[.]* is the modified Bessel function of the second kind (Arfken and Weber, 2001).

If Eq.(5.4) is integrated between 0 and y, we can get the CDF of the fracture diameter distribution:

$$F(y) = \int_c^y f(y)dy = 1 - \frac{BesselK[0, Ay]}{BesselK[0, Ac]}. \tag{5.5}$$

Eq.(5.5) will be used as the sampling formula when I simulate fracture diameters later.

Tonon and Chen (2007) also present the closed-form expression of the average diameter if the trace length follows exponential distribution:

$$\overline{d} = \frac{\pi}{2ABesselK[0, cA]}, \tag{5.6}$$

where $\overline{d}$ is the average fracture diameter, A is the parameter of exponential distribution $f(x) = Ae^{-Ax}$ of the trace length. In fact, the average trace length is $\overline{L}$=1/A, because the mean of the exponential distribution is the reciprocal of the exponential distribution parameter A.

5.2.2.3 Intensity spatial correlation analysis and simulation

1) Simulation domain and grids

If the original coordinate system is set as: X points to the east, Y points to the north, and Z points upwards, then the coordinate system for simulation domain is set as: Y' is horizontal and parallel to the tunnel axis; X' is orthogonal to Y' in the horizontal plane; Z' points upwards; and the origin locates at tunnel center, as shown in Figure 5.12. Starting from the geotechnical profile (Figure 5.8), the cross section is simplified as shown in Figure 5.12. In order to ensure accuracy in the simulation and reduce calculation time, the simulation domain is limited to the area within dashed line, which is three tunnel diameters above, left and right to the tunnel axis, and half a tunnel diameter below the tunnel axis. In the longitudinal direction, the domain extends 2000 feet. Above the upper boundary of the simulation domain, the ground is assumed to be hydraulically homogeneous in each zone (soil zone, transition zone and bedrock). In the simulation domain, rock fractures are simulated and water flows through the fracture network from the upper domain into the tunnel. Boundary conditions are given in Section 5.2.2.7.

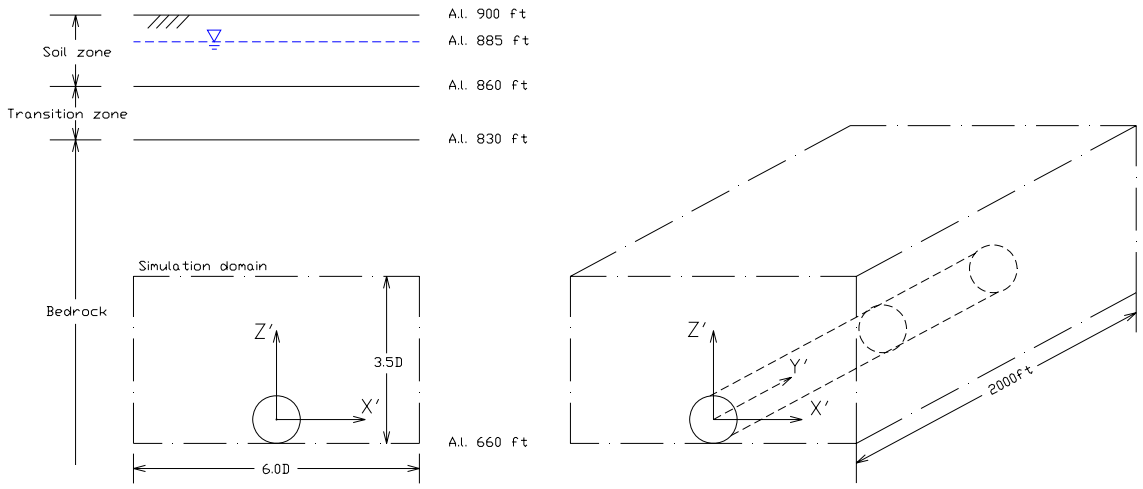

Figure 5.12 Cross section of simulation domain

The simulation grid is different for different fracture sets because they have different orientations and different average diameter. For example, for fracture set 3 (open joints, main water transmission fracture set), the average normal to the fracture has orientation α/β=335° /57° , the tunnel axis has the orientation $\alpha_t/0$=162° /0° . Therefore, as shown in Figure 5.13, all fractures project onto the cross section of Figure 5.12 as ellipses.

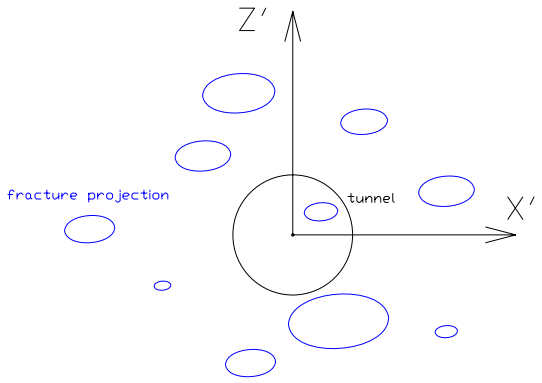

Figure 5.13 Fracture set 3 projections onto tunnel cross section

The rotation angle γ from X'-Y'-Z' to X''-Y''-Z'' in Figure 3.14 can be determined by using Eq.(3.63); in this case, $\gamma = -85.5°$ (clockwise for negative angles). Recall that angle θ is the angle between the fracture normal and the tunnel axis. When a fracture projects onto the tunnel cross-section plane, the minor axis of the ellipse is equal to the fracture diameter times $\cos\theta$. For fracture set 3, θ= 57.3° , which is obtained from the following equation (Priest, 1993).

$$\theta = \arccos\left[\cos\left(\alpha - \alpha_t\right)\cdot\cos\beta\right] \tag{5.7}$$

Simulation scanlines are located with a regular spacing ($l_{x''} = \overline{L_{x''}}/C_{P2}$ $= 0.866\bar{D}\cdot\cos\theta/C_{P2}$ and $l_{z''} = \overline{L_{z''}}/C_{P2} = 0.866\bar{D}/C_{P2}$, $\bar{D} = 12.73 ft$, Eq.(3.61)) in X'' and Z'' directions. C_{P2} is obtained as 1.6 from Figure 1.7 by using θ=57.3 (Table

5.12) and K=17.2 (Table 5.10). In Y'' direction, they are subdivided into intervals of 20 feet. There is no specific reason to choose 20 feet as the interval length. Based on the author's experience, however, this is a good compromise between a small number of nodes and accuracy. The whole simulation grid can be seen in Figure 5.14.

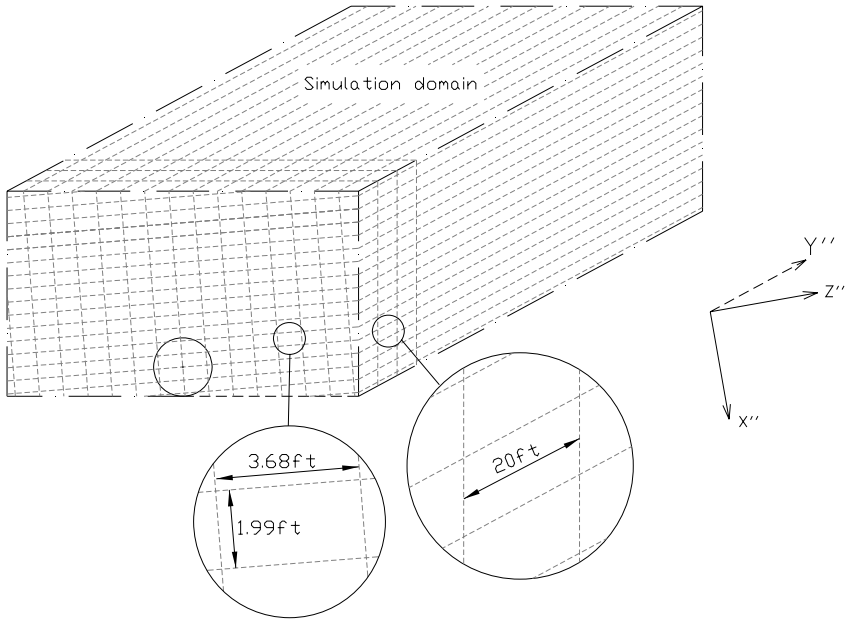

Figure 5.14 Simulation grid for fracture set 3

Similarly, simulation grids for fracture sets 1 and 2 can be built using the same procedure. All parameters for simulation grids are summarized in Table 5.12.

Table 5.12 Simulation grid parameters

Set	θ	C_{p2}	γ	Grid spacing		
				$d_{X''}$	$d_{Y''}$	$d_{Z''}$
1	79.3	1.6	14.3	0.74	20.00	4.01
2	20.6	1.0	14.3	8.00	20.00	8.55
3	57.3	3.0	-85.5	1.99	20.00	3.68

2) Spatial correlation analysis

As described in Chapter 3, fracture intensity has a certain spatial correlation. This spatial correlation depicts specific fracture spatial arrangement patterns, which are typically clustered rather than regular or random. In this case study, the observation

scanlines are drawn on the tunnel along the tunnel axis. Each scanline is subdivided into 20-foot intervals.

In order to use the observed intensity values in later simulation as conditional data, observation scanlines are located over or as close as possible to simulation scanlines. Table 5.13 shows coordinates of observation scanlines for each fracture set in each $X"\text{-}Y"\text{-}Z"$ system. One example for scanlines of fracture set 3 are shown in Figure 5.15.

Table 5.13 Coordinates of observation scanlines (ft)

	Scanline 1		Scanline 2		Scanline 3	
Set	$X"$	$Y"$	$X"$	$Y"$	$X"$	$Y"$
1	-11.89	6.42	3.57	12.84	13.08	0.00
2	-8.00	8.55	8.00	8.55	-	-
3	-5.96	-11.03	-5.96	11.03	-	-

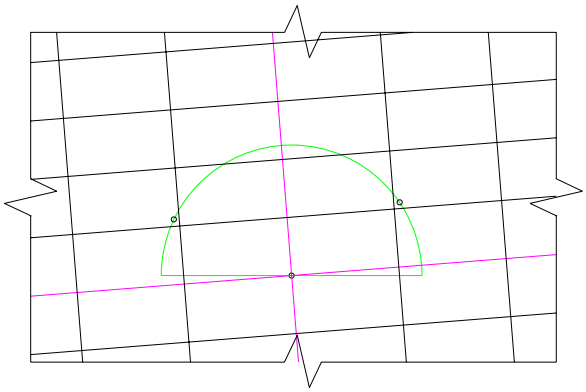

Figure 5.15 Scanlines for fracture set 3 (cross section view); two points represent the scanlines

Each 1,000-foot-long scanline is subdivided into fity 20-foot long intervals. For each interval, the fractures intersecting scanline (fracture intensities) are counted. The data are in Appendix M.

There are two methods to analyze the semivariograms (Deutsch and Journel, 1998) of intensity. One is based on the assumption that variables are Gaussian distributed,

and the other is based on non-parametric methods. Correspondingly, there are also two simulation methods: Gaussian sequential simulation and indicator sequential simulation (Section 3.2). After several trials during research, Gaussian method was found not suitable to fracture intensity simulation because the data has a highly skewed distribution. Its spatial correlation model cannot be reproduced very well; even normal score transformation (Deutsch and Journel, 1998) is performed to the raw data. On the other hand, the non-parametric method gives a good results and it is used for analyzing the semivariograms of fracture intensity. The indicator sequential simulation is also used for later simulations.

As described in Chapter 3, several thresholds need to be picked if a non-parametric method is used. The fracture intensity distributions for all fracture sets are shown in Table 5.14 and Figure 5.16.

Table 5.14 Fracture intensity distributions

Set		Intensity (fracture/20ft)				
		0	1	2	3	4
Numbers	1	130	11	7	1	1
	2	69	22	6	1	2
	3	66	26	3	5	0
Percentage	1	86.7%	7.3%	4.7%	0.7%	0.7%
	2	69%	22%	6%	1%	2%
	3	66%	26%	3%	5%	0%

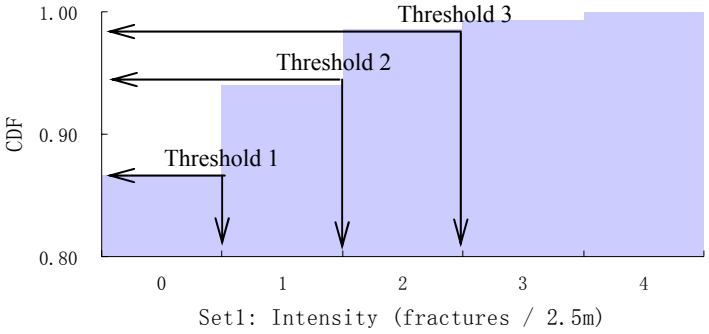

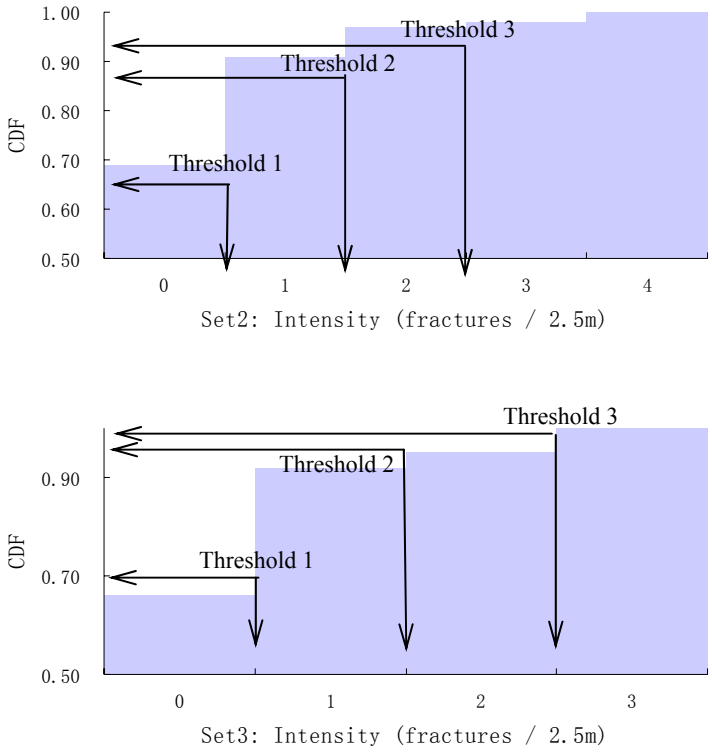

Figure 5.16 Intensity CDFs for three fracture sets

As described in Section 3.3.1.1, thresholds typically equally subdivide the intensity CDF. However, here the minimum threshold that can be selected is 0.5. 2.5 is a critical value for the intensity because it will control the percentage of cells which contain fractures more than 2.5. So as not to miss information between 0.5 and 2.5, 1.5 is also chosen. Therefore, 0.5, 1.5, and 2.5 are picked as thresholds for semivariogram analysis and later indicator simulation. GAM.EXE (Deutsch and Journel, 1998) is used to compute the intensity semivariograms. Semivariograms in the Y" direction for three thresholds are shown in Figure 5.17.

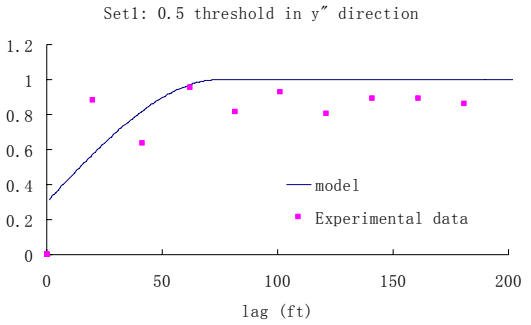
Set1: 0.5 threshold in y″ direction
1.2
1
0.8
0.6
0.4
0.2
0
0
50
100
150
200
lag (ft)
model
Experimental data

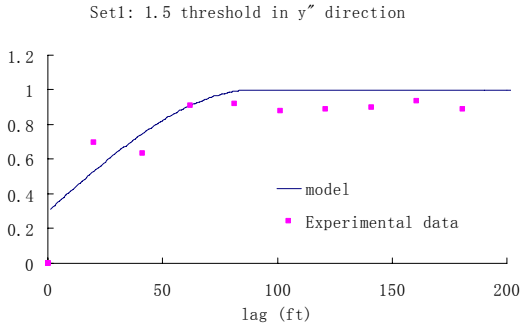
Set1: 1.5 threshold in y″ direction
1.2
1
0.8
0.6
0.4
0.2
0
0
50
100
150
200
lag (ft)
model
Experimental data

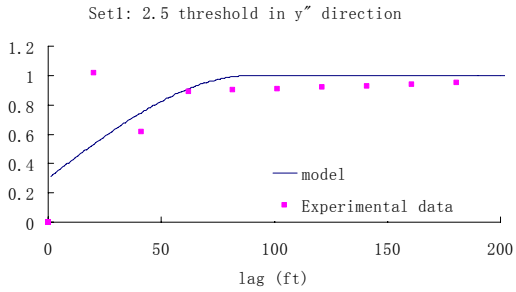
Set1: 2.5 threshold in y″ direction
1.2
1
0.8
0.6
0.4
0.2
0
0
50
100
150
200
lag (ft)
model
Experimental data

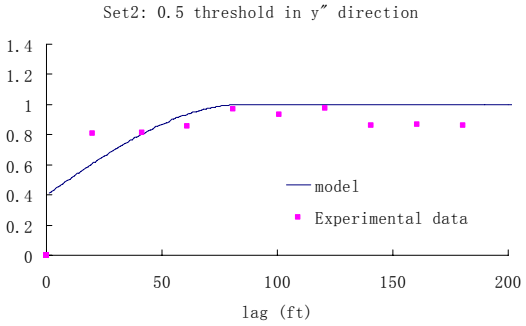
Set2: 0.5 threshold in y″ direction
1.4
1.2
1
0.8
0.6
0.4
0.2
0
0
50
100
150
200
lag (ft)
model
Experimental data

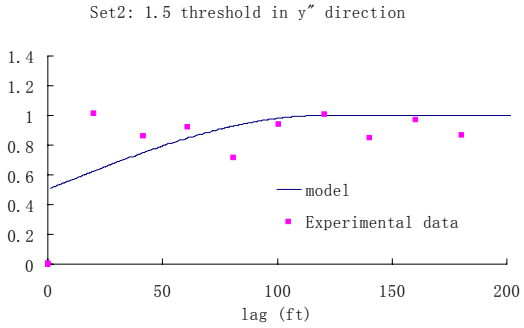
Set2: 1.5 threshold in y″ direction
1.4
1.2
1
0.8
0.6
0.4
0.2
0
0
50
100
150
200
lag (ft)
model
Experimental data

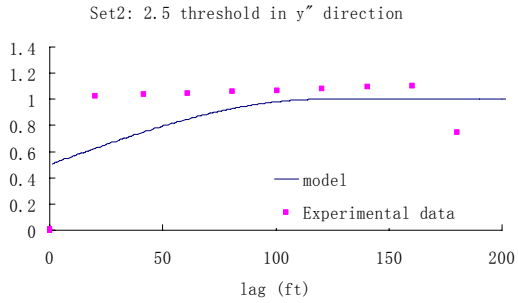
Set2: 2.5 threshold in y″ direction
1.4
1.2
1
0.8
0.6
0.4
0.2
0
0
50
100
150
200
lag (ft)
model
Experimental data

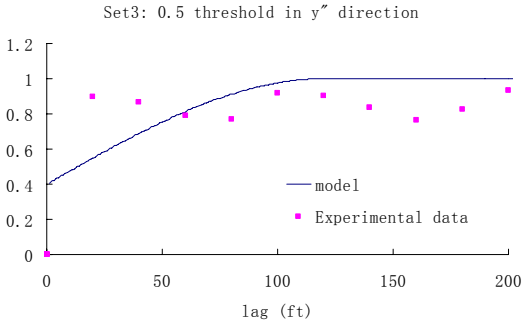
Set3: 0.5 threshold in y″ direction
1.2
1
0.8
0.6
0.4
0.2
0
0
50
100
150
200
lag (ft)
model
Experimental data

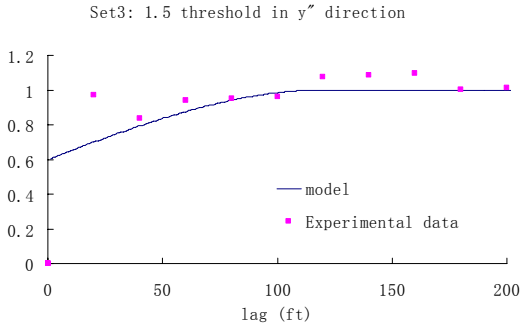
Set3: 1.5 threshold in y″ direction
1.2
1
0.8
0.6
0.4
0.2
0
0
50
100
150
200
lag (ft)
model
Experimental data

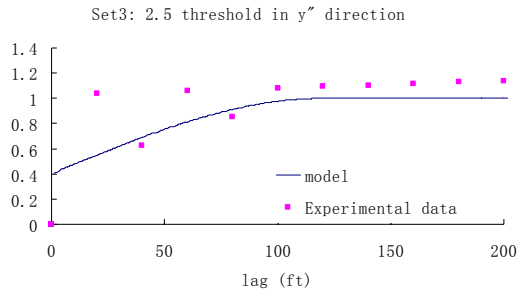

Figure 5.17 Semivariograms of intensity thresholds 0.5, 1.5 and 2.5 for three fracture sets

If spherical models (Chapter 3, Eq.(3.11)) are used to fit the experimental data sets (solid lines in the above figures), semivariogram model parameters are obtained as shown in Table 5.15. As explained in Chapter 3, because there are limited data in the $X"\text{-}Z"$ plane, it is assumed that fractures are more likely to happen and propagate in the plane orthogonal to the fracture normal. Therefore, long ranges are set for the $X"$ and $Z"$ directions. In this case, 400 feet is chosen for three fracture sets.

Table 5.15 Spatial correlation model parameters

Set	Intensity threshold	Nugget effect	Range (ft)		
			X''	Y''	Z''
1	0.5	0.3	400	75	400
	1.5	0.3	400	90	400
	2.5	0.3	400	90	400
2	0.5	0.4	400	85	400
	1.5	0.5	400	120	400
	2.5	0.5	400	120	400
3	0.5	0.4	400	120	400
	1.5	0.6	400	120	400
	2.5	0.4	400	120	400

3) Intensity simulation

Based on the parameters listed in Table 5.15 and the conditional indicator sequential simulation method (Chapter 4), SISIM.EXE (Deutsch and Journel, 1998) was used to simulate the fracture intensity in the proposed domain. It is hard to visually show

all simulation results in three dimensions. One slice at Y''=190 ft is ploted in Figure 5.18 to show what the simulation result looks like.

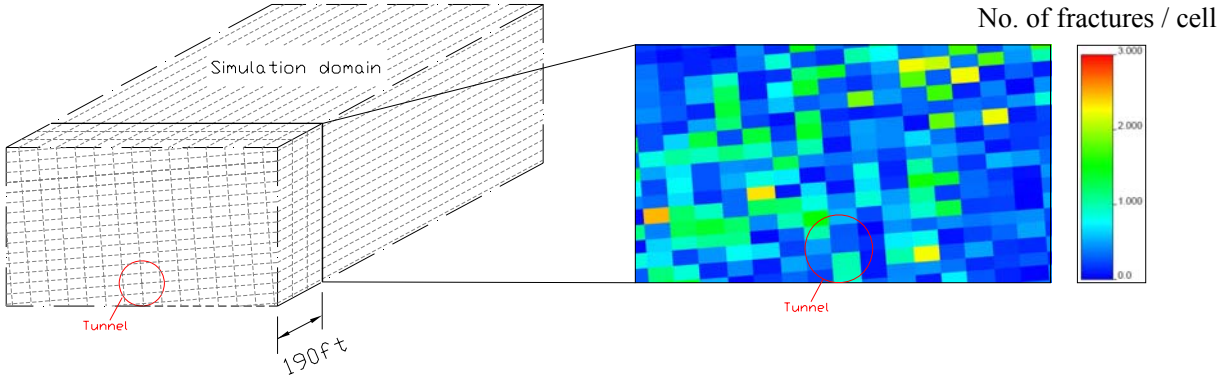

Figure 5.18 Intensity simulation result on one slice (at Y''=190ft) for fracture set 3

Similarly, intensities of fracture sets 1 and 2 are also implemented on their simulation grids with the conditional data observed on scanlines.

5.2.2.4 Locating fractures

In Step 5.2.2.3, the fracture intensity is simulated in each cell with a certain spatial correlation between cells (semivariogram models). Now, individual fractures are Poisson located in each cell. This randomness should not smear the existing spatial correlation because the cell size is relatively much smaller than the correlation ranges. The fracture center coordinates (X''_C, Y''_C, Z''_C) are sampled by:

$$\begin{aligned} X''_C &= X''_0 + (R_1 - 0.5) S_x \\ Y''_C &= Y''_0 + (R_2 - 0.5) S_y \\ Z''_C &= Z''_0 + (R_3 - 0.5) S_z , \end{aligned} \tag{5.8}$$

where X''_0, Y''_0, Z''_0 are the cell center coordinates; R_1, R_2, R_3 are random numbers between 0 and 1; and $S_{x''}$, $S_{y''}$, $S_{z''}$ are cell dimensions in X'', Y'' and Z'' directions, respectively.

As far as the fracture orientation, Eq.(5.3) can be used. If a random number from 0 to 1 is assigned to p and the Fisher distribution parameter K is taken from Table 5.10, then the angle θ between a simulated direction and the mean value (Table 5.10) is calculated using Eq.(5.3). If the other angle φ is randomly picked from 0 to 360 (uniform distribution is chosen), then the directional cosines in the global xyz system are:

$$\begin{bmatrix} n_x \\ n_y \\ n_z \end{bmatrix} = \begin{bmatrix} \cos\alpha & \sin\alpha & 0 \\ -\sin\alpha & \cos\alpha & 0 \\ 0 & 0 & 1 \end{bmatrix} \begin{bmatrix} 1 & 0 & 0 \\ 0 & \cos\beta & \sin\beta \\ 0 & -\sin\beta & \cos\beta \end{bmatrix} \begin{bmatrix} \sin\theta\cos\varphi \\ \cos\theta \\ \sin\theta\sin\varphi \end{bmatrix}, \quad (5.9)$$

where α is the mean trend of fracture normal and β is the mean plunge of fracture normal (downwards) given in Table 5.10. The globle xyz system is as follows: z points upwards, y points to North, x points to East. See Appendix E for coordinate system rotation details.

5.2.2.5 Fracture diameter sampling

Starting from the cumulative distribution function for the diameter (Eq.(5.5)) derived from the trace length distribution, for each fracture set fracture diameters are sampled by using the Monte Carlo method. In Eq.(5.5), the minimum diameter (c) in the distribution needs to be set. One foot is used for the minimum diameter. Actually, there would have been no major difference if I had choosen a number between zero and a couple of feet for parameter c, because very small diameter fractures have very small aperture, which are typically filled with minerals during the geological history of the rock mass. Even if they are not filled, flow always follows prominent openings instead of fine apertures because small openings have high resistance to the flow.

5.2.2.6 Sampling fracture aperture and assigning hydraulic conductivity

Once fracture diameters are sampled, fracture apertures can be sampled from its CDF. However, because there are no hydraulic aperture measurements in this project, the published trace length-aperture relationship (in Figure 3.9) is used as the first estimation. Once the diameters are simulated, the trace length can be obtained from Eq.(3.57).

Here the obtained aperture is the mechanical aperture, not the hydraulic aperture. However, it is the hydraulic aperture that controls the flow in the fracture. The hydraulic aperture may be estimated by using Barton's (Barton et al., 1985) model based on the mechanical aperture and the joint roughness coefficient (JRC). However, there is no JRC measurement in this project. As mentioned in Section 3.1.4, Lee et al. (2001) carried out hydraulic tests and determined that the ratio of the hydraulic aperture to the mechanical aperture is about 0.20. This ratio between the mechanical and hydraulic aperture is used here.

The relationship (Eq.(3.56)) is calibrated by flow data during the early construction. The calibrated parameter is used to carry out further simulations in portions of the rock mass where the tunnel has not yet been excavated. The calibrated relationship can be seen in Table 5.16, in which trace lengths and mechanical apertures are in minimeter.

Table 5.16 Calibrated trace length-mechanical aperture relationships

Set	Relationship
1	$L = 69721 \cdot b^{0.7}$
2	$L = 81330 \cdot b^{0.7}$
3	$L = 91197 \cdot b^{0.7}$

In order to save computing memory and ensure accuary, fractures with a diameter less then 3m or hydraulic aperture less than 0.05mm are ignored because small fractures have very small apertures, and are not likely to intersect other fractures. Because of cubic law, most of the flow concentrates in large fractures.

5.2.2.7 Defining and assigning boundaries

In the simulation domain, boundaries include a recharge boundary (outer boundary), which is located in the upper boundary of the simulation domain (Figure 5.12), and a discharge boundary (tunnel).

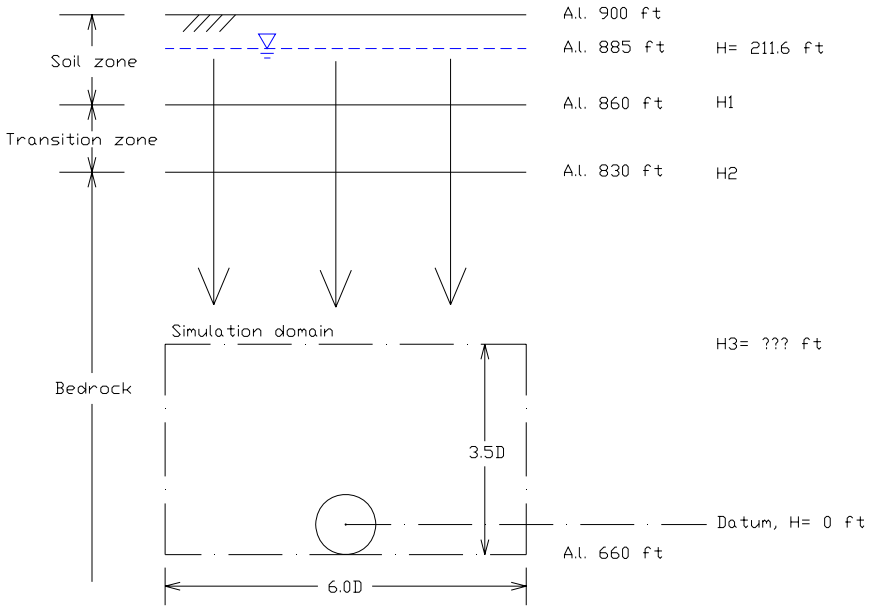

Figure 5.19 Sketch for upper boundary head calculation

If the tunnel axis is set as the datum where the elevation head is zero, then the total head at static head level is 211.6 feet. Because during construction the tunnel is a drained boundary where the pressure head is zero, the total head at the tunnel wall varies from –R to R, where R is tunnel radius. Since the tunnel dimension is very small compared to the overlaying rock mass, the total head at the tunnel perimeter can be considered as zero everywhere. The analytical solution in Lei (1999 and 2000) given in Section 2.3.2.3.1.3 indicates that this simplification brings no major difference if the tunnel is deep.

In order to determine the total head at the upper boundary of the simulation domain, let us assume that steady state flow goes from the static head level (total head =

211.6 feet) to the tunnel boundary (total head = 0 feet). The materials in each zone (soil, transition zone, and bedrock) have homogeneous hydraulic conductivities. From the project GBR, the approximate hydraulic conductivity for each zone is listed in Table 5.17.

Table 5.17 Appoximate hydraulilc conductivity of different layers

layer	k cm/s
Soil (silty sand)	5×10^{-5}
Transition zone	1×10^{-5}
Bedrock (above simulation domain)	5×10^{-6}
Bedrock (in simulation domain)	1×10^{-6}

Form Darcy's law, the flow rate is equal to the product of the hydraulic conductivity of the medium and the pressure drop, all divided by the length over which the pressure drop takes place:

$$q = -k \cdot \frac{\Delta H}{L}. \tag{5.10}$$

For a flow system composed of a series of different hydraulic conductivities, we have:

$$q = -k_s \cdot \frac{H - H_1}{L_s} = -k_t \cdot \frac{H_1 - H_2}{L_t} = -k_{r-up} \cdot \frac{H_2 - H_3}{L_{r-up}} = -k_{r-low} \cdot \frac{H_3 - 0}{L_{r-low}}, \tag{5.11}$$

where subscript s indicates soil, t indicates transition zone, r-up indicates bedrock above simulation zone, and r-low indicates bedrock in simulation zone.

By solving Eq(5.11), the head at the simulation upper boundary (H_3) is 171.4 feet (52.2m), which can be used as the constant head recharge boundary at the top of simulation domain.

For the tunnel boundary, curved intersections with fractures and boundary cannot be dealt with in the analytical-numerical method of Section 4.2. Therefore, a regular octagon with an equivalent area is used to represent the circular tunnel, as shown in Figure 5.20. Because the pressure head at the tunnel perimeter is zero during construction, the total head on each side of the regular octagon approximately equals the

elevation at the center of each side. The laterial boundaries are set as no flow boundaries by removing fractures out of the simulation domain. All boundary input can be found in Table 5.18.

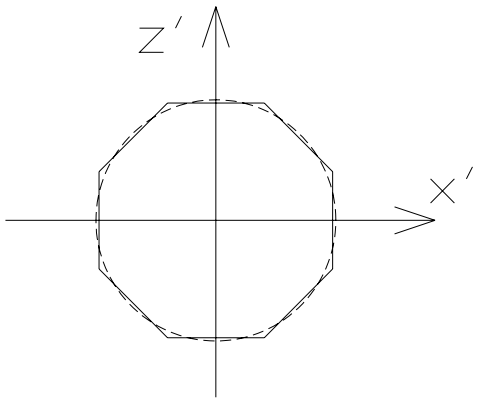

Figure 5.20 Equivalent tunnel cross section

Table 5.18 Input list of boundaries

Boundary No.	Boundary Location Type*	Point on the plane			Orientation of normal			Type †	Boundary value (m or m/s)
		X (m)	Y (m)	Z (m)	nx	ny	nz		
1	1(recharge)	0.000	0.000	24.44	0.000	0.000	-1.000	1	52.25
2	2(tunnel)	0.000	0.000	3.966	0.000	0.000	1.000	1	3.97
3	2(tunnel)	0.000	0.000	5.609	0.673	0.219	0.707	1	2.80
4	2(tunnel)	3.772	1.226	0.000	0.951	0.309	0.000	1	0.00
5	2(tunnel)	0.000	0.000	-5.609	0.673	0.219	-0.707	1	-2.80
6	2(tunnel)	0.000	0.000	-3.966	0.000	0.000	-1.000	1	-3.97
7	2(tunnel)	0.000	0.000	-5.609	-0.673	-0.219	-0.707	1	-2.80
8	2(tunnel)	-3.772	-1.226	0.000	-0.951	-0.309	0.000	1	0.00
9	2(tunnel)	0.000	0.000	5.609	-0.673	-0.219	0.707	1	2.80

Note: * 1 indicates outer boundary; 2 indicates inner boundary.

† 1 indicates constant head boundary; 2 indicates constant flow boundary.

5.2.2.8 Combining all fracture sets, generating fracture network and running flow analysis in the fracture network

After all fracture properties were simulated (including location, orientation, diameter, aperture and hydraulic conductivity), all three fracture sets were put into one

input file and code *FractureFlow* was run. Code *FractureFlow* implements the following steps: fracture-fracture and fracture-boundary intersections, out-of-domain intersection removal, dead-end removal, cross-intersection subdivision, and flow solution.

5.2.2.9 Results, interpretation, and comparison with observed flow data

5.2.2.9.1 Results

Twenty realizations were carried out. The number of simulated fractures, the number of intersections in the simplified discrete fracture network, and the number of fractures that form each network are summarized in Table 5.19. Twenty realizations without spatial correlation were also carried out, which are shown in Table 5.20.

Table 5.19 Summary of simulation results with spatial correlation

Realization No.	Simulated fracture No.				Final No. of fractures	Final Intersection No. in DFN
	Set 1	Set 2	Set 3	Total		
1	191	301	708	1200	900	3669
2	182	212	758	1152	786	3315
3	151	303	483	937	618	2161
4	152	236	655	1043	715	2366
5	199	305	730	1234	905	4008
6	221	231	826	1278	965	4571
7	183	200	948	1331	992	4055
8	154	276	594	1024	731	2731
9	150	225	822	1197	909	4298
10	232	262	744	1238	896	3675
11	241	249	866	1356	1066	4951
12	207	357	577	1141	854	3436
13	170	240	745	1155	883	3856
14	158	245	737	1140	842	3030
15	252	259	782	1293	952	3814
16	257	253	583	1093	805	3338
17	142	253	948	1343	957	4131
18	164	167	552	883	619	2403
19	286	300	877	1463	1128	5201
20	245	239	743	1227	903	3367

Table 5.20 Summary of simulation results without spatial correlation

Realization No.	Simulated fracture No.				Final No. of fractures	Final Intersection No. in DFN
	Set 1	Set 2	Set 3	Total		
1	163	209	607	979	690	2140
2	164	200	629	993	721	2216
3	154	189	642	985	700	2062
4	141	180	586	907	582	1623
5	178	203	606	987	679	2070
6	132	198	620	950	655	1845
7	142	183	633	958	683	1884
8	144	207	596	947	698	1991
9	146	177	651	974	659	2173
10	163	198	636	997	712	2113
11	150	214	606	970	695	2108
12	157	197	635	989	707	2041
13	159	188	632	979	724	2164
14	137	186	595	918	636	1715
15	175	188	600	963	698	2022
16	127	191	627	945	682	1948
17	142	185	629	956	633	1864
18	147	205	591	943	648	1963
19	143	176	659	978	707	2213
20	171	201	626	998	733	2143

Note: The number of intersections (NI) increases exponentially with the number of fractures (NF), and the number of entries in the stiffness matrix of the flow equation system are the square of NI. In order to save computer memory, fractures which have diameter less then 3m or hydraulic aperture less than 0.05mm were ignored.

The total flow rates and flow rates normalized by the tunnel length with spatial correlation are summarized in Table 5.21. The total flow rates and flow rates normalized by the tunnel length without spatial correlation are summarized in Table 5.22.

Table 5.21 Summary of total flow rates with spatial correlation

Realization No.	Total flow rate		Flow rate/tunnel length	
	L/s	gpm	L/s/100m	gpm/mile
1	2.42	38.3	0.79	202.4
2	2.09	33.1	0.69	174.8
3	1.01	16.0	0.33	84.7
4	2.71	43.0	0.89	227.1
5	3.02	47.9	0.99	252.9

6	2.56	40.6	0.84	214.2
7	3.86	61.1	1.27	322.9
8	2.54	40.2	0.83	212.4
9	1.94	30.7	0.64	162.1
10	1.90	30.0	0.62	158.6
11	2.60	41.2	0.85	217.7
12	1.98	31.4	0.65	165.9
13	3.06	48.5	1.00	256.0
14	1.83	29.0	0.60	153.0
15	2.49	39.4	0.82	208.2
16	2.07	32.8	0.68	172.9
17	2.96	47.0	0.97	248.1
18	2.27	35.9	0.74	189.6
19	3.18	50.4	1.04	266.2
20	4.13	65.5	1.36	345.9

Table 5.22 Summary of total flow rates without spatial correlation

Realization No.	Total flow rate		Flow rate/tunnel length	
	L/s	gpm	L/s/100m	gpm/mile
1	1.41	22.3	0.46	117.9
2	1.53	24.2	0.50	127.6
3	1.31	20.7	0.43	109.4
4	1.09	17.3	0.36	91.3
5	1.48	23.5	0.49	124.1
6	1.00	15.8	0.33	83.3
7	1.45	23.0	0.48	121.6
8	1.84	29.2	0.60	154.1
9	1.87	29.7	0.61	156.7
10	1.90	30.1	0.62	158.9
11	1.64	26.1	0.54	137.6
12	1.31	20.7	0.43	109.4
13	1.87	29.6	0.61	156.3
14	0.76	12.0	0.25	63.3
15	2.03	32.1	0.66	169.6
16	1.14	18.1	0.37	95.5
17	1.14	18.1	0.37	95.5
18	2.30	36.5	0.76	192.7
19	1.71	27.1	0.56	143.0
20	1.45	23.0	0.48	121.6

5.2.2.9.2 Analysis and interpretation

The total flow rates per tunnel length from the 20 individual realizations (in Table 5.21) are shown in Figure 5.21. The average of these 20 flow rates is 0.83 L/s/100m

(211.8 gpm/mile). The standard derivation is 0.23 L/s/100m (58.7 gpm/mile), which gives a coefficient of variation equal to 27.7 percent.

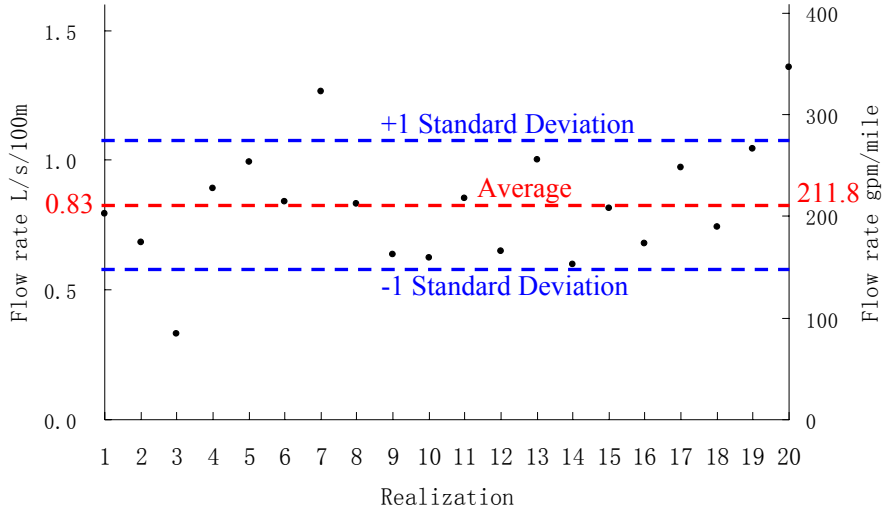

Figure 5.21 Flow rates per tunnel length of 20 realizations with spatial correlation

As shown in Figure 5.22, for the no spatial correlation case, the average of 20 flow rates (in Table 5.22) is 0.5 L/s/100m (126.5 gpm/mile). The standard derivation is 0.124 L/s/100m (31.6 gpm/mile), which gives a coefficient of variation equal to 25.0 percent.

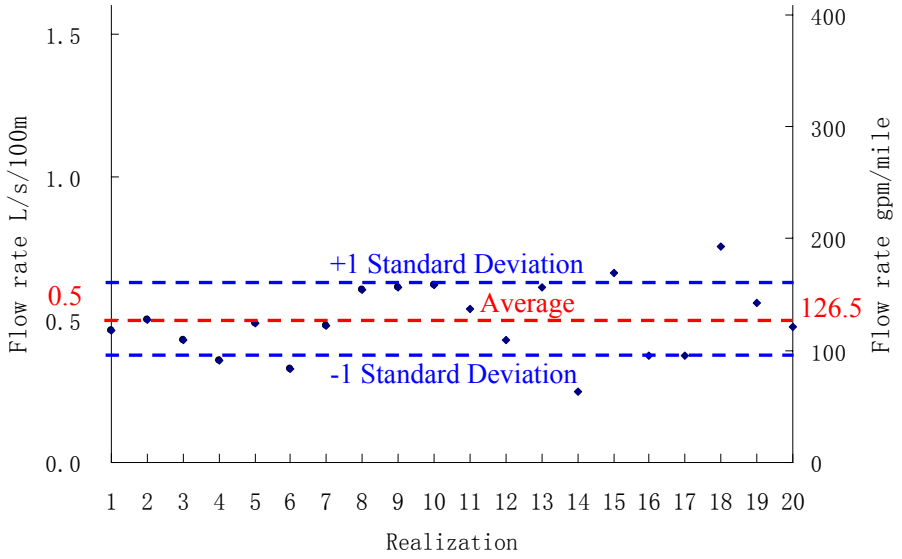

Figure 5.22 Flow rates per tunnel length of 20 realizations without spatial correlation

To illustrate, Figure 5.23 plots the flow rates and flow locations for realization No. 1 (in Table 5.21) with spatial correlation; all other plots may be found in Appendix N. Figure 5.24 plots the flow rates and flow locations for realization No. 1 (in Table 5.22) without spatial correlation; all other plots may be found in Appendix O. As shown in Figure 5.23, the flow is not uniformly distributed along the simulated tunnel length. However, for the no fracture spatial correlation case, the flow is more uniform, as shown in Figure 5.24. The locally non-perfect uniformity is caused by the discrete fracture network model.

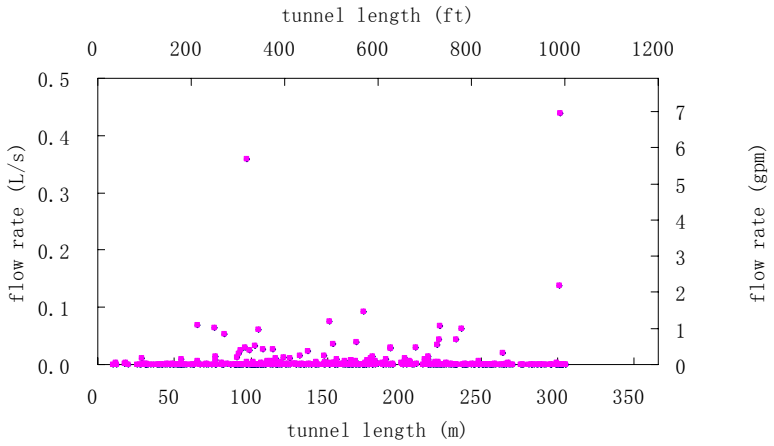

Figure 5.23 Flow rates at different tunnel location with spatial correlation (Realization No.1)

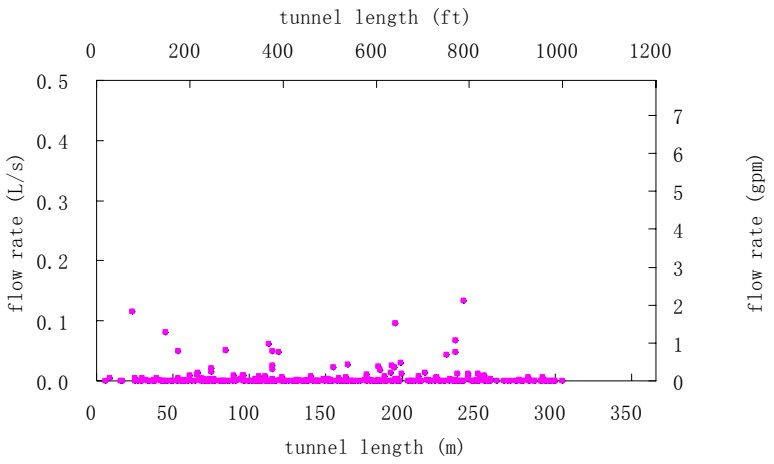

Figure 5.24 Flow rates at different tunnel location without spatial correlation (Realization No.1)

As shown in Table 5.23, there are three major flow events (each flow event is greater than 0.1 L/s), which account for 0.935 L/s (i.e., 38.6 percent of the total flow). There are eight medium flow events (each flow events is between 0.1 and 0.05 L/s), which account for 0.544 L/s (i.e., 22.5 percent of the total flow). All other 224 flow events (each flow event is less than 0.05 L/s) account for 0.940 L/s (i.e. 38.8 percent of the total flow). The average values of 20 realizations with spatial correlation are summarized in Table 5.24. On average, the major flow events (each flow is greater than>0.1 L/s) only occured five times. The flow at these five locations accounts for 40.4 percent of the total flow. According to the flow measurements (see Appendix K), there are six major flow events (>0.1 L/s, or 1.59 gpm) in this region, which are: ~2 gpm, ~2 gpm, 3~4 gpm, 3~4 gpm, ~2 gpm and ~4 gpm. The simulation occurrence of major flow events (5) matches the real measurements well (6). As for the no spatial correlation simulation, the occurrence of major flow events and percentage of total flow are also summarized in Table 5.24. The occurrence of major events (2.3) is less than half of the measured major events occurrence (6). The percentage of total flow in the major flow range is 21.8 percent, which is also much lower than the measurement (42.5 percent). In

no spatial correlation simulation, around half (46.2 percent) of the flow contributed by the medium flow events (0.1~0.05 L/s), which means the flow with fracture spatial correlation is more concentrated than the flow without fracture spatial correlation.

Table 5.23 Flow events summary of Realization No.1

Flow range L/s	Occurrence	Total flow rate in this range L/s	Percentage of Total flow
> 0.1	3	0.935	38.7%
0.1 ~ 0.05	8	0.544	22.5%
<0.05	224	0.940	38.8%

Table 5.24 The average flow events summary of 20 realizations

	Simulation Average with spatial correlation		Simulation Average without spatial correlation		Field measurements	
Flow range L/s	Occurrence	Percentage of Total flow	Occurrence	Percentage of Total flow	Occurrence	Percentage of Total flow
>0.1	5.0	40.4%	2.3	21.8%	6	42.5%
0.1 ~ 0.05	5.4	15.1%	7.5	46.2%	No data	No data
<0.05	238.2	44.5%	174.1	32.0%	No data	No data

From Figure 5.23, Table 5.23 and Table 5.24, we can find that the simulations are consistent with Raymer's statement (2005) that "*most of the inflow occurs in a few places, some of the inflow occurs in many places, and much of the tunnel is dry.*" The reason why this phenomenon occurs is that fluid only flows in connected fractures and fractures are clustered. This phenomenon cannot be reproduced by any continous model (Sections 2.2 and 2.3) whether analytical or numerical, and may not be reproduced by discontinous models (Section 2.4) if rock fractures are clustered and these models are not able to simulate clustering.

5.2.2.9.3 Comparison with flow measurements

All of the flow amounts yielded by the tunnel itself and introduced during construction are recorded in this project. By subtracting the flow amount introduced during construction from the total water amount pumped from the tunnel, the water produced by the tunnel and the construction shaft is summaried in Table 5.25 and Figure 5.25.

Table 5.25 Flow comparison between simulation and measurements

Measured Date	Total flow L/s (gpm)	Tunnel length km (mile)	Total flow per tunnel length L/s/100m (gpm/mile)	Averaged simulated flow L/s/100m (gpm/mile)
10/15/2009	6.1 (97.1)	0.518 (0.32)	1.18 (301.6)	0.83 (211.8)
12/6/2009	10.0 (158.7)	1.372 (0.85)	0.73 (186.2)	
1/15/2010	12.6 (200.0)	1.859 (1.16)	0.68 (173.1)	
2/26/2010	13.6 (214.9)	2.377 (1.48)	0.57 (145.5)	
3/15/2010	19.8 (314.0)	2.621 (1.63)	0.76 (192.8)	

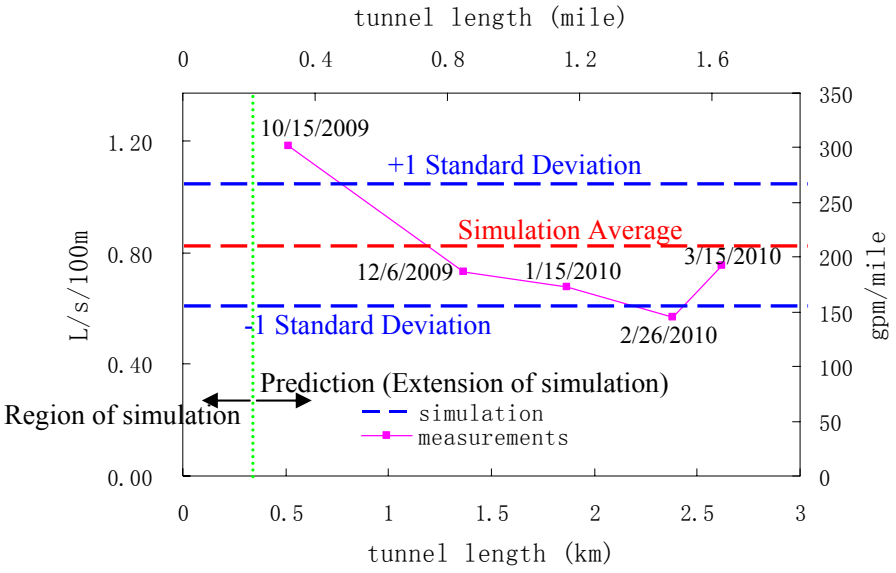

Figure 5.25 Flow rate measurements during construction

The dash lines in Figure 5.25 represent the simulation average and +/- one standard deviation. The flow in the first 300m (1000ft) is the simulation results. The next 2700m is the extension of the first portion. From Figure 5.25, the simulation result is very

close to the measurements, especially as the tunnel gets longer. The flow rate at 0.5km (10/15/2009) is around 45 percent higher than the others (and the simulations). The reason could be that the entire excavated tunnel was near the construction shaft, which drained out the water around it and distorted the reading for the tunnel. However, when the excavated tunnel was longer, the effect of the shaft was not prominent because the flow rate shown in Figure 5.25 is normalized by the tunnel length. The flow rate at 2.4km (2/26/2010) is slightly lower than the others (and the simulations) perhaps because there is less precipitation during the winter season, which was the main recharge source for the groundwater. Because of the lagged effect of surface water to groundwater, the low flow rate happened in the end of February.

5.3 Conclusions and future work

In this section, conclusions of this research are drawn, including findings, simulation methods, and results. Possible future work is highlighted, which could take advantage of this simulation procedure and be applied to the industry.

5.3.1 CONCLUSIONS

5.3.1.1 Findings

1.1 In hard rock tunnel, "*most of the inflow occurs in a few places, some of the inflow occurs in many places, and much of the tunnel is dry*" (Raymer, 2005).

1.2 The reason for Finding 1.1 is that rock fractures are commonly distributed in a clustered pattern, rather than in a random or regular pattern.

1.3 Larger fractures (with larger aperture) tend to occur in the more intense fracture zones.

5.3.1.2 Methodology

2.1 The spatial arrangement (clustering properites) of rock fractures can be modeled by the semi-variogram of fracture intensity.

2.2 Because the fracture intensity is typically skewed distributed, the Sequential Indicator Simulation (SIS) is a better simulation technique than Sequential Gaussian Simulation (SGS), because SIS is a non-parametric method, whereas SGS needs the assumption of multi-variate Gaussianity for the data.

2.3 The Monte Carlo sampling could be used to reproduce the property 1.3 because the CDF of the aperture is very steep in the small aperture range and very flat in the large aperture range.

2.4 Poisson locating fractures in each simulation cell does not affect the global spatial arrangement and, in turn, the fluid flow in the medium, although the spatial correlation between fractures in each cell cannot be reproduced.

2.5 Complicated flow fields in discrete fracture networks can be simulated and modeled by the analytical-numerical method developed here on the basis of the work published by Long et al. (1985).

5.3.1.3 General results

3.1 The precision of simulating flow in fractured media largely depends on the representation of the fracture clustering property, which could be reproduced with the proposed algorithm.

3.2 The model parameters can be calibrated and validated by comparing fracture and flow measurements during tunnel construction.

3.3 The discrete fracture network model with clustering property can reproduce Finding 1.1, which cannot be done by any continous model, whether analytical or numerical, and may not be done by some discontinous models if rock fractures are clustered.

5.3.2 FUTURE WORK

1. The method presented in this dissertation is based on the basic assumption that all fractures have a circular shape. Although this assumption allows one to use Long et al.'s (1985) analytical-numerical method, it would be more general if the fracture shape could be extended to the elliptical shape. The most difficult work is to find the analytical solution to the potential in an ellipse caused by a point source in it.

2. The other two assumptions of this research are steady state flow and constant boundary conditions (total head or flow rate). More research can be done to extend this method to make it applicable to transient flow and varied boundary conditions.

3. Future research could be done on the relationship between fracture mechanical aperture and hydraulic aperture by considering rock type, diagenesis, filling, normal stress and shear stress of fractures based on the existing results in this area.

4. Laubach's (2003) approach could be introduced into this research to identify sealed and open fractures. Since this is done on thin sections of rock cores by measuring the abundance of rock-mass cement that precipitated after fractures ceased to open, the simulation will be more accurate.

5. As for spatial correlation simulation, only fracture intensity is considered in this work. Co-kriging can consider more than one variable spatial correlation. For example, fracture intensity and fracture aperture (or trace length) could have a certain spatial arrangement. It is possible to use co-kriging as the engine to run simulations, which could reproduce the spatial correlation of intensity and other properties together.

6. More validations by tunnel case histories could be done to simplify or finally formulate a simulation procedure that can be widely used in the tunnel industry.

APPENDIX

Appendix A: Heaviside step function

The Heaviside step function, also called the unit step function, is a discontinuous function whose value is zero for negative argument and one for positive argument.

The Heaviside function is the integral of the Dirac delta function:

$$H(x) = \int_{-\infty}^{x} \delta(t)\, dt$$

where, $\delta(t)$ is the Dirac delta function, which is defined by:

$$\delta(t) = \begin{cases} +\infty, t = 0 \\ 0, \quad t \neq 0 \end{cases} \text{ constrain to } \int_{-\infty}^{\infty} \delta(t)\, dt = 1$$

An Discrete form of the Heaviside step function, as a function of a discrete variable n:

$$H[n] = \begin{cases} 0, n < 0 \\ 1, n \geq 0 \end{cases}$$

where, n is an integer.

Appendix B: Summary of analytical flow models

1. Transient flow models

1) Constant head test solution of Jacob and Lohman (1952)

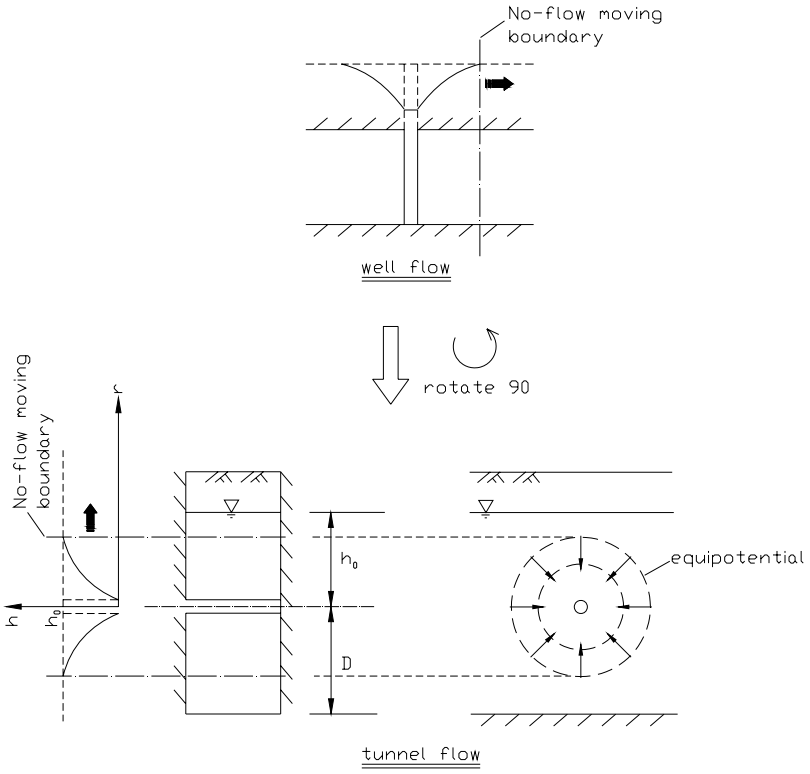

$$Q = 2\pi T s_w \cdot G(\alpha)$$

where $\alpha = \dfrac{Tt}{Sr_w^{\,2}}$, $G(\alpha) = \dfrac{4\alpha}{\pi}\int_0^\infty x e^{-\alpha x^2}\left\{\dfrac{\pi}{2} + \tan^{-1}\left[\dfrac{Y_0(x)}{J_0(x)}\right]\right\} dx$

in which $J_0(x)$ and $Y_0(x)$ are Bessel functions of zero order of the first and second kinds.

$G(\alpha) \cong \dfrac{1}{\ln\left(1+\sqrt{\pi\alpha}\right)}$ Perrochet, 2005a

2) A progressive tunnel drilling through homogeneous formations can be considered by this simplification. (Perrochet, 2005b)

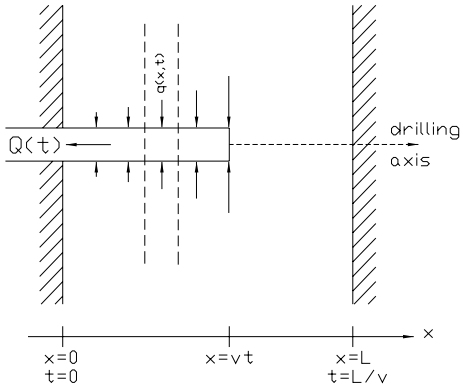

$$Q(t)=\int_0^{vt}\frac{2\pi K s_t H(L-x)}{\ln\left(1+\sqrt{\frac{\pi K}{S r_0^{\,2}}\left(t-\frac{x}{v}\right)}\right)}dx$$

3) A progressive tunnel drilling through heterogeneous formations can be considered by this simplification. (Perrochet & Dematteis, 2007)

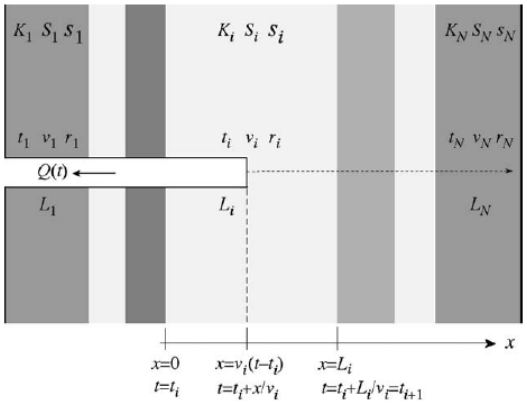

$$Q(\alpha)=2\pi\sum_{i=1}^{N}H(t-t_i)\times\int_0^{v_i(t-t_i)}\frac{K_i s_i H(L_i-x)}{\ln\left[1+\sqrt{\frac{\pi K_i}{S_i r_i^{\,2}}\left(t-t_i-\frac{x}{v_i}\right)}\right]}dx$$

where $t_i=\sum_{j=1}^{i-1}\frac{L_j}{v_j}$, $t_1=0$ with t_{N+1} as the total drilling time.

4) A approximate solution for a constant drawdown well or tunnel in the presence of an infinite linear constant head boundary in an ideal confined aquifer. (Renard, 2005)

$$\frac{Q(t)}{2\pi T s_w} \cong \frac{A}{\ln\left(1+\sqrt{\frac{\pi T t}{r_w{}^2 S}}\right)} + \frac{B}{\ln\left(\frac{2R}{r_w}-1\right)} + C$$

$$A = \frac{2}{\pi}\arctan\left[\frac{(2R/r_w-2)^2}{\pi T t/(r_w{}^2 S)}\right]$$

$$B = \frac{2}{\pi}\arctan\left[\frac{\pi T t/(r_w{}^2 S)}{(2R/r_w-2)^2}\right]$$

$$C = \frac{AB}{2}\frac{\ln\left[(2R/r_w-1)(\sqrt{2}R/r_w-\sqrt{2}+1)\right]}{\left[\ln(2R/r_w-1)\right]^2 \ln(\sqrt{2}R/r_w-\sqrt{2}+1)}$$

2. Early linear flow model (Kawecki, 2000; Löw, 2002)

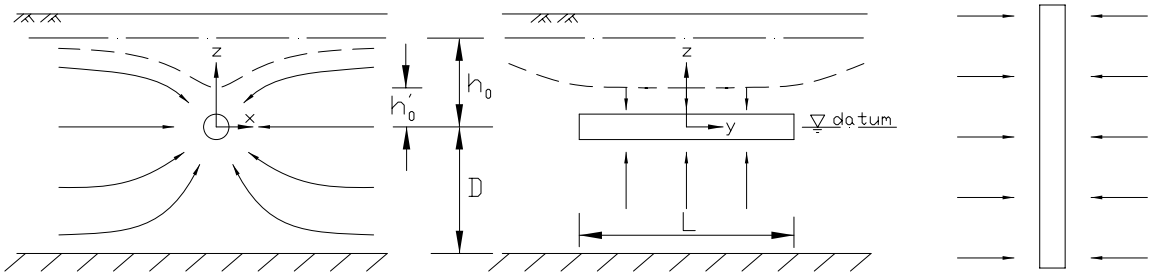

tunnel end view tunnel side view tunnel plan view

$$h_0 - h_t = \frac{1}{\sqrt{\pi}} \cdot \frac{2Q}{LK_x(h_0'+h_0+2D)} \cdot \sqrt{\frac{(h_0'+h_0+2D)K_x t}{2S_y}} + \frac{Q}{2\pi L\sqrt{K_x K_z}} \cdot \sigma_z$$

where $\sigma_z = \ln\left(\frac{h_0'+D}{2\pi r_0}\right) + 0.25 \cdot \ln\left(\frac{K_x}{K_z}\right) - \ln\left(\sin\frac{180^0 D}{h_0'+D}\right)$

$$h_0' = h_t + \frac{Q}{2\pi L\sqrt{K_x K_z}} \cdot \sigma_z$$

3. Steady flow models

1) Constant head model

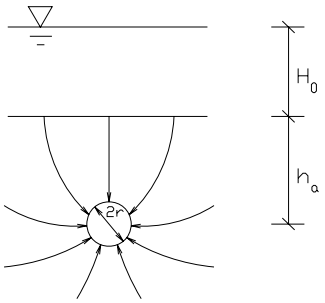

(a) $Q = \dfrac{2\pi KL\left(H_0 + h_a\right)}{\ln\left(2h_a / r_0\right)}$ (Goodman et al., 1965)

$$Q = \frac{2\pi KLh'}{\ln\left(2h' / r\right)}$$

(b) Using Green's function method (El Tani, 1999) to consider different tunnel section and anisotropic, non-homogenous aquifer

Tunnel section and aquifer properties	Permeability	Water inflow [1]
Tunnel of square section. c : side length. h : centre depth. [2] Isotropic and homogeneous aquifer. [3]	k [4]	$Q = \frac{2\pi k\, h_r}{\frac{6-\pi}{4} + \ln\frac{2^{3/4} h}{c}}$ [5]
Tunnel of elliptical section. a and b : horizontal and vertical semi-axis. h : centre depth.	k	$Q = \frac{2\pi k\, h_r}{\ln\frac{4h}{a+b}\sqrt{1+\frac{a^2-b^2}{4h^2}}}$ [6]
Two circular identical tunnels. r : radius. h : depth of centres. 2d : distance of centres. [7]	k	$Q = \frac{2\pi k\, h_r}{\ln\frac{2h}{r}\frac{\sqrt{d^2+h^2}}{d}}$
Two circular identical tunnels. r : radius. h : depth of centres. 2d : distance of centres. H : depth of an impervious layer. [8]	k	$Q = \frac{2\pi k\, h_r}{\ln\frac{4}{\pi}\frac{H}{r}\frac{\mathrm{tg}(\pi h/2H)}{\mathrm{th}(\pi d/2H)}\sqrt{\frac{\mathrm{ch}(\pi d/H)-\cos(\pi h/H)}{\mathrm{ch}(\pi d/H)+\cos(\pi h/H)}}}$
Tunnel of circular section. r : radius. h : centre depth. Anisotropic aquifer.	k_H k_V [9]	$Q = \frac{2\pi\sqrt{k_H k_V}\, h_r}{\ln\frac{4h}{r}\frac{\sqrt{k_H}}{\sqrt{k_H}+\sqrt{k_V}}\sqrt{1+\frac{k_V-k_H}{k_H}\frac{r^2}{4h^2}}}$ [10]
Tunnel of circular section. r : radius. h : centre depth. Non-homogeneous aquifer.	$ke^{-2\alpha z}$ [11]	$Q = 2\pi k e^{-2\alpha h}\frac{h_r I_0(\alpha r) - r I_1(\alpha r)}{K_0(\alpha r) - I_0(\alpha r)K_0(2\alpha h)}$ [12]

[1] The quantity of water that flows into the tunnel is Q and is in (m^3/s/meter of tunnel) and per tunnel if there is more than one. It is transformed into (l/s/km of tunnel) when it is multiplied by 10^6.

[2] h is the depth of the centre of the tunnel below the water table or sea bottom for undersea tunnels.

[3] Aquifers in the following are isotropic unless the contrary is mentioned and homogeneous unless the contrary is mentioned.

[4] k (m/s).

[5] Resultant head is $h_r = h - p_T/\gamma$ (m). p_T is the mean pressure on the tunnel edge and γ the specific weight of water. p_T is zero for a drained tunnel and different from zero for a partially drained tunnel.
For undersea tunnels, sea depth is added to the resultant head which becomes $h_r = h + h_S - p_T/\gamma$ where h_S is sea depth.

[6] Approximated integration with $(a^2 - b^2)/h^2 < 1$.

[7] $2d > 2r$.

[8] H is the depth of an impervious base below the water table or sea bottom for an undersea tunnel.
$H > h + r$ and $2d > 2r$.

[9] k_H is the horizontal permeability and k_V is the vertical permeability.

[10] Approximated integration with $(k_V - k_H)r^2/k_H h^2 < 1$.

[11] α (m^{-1}) is the intensity of the non-homogeneity. z is the depth below the water table or sea bottom for an undersea tunnel.

[12] $I_0(x)$, $I_1(x)$ and $K_0(x)$ are modified Bessel functions of the first kind of order zero and one and the second kind of order zero.

(c) the same model, other method (Lei, 1999)

$$Q = \frac{2\pi KL\left(H_0 - h_t + p_a/\gamma_w\right)}{\ln\left[h_a/r_0 + \sqrt{\left(h_a/r_0\right)^2 - 1}\right]}$$

(d) Heuer's empirical method, which is based on the solution of Goodman and considers the permeability property of rock mass, and thus more useful in industry. (graph method) (Heuer, 1995; Heuer, 2005)

(e) extended solution of Goodman's (have a changing hydraulic conductivity) (Zhang & Franklin, 1993)

$$Q = \frac{2LK_1\pi \exp\left[-a_1 h_a\right]\cdot\left[\exp\left(a_1 H_0\right)-1\right]}{a_1\left[K_0\left(\frac{A}{2}r_0\right)-K_0\left(Ah_a\right)\right]}$$

For A=0 (the hydraulic conductivity does not change with depth), it is simplified to Goodman's solution.

2) Dupuit horizontal flow model

(a) semi-empirical solution (Goodman et al., 1965)

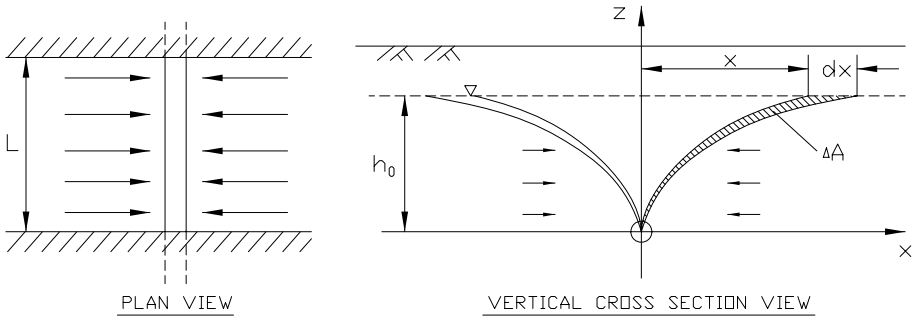

$$Q = \sqrt{\frac{8KL^2 h_0{}^3 S_y t}{3C}}$$

(b) Lateral model (Raymer, 2005)

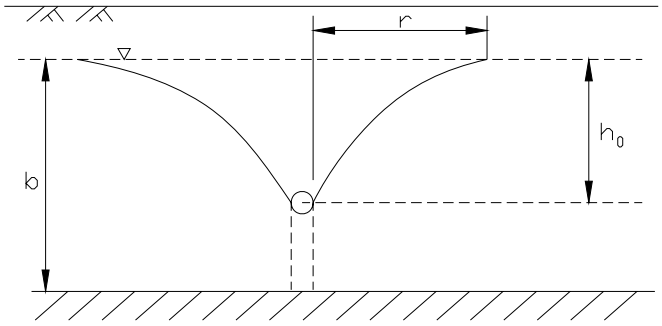

$$Q = 2L\sqrt{2WTh_0}'$$

(c) solution assuming elliptical water table (Perrochet & Musy, 1992)

Case 1:

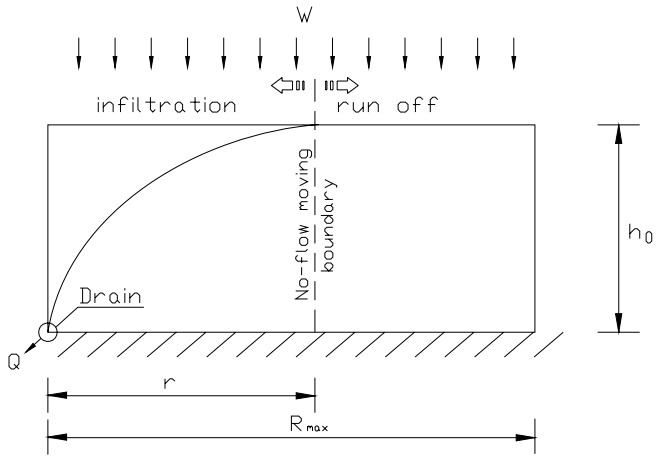

$$q(t) = \frac{Kh_0^{\,2}}{r}$$

$$r(t) = \sqrt{\left(R_0^{\,2} - \frac{Kh_0^{\,2}}{W}\right)\exp\left[-\left(\frac{8W}{S_y(4-\pi)h_0}\right)^t\right] + \frac{Kh_0^{\,2}}{W}}$$

Case 2:

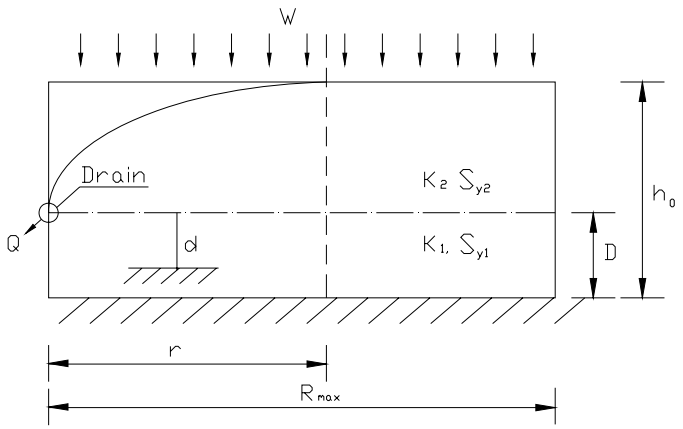

Perrochet and Musy's lateral flow model (case 2)

$$q(t)=\frac{\left[2K_2d+K_1(h_0-D)\right](h_0-D)}{r}$$

$$r(t)=\sqrt{\left(R_0{}^2-\frac{\left[2K_2d+K_1(h_0-D)\right](h_0-D)}{W}\right)\exp\left[-\left(\frac{8W}{S_{y1}(4-\pi)(h_0-D)}\right)^t\right]+\frac{\left[2K_2d+K_1(h_0-D)\right](h_0-D)}{W}}$$

3) other classical steady state flow models

(a) steady state flow into tunnel face (point-sink flow)

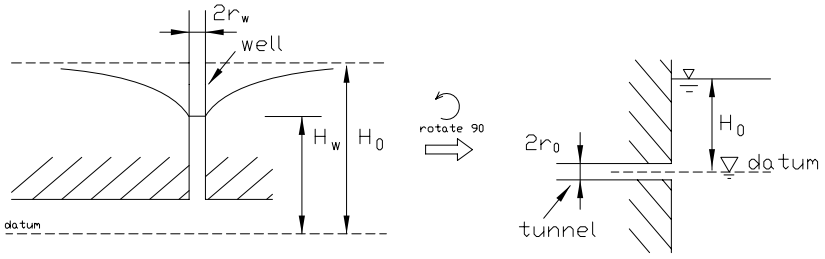

well flow tunnel face flow

$$Q=2\pi Kr_0H_0$$

(b) steady state flow into partially penetrated tunnel

(b-1) semi-infinite confined aquifer

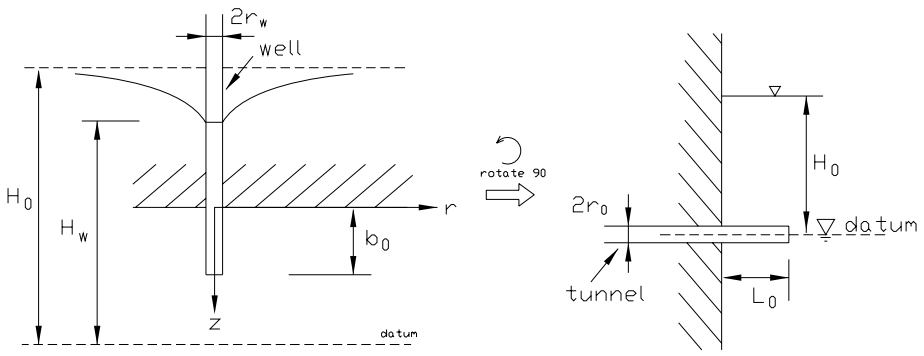

well flow tunnel flow

$$Q = \frac{4\pi K L_0 H_0}{Arsh\frac{0.25L_0}{r_0} + Arsh\frac{1.75L_0}{r_0}}$$

(b-2) finite confined aquifer

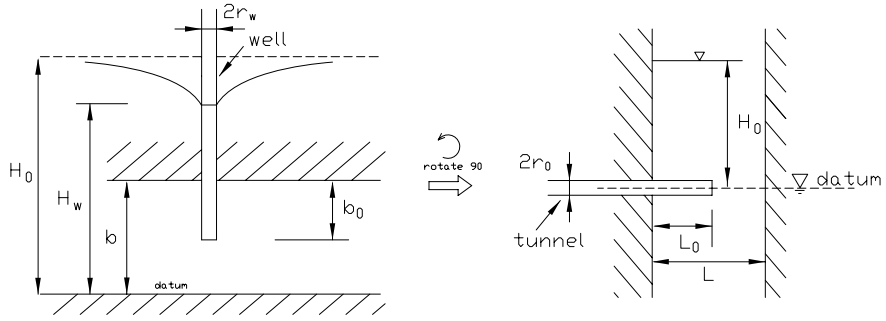

well flow tunnel flow

$$Q = \frac{4\pi K L_0 H_0}{2\ln\frac{4L}{r_0} - f(\alpha) - 2\alpha\ln\frac{4L}{R}}$$

$$Q = \frac{2\pi K L_0 H_0}{\ln\frac{R}{r_0}\left[1 + 7\sqrt{\frac{r_0}{2L_0}}\cdot\cos\left(\frac{\pi L_0}{2L}\right)\right]}$$

Appendix C: Bessel function

The solutions to the modified Bessel differential equation

$$x^2\frac{d^2y}{d^2x}+x\frac{dy}{dx}-\left(x^2+n^2\right)y=0$$

are the modified Bessel function of the first and second kinds, and can be written as:

$$y=a_1J_n\left(-ix\right)+a_2Y_n\left(-ix\right)$$

$$=c_1I_n\left(x\right)+c_2BesselK\left[n,x\right]$$

where, $J_n\left(x\right)$ is a Bessel function of the first kind, $Y_n\left(x\right)$ is a Bessel function of the second kind, $I_n\left(x\right)$ is a modified Bessel function of the first kind, and $BesselK\left[n,x\right]$ is the modified Bessel function of the second kind.

- The integral formula of $J_n\left(x\right)$ is:

$$J_n\left(x\right)=\frac{1}{\pi}\int_0^{\pi}\cos\left(n\theta-x\sin\theta\right)d\theta$$

- The integral formula of $Y_n\left(x\right)$ is:

$$Y_n\left(x\right)=\frac{1}{\pi}\int_0^{\pi}\sin\left(x\sin\theta-n\theta\right)d\theta-\frac{1}{\pi}\int_0^{\infty}\left[e^{nt}+\left(-1\right)^n e^{-nt}\right]e^{-x\sinh t}dt$$

- The integral formula of $I_n\left(x\right)$ is:

$$I_n\left(x\right)=\frac{1}{\pi}\int_0^{\pi}e^{x\cos\theta}\cos\left(n\theta\right)d\theta$$

- The integral formula of $BesselK\left[n,x\right]$ is:

$$BesselK\left[n,x\right]=\frac{\Gamma\left(n+1/2\right)\left(2x\right)^n}{\sqrt{\pi}}\int_0^{\infty}\frac{\cos\theta}{\left(\theta^2+x^2\right)^{n+1/2}}d\theta$$

Appendix D: Divergence operator and gradient operator

Divergence operator:

If let x, y, z be a system of Cartesian coordinates on a 3-dimensional Euclidean space, and let **i**, **j**, **k** be the corresponding basis of unit vectors. The divergence of a continuously differentiable vector field **F** = U**i** + V**j** + W**k** is equal to the scalar-valued function:

$$\nabla \cdot \mathbf{F} = div\, \mathbf{F} = \frac{\partial U}{\partial x} + \frac{\partial V}{\partial y} + \frac{\partial W}{\partial z}$$

Gradient operator:

If let x, y, z be a system of Cartesian coordinates on a 3-dimensional Euclidean space, and let **i**, **j**, **k** be the corresponding basis of unit vectors. The gradient of a scalar function *f* (x, y, z) is:

$$\nabla f = grad\ f = \frac{\partial f}{\partial x}\mathbf{i} + \frac{\partial f}{\partial y}\mathbf{j} + \frac{\partial f}{\partial z}\mathbf{k}$$

Appendix E: Coordinate system rotation for orientation simulation

If the true orientation of fracture normal is α / β, where α is trend (0~360) and β is plunge (downwards, 0~90), then I build a x_2-y_2-z_2 system in which x2 is horizontal (from global system point of view), y2 goes through the unit vector of true orientation, as shown in following figure.

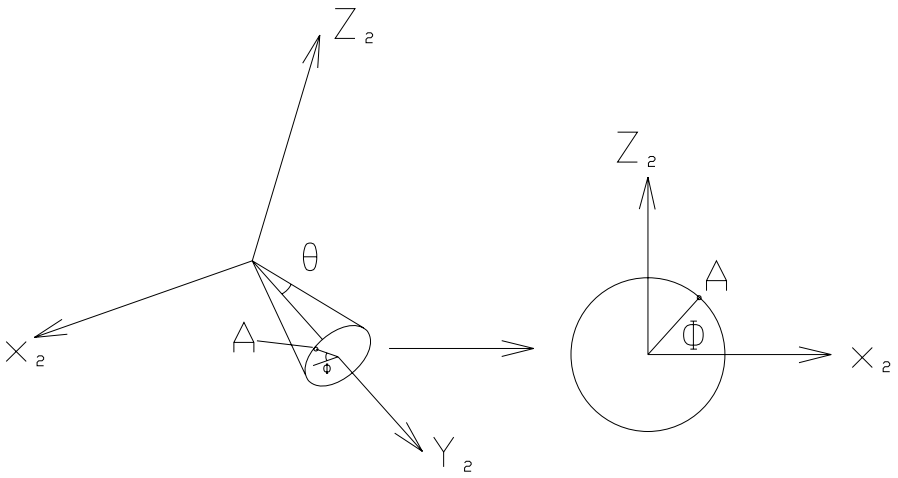

A is the point on a unit sphere and has the angle θ between the 'true' direction (y_2). Here ϕ is a random angle between 0 and 360.

A has the coordinates $\left(n_{x2}, n_{y2}, n_{z2}\right) = \left(\sin\theta\cos\phi, \cos\theta, \sin\theta\sin\phi\right)$ in system x_2-y_2-z_2.

If we rotate the system about x_2 axis with angle β to let y_2 be horizontal and z_2 be vertical to get system, x_1-y_1-z_1, as shown in the following figure.

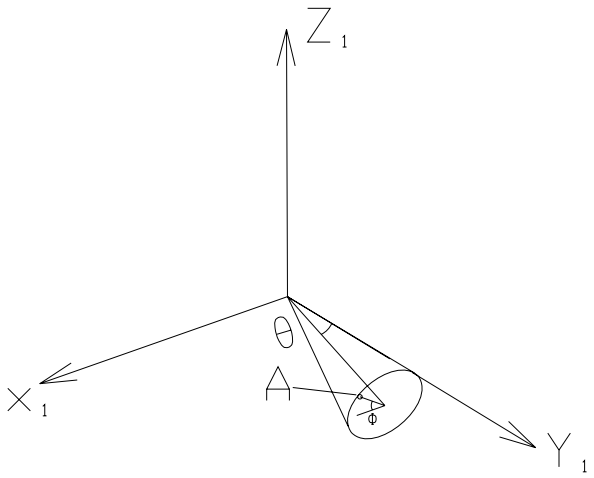

A has the coordinates $\left(n_{x1}, n_{y1}, n_{z1}\right)$ in system x_1-y_1-z_1.

$$\begin{bmatrix} n_{x1} \\ n_{y1} \\ n_{z1} \end{bmatrix} = \begin{bmatrix} 1 & 0 & 0 \\ 0 & \cos\beta & \sin\beta \\ 0 & -\sin\beta & \cos\beta \end{bmatrix} \begin{bmatrix} n_{x2} \\ n_{y2} \\ n_{z2} \end{bmatrix} = \begin{bmatrix} 1 & 0 & 0 \\ 0 & \cos\beta & \sin\beta \\ 0 & -\sin\beta & \cos\beta \end{bmatrix} \begin{bmatrix} \sin\theta\cos\varphi \\ \cos\theta \\ \sin\theta\sin\varphi \end{bmatrix}$$

If we rotate the system about z_2 axis with angle α to let y_1 point to north and x_1 point to east to get system, x-y-z (global system), as shown in the following figure.

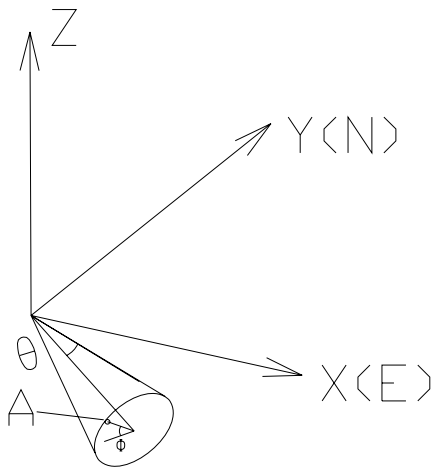

A has the coordinates $\left(n_x, n_y, n_z\right)$ in system x-y-z (global system).

$$\begin{bmatrix} n_x \\ n_y \\ n_z \end{bmatrix} = \begin{bmatrix} \cos\alpha & \sin\alpha & 0 \\ -\sin\alpha & \cos\alpha & 0 \\ 0 & 0 & 1 \end{bmatrix} \begin{bmatrix} n_{x1} \\ n_{y1} \\ n_{z1} \end{bmatrix} = \begin{bmatrix} \cos\alpha & \sin\alpha & 0 \\ -\sin\alpha & \cos\alpha & 0 \\ 0 & 0 & 1 \end{bmatrix} \begin{bmatrix} 1 & 0 & 0 \\ 0 & \cos\beta & \sin\beta \\ 0 & -\sin\beta & \cos\beta \end{bmatrix} \begin{bmatrix} \sin\theta\cos\varphi \\ \cos\theta \\ \sin\theta\sin\varphi \end{bmatrix}$$

This is the formula of randomly sampling an orientation which has the angle θ between the 'true' direction α / β.

Appendix F: Indicator Kriging example

If the following data (Fig. App F.1) are considered, the semi-variogram model (isotropic) is:

$$\gamma(\mathbf{h}) = \begin{cases} 0.2 + 0.8\left(\frac{3}{2}\frac{|\mathbf{h}|}{a} - \frac{1}{2}\frac{(|\mathbf{h}|)^3}{a^3}\right), & |\mathbf{h}| < a \\ 1, & |\mathbf{h}| \geq a \end{cases} \qquad \text{(App F.1)}$$

in which, a = 2 m.

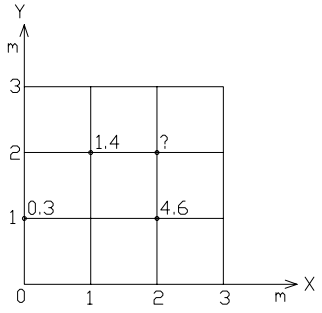

Fig. App F.1 Original data

If threshold "3" is selected, then the original data could be transformed into binary data set (Fig. App F.2):

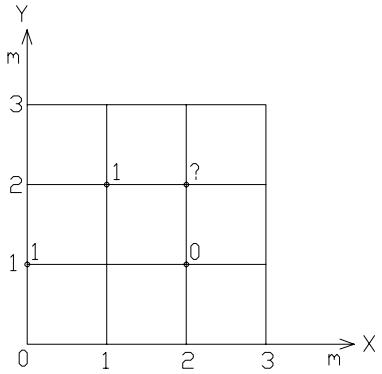

Fig. App F.2 Transformed data

For ordinary indicator kriging at location "?", from Eq.(3.47), one obtains the following equation system:

$$\begin{cases} \lambda_1 C_{11} + \lambda_2 C_{12} + \lambda_3 C_{13} + \mu = C_{10} \\ \lambda_1 C_{21} + \lambda_2 C_{22} + \lambda_3 C_{23} + \mu = C_{20} \\ \lambda_1 C_{31} + \lambda_2 C_{32} + \lambda_3 C_{33} + \mu = C_{30} \\ \lambda_1 + \lambda_2 + \lambda_3 = 1 \end{cases} \quad \text{(App F.2)}$$

where the subscript "1" indicates the datum at (1,2), "2" indicates the datum at (0,1), "3" indicates the datum at (2,1), and "0" indicates the estimated datum at (2,2). C_{ij} indicates the covariance between datum i and j, which can be compute by $1-\gamma_{ij}$.

By using semi-variogram model (App F.1), App F.2 becomes:

$$\begin{cases} \lambda_1 \cdot 1.000 + \lambda_2 \cdot 0.093 + \lambda_3 \cdot 0.093 + \mu = 0.250 \\ \lambda_1 \cdot 0.093 + \lambda_2 \cdot 1.000 + \lambda_3 \cdot 0.000 + \mu = 0.000 \\ \lambda_1 \cdot 0.093 + \lambda_2 \cdot 0.000 + \lambda_3 \cdot 1.000 + \mu = 0.250 \\ \lambda_1 + \lambda_2 + \lambda_3 = 1 \end{cases} \quad \text{(App F.3)}$$

By solving Eq.(App F.3), one obtains the coefficients:

$$\begin{cases} \lambda_1 = 0.4049 \\ \lambda_2 = 0.1726 \\ \lambda_3 = 0.4226 \end{cases} \quad \text{(App F.4)}$$

Then the estimation at location "?" can be obtained by Eq.(3.46):

$$I = \lambda_1 \cdot I_1 + \lambda_2 \cdot I_2 + \lambda_3 \cdot I_3 = 0.4049 \cdot 1 + 0.1726 \cdot 1 + 0.4226 \cdot 0 = 0.5775$$

Similarly, if the threshold is selected as "1", the transformed data becomes:

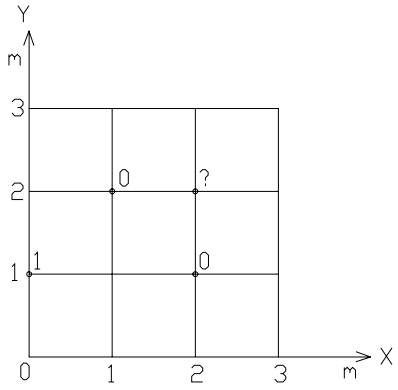

The estimation at the location "?" is 0.1726.

Appendix G: Luenberger Theorem

Let H be a Hilbert space and let $\{y_1, y_2, ..., y_n\}$ be a set of linearly independent vectors in H. Among all vectors $I(\mathbf{u}) \in H$ satisfying $(I(\mathbf{u}) \mid y_1) = c_1$, $(I(\mathbf{u}) \mid y_2) = c_2$,., $(I(\mathbf{u}) \mid y_n) = c_n$, the vector: $I^*(\mathbf{u}) = \sum_{\alpha=1}^{n} \lambda_\alpha \cdot y_\alpha$ is the one that has the minimum norm and the weights are solution to the system:

$$
\begin{aligned}
&y_1 \mid y_1 \cdot \lambda_1 + y_2 \mid y_1 \cdot \lambda_2 + ... + y_n \mid y_1 \cdot \lambda_n = c_1 \\
&y_1 \mid y_2 \cdot \lambda_1 + y_2 \mid y_2 \cdot \lambda_2 + ... + y_n \mid y_2 \cdot \lambda_n = c_2 \\
&\vdots \\
&y_1 \mid y_n \cdot \lambda_1 + y_2 \mid y_n \cdot \lambda_2 + ... + y_n \mid y_n \cdot \lambda_n = c_n
\end{aligned}
$$

Appendix H: Pedernales fall state park fracture data

1. Original spacing and aperture data

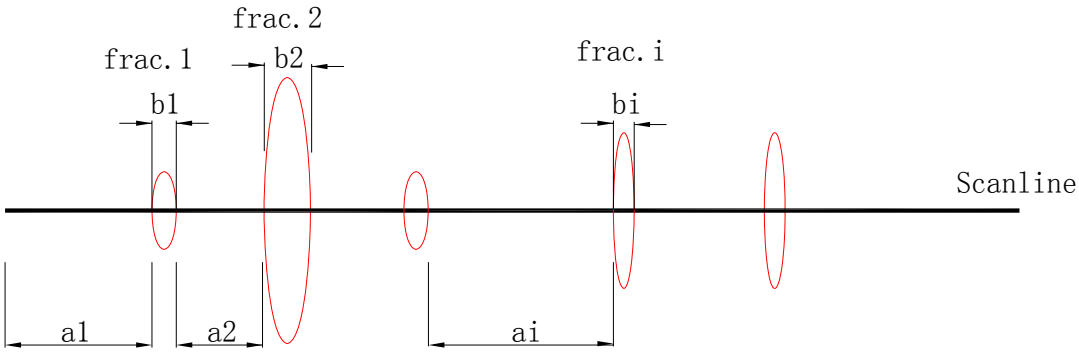

unit (mm)

No.	ai	bi	No.	ai	bi	No.	ai	bi	No.	ai	bi
1	5.490	0.140	29	0.610	1.400	57	6.900	0.115	85	15.200	0.175
2	7.000	0.050	30	0.330	0.265	58	4.900	0.060	86	8.700	0.060
3	86.680	0.175	31	1.100	0.215	59	57.000	0.075	87	1.100	0.620
4	22.500	0.050	32	0.920	0.140	60	6.500	0.075	88	0.400	0.075
5	1.700	0.050	33	3.550	0.060	61	27.300	0.095	89	6.000	0.060
6	164.000	0.060	34	9.100	0.060	62	47.110	0.075	90	4.860	0.075
7	3.100	0.075	35	22.100	0.060	63	21.600	0.060	91	3.300	0.095
8	12.200	0.050	36	0.350	0.075	64	21.000	0.095	92	43.780	0.140
9	4.240	0.115	37	0.310	0.265	65	5.400	0.095	93	192.000	0.330
10	0.490	0.115	38	163.350	0.215	66	0.400	0.115	94	129.000	0.215
11	0.095	0.050	39	314.340	0.050	67	13.500	0.500	95	81.500	0.175
12	0.610	0.215	40	7.000	0.215	68	0.750	0.140	96	3.900	1.750
13	2.700	0.265	41	2.100	0.075	69	0.500	0.060	97	4.950	0.060
14	0.900	0.095	42	134.500	0.400	70	7.100	0.950	98	445.640	0.215
15	0.900	0.075	43	3.400	0.075	71	3.000	0.095	99	16.700	0.400
16	24.690	0.330	44	0.300	0.075	72	4.300	0.050	100	10.700	0.095
17	1.000	1.150	45	0.310	0.060	73	6.000	0.095	101	1.800	1.150
18	2.000	0.265	46	4.600	0.050	74	1.100	0.075	102	65.500	0.075
19	0.500	0.215	47	8.100	0.140	75	2.800	0.075	103	192.000	2.150
20	7.900	2.150	48	116.090	0.075	76	3.100	0.060	104	17.500	0.500
21	5.505	0.095	49	24.260	0.060	77	2.500	0.075	105	3.900	0.950
22	3.100	1.150	50	3.290	0.060	78	0.600	0.750	106	5.500	0.620
23	5.130	0.075	51	1.200	0.115	79	49.700	0.095	107	12.000	0.950
24	5.840	0.265	52	3.200	0.060	80	16.500	0.115	108	4.000	0.500
25	0.080	0.075	53	1.380	0.175	81	2.700	0.095	109	2.500	0.500
26	1.550	0.215	54	17.000	0.075	82	0.640	0.215	110	15.000	0.620
27	0.250	0.215	55	2.630	0.175	83	3.200	0.115	111	3.000	0.500
28	2.600	2.700	56	6.500	0.140	84	2.700	0.095	112	4.000	0.620

No.	ai	bi	No.	ai	bi	No.	ai	bi	No.	ai	bi
113	5.000	1.400	167	3.000	0.265	221	9.000	0.620	275	1.000	0.050
114	4.000	0.750	168	18.000	0.075	222	1.500	0.140	276	39.000	0.050
115	37.500	1.150	169	5.000	0.075	223	1.000	0.215	277	3.000	0.095
116	9.000	0.950	170	2.000	0.500	224	8.000	0.050	278	13.000	0.050
117	7.000	0.060	171	1.000	0.140	225	1.000	0.215	279	3.000	0.050
118	30.900	0.750	172	4.000	0.095	226	1.000	0.140	280	6.000	0.060
119	11.700	0.075	173	4.000	0.500	227	11.000	0.140	281	55.000	0.050
120	53.200	0.140	174	40.000	0.500	228	3.000	0.950	282	53.000	0.075
121	28.500	0.400	175	20.000	0.095	229	12.000	0.050	283	58.000	0.050
122	41.000	1.150	176	6.000	0.075	230	6.000	18.000	284	9.000	0.095
123	18.000	0.140	177	61.000	0.500	231	5.000	0.075	285	1.000	0.050
124	6.500	0.950	178	2.000	4.200	232	3.000	0.095	286	1.000	0.050
125	9.000	0.750	179	12.000	0.265	233	5.000	0.140	287	4.000	0.950
126	12.500	0.750	180	11.000	0.140	234	2.000	0.175	288	1.500	0.075
127	36.000	0.620	181	18.000	0.050	235	9.000	0.140	289	10.000	0.050
128	70.000	0.500	182	36.000	0.215	236	6.000	0.095	290	12.000	0.095
129	7.100	0.500	183	8.000	0.050	237	1.000	0.750	291	13.000	0.050
130	22.500	1.150	184	20.000	0.050	238	1.000	0.075	292	3.000	0.050
131	0.610	0.140	185	1.000	0.075	239	2.000	0.095	293	1.000	0.330
132	34.000	0.095	186	25.000	0.075	240	5.000	0.140	294	16.000	0.400
133	157.000	0.750	187	10.000	0.095	241	3.000	0.095	295	68.000	0.075
134	17.000	3.200	188	3.000	0.095	242	1.000	0.620	296	2.000	0.400
135	8.000	1.400	189	1.000	0.140	243	5.000	0.620	297	5.000	0.265
136	13.500	1.750	190	3.000	0.075	244	23.000	0.050	298	212.000	0.050
137	8.000	0.750	191	59.000	1.150	245	5.000	0.095	299	121.000	0.215
138	4.000	0.175	192	3.000	0.075	246	11.000	0.330	300	60.000	0.400
139	2.500	0.265	193	17.000	0.175	247	4.000	0.075	301	95.000	0.095
140	12.000	0.095	194	2.000	0.330	248	1.000	0.050	302	86.000	0.060
141	13.000	0.175	195	1.000	0.140	249	2.000	0.140	303	128.000	0.500
142	5.000	0.075	196	1.000	0.330	250	15.000	0.075	304	43.000	0.500
143	6.000	0.075	197	1.000	0.620	251	30.000	0.215	305	48.000	0.400
144	2.000	0.075	198	4.000	0.215	252	38.000	0.140	306	80.000	0.060
145	4.000	0.095	199	2.000	1.150	253	4.000	0.075	307	2.500	0.175
146	0.700	0.140	200	2.000	0.500	254	11.000	0.060	308	4.040	0.750
147	4.000	0.095	201	13.000	0.095	255	50.000	0.750	309	1.150	0.750
148	7.000	0.095	202	1.000	0.075	256	16.000	0.060	310	0.500	0.500
149	7.000	1.500	203	1.000	1.150	257	6.000	0.050	311	70.000	0.075
150	5.000	0.215	204	6.000	0.265	258	4.000	0.050	312	10.000	1.400
151	28.000	0.215	205	1.000	0.500	259	13.000	0.050	313	48.000	0.140
152	3.000	0.500	206	21.000	0.075	260	34.000	0.095	314	283.000	0.175
153	9.000	0.140	207	26.000	0.095	261	7.000	0.050	315	21.000	0.620
154	27.000	0.215	208	17.000	0.075	262	2.000	0.050	316	44.000	0.095
155	52.000	0.950	209	3.000	0.140	263	1.000	0.050	317	2.000	0.140
156	13.000	2.400	210	32.000	2.900	264	10.000	0.050	318	20.000	0.750
157	24.000	0.095	211	1.000	0.050	265	4.000	0.050	319	9.000	0.050
158	112.000	0.265	212	1.000	0.140	266	11.000	0.050	320	3.000	0.050
159	78.000	0.330	213	1.000	0.050	267	72.000	0.050	321	24.000	0.050
160	14.000	0.095	214	19.000	0.500	268	42.000	1.150	322	85.000	0.050
161	13.000	0.140	215	27.000	0.140	269	36.000	0.400	323	26.000	0.050
162	12.000	0.095	216	2.000	0.140	270	70.000	0.050	324	4.000	0.075
163	47.000	5.000	217	2.000	0.050	271	42.000	0.050	325	3.000	0.060
164	15.000	0.950	218	12.000	0.175	272	46.000	0.050	326	3.000	0.175
165	3.000	0.140	219	3.000	0.265	273	4.000	0.095	327	4.000	0.115
166	22.000	0.750	220	12.000	0.175	274	11.000	0.050	328	18.000	0.620

No.	ai	bi	No.	ai	bi	No.	ai	bi	No.	ai	bi
329	25.000	0.075	383	1.000	0.050	437	119.000	0.050	491	34.000	0.620
330	39.000	0.095	384	1.000	0.050	438	18.000	0.050	492	1.750	0.265
331	3.000	0.075	385	1.000	0.050	439	39.000	0.050	493	44.000	0.075
332	71.000	1.750	386	1.000	0.050	440	15.000	0.050	494	28.000	0.330
333	47.000	0.050	387	78.000	0.050	441	10.000	0.050	495	34.000	0.075
334	14.000	0.215	388	4.000	0.060	442	253.000	0.075	496	1.400	1.400
335	71.000	0.620	389	23.000	0.140	443	120.000	0.060	497	0.330	0.095
336	15.000	0.400	390	146.000	0.060	444	85.000	0.050	498	0.500	0.095
337	54.000	0.050	391	7.000	0.075	445	16.000	0.115	499	24.990	0.620
338	52.000	0.140	392	44.000	0.050	446	45.000	0.075	500	6.030	0.075
339	11.000	0.050	393	57.000	0.050	447	26.000	0.050	501	4.000	0.050
340	88.000	0.060	394	5.000	0.050	448	72.000	0.095	502	2.125	0.075
341	32.000	0.175	395	6.000	0.050	449	64.000	0.500	503	0.175	0.095
342	138.000	0.050	396	92.000	0.265	450	36.000	0.075	504	4.000	0.750
343	83.000	1.750	397	107.000	0.075	451	60.000	0.050	505	33.030	0.950
344	2.000	0.400	398	53.000	0.050	452	11.000	0.075	506	28.000	0.050
345	5.000	0.075	399	380.000	0.060	453	8.000	0.050	507	24.030	0.115
346	1.000	0.115	400	1.000	0.050	454	2.000	0.075	508	56.430	0.050
347	59.000	0.500	401	50.000	0.095	455	1.000	0.060	509	74.000	0.115
348	2.000	0.175	402	179.000	0.075	456	16.000	0.050	510	3.630	0.050
349	109.000	0.620	403	103.000	0.050	457	2.000	0.265	511	6.000	0.115
350	40.000	4.000	404	102.000	0.400	458	5.000	0.140	512	40.000	0.140
351	124.000	0.095	405	50.000	0.060	459	62.000	0.075	513	2.000	0.500
352	47.000	0.095	406	11.000	0.050	460	2.000	0.050	514	18.030	0.095
353	4.000	0.115	407	5.000	0.050	461	86.000	0.050	515	9.000	0.265
354	40.000	0.330	408	45.000	0.060	462	14.000	0.095	516	8.000	0.140
355	24.000	0.075	409	48.000	0.050	463	50.000	0.050	517	2.000	0.115
356	152.000	0.500	410	15.000	0.075	464	27.000	0.050	518	13.180	1.750
357	9.000	0.075	411	106.000	0.140	465	46.000	0.060	519	1.400	0.050
358	118.000	0.075	412	22.000	0.115	466	58.000	0.050	520	0.400	0.095
359	25.000	0.140	413	78.000	0.075	467	1.000	0.050	521	1.150	0.075
360	133.000	0.050	414	36.000	0.115	468	1.000	0.050	522	4.000	0.175
361	1.000	0.095	415	1.000	0.060	469	29.000	0.050	523	8.000	0.400
362	1.000	0.115	416	124.000	0.075	470	1.000	0.050	524	1.750	0.620
363	2.000	0.265	417	5.000	0.050	471	10.000	0.050	525	1.400	0.050
364	40.000	0.050	418	364.000	0.050	472	199.000	0.075	526	32.000	0.095
365	65.000	0.060	419	42.000	0.095	473	6.000	0.095	527	1.400	0.050
366	19.000	0.175	420	13.000	0.050	474	102.000	0.095	528	29.030	4.000
367	3.000	0.050	421	9.000	0.050	475	13.000	0.265	529	20.000	0.050
368	1.000	0.060	422	175.000	0.115	476	31.000	0.075	530	8.000	0.075
369	5.000	0.050	423	5.000	0.095	477	44.000	0.060	531	1.150	2.150
370	4.000	0.050	424	62.000	0.050	478	138.000	0.750	532	0.950	0.095
371	325.000	0.075	425	120.000	0.050	479	161.000	0.050	533	0.750	0.050
372	2.000	0.095	426	1.000	0.050	480	51.000	0.050	534	0.095	0.050
373	131.000	0.265	427	531.000	0.215	481	90.000	0.620	535	1.055	0.050
374	1.000	0.095	428	10.000	0.060	482	5.000	0.115	536	42.000	4.500
375	20.000	0.075	429	20.000	0.050	483	39.000	0.050	537	47.000	0.050
376	436.000	0.265	430	45.000	0.060	484	2.000	0.050	538	46.000	0.050
377	28.000	0.140	431	77.000	0.095	485	1.000	0.050	539	57.780	0.050
378	37.000	0.050	432	73.000	0.115	486	104.000	0.050	540	451.755	0.050
379	221.000	0.140	433	54.000	0.050	487	38.000	0.060	541	56.000	0.075
380	85.000	0.400	434	28.000	0.075	488	355.000	0.050	542	0.950	0.095
381	63.000	0.050	435	5.000	0.115	489	15.000	0.500	543	90.000	0.175
382	8.000	0.050	436	17.000	0.140	490	34.000	0.140	544	33.060	0.075

No.	ai	bi	No.	ai	bi	No.	ai	bi	No.	ai	bi
545	1.400	0.175	599	6.000	0.215	653	15.000	0.140	707	29.000	1.150
546	1.800	0.050	600	4.000	0.050	654	37.000	0.095	708	3.300	0.050
547	10.000	0.750	601	2.000	0.265	655	16.000	0.750	709	35.000	0.060
548	43.000	0.050	602	4.030	0.095	656	99.000	0.095	710	1.150	0.095
549	196.000	0.075	603	15.000	0.050	657	4.000	0.115	711	0.500	0.095
550	501.000	0.215	604	79.000	0.095	658	8.000	0.140	712	2.150	0.050
551	18.000	0.075	605	2.000	0.115	659	6.000	0.620	713	26.000	0.500
552	197.090	0.050	606	5.000	2.150	660	47.000	0.075	714	43.000	0.095
553	497.030	0.050	607	5.000	0.115	661	11.000	0.620	715	187.000	0.950
554	104.780	0.050	608	7.000	0.265	662	19.030	0.400	716	386.000	0.050
555	22.430	0.115	609	103.000	0.050	663	26.000	0.060	717	50.000	0.500
556	127.030	0.265	610	13.000	0.175	664	5.500	0.050	718	90.000	1.400
557	35.000	0.750	611	1.150	0.115	665	68.030	0.060	719	200.000	0.095
558	43.000	0.095	612	2.500	0.215	666	9.000	0.215	720	0.750	0.075
559	5.000	0.115	613	38.000	0.330	667	6.000	0.050	721	63.000	0.050
560	14.000	0.140	614	16.000	0.050	668	54.000	0.075	722	0.950	0.060
561	13.780	8.000	615	12.000	0.095	669	40.000	0.095	723	101.000	0.400
562	35.000	0.075	616	2.530	0.050	670	11.000	0.265	724	224.000	0.140
563	2.000	0.620	617	4.780	0.095	671	6.030	0.140	725	1.750	0.115
564	135.000	0.075	618	0.950	0.050	672	4.000	0.500	726	2.650	0.140
565	19.000	0.500	619	5.060	0.050	673	3.000	4.000	727	6.000	0.095
566	12.000	0.140	620	143.000	1.150	674	0.600	0.215	728	1.750	0.265
567	13.000	0.140	621	133.000	0.095	675	11.000	0.060	729	125.000	0.330
568	14.000	0.215	622	7.000	0.095	676	1.400	0.175	730	9.000	1.150
569	1.400	0.950	623	51.000	0.095	677	3.000	0.095	731	16.000	0.215
570	28.000	0.140	624	84.000	0.115	678	9.530	0.050	732	43.000	0.050
571	1.400	0.075	625	27.000	0.175	679	3.500	0.060	733	72.000	0.050
572	13.000	0.075	626	4.000	0.215	680	0.500	0.095	734	47.000	0.050
573	7.000	8.000	627	20.000	0.265	681	5.000	0.500	735	24.000	0.075
574	16.000	0.175	628	30.000	0.620	682	22.130	0.950	736	4.000	0.050
575	19.000	0.175	629	13.000	0.095	683	29.000	0.950	737	53.000	0.075
576	40.000	0.115	630	7.000	0.400	684	0.300	0.050	738	0.950	0.265
577	38.000	0.265	631	19.000	0.050	685	0.200	1.150	739	2.000	0.500
578	7.000	0.050	632	18.000	0.400	686	109.000	0.330	740	5.000	0.950
579	4.000	0.620	633	0.750	0.060	687	12.000	0.050	741	5.000	0.050
580	11.000	0.265	634	3.000	0.095	688	20.590	0.075	742	65.000	0.620
581	2.000	0.400	635	12.000	0.215	689	0.600	2.650	743	60.000	0.050
582	28.000	0.075	636	2.150	0.265	690	4.000	0.950	744	4.000	0.115
583	5.000	0.075	637	29.000	0.215	691	21.000	0.265	745	8.000	0.175
584	81.030	0.330	638	20.000	0.095	692	23.000	2.650	746	3.500	0.050
585	132.000	0.750	639	26.000	0.075	693	53.000	0.500	747	3.300	0.075
586	13.180	0.050	640	1.150	0.115	694	56.000	0.215	748	152.000	0.140
587	2.500	0.095	641	19.000	0.175	695	25.000	0.075	749	163.000	0.050
588	19.000	0.075	642	70.000	1.750	696	53.000	0.215	750	539.000	0.400
589	234.000	0.140	643	13.000	2.150	697	35.000	0.750	751	158.000	0.075
590	66.000	0.075	644	7.000	0.750	698	17.000	1.750	752	1.750	0.095
591	5.000	1.150	645	2.000	2.150	699	169.000	1.150	753	321.000	0.215
592	48.000	0.115	646	11.000	0.050	700	45.000	0.400	754	13.000	0.215
593	62.000	0.095	647	217.030	0.095	701	37.000	0.095	755	95.000	0.115
594	97.000	0.115	648	162.000	0.500	702	8.000	0.265	756	2.150	0.075
595	26.000	0.050	649	11.000	0.050	703	44.000	0.950	757	623.000	0.950
596	88.000	0.075	650	24.000	0.095	704	2.650	0.330	758	75.000	0.950
597	7.000	0.140	651	35.000	0.095	705	0.650	0.215	759	182.000	1.750
598	4.000	0.175	652	4.000	0.140	706	14.000	0.620	760	27.000	0.075

No.	ai	bi	No.	ai	bi	No.	ai	bi	No.	ai	bi
761	75.000	0.050	815	3.500	0.095	869	4.000	0.400	…..	…….	……
762	65.000	0.215	816	308.000	0.060	870	236.000	0.400			
763	5.000	0.050	817	120.000	0.075	871	27.000	0.140			
764	5.000	0.175	818	3.300	0.140	872	34.000	1.750			
765	152.000	0.050	819	2.150	0.050	873	114.000	0.095			
766	385.000	0.175	820	17.000	0.050	874	108.000	0.050			
767	4.000	0.075	821	2.500	0.050	875	12.000	0.750			
768	503.000	0.095	822	38.000	0.075	876	886.000	7.000			
769	61.000	0.140	823	0.750	0.075	877	2.650	0.950			
770	16.000	0.050	824	450.000	0.075	878	545.000	0.750			
771	149.000	0.060	825	21.000	0.095	879	358.000	0.050			
772	370.000	0.050	826	5.500	0.050	880	2.150	0.115			
773	883.000	0.095	827	841.000	0.050	881	12.000	0.050			
774	1060.000	0.115	828	0.500	0.075	882	43.000	0.750			
775	5.000	0.050	829	6.000	0.075	883	25.000	0.075			
776	10.000	0.050	830	264.000	0.060	884	86.000	1.400			
777	273.000	0.060	831	283.000	0.050	885	21.000	0.140			
778	654.000	0.750	832	681.000	0.050	886	6.000	0.115			
779	45.000	0.050	833	20.000	0.075	887	7.000	0.330			
780	5.000	0.050	834	11.000	0.095	888	1.400	0.060			
781	182.000	0.140	835	46.000	0.750	889	56.000	0.115			
782	7.000	0.050	836	5.000	0.750	890	124.000	0.400			
783	57.000	0.095	837	278.000	0.060	891	9.000	0.050			
784	126.000	1.750	838	40.000	0.050	892	4.500	0.750			
785	479.000	0.075	839	109.000	0.075	893	77.000	2.650			
786	2260.000	0.050	840	4.000	0.060	894	16.000	0.050			
787	3.300	0.050	841	44.000	0.265	895	26.000	0.265			
788	467.000	0.050	842	241.000	0.175	896	94.000	0.075			
789	747.000	0.215	843	30.000	0.050	897	2.150	1.750			
790	0.950	0.140	844	210.000	0.050	898	36.000	0.050			
791	48.000	0.060	845	369.000	0.060	899	128.000	0.140			
792	1626.000	0.075	846	462.000	0.095	900	43.000	0.095			
793	54.000	0.115	847	692.000	0.075	901	27.000	0.050			
794	71.000	0.050	848	203.000	0.140	902	178.000	0.050			
795	140.000	0.750	849	285.000	0.095	903	46.000	0.075			
796	235.000	0.050	850	83.000	0.500	904	282.000	0.095			
797	374.000	0.095	851	6.000	0.095	905	0.900	0.050			
798	228.000	0.050	852	1142.000	0.115	906	0.215	0.750			
799	19.000	0.050	853	620.000	0.095	907	13.000	0.050			
800	215.000	0.095	854	5.500	0.075	908	128.000	0.140			
801	70.000	0.115	855	16.000	0.115	909	109.000	0.075			
802	380.000	0.075	856	47.000	0.050	910	34.000	0.750			
803	501.000	0.050	857	2.650	0.075	911	13.000	0.050			
804	35.000	0.175	858	287.000	0.095	912	16.000	0.265			
805	40.000	0.140	859	226.000	0.050	913	73.000	0.075			
806	86.000	0.050	860	38.000	0.500	914	52.000	0.115			
807	446.000	0.060	861	208.000	0.620	915	20.000	2.150			
808	20.000	0.050	862	209.000	0.075	916	5.000	0.500			
809	163.000	0.050	863	147.000	0.215	917	63.000				
810	26.000	0.075	864	21.000	0.140						
811	1145.000	0.050	865	33.000	0.175						
812	644.000	0.075	866	188.000	0.115						
813	191.000	0.050	867	148.000	0.750						
814	349.000	0.050	868	65.000	0.115						

2. Intensity data

Location (m)	Intensity (No./m)	Location (m)	Intensity (No./m)
0.5	41	30.5	5
1.5	53	31.5	1
2.5	25	32.5	3
3.5	42	33.5	7
4.5	93	34.5	2
5.5	43	35.5	0
6.5	16	36.5	2
7.5	28	37.5	1
8.5	18	38.5	3
9.5	16	39.5	3
10.5	20	40.5	5
11.5	8	41.5	3
12.5	18	42.5	8
13.5	9	43.5	0
14.5	17	44.5	3
15.5	29	45.5	10
16.5	11	46.5	3
17.5	52	47.5	5
18.5	10	48.5	10
19.5	4	49.5	4
20.5	31	50.5	2
21.5	28	51.5	4
22.5	34	52.5	1
23.5	40	53.5	9
24.5	29	54.5	8
25.5	8	55.5	6
26.5	26	56.5	3
27.5	3	57.5	23
28.5	7		
29.5	8		

3. Semivariogram data

Lag (m)	Threshold				
	3 frac./m	5 frac./m	8 frac./m	15 frac./m	30 frac./m
1	0.74	0.72	0.50	0.45	0.60
2	0.75	0.69	0.62	0.34	0.68
3	0.92	0.70	0.37	0.39	0.55
4	1.09	0.80	0.53	0.59	0.78
5	1.11	0.64	0.54	0.48	0.72
6	0.89	0.79	0.51	0.53	0.81
7	0.91	0.67	0.72	0.58	0.97
8	1.01	0.73	0.61	0.64	0.99
9	0.86	0.88	0.58	0.61	1.01
10	1.23	0.90	0.85	0.75	1.03
11	1.25	1.01	0.74	0.72	1.05
12	1.10	0.69	0.71	0.65	0.91
13	1.12	0.91	0.82	0.80	0.93
14	1.15	0.98	0.97	0.63	0.95
15	0.88	0.84	0.95	0.79	0.98
16	0.90	1.08	0.87	0.76	0.82
17	1.13	0.94	1.04	0.78	0.65
18	1.16	1.08	1.12	0.85	0.76
19	1.19	1.05	0.99	0.87	0.59
20	1.44	1.08	1.13	0.89	0.80

Appendix I: Derivation of Potential due to image source

This appendix is from Long et al. (1985).

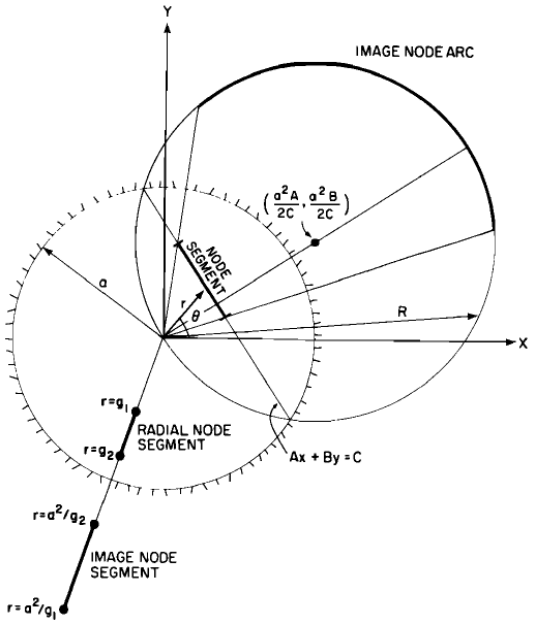

The equation of the line on which the intersection lies can be given as $Ax + By = C$.

Changing to radial coordinates, let $x = r\cos\theta$ and $y = r\sin\theta$. Then the equation is:

$$Ar\cos\theta + Br\sin\theta = C \quad \text{or} \quad r = \frac{C}{A\cos\theta + B\sin\theta}$$

- If $C \neq 0$ (non-radial segment), the distance R from the origin to the image arc is:

$$R = \frac{a^2}{r} = \frac{a^2}{C}\left(A\cos\theta + B\sin\theta\right)$$

Returning to Cartesian coordinates, if (x, y) is a point on the image arc, then

$$\cos\theta = \frac{x}{R} = \frac{x}{\sqrt{x^2 + y^2}} \quad \text{and} \quad \sin\theta = \frac{y}{R} = \frac{y}{\sqrt{x^2 + y^2}}$$

So we have: $\left(x - \frac{a^2A}{2C}\right)^2 + \left(y - \frac{a^2B}{2C}\right)^2 = \frac{a^4}{4C^2}\left(A^2 + B^2\right)$

which is the equation of a circle centered at $\left(\frac{a^2 A}{2C}, \frac{a^2 B}{2C}\right)$ with radius $\frac{a^2\sqrt{A^2+B^2}}{2|C|}$, and the ranges of x and y are corresponded to the angle $\theta_1 \le \theta \le \theta_2$.

- If $C = 0$ (radial segment), the equation of the image segment is a line $\theta = \tan^{-1}\left(-\frac{A}{B}\right)$ and the end points are given by a^2 / g_1 and a^2 / g_2, where a is the radius of the fracture, and g_1 and g_2 are the distances from the end points of the intersection to the center of the fracture.

Appendix J: Derivation of Potential due to source itself

This appendix is from Long et al. (1985).

When we wish to calculate the average of total potential on a given intersection, we can easily evaluate the potential contribution due to all the other intersections and their images on the intersection of interest. However, the contribution of the intersection itself cannot strictly be obtained in the same way because the potential due to the source is not defined on the source itself. Hence we derive an expression for the average potential on a line segment parallel to the line source a short distance, $\pm\varepsilon$, away from it.

The potential contribution due to a point source is given as

$$\phi(x, y) = -\frac{Q}{2\pi} \ln r \tag{A1}$$

where r is the distance to the point (x, y). As in (6), we integrate a series of such sources, each of strength $Q/l\, d\xi$ along a line segment on the x axis, $0 \le x \le l$, to obtain the potential due to a line source:

$$\phi(x, y) = -\frac{Q}{2\pi l} \int_0^l \ln [y^2 + (x - \xi)^2]^{1/2}\, d\xi \tag{A2}$$

where r is now equal to $[y^2 + (x - \xi)^2]^{1/2}$. Integrating, we have

$$\begin{aligned}\phi(x, y) = -\frac{Q}{4\pi l} \Bigg\{ & (l - x) \ln [y^2 + (x - l)^2] - 2l \\ & + 2|y| \tan^{-1}\left(\frac{l - x}{|y|}\right) + x \ln [y^2 + x^2] \\ & - 2|y| \tan^{-1}\left(-\frac{x}{|y|}\right)\Bigg\}\end{aligned} \tag{A3}$$

We now examine the average value of ϕ on a line segment at $y = \pm\varepsilon$ and $0 \le x \le l$:

$$\bar{\phi} = \frac{1}{l} \int_0^l \phi(x, \varepsilon)\, dx$$

$$\begin{aligned}\bar{\phi} = -\frac{Q}{4\pi l^2} \Big[& (l^2 - \varepsilon^2) \ln (l^2 + \varepsilon^2) - 3l^2 \\ & + 4l|\varepsilon| \tan^{-1} \frac{l}{|\varepsilon|} + \varepsilon^2 \ln \varepsilon^2\Big]\end{aligned} \tag{A4}$$

Equation (A4) can be used to evaluate the potential contribution of the source on itself by allowing ε to take the value of $\frac{w}{2}$, where w is the width of the intersection. However, if ε is very small we can use the expression

$$\bar{\phi} = -\frac{Q}{4\pi l^2} (l^2 \ln l^2 - 3l^2) \tag{A5}$$

because

$$\begin{aligned}\lim_{\varepsilon \to 0} (\varepsilon^2 \ln \varepsilon^2) &= \lim_{\varepsilon \to 0} \frac{f(\varepsilon)}{g(\varepsilon)} = \lim_{\varepsilon \to 0} \frac{f'(\varepsilon)}{g'(\varepsilon)} \\ &= \lim_{\varepsilon \to 0} \frac{2 \ln \varepsilon}{\varepsilon^2} = \lim_{\varepsilon \to 0} \frac{2\varepsilon^{-1}}{-2\varepsilon^{-3}} = 0\end{aligned}$$

by l'Hospital's rule.

Appendix K: Fracture Mapping

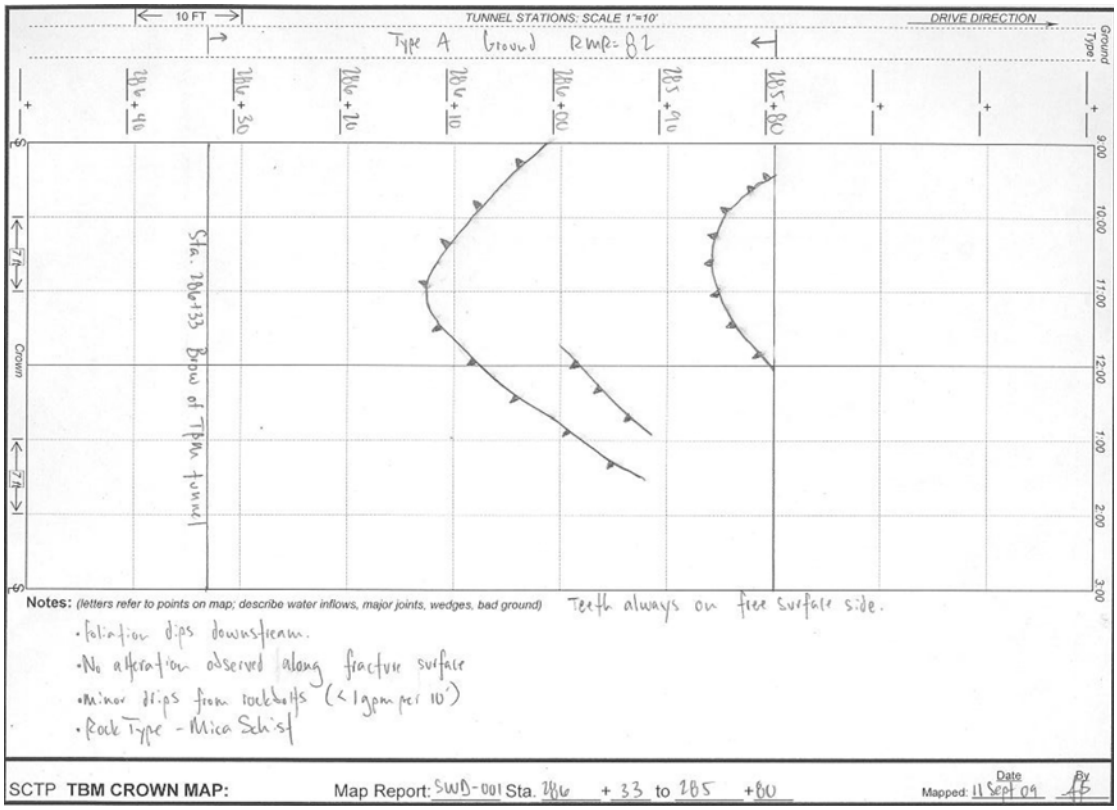

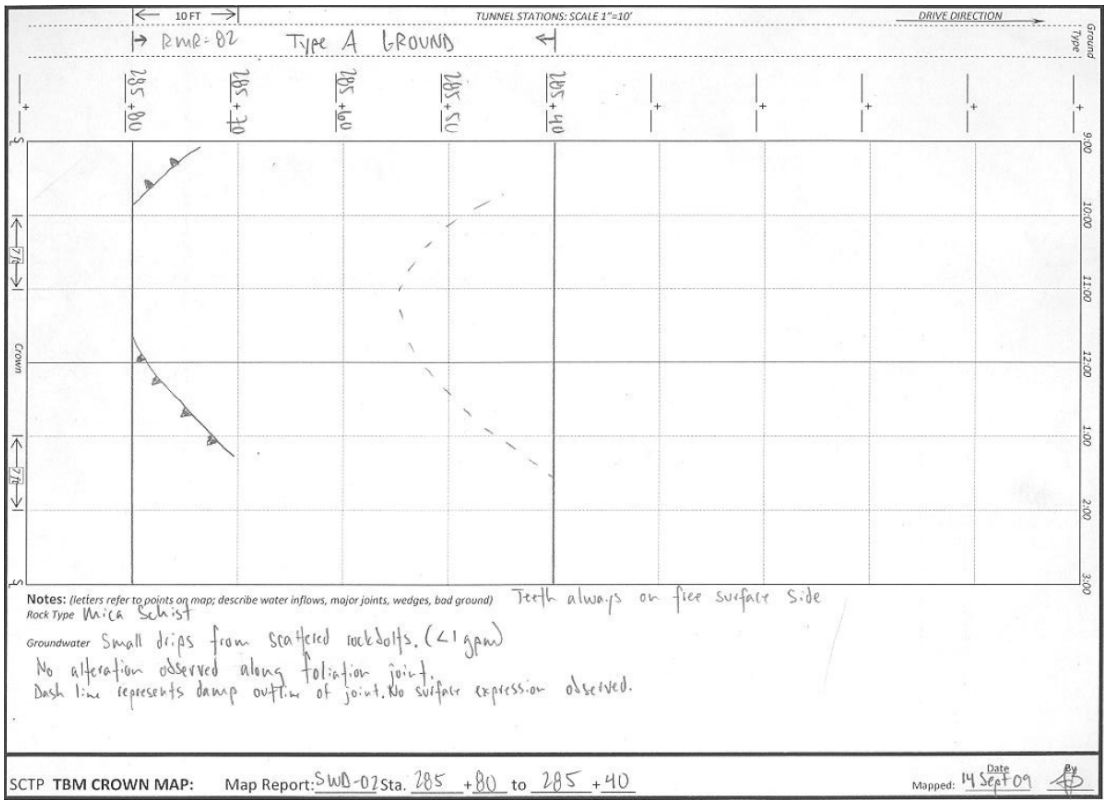

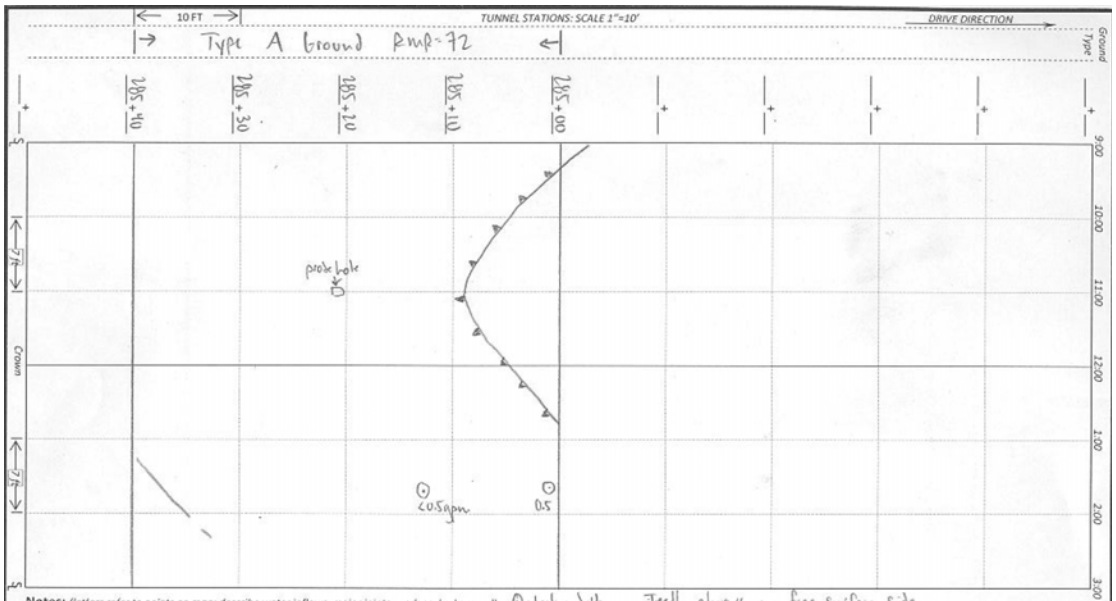

Notes: *(letters refer to points on map; describe water inflows, major joints, wedges, bad ground)* ⊙=Leaky bolt Teeth always on free surface side.

Rock Type Mica Schist

Groundwater @ 285+20 @ 11:00, the probe hole was encountered. A sustained inflow of approximately 1-2 gpm. Small seeps from rockbolts, with a total combined inflow of <1 gpm.

- Ground is massive w/ few foliation joints.
- Foliation joint @ Sta. 285+09, has minor clay along surface.

SCTP **TBM CROWN MAP:** Map Report: SWD-03 Sta. 285 +40 to 285 +00 Mapped: Date 15 Sept 09 By AB

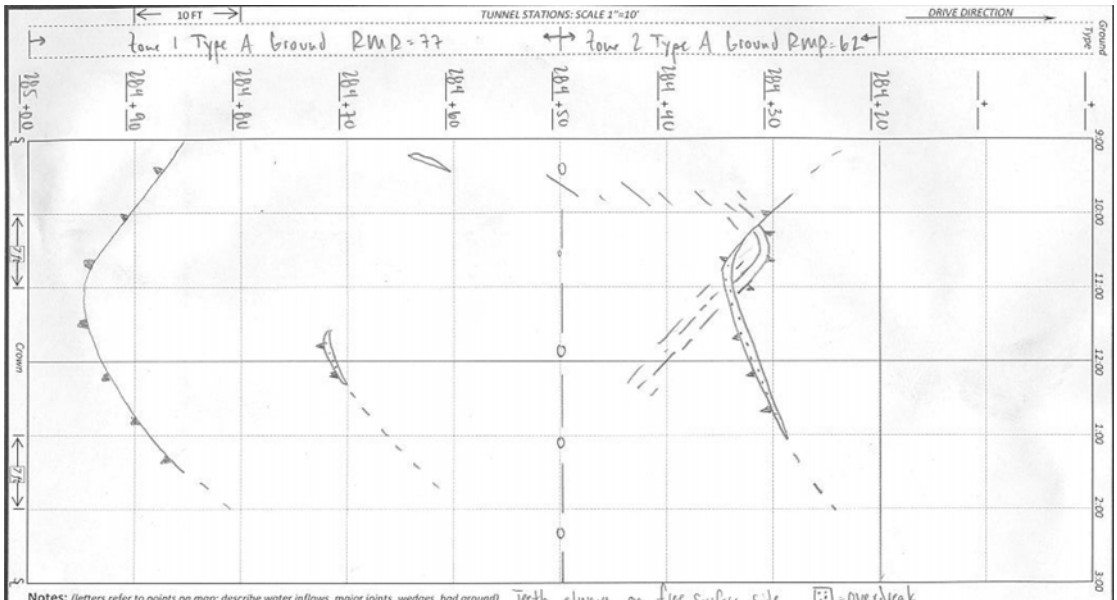

Notes: *(letters refer to points on map; describe water inflows, major joints, wedges, bad ground)* Teeth always on free surface side ⁘=Overbreak

Rock Type Mica Schist

Groundwater In Zone 2, @ the intersection of foliation and high angle joint set, approximately 2 gpm from scattered areas.

Small amount of overbreak along foliation joint as it crosses the crown & intersects high angle joint set.

SCTP **TBM CROWN MAP:** Map Report: SWD-04 Sta. 285 +00 to 284 +20 Mapped: Date 16 Sept 09 By AB

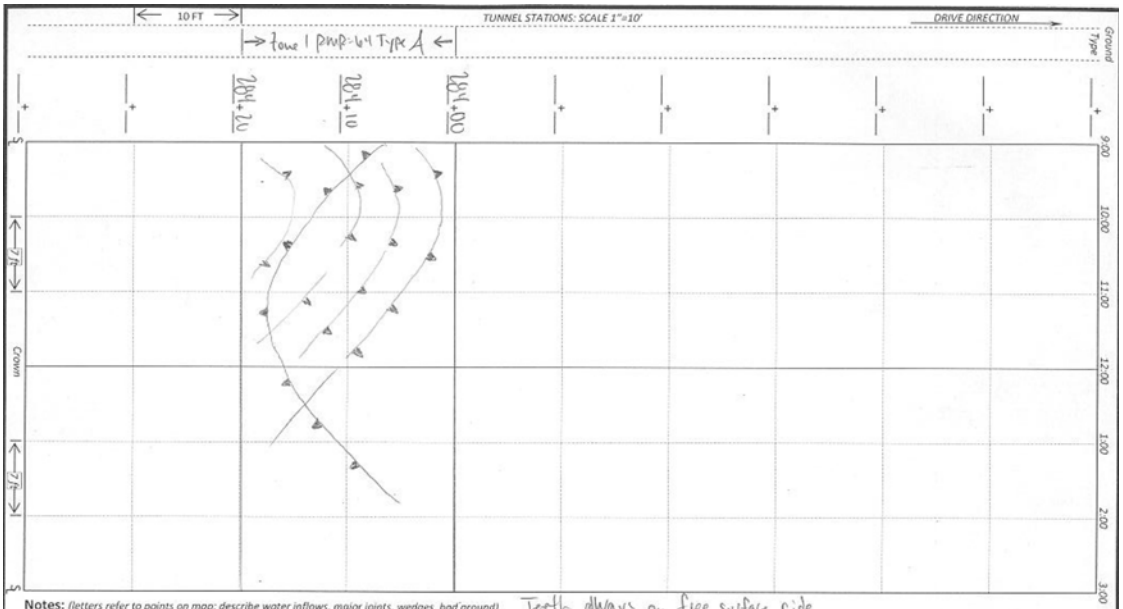

Notes: *(letters refer to points on map; describe water inflows, major joints, wedges, bad ground)* Teeth always on free surface side

Rock Type Mica Schist

Groundwater Scattered drips from rockbolts <1 gpm.

foliation and high angle joint set intersect between 10:00 and 11:00. Small chips are produced.

SCTP **TBM CROWN MAP:** Map Report: SWD-05 Sta. 284 +20 to 284 +00 Mapped: Date 17 Sept 09 By AB

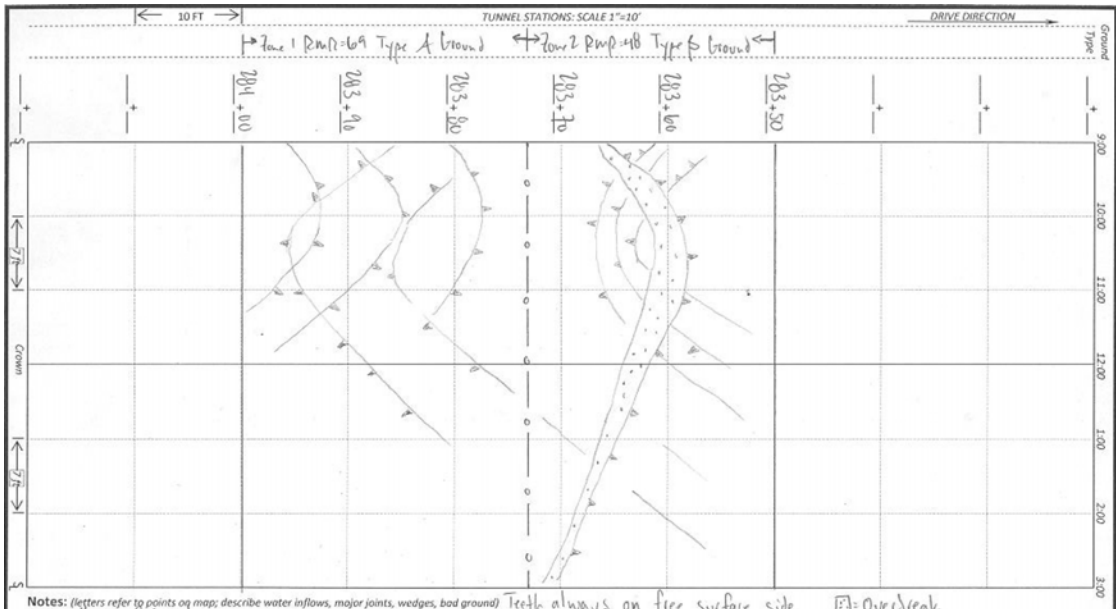

Notes: *(letters refer to points on map; describe water inflows, major joints, wedges, bad ground)* Teeth always on free surface side. ⊡ = Overbreak

Rock Type Mica Schist

Groundwater Drips and seeps from rockbolts. Approximately 2 gpm from Zone 2.

Ground is blocky in Zone 2. Overbreak ranges from 2 to 8 inches.

Clay observed along high angle joint set in Zone 2.

SCTP **TBM CROWN MAP:** Map Report: SWD-06 Sta. 284 +00 to 283 +50 Mapped: Date 18 Sept 09 By AB

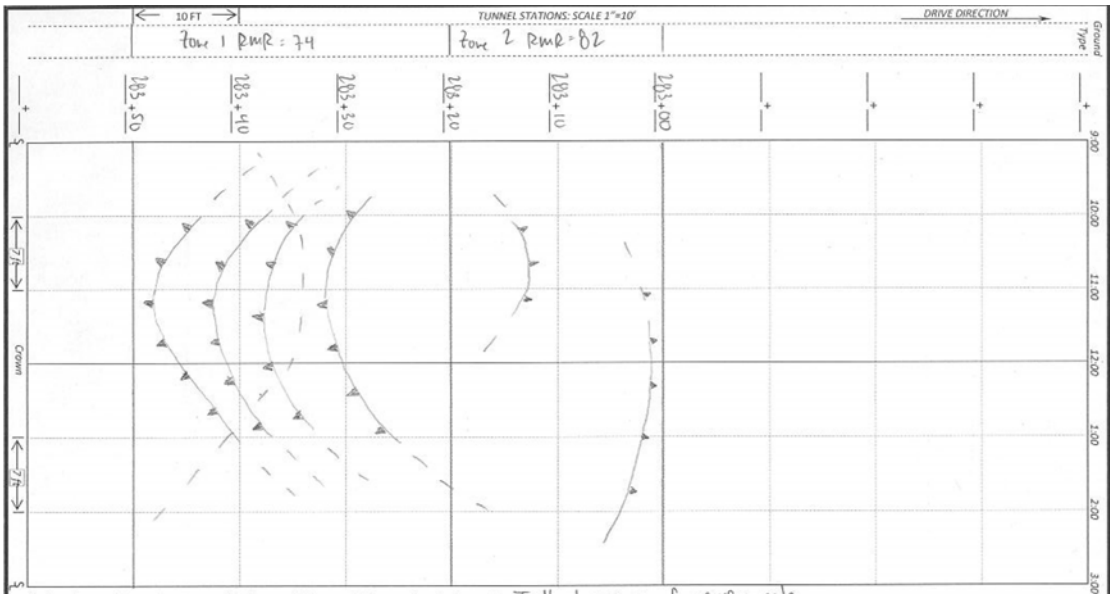

Notes: *(letters refer to points on map; describe water inflows, major joints, wedges, bad ground)* • Teeth always on free surface side.

Rock Type Mica Schist

Groundwater between 283+50 to 283+20, approximately 3-4 gpm. Seeps are from foliation joints ± rockbolts.

- Minor jointing along foliation
- Discontinuous joints in both zones. Represented by dashed line.
- Overall Type A ground

SCTP **TBM CROWN MAP:** Map Report: SWB-07 Sta. 283 +50 to 283 +00 Mapped: Date 29 Sept 09 By AD

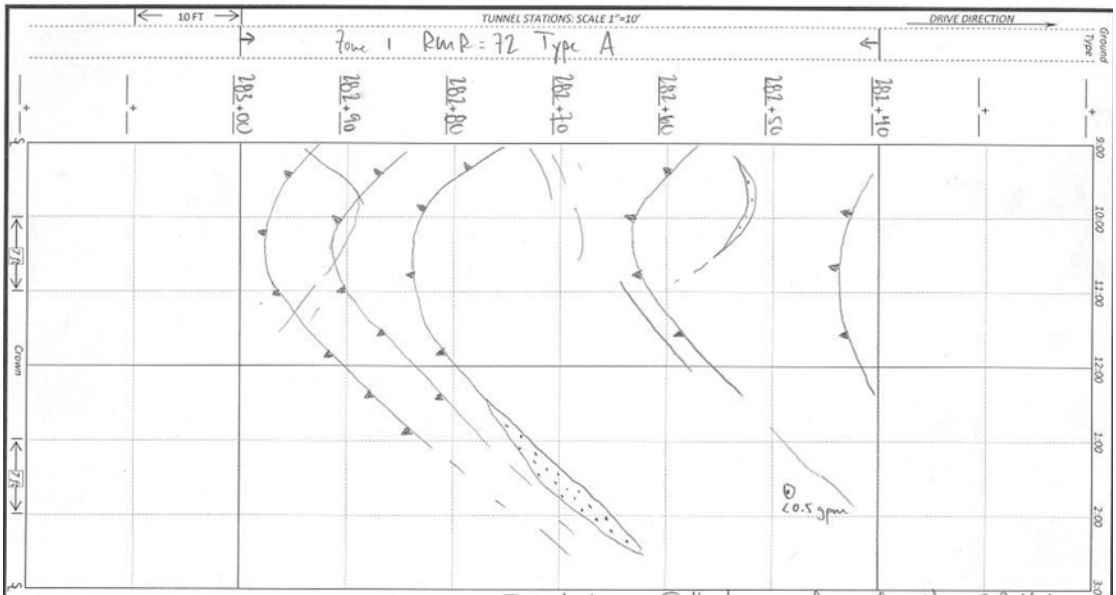

Notes: *(letters refer to points on map; describe water inflows, major joints, wedges, bad ground)* ⊡ - Overbreak Teeth always on free surface side. R = Rockbolt

Rock Type Mica Schist

Groundwater Numerous drips ± seeps from within mapped inflow. Inflow is less than 1 gpm per 10 feet.

Minor chipping along foliation

Minor areas of overbreak @ 282+70 ± 282+52

Random high angle joints in combination w/ foliation joints forms small chips

- Overall Type A ground

SCTP **TBM CROWN MAP:** Map Report: SWB-08 Sta. 283 +00 to 282 +40 Mapped: Date 30 Sept 09 By AD

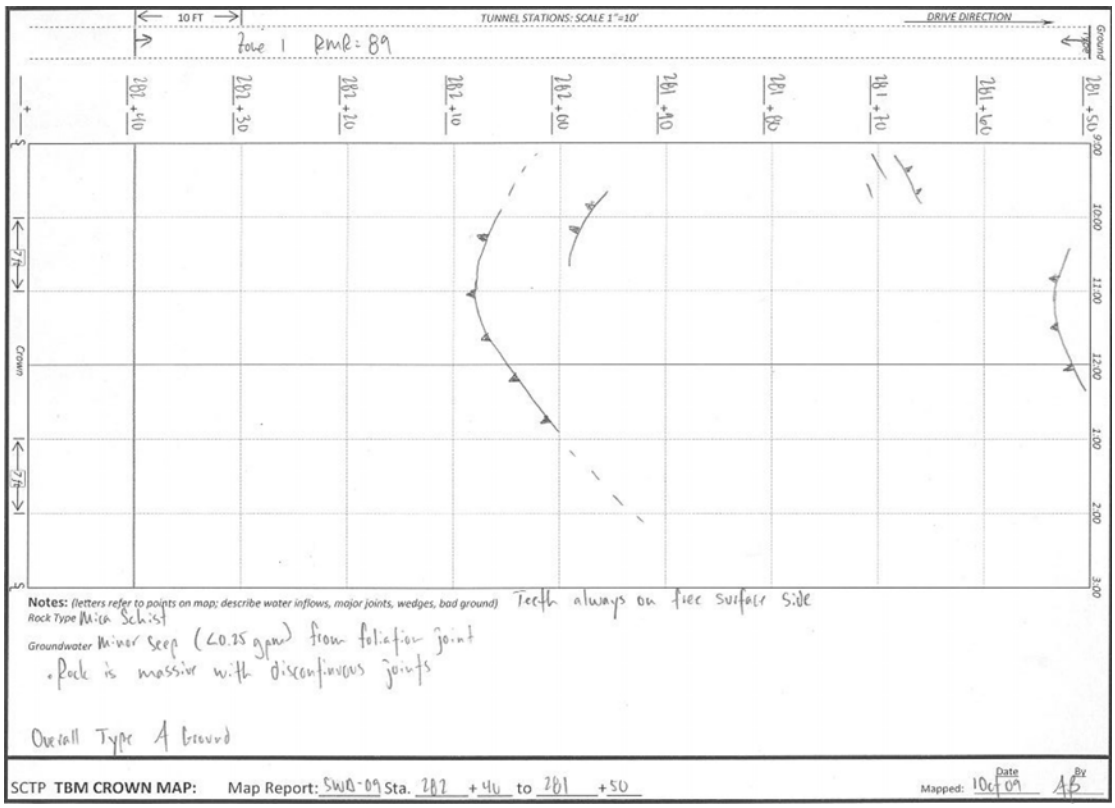

Notes: *(letters refer to points on map; describe water inflows, major joints, wedges, bad ground)* Teeth always on free surface side
Rock Type Mica Schist
Groundwater Minor seep (<0.25 gpm) from foliation joint
•Rock is massive with discontinuous joints

Overall Type A ground

SCTP **TBM CROWN MAP:** Map Report: SWB-09 Sta. 282 +40 to 281 +50 Mapped: Date 10Oct09 By AB

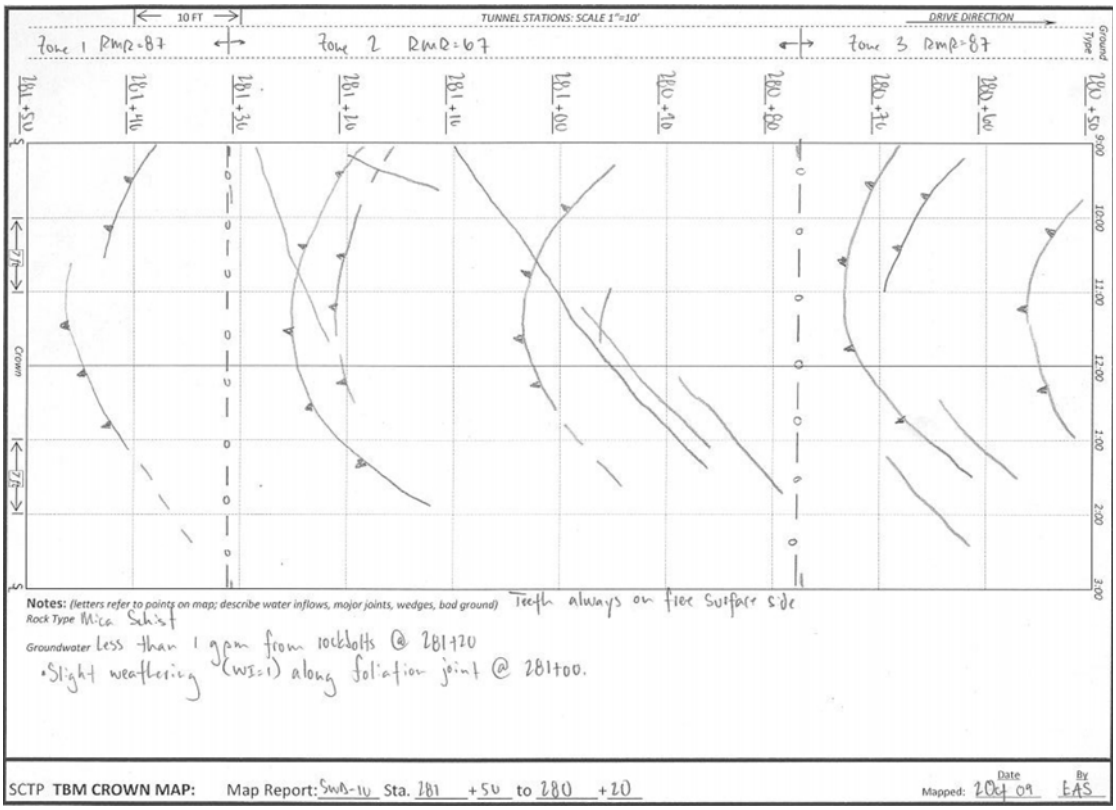

Notes: *(letters refer to points on map; describe water inflows, major joints, wedges, bad ground)* Teeth always on free surface side
Rock Type Mica Schist
Groundwater Less than 1 gpm from rockbolts @ 281+20
•Slight weathering (WS=1) along foliation joint @ 281+00.

SCTP **TBM CROWN MAP:** Map Report: SWB-10 Sta. 281 +50 to 280 +20 Mapped: Date 20Oct09 By EAS

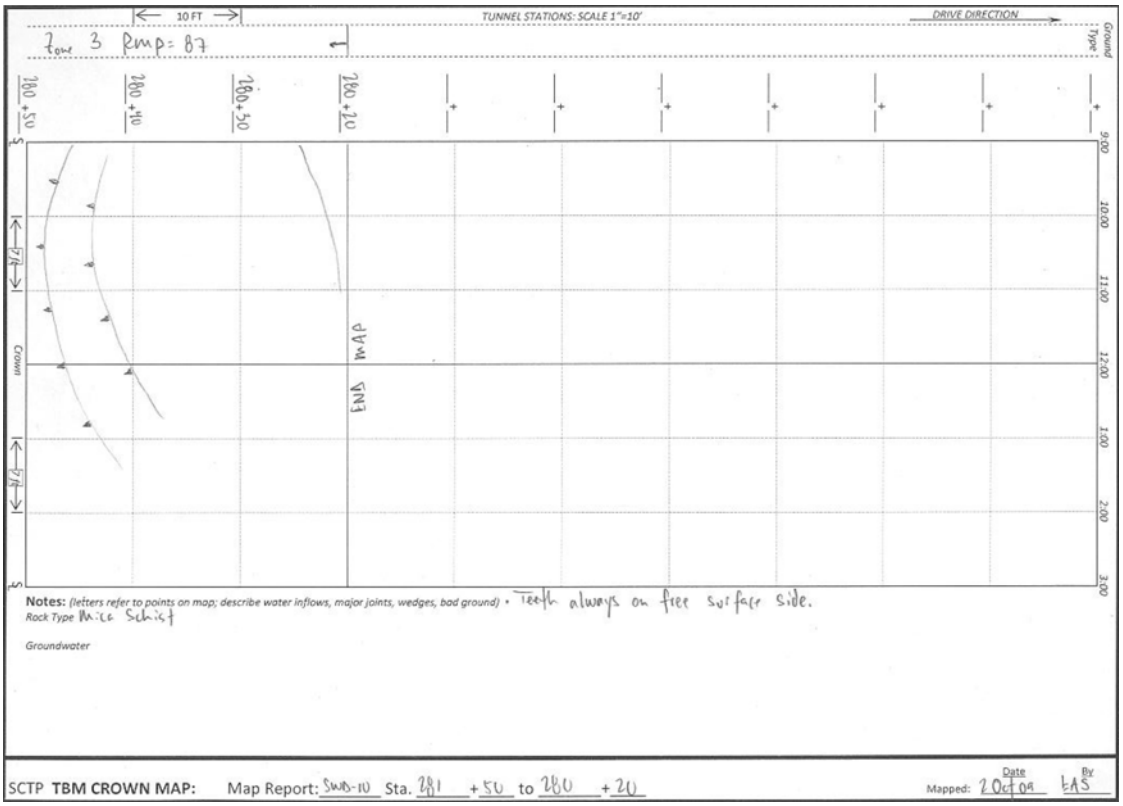
10 FT
TUNNEL STATIONS: SCALE 1"=10'
DRIVE DIRECTION
Ground Type
Zone 3 RMR=87
280+50
280+40
280+30
280+20
9:00
10:00
11:00
12:00
1:00
2:00
3:00
10 FT
Crown
10 FT
MAP
END
Notes: (letters refer to points on map; describe water inflows, major joints, wedges, bad ground) • Teeth always on free surface side.
Rock Type Mica Schist
Groundwater
SCTP TBM CROWN MAP: Map Report: SWD-10 Sta. 281 +50 to 280 +20
Mapped: Date 20 Oct 09 By EAS

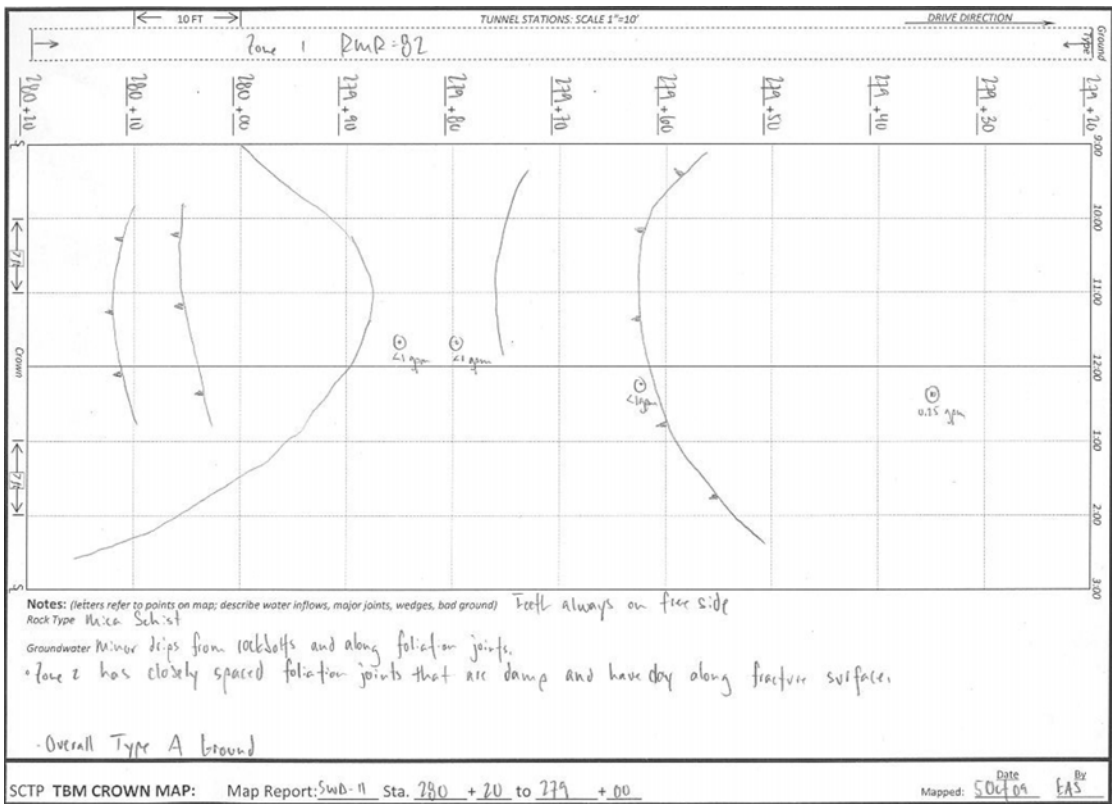
10 FT
TUNNEL STATIONS: SCALE 1"=10'
DRIVE DIRECTION
Ground Type
Zone 1 RMR=82
280+10
280+10
280+00
279+90
279+80
279+70
279+60
279+50
279+40
279+30
279+20
9:00
10:00
11:00
12:00
1:00
2:00
3:00
10 FT
Crown
10 FT
<1 gpm
<1 gpm
<1gpm
0.25 gpm
Notes: (letters refer to points on map; describe water inflows, major joints, wedges, bad ground) Teeth always on free side
Rock Type Mica Schist
Groundwater Minor drips from rockbolts and along foliation joints.
• Zone 2 has closely spaced foliation joints that are damp and have clay along fracture surfaces.
- Overall Type A Ground
SCTP TBM CROWN MAP: Map Report: SWD-11 Sta. 280 +20 to 279 +00
Mapped: Date 20 Oct 09 By EAS

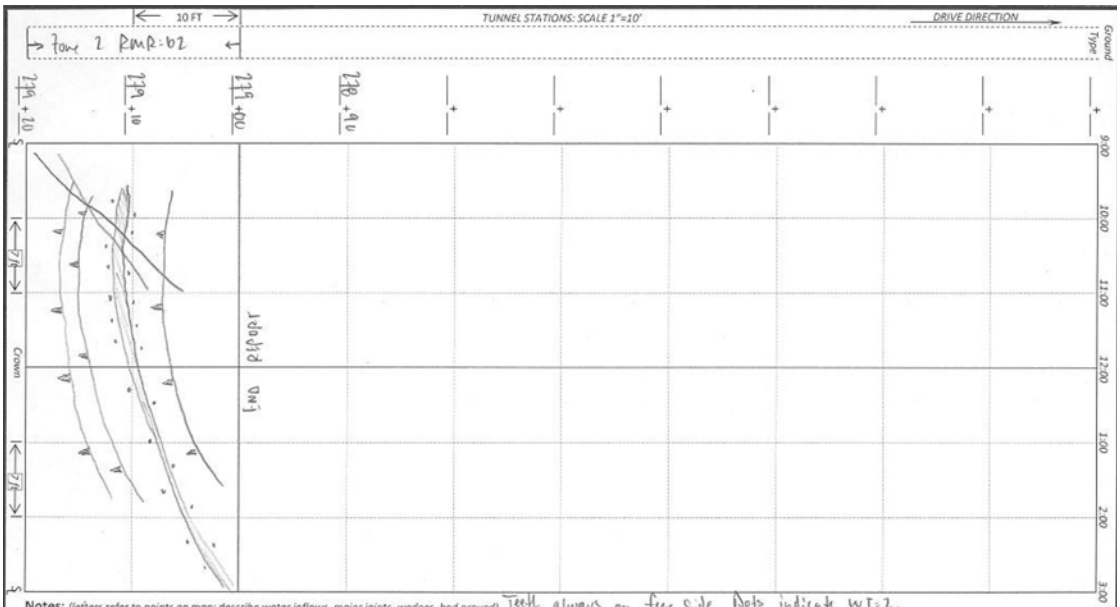

Notes: *(letters refer to points on map; describe water inflows, major joints, wedges, bad ground)* Teeth always on free side. Dots indicate WI=2.

Rock Type Mica Schist

Groundwater Minor drips from rockbolts and along foliation joints

SCTP **TBM CROWN MAP:** Map Report: SWB-11 Sta. 280 +20 to 279 +00 Mapped: Date 5 Oct 09 By KAS

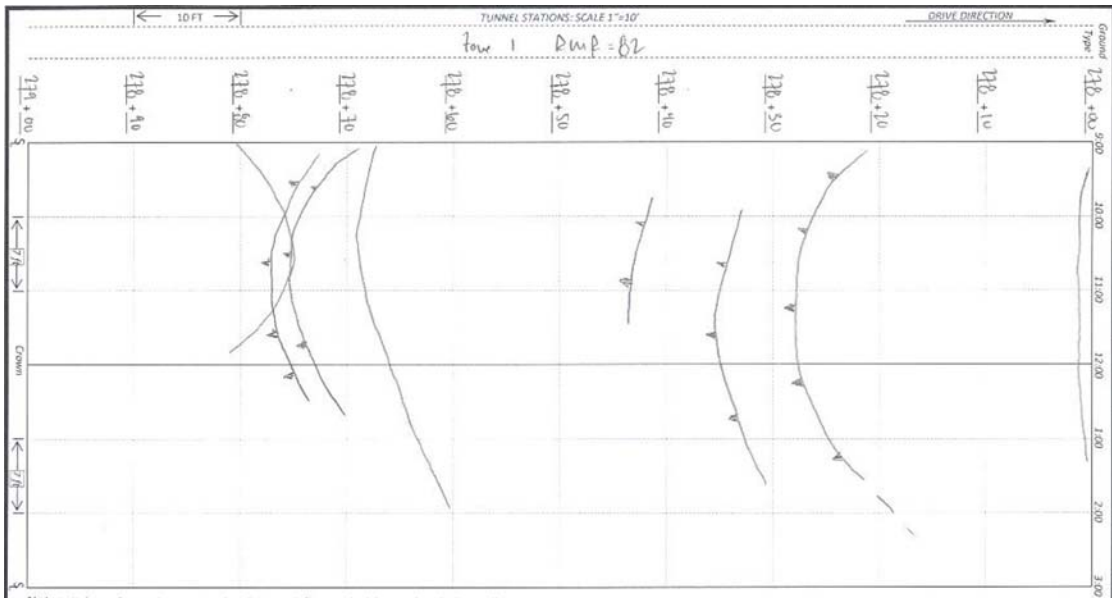

Notes: *(letters refer to points on map; describe water inflows, major joints, wedges, bad ground)*

Rock Type Mica Schist

Groundwater Minor drips @ 278+35.

*Minor chipping along foliation joints

Overall Type A ground

SCTP **TBM CROWN MAP:** Map Report: SWB-12 Sta. 279 +64 to 278 +00 Mapped: Date 6 Oct 09 By KAS

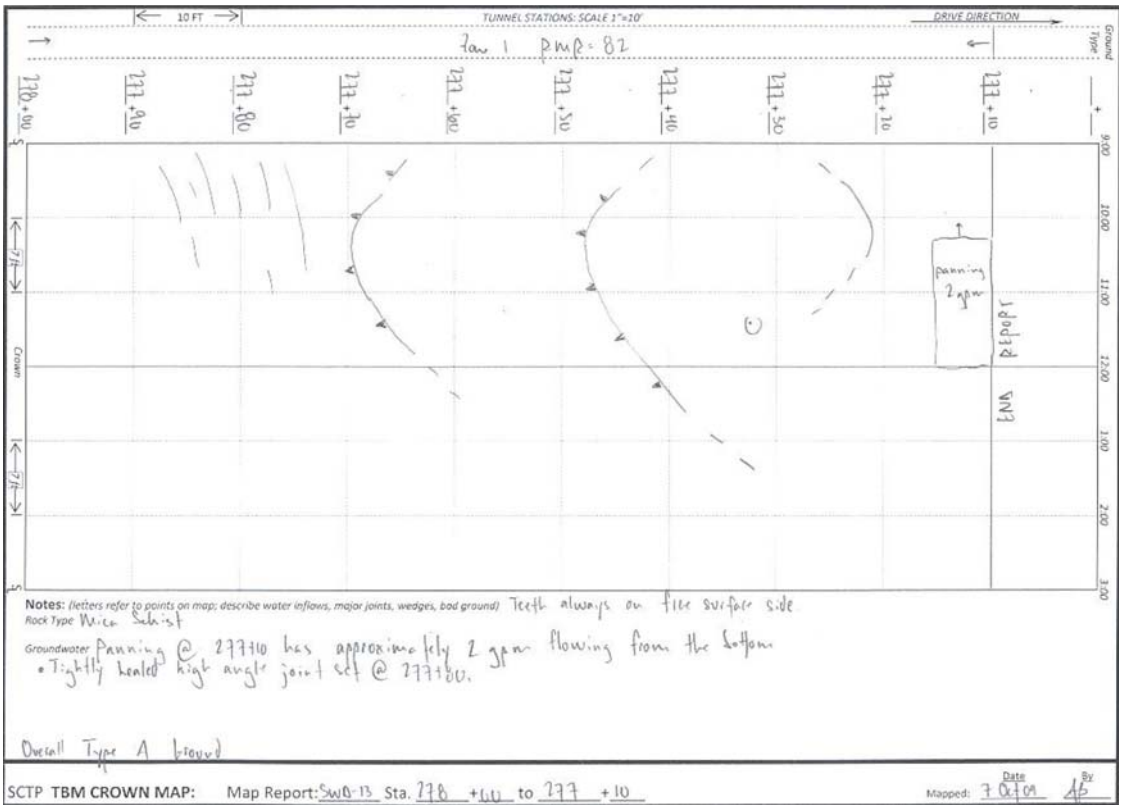
10 FT
TUNNEL STATIONS: SCALE 1"=20'
DRIVE DIRECTION
Ground Type
Zone 1 RMR = 82
277+90
277+80
277+70
277+60
277+50
277+40
277+30
277+20
277+10
9:00
10:00
11:00
12:00
1:00
2:00
3:00
7ft
Crown
7ft
Panning 2 gpm
Notes: (letters refer to points on map; describe water inflows, major joints, wedges, bad ground) Teeth always on free surface side
Rock Type Mica Schist
Groundwater Panning @ 277+10 has approximately 2 gpm flowing from the bottom
• Tightly healed high angle joint set @ 277+80.
Overall Type A Ground
SCTP TBM CROWN MAP: Map Report: SWD-13 Sta. 278 +40 to 277 +10
Mapped: 7 Oct 09 By

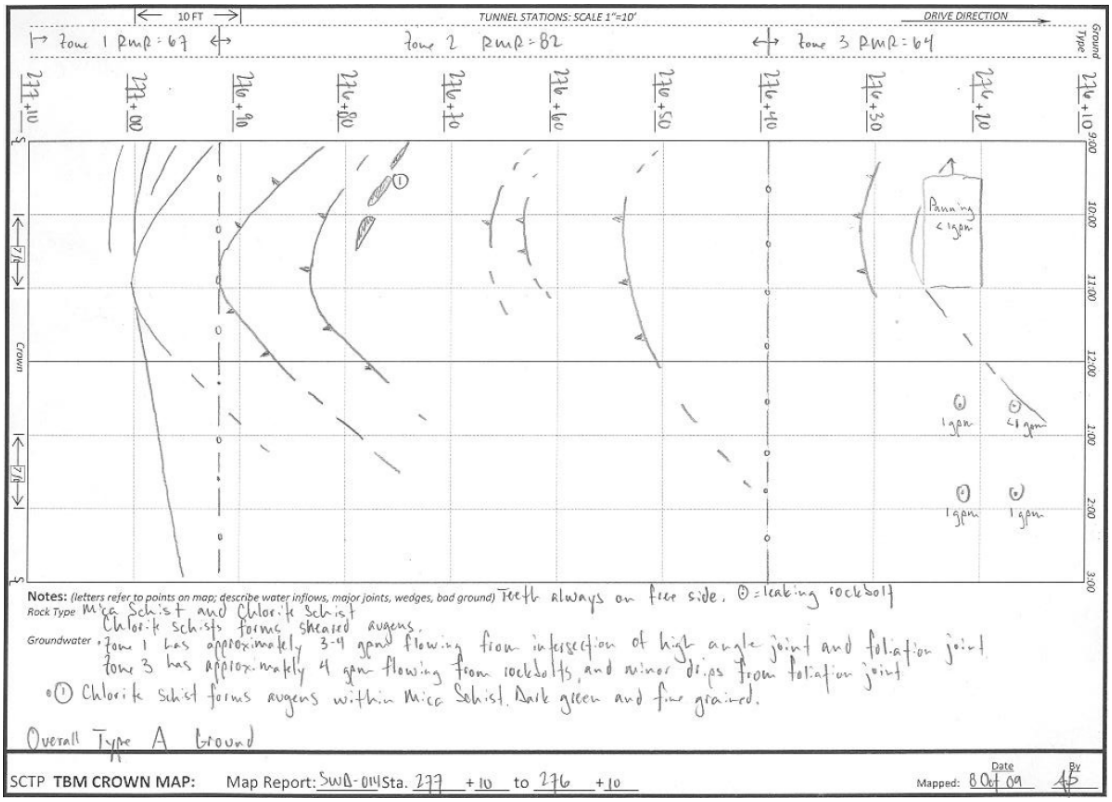
10 FT
TUNNEL STATIONS: SCALE 1"=10'
DRIVE DIRECTION
Ground Type
Zone 1 RMR = 67
Zone 2 RMR = 82
Zone 3 RMR = 64
277+10
277+00
276+90
276+80
276+70
276+60
276+50
276+40
276+30
276+20
276+10
9:00
10:00
11:00
12:00
1:00
2:00
3:00
7ft
Crown
7ft
Panning <1gpm
1gpm
<1gpm
1gpm
1gpm
Notes: (letters refer to points on map; describe water inflows, major joints, wedges, bad ground) Teeth always on free side. ⊙=leaking rockbolt
Rock Type Mica Schist and Chlorite Schist
Chlorite schists forms sheared augens.
Groundwater • Zone 1 has approximately 3-4 gpm flowing from intersection of high angle joint and foliation joint
Zone 3 has approximately 4 gpm flowing from rockbolts, and minor drips from foliation joint
• ① Chlorite Schist forms augens within Mica Schist. Dark green and fine grained.
Overall Type A Ground
SCTP TBM CROWN MAP: Map Report: SWD-014 Sta. 277 +10 to 276 +10
Mapped: 8 Oct 09 By

Appendix L: Simulated fracture traces

Tunnel axis direction: 162/0

Tunnel diameter: 27.73 feet

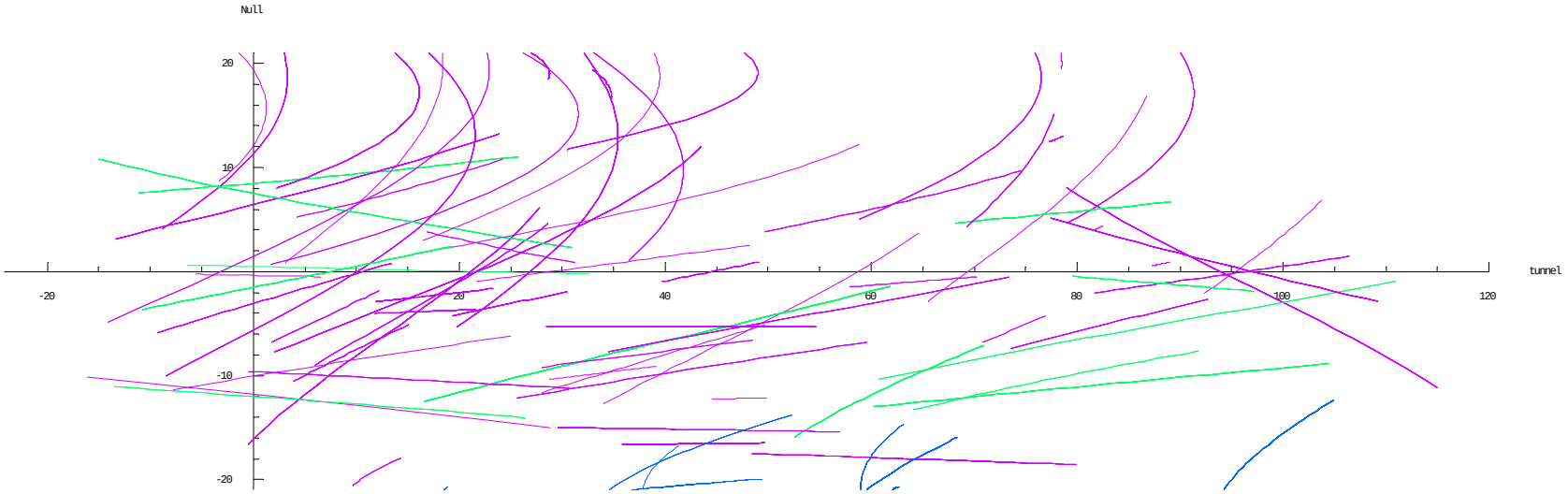

1. Fracture Set 1 (normal to fracture: 84/15, Fisher parameter K: 20.51)

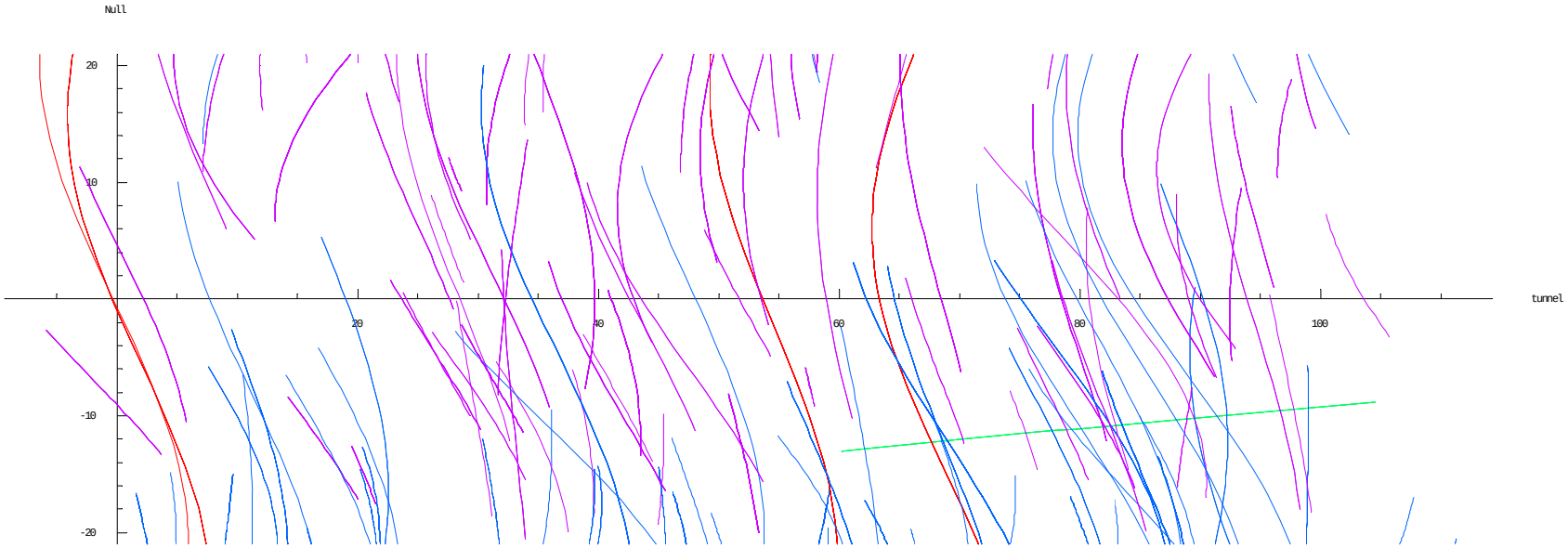

2. Fracture Set 2 (normal to fracture: 2/5, Fisher parameter K: 32.92)

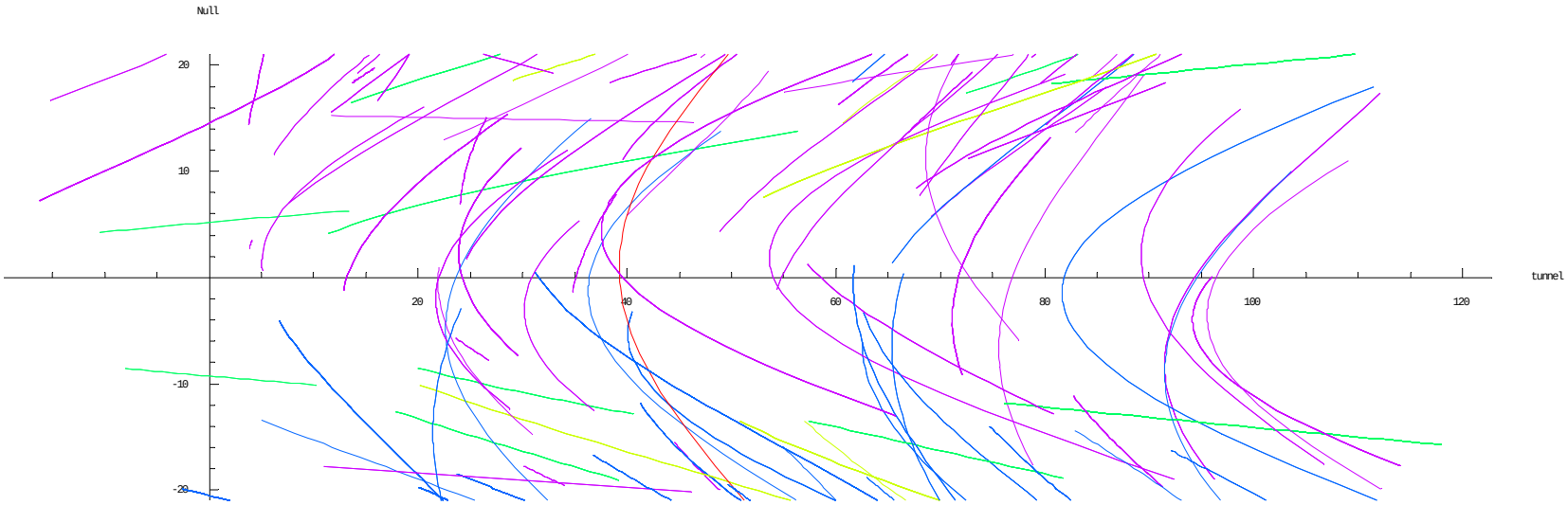

3. Fracture Set 3 (normal to fracture: 335/57, Fisher parameter K: 17.22)

Appendix M: Fracture intensity for South Cobb tunnel

Fracture set 1: X'', Y'' and Z'' units: ft. intensity unit: fractures / 20 ft

Scanline 1					Scanline 2					Scanline 3				
No.	X''	Y''	Z''	Intensity	No.	X''	Y''	Z''	Intensity	No.	X''	Y''	Z''	Intensity
1	-11.89	10.00	-6.42	0	1	3.57	10.00	12.84	0	1	13.08	10.00	0.00	0
2	-11.89	30.00	-6.42	0	2	3.57	30.00	12.84	0	2	13.08	30.00	0.00	0
3	-11.89	50.00	-6.42	0	3	3.57	50.00	12.84	0	3	13.08	50.00	0.00	0
4	-11.89	70.00	-6.42	0	4	3.57	70.00	12.84	0	4	13.08	70.00	0.00	0
5	-11.89	90.00	-6.42	0	5	3.57	90.00	12.84	0	5	13.08	90.00	0.00	0
6	-11.89	110.00	-6.42	0	6	3.57	110.00	12.84	0	6	13.08	110.00	0.00	0
7	-11.89	130.00	-6.42	0	7	3.57	130.00	12.84	0	7	13.08	130.00	0.00	0
8	-11.89	150.00	-6.42	1	8	3.57	150.00	12.84	2	8	13.08	150.00	0.00	0
9	-11.89	170.00	-6.42	0	9	3.57	170.00	12.84	0	9	13.08	170.00	0.00	0
10	-11.89	190.00	-6.42	4	10	3.57	190.00	12.84	1	10	13.08	190.00	0.00	0
11	-11.89	210.00	-6.42	2	11	3.57	210.00	12.84	0	11	13.08	210.00	0.00	0
12	-11.89	230.00	-6.42	2	12	3.57	230.00	12.84	1	12	13.08	230.00	0.00	1
13	-11.89	250.00	-6.42	0	13	3.57	250.00	12.84	0	13	13.08	250.00	0.00	0
14	-11.89	270.00	-6.42	0	14	3.57	270.00	12.84	0	14	13.08	270.00	0.00	0
15	-11.89	290.00	-6.42	0	15	3.57	290.00	12.84	0	15	13.08	290.00	0.00	0
16	-11.89	310.00	-6.42	1	16	3.57	310.00	12.84	0	16	13.08	310.00	0.00	0
17	-11.89	330.00	-6.42	2	17	3.57	330.00	12.84	0	17	13.08	330.00	0.00	0
18	-11.89	350.00	-6.42	1	18	3.57	350.00	12.84	0	18	13.08	350.00	0.00	0
19	-11.89	370.00	-6.42	0	19	3.57	370.00	12.84	0	19	13.08	370.00	0.00	0
20	-11.89	390.00	-6.42	0	20	3.57	390.00	12.84	0	20	13.08	390.00	0.00	0
21	-11.89	410.00	-6.42	0	21	3.57	410.00	12.84	0	21	13.08	410.00	0.00	0
22	-11.89	430.00	-6.42	2	22	3.57	430.00	12.84	0	22	13.08	430.00	0.00	0
23	-11.89	450.00	-6.42	0	23	3.57	450.00	12.84	0	23	13.08	450.00	0.00	0
24	-11.89	470.00	-6.42	0	24	3.57	470.00	12.84	0	24	13.08	470.00	0.00	0
25	-11.89	490.00	-6.42	1	25	3.57	490.00	12.84	0	25	13.08	490.00	0.00	0
26	-11.89	510.00	-6.42	0	26	3.57	510.00	12.84	0	26	13.08	510.00	0.00	0
27	-11.89	530.00	-6.42	0	27	3.57	530.00	12.84	0	27	13.08	530.00	0.00	0
28	-11.89	550.00	-6.42	0	28	3.57	550.00	12.84	0	28	13.08	550.00	0.00	0
29	-11.89	570.00	-6.42	0	29	3.57	570.00	12.84	0	29	13.08	570.00	0.00	0
30	-11.89	590.00	-6.42	0	30	3.57	590.00	12.84	0	30	13.08	590.00	0.00	0
31	-11.89	610.00	-6.42	1	31	3.57	610.00	12.84	1	31	13.08	610.00	0.00	0
32	-11.89	630.00	-6.42	0	32	3.57	630.00	12.84	0	32	13.08	630.00	0.00	0
33	-11.89	650.00	-6.42	0	33	3.57	650.00	12.84	0	33	13.08	650.00	0.00	0
34	-11.89	670.00	-6.42	0	34	3.57	670.00	12.84	0	34	13.08	670.00	0.00	0
35	-11.89	690.00	-6.42	2	35	3.57	690.00	12.84	0	35	13.08	690.00	0.00	0
36	-11.89	710.00	-6.42	0	36	3.57	710.00	12.84	0	36	13.08	710.00	0.00	0
37	-11.89	730.00	-6.42	1	37	3.57	730.00	12.84	0	37	13.08	730.00	0.00	0
38	-11.89	750.00	-6.42	0	38	3.57	750.00	12.84	0	38	13.08	750.00	0.00	0
39	-11.89	770.00	-6.42	0	39	3.57	770.00	12.84	0	39	13.08	770.00	0.00	0
40	-11.89	790.00	-6.42	0	40	3.57	790.00	12.84	0	40	13.08	790.00	0.00	0
41	-11.89	810.00	-6.42	3	41	3.57	810.00	12.84	0	41	13.08	810.00	0.00	0
42	-11.89	830.00	-6.42	2	42	3.57	830.00	12.84	0	42	13.08	830.00	0.00	0
43	-11.89	850.00	-6.42	0	43	3.57	850.00	12.84	0	43	13.08	850.00	0.00	0
44	-11.89	870.00	-6.42	1	44	3.57	870.00	12.84	0	44	13.08	870.00	0.00	0
45	-11.89	890.00	-6.42	0	45	3.57	890.00	12.84	0	45	13.08	890.00	0.00	0
46	-11.89	910.00	-6.42	0	46	3.57	910.00	12.84	0	46	13.08	910.00	0.00	0
47	-11.89	930.00	-6.42	0	47	3.57	930.00	12.84	0	47	13.08	930.00	0.00	0
48	-11.89	950.00	-6.42	0	48	3.57	950.00	12.84	0	48	13.08	950.00	0.00	0
49	-11.89	970.00	-6.42	0	49	3.57	970.00	12.84	0	49	13.08	970.00	0.00	0
50	-11.89	990.00	-6.42	0	50	3.57	990.00	12.84	0	50	13.08	990.00	0.00	0

Fracture set 2: X'', Y'' and Z'' units: ft. intensity unit: fractures / 20 ft

Scanline 1					Scanline 2				
No.	X''	Y''	Z''	Intensity	No.	X''	Y''	Z''	Intensity
1	-8.00	10.00	8.55	0	1	8.00	10.00	8.55	0
2	-8.00	30.00	8.55	0	2	8.00	30.00	8.55	0
3	-8.00	50.00	8.55	0	3	8.00	50.00	8.55	0
4	-8.00	70.00	8.55	0	4	8.00	70.00	8.55	0
5	-8.00	90.00	8.55	0	5	8.00	90.00	8.55	0
6	-8.00	110.00	8.55	0	6	8.00	110.00	8.55	0
7	-8.00	130.00	8.55	0	7	8.00	130.00	8.55	0
8	-8.00	150.00	8.55	0	8	8.00	150.00	8.55	0
9	-8.00	170.00	8.55	0	9	8.00	170.00	8.55	0
10	-8.00	190.00	8.55	0	10	8.00	190.00	8.55	0
11	-8.00	210.00	8.55	0	11	8.00	210.00	8.55	0
12	-8.00	230.00	8.55	0	12	8.00	230.00	8.55	0
13	-8.00	250.00	8.55	0	13	8.00	250.00	8.55	1
14	-8.00	270.00	8.55	1	14	8.00	270.00	8.55	0
15	-8.00	290.00	8.55	0	15	8.00	290.00	8.55	1
16	-8.00	310.00	8.55	0	16	8.00	310.00	8.55	0
17	-8.00	330.00	8.55	0	17	8.00	330.00	8.55	0
18	-8.00	350.00	8.55	0	18	8.00	350.00	8.55	0
19	-8.00	370.00	8.55	0	19	8.00	370.00	8.55	0
20	-8.00	390.00	8.55	0	20	8.00	390.00	8.55	0
21	-8.00	410.00	8.55	1	21	8.00	410.00	8.55	0
22	-8.00	430.00	8.55	0	22	8.00	430.00	8.55	0
23	-8.00	450.00	8.55	1	23	8.00	450.00	8.55	0
24	-8.00	470.00	8.55	1	24	8.00	470.00	8.55	0
25	-8.00	490.00	8.55	1	25	8.00	490.00	8.55	0
26	-8.00	510.00	8.55	0	26	8.00	510.00	8.55	3
27	-8.00	530.00	8.55	0	27	8.00	530.00	8.55	1
28	-8.00	550.00	8.55	2	28	8.00	550.00	8.55	1
29	-8.00	570.00	8.55	1	29	8.00	570.00	8.55	0
30	-8.00	590.00	8.55	2	30	8.00	590.00	8.55	0
31	-8.00	610.00	8.55	0	31	8.00	610.00	8.55	0
32	-8.00	630.00	8.55	2	32	8.00	630.00	8.55	0
33	-8.00	650.00	8.55	0	33	8.00	650.00	8.55	1
34	-8.00	670.00	8.55	0	34	8.00	670.00	8.55	0
35	-8.00	690.00	8.55	4	35	8.00	690.00	8.55	4
36	-8.00	710.00	8.55	0	36	8.00	710.00	8.55	0
37	-8.00	730.00	8.55	1	37	8.00	730.00	8.55	1
38	-8.00	750.00	8.55	1	38	8.00	750.00	8.55	0
39	-8.00	770.00	8.55	2	39	8.00	770.00	8.55	2
40	-8.00	790.00	8.55	1	40	8.00	790.00	8.55	1
41	-8.00	810.00	8.55	0	41	8.00	810.00	8.55	0
42	-8.00	830.00	8.55	0	42	8.00	830.00	8.55	0
43	-8.00	850.00	8.55	0	43	8.00	850.00	8.55	0
44	-8.00	870.00	8.55	0	44	8.00	870.00	8.55	0
45	-8.00	890.00	8.55	1	45	8.00	890.00	8.55	0
46	-8.00	910.00	8.55	1	46	8.00	910.00	8.55	1
47	-8.00	930.00	8.55	2	47	8.00	930.00	8.55	0
48	-8.00	950.00	8.55	1	48	8.00	950.00	8.55	1
49	-8.00	970.00	8.55	1	49	8.00	970.00	8.55	0
50	-8.00	990.00	8.55	0	50	8.00	990.00	8.55	0

Fracture set 3: X'', Y'' and Z'' units: ft. intensity unit: fractures / 20 ft

Scanline 1					Scanline 2				
No.	X''	Y''	Z''	Intensity	No.	X''	Y''	Z''	Intensity
1	-5.96	10.00	-11.03	1	1	-5.96	10.00	11.03	0
2	-5.96	30.00	-11.03	0	2	-5.96	30.00	11.03	0
3	-5.96	50.00	-11.03	1	3	-5.96	50.00	11.03	0
4	-5.96	70.00	-11.03	0	4	-5.96	70.00	11.03	1
5	-5.96	90.00	-11.03	1	5	-5.96	90.00	11.03	0
6	-5.96	110.00	-11.03	1	6	-5.96	110.00	11.03	1
7	-5.96	130.00	-11.03	0	7	-5.96	130.00	11.03	0
8	-5.96	150.00	-11.03	0	8	-5.96	150.00	11.03	0
9	-5.96	170.00	-11.03	1	9	-5.96	170.00	11.03	1
10	-5.96	190.00	-11.03	1	10	-5.96	190.00	11.03	0
11	-5.96	210.00	-11.03	2	11	-5.96	210.00	11.03	0
12	-5.96	230.00	-11.03	3	12	-5.96	230.00	11.03	1
13	-5.96	250.00	-11.03	1	13	-5.96	250.00	11.03	0
14	-5.96	270.00	-11.03	3	14	-5.96	270.00	11.03	0
15	-5.96	290.00	-11.03	0	15	-5.96	290.00	11.03	1
16	-5.96	310.00	-11.03	3	16	-5.96	310.00	11.03	0
17	-5.96	330.00	-11.03	1	17	-5.96	330.00	11.03	3
18	-5.96	350.00	-11.03	1	18	-5.96	350.00	11.03	0
19	-5.96	370.00	-11.03	0	19	-5.96	370.00	11.03	0
20	-5.96	390.00	-11.03	1	20	-5.96	390.00	11.03	0
21	-5.96	410.00	-11.03	0	21	-5.96	410.00	11.03	1
22	-5.96	430.00	-11.03	0	22	-5.96	430.00	11.03	0
23	-5.96	450.00	-11.03	0	23	-5.96	450.00	11.03	0
24	-5.96	470.00	-11.03	1	24	-5.96	470.00	11.03	1
25	-5.96	490.00	-11.03	1	25	-5.96	490.00	11.03	0
26	-5.96	510.00	-11.03	1	26	-5.96	510.00	11.03	0
27	-5.96	530.00	-11.03	2	27	-5.96	530.00	11.03	0
28	-5.96	550.00	-11.03	1	28	-5.96	550.00	11.03	0
29	-5.96	570.00	-11.03	0	29	-5.96	570.00	11.03	0
30	-5.96	590.00	-11.03	0	30	-5.96	590.00	11.03	0
31	-5.96	610.00	-11.03	0	31	-5.96	610.00	11.03	0
32	-5.96	630.00	-11.03	0	32	-5.96	630.00	11.03	0
33	-5.96	650.00	-11.03	0	33	-5.96	650.00	11.03	0
34	-5.96	670.00	-11.03	0	34	-5.96	670.00	11.03	0
35	-5.96	690.00	-11.03	0	35	-5.96	690.00	11.03	0
36	-5.96	710.00	-11.03	0	36	-5.96	710.00	11.03	0
37	-5.96	730.00	-11.03	2	37	-5.96	730.00	11.03	0
38	-5.96	750.00	-11.03	0	38	-5.96	750.00	11.03	0
39	-5.96	770.00	-11.03	0	39	-5.96	770.00	11.03	0
40	-5.96	790.00	-11.03	0	40	-5.96	790.00	11.03	0
41	-5.96	810.00	-11.03	0	41	-5.96	810.00	11.03	0
42	-5.96	830.00	-11.03	1	42	-5.96	830.00	11.03	0
43	-5.96	850.00	-11.03	1	43	-5.96	850.00	11.03	0
44	-5.96	870.00	-11.03	0	44	-5.96	870.00	11.03	0
45	-5.96	890.00	-11.03	0	45	-5.96	890.00	11.03	0
46	-5.96	910.00	-11.03	3	46	-5.96	910.00	11.03	0
47	-5.96	930.00	-11.03	1	47	-5.96	930.00	11.03	0
48	-5.96	950.00	-11.03	0	48	-5.96	950.00	11.03	0
49	-5.96	970.00	-11.03	1	49	-5.96	970.00	11.03	0
50	-5.96	990.00	-11.03	1	50	-5.96	990.00	11.03	0

Appendix N: Flow rates and locations of 20 realizations with spatial correlation

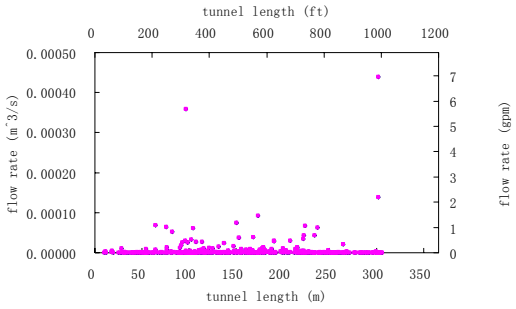

Realization No. 1

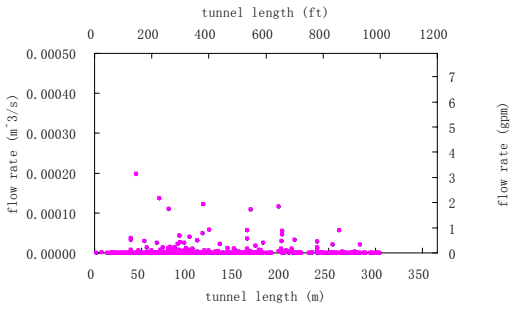

Realization No. 2

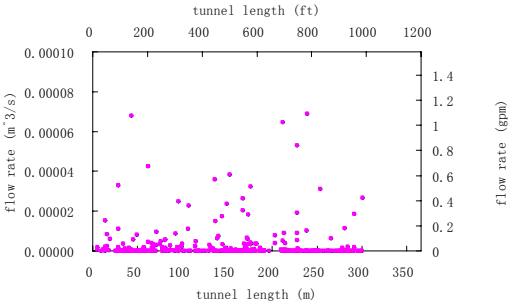

Realization No. 3

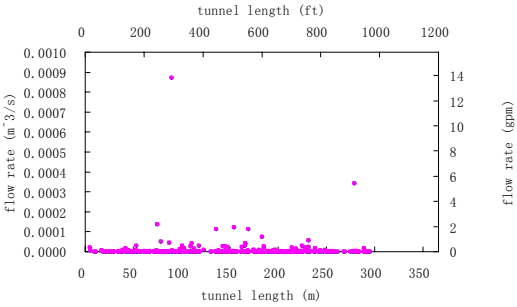

Realization No. 4

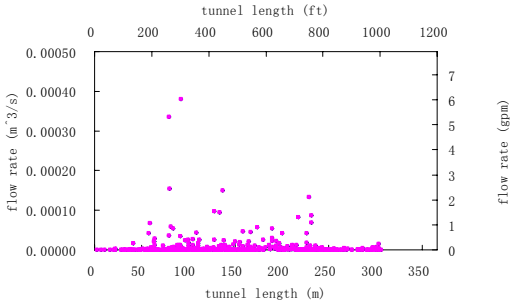

Realization No. 5

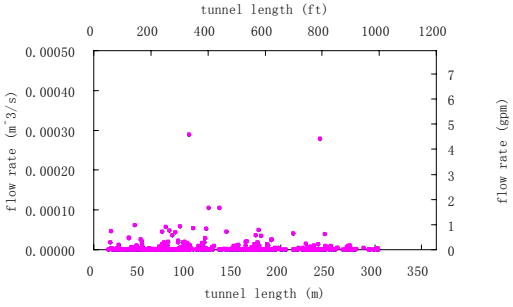

Realization No. 6

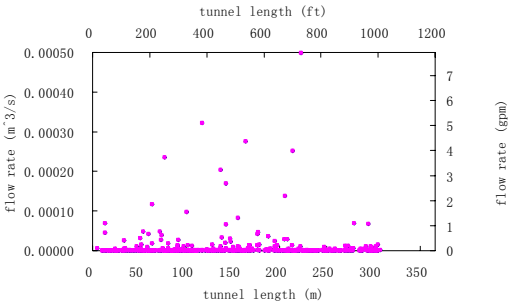

Realization No. 7

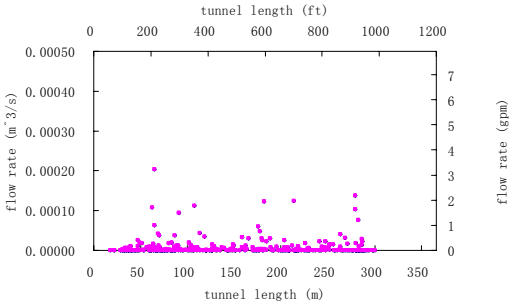

Realization No. 8

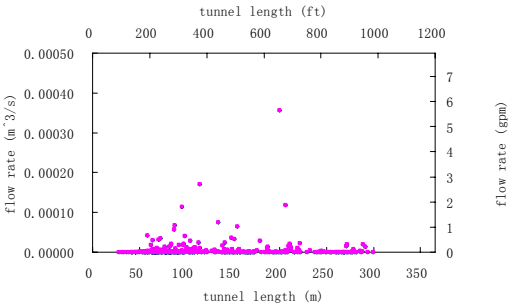

Realization No. 9

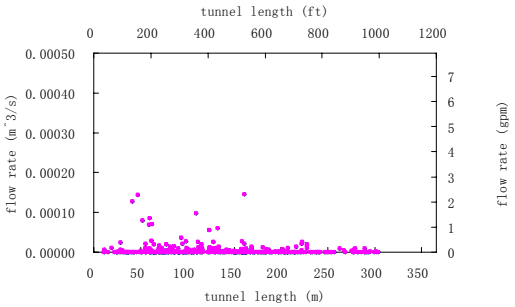

Realization No. 10

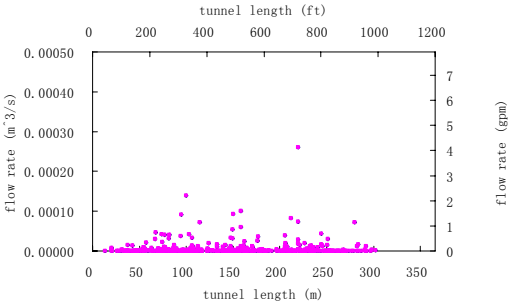

Realization No. 11

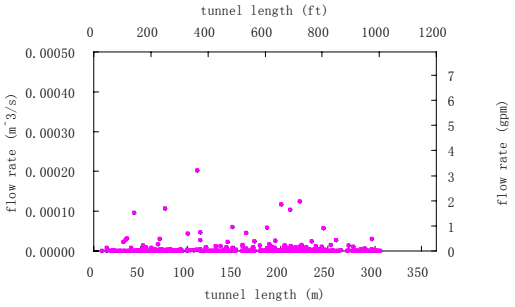

Realization No. 12

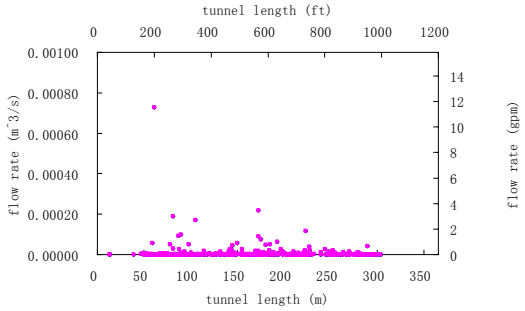

Realization No. 13

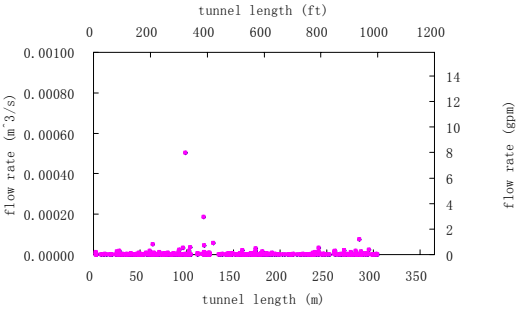

Realization No. 14

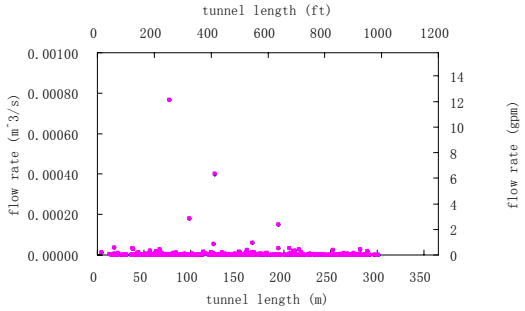

Realization No. 15

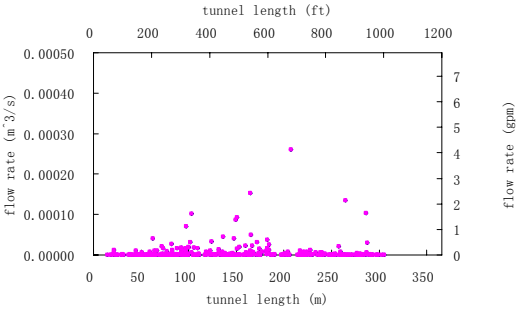

Realization No. 16

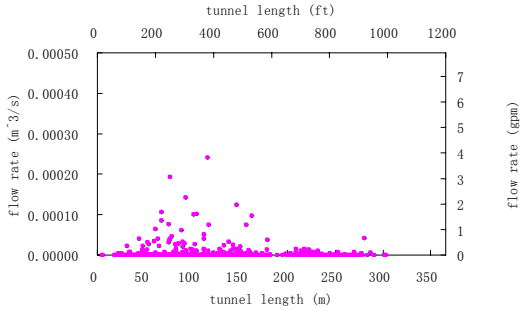

Realization No. 17

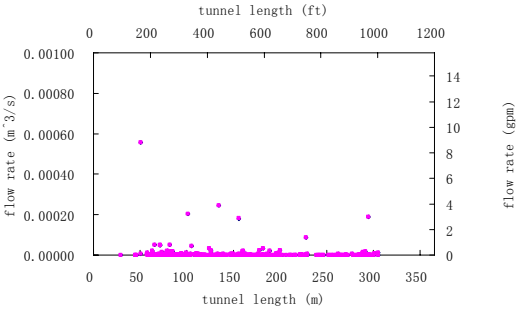

Realization No. 18

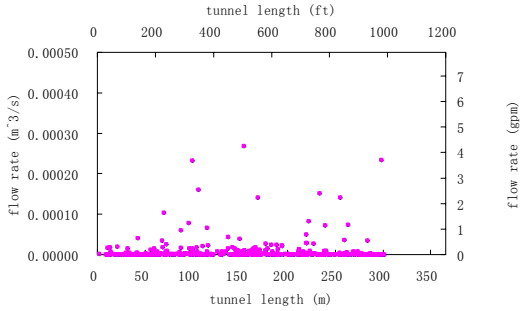

Realization No. 19

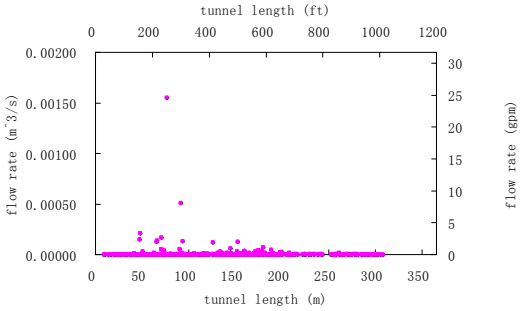

Realization No. 20

Appendix O: Flow rates and locations of 20 realizations without spatial correlation

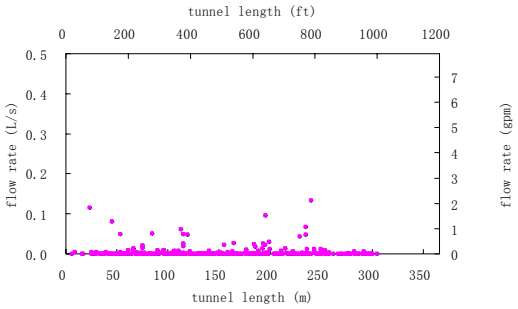

Realization No. 1

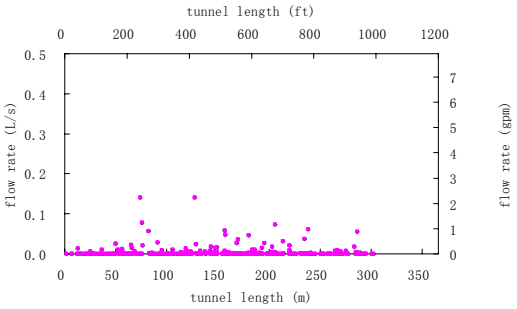

Realization No. 2

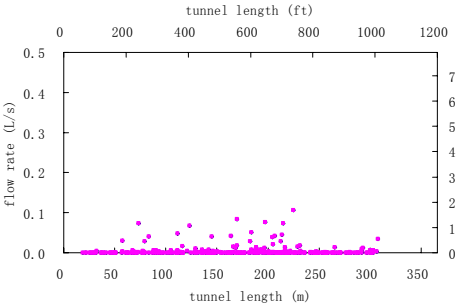

Realization No. 3

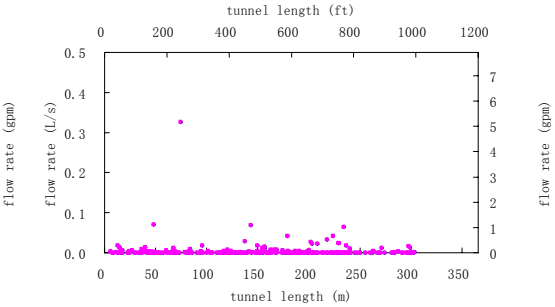

Realization No. 4

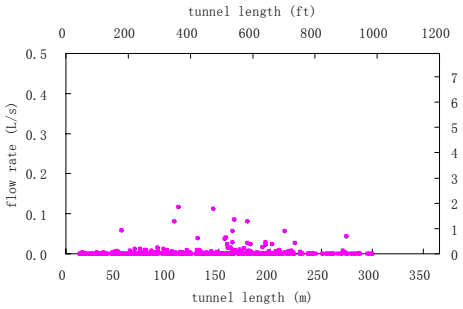

Realization No. 5

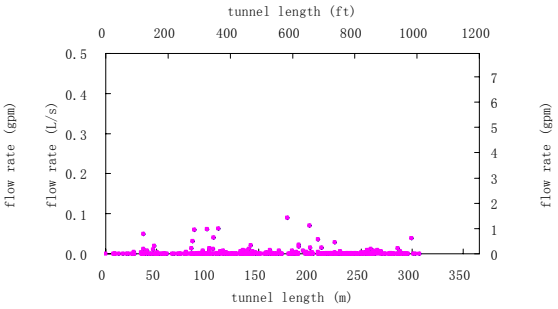

Realization No. 6

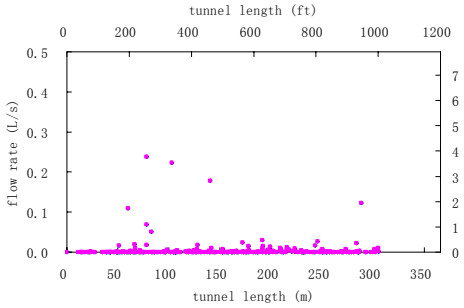

Realization No. 7

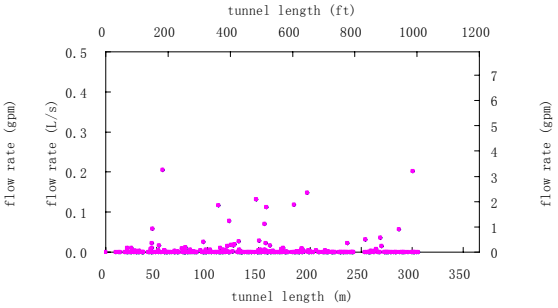

Realization No. 8

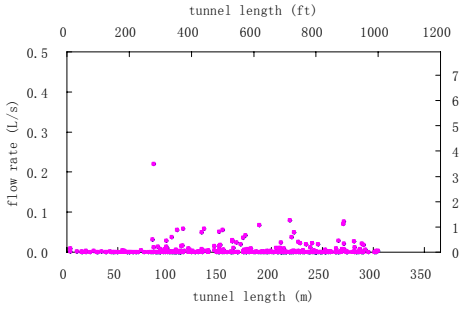

Realization No. 9

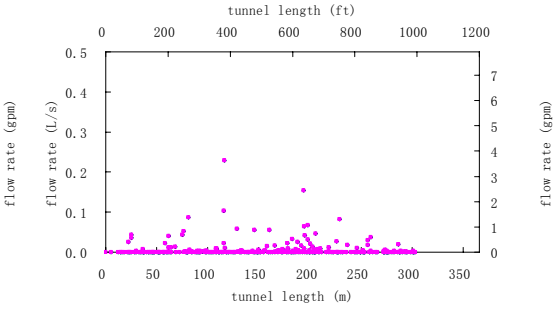

Realization No. 10

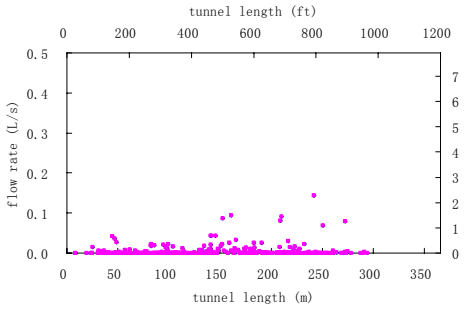

Realization No. 11

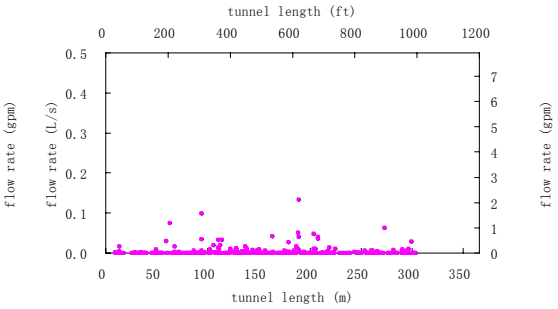

Realization No. 12

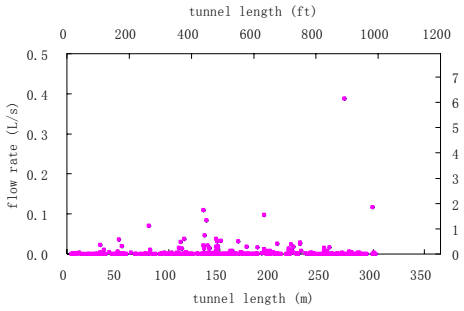

Realization No. 13

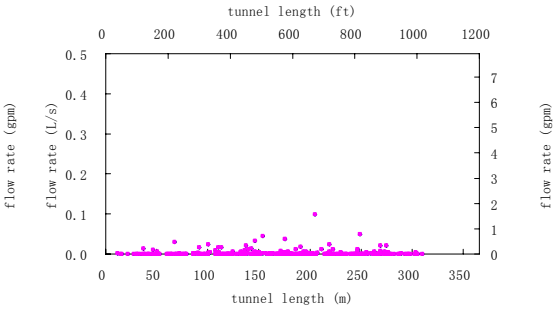

Realization No. 14

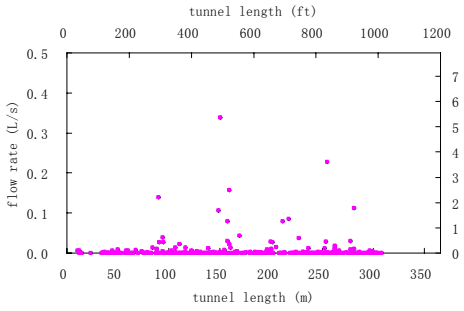

Realization No. 15

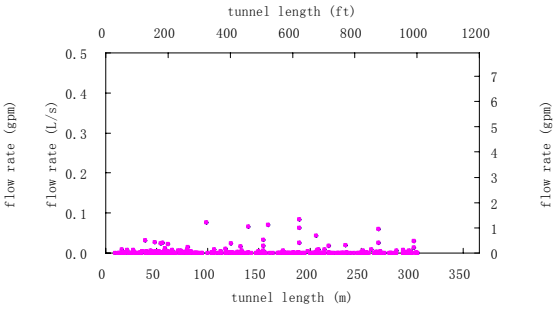

Realization No. 16

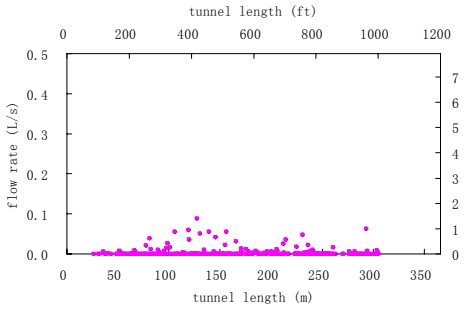

Realization No. 17

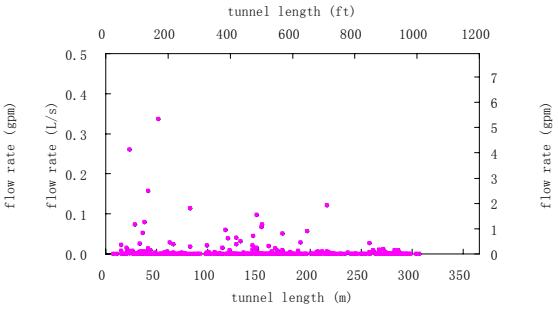

Realization No. 18

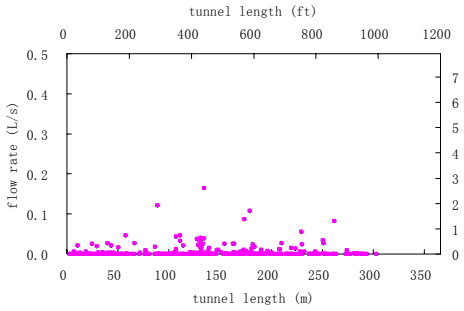

Realization No. 19

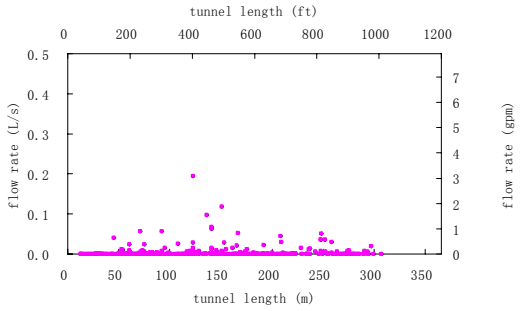

Realization No. 20

REFERENCES

(UTRC), U.T.R.C. (1996). Ground-water Inflow into Tunnels Subcommittee Presentation Handout. In., Los Angeles, California.

Aler, J., Mouza, J.D., and Arnound, M. (1996). Measurement of the fragmentation efficiency of rock mass blasting and its mining applications. *International Journal of Rock Mechanics and Mining Science and Geomechanics Abstracts 33(2)*, 125-140.

Arfken, G.B., and Weber, H.J. (2001). Mathematical methods for physics. Academic Press, San Diego.

Attewell, P.B., and Farmer, I.W. (1976). Principles of Engineering Geology. Chapman and Hall, London.

Baecher, G.B., and Lanney, N.A. (1978). Trace length biases in joint surveys. *Proc. U.S. Symposium on Rock Mechanics, 19th*, pp. 56-65.

Baecher, G.B., Lanney, N.A., and Einstein, H.H. (1977). Statistical description of rock properties and sampling. *Proc. U.S. Symposium on Rock Mechanics, 18th*, pp. 5C1.1-5C1.8.

Barton, C.A., and Larson, E. (1985). Fractal geometry of two-dimensional fracture networks at Yucca Mountain, southwestern Nevada. *Proceedings of International Symposium on Fundamentals of Rock Joints* (Stephansson, O., Ed.). International Society for Rock Mechanics, Lulea, Sweden.

Barton, C.A., and Zoback, M.D. (1992). Self-similar distribution and properties of macroscopic fractures at depth in crystalline rock in the Cajon Pass scientific drill hole. *Journal of Geophysical research 97(B4)*, 5181-5200.

Barton, N.R., Bandis, S.C., and Bakhtar, K. (1985). Strength, deformation, and conductivity coupling of rock joints. *International Journal of Rock Mechanics and Mining Sciences and Geomechanics Abstracts 22(3)*, 121-140.

Bayuk, I.O., and Chesnokov, E.M. (1998). Correlation between elastic and transport properties of porous cracked anisotropic media. *Physics and chemistry of the earth 23*, 361-366.

Belfield, W.C. (1998). Incorporating spatial distribution into stochastic modelling of fractures: multifractals and Lévy-stable statistics. *Journal of Structural Geology 20(4)*, 473-486.

Belfield, W.C., and Sovich, J.P. (1995). Fracture statistics from horizontal wellbores. *The Journal of Canadian Petroleum Technology 34(6)*, 47-50.

Berkowitz, B. (2002). Characterizing flow and transport in fractured geological media: a review. *Advances in Water Resources 25*, 861-884.

Billaux, D., Chiles, J.P., Hestir, K., and Long, J. (1989). Three-dimensional statistical modelling of a fractured rock mass--an example from the Fanay-Augères mine.

International Journal of Rock Mechanics and Mining Science and Geomechanics Abstracts 26(3-4), 281-299.

Bour, O., and Davy, P. (1999). Clustering and size distributions of fault patterns: theory and measurements. *Geophysical Research Letters 26(13)*, 2001-2004.

Caers, J. Direct sequential indicator simulation,

http://pangea.stanford.edu/~jcaers/papers/dsisimSA.pdf (last access May 19, 2010).

Call, R.D., Savely, J.P., and Nicholas, D.E. (1976). Estimation of joint set characteristics form surface mapping data. *Proceedings of 17th US symposium on rock mechanics*, Vol. 2B2, pp. 1-9.

Castaing, C., Halawani, M.A., Gervais, F., Chilès, J.P., Genter, A., Bourgine, B., Ouillon, G., Brosse, J.M., Martin, P., Genna, A., and Janjou, D. (1996). Scaling relationships in intraplate fracture systems related to Red Sea rifting. *Tectonophysics 261*, 291-314.

Cawsey, D.C. (1977). The measurement of fracture patterns in the Chalk of Southern England. *Engineering Geology 11(3)*, 201-215.

Chilès, J.P. (1988). Fractal and geostatistical methods for modeling of a fracture network. *Mathematical Geology 20(6)*, 631-654.

Chiles, J.-P., and Delfiner, P. (1999). Geostatistics : Modeling Spatial Uncertainty. John Wiley and Sons, Inc., New York.

Cladouhos, T.T., and Marrett, R. (1996). Are fault growth and linkage models consistent with power-law distributions of fault lengths? *Journal of Structural Geology 18(2-3)*, 281-293.

Clark, M.B., Brantley, S.L., and Fisher, D.M. (1995). Power-law vein-thickness distributions and positive feedback in vein growth. *Geology 23(11)*, 975-978.

Clark, R.M., and Cox, S.J.D. (1996). A modem regression approach to determining fault displacement-length scaling relationships. *Journal of Structural Geology 18(2/3)*, 147-152.

Clark, R.M., Cox, S.J.D., and Laslett, G.M. (1999). Generalizations of power law distributions applicable to sampled fault-trace lengths: model choice, parameter estimation and caveats. *Geophysical Journal International 136*, 357.

Cowie, P.A., and Scholz, C.H. (1992). Displacement-length scaling relationship for faults: data synthesis and discussion. *Journal of Structural Geology 14(10)*, 1149-1156.

Cravero, M., Piana, F., Ponti, S., Tallone, S., Balestro, G., and M., M. (2006). Analysis of fracture patterns constrained by suitable geological model. In *The 41st U.S. Symposium on Rock Mechanics (USRMS): "50 Years of Rock Mechanics - Landmarks and Future Challenges."* Golden, Colorado.

Cruden, D.M. (1977a). Decribing the size of discontinuities. *International Journal of Rock Mechanics and Mining Science and Geomechanics Abstracts 14*, 133-137.

Cruden, D.M. (1977b). Describing the size of fractures. *International Journal of Rock Mechanics and Mining Science and Geomechanics Abstracts 14(3)*, 133-137.

Davy, P. (1993). On the frequency-length Distribution of the san Andreas Fault system *Journal of Geophysical research 98(B7)*, 12,141-112,151.

Dawers, N.H., Anders, M.H., and Scholz, C.H. (1993). Growth of normal faults. Displacement-length scaling. *Geology 21(12)*, 1107-1110.

Deans, S.R. (1983). The Radon Transform and Some of Its Applications. John Wiley and Sons, New York.

Dershowitz, W.S., and Einstein, H.H. (1988). Characterizing roch joint geometry with joint system models. *Rock Mechanics and Rock Engineering 21*, 21-51.

Deutsch, C.V., and Journel, A.G. (1998). GSLIB Geostatistical Software Library and User's Guide. Oxford University Press, New York.

Dixon, P.M. (2002). Ripley's K function. In *Encyclopedia of Environmetrics*, (El-Shaarawi, A.H., and Piegorsch, W.W., Eds.). John Wiley and Sons, Ltd, Chichester.

Dowd, P.A., Xu, C., Mardia, K.V., and Fowell, R.J. (2007). A Comparison of Methods for the Stochastic Simulation of Rock Fractures. *Mathematical Geology 39*, 697-714.

Duncan, A.C. (1981). A review of Cartesian coordinate construction from a sphere, for generation of two-dimensional geological net projections. *Computers and Geosciences 7(4)*, 367-385.

Einstein, H.H., and Baecher, G.B. (1983). Probabilistic and statistical methods in engineering geology. *Rock Mechanics and Rock Engineering 16*, 39-72.

Einstein, H.H., Baecher, G.B., and Veneziano, D. (1979). Risk analysis for rock slopes in open pit mines. In *Series of reports to U.S. Bureau of Mines. Pub. Nos. R80-17 to R80-22*. Department of Civil Engineering, Massachusetts Institute of Technology, Cambridge.

El Tani, M. (1999). Water inflow into tunnels. *Challenges for the 21st Century (ITA world tunnel congress, proceedings of the world tunnel congress'99)*, (Alten, T., et al., Eds.), pp. 61-70. Taylor and Francis, Oslo, Norway.

Fisher, R. (1953). Dispersion on a sphere. *Proceedings of the Royal Society of London A217*, 295-305.

Gale, J.F.W. (2002). Specifying lengths of horizontal wells in fractured reservoirs. *SPE Reservoir Evaluation and Engineering*, 266-272.

Gale, J.F.W., and Gomez, L.A. (2007). Late opening-mode fractures in karst-brecciated dolostones of the Lower Ordovician Ellenburger Group, west Texas: Recognition, characterization, and implications for fluid flow. *AAPG Bulletin 91(7)*, 1005-1023.

Gale, J.F.W., Laubach, S.E., Marrett, R.A., Olson, J.E., Holder, J., and Reed, R.M. (2004). Predicting and characterizing fractures in dolostone reservoirs: using the link between diagenesis and fracturing. In *The Geometry and Petrogenesis of Dolomite*

Hydrocarbon Reservoirs, (Braithwaite, C.J.R., et al., Eds.), Vol. 235, pp. 177-192. Geological Society, London.

Gale, J.F.W., Laubach, S.E., Olson, J., and Marrett, R. (2005). Using the link between diagenesis and fracturing to accurately predict, characterize, and model fluid-flow in fractured carbonate rocks. In *the 2005 SPE Latin American and Caribbean Petroleum Engineering Conference*. Rio de Janeiro, Brazil.

Gauthier, B.D.M., and Lake, S.D. (1993). Probabilistic modeling of faults below the limit of seismic resolution in Pelican field, North Sea, offshore United Kingdom. *AAPG Bulletin 77(5)*, 761-777.

Gillespie, P.A., Howard, C.B., Walsh, J.J., and Watterson, J. (1993). Measurement and characterization of spatial distributions of fractures. *Tectonophysics 226(1-4)*, 113-141.

Gillespie, P.A., Walsh, J.J., and Watterson, J. (1992). Limitations of dimension and displacement data from single faults and the consequences for data analysis and interpretation. *Journal of Structural Geology 14*, 1157-1172.

Gillespie, P.A., Walsh, J.J.W., J., Bonson, C.G., and Manzocchi, T. (2001). Scaling relationships of joint and vein arrays from The Burren, Co. Clare, Ireland. *Journal of Structural Geology 23(2-3)*, 183-201.

Gomez, L.A., and Laubach, S.E. (2006). Rapid digital quantification of microfracture populations. *Journal of Structural Geology 28(3)*, 408-420.

Gomez, L.A., and Marrett, R. (Manuscript Draft). Traditional Analyses of Fracture Spatial Arrangement. *Journal of Structural Geology*.

Goodman, R.E., Moye, D.G., Schalkwyk, A.V., and I., J. (1965). Ground water inflows during tunnel driving. *Engineering Geology, Bulletin of AEG 2(1)*, 39-56.

Goovaerts, P. (1997). Geostatistics for natural resources evaluation. Oxford University Press, New York.

Gross, M.R. (1993). The origin and spacing of cross joints: Examples from the Monterrey Formation, Santa Barbara coastline, California. *Journal of Structural Geology 15(6)*, 737-737.

Gross, M.R., and Engelder, T. (1995). Strain accommodated by brittle failure in adjacent units of the Monterey Formation, U.S.A.: scale effects and evidence for uniform displacement boundary conditions. *Journal of Structural Geology 17(9)*, 1303-1318.

Gudmundsson, A. (1987a). Geometry, formation and development of tectonic fractures on the Reykjanes Peninsula, southwest Iceland. *Tectonophysics 139*, 295-308.

Guichardet, A. (1972). Conditionally positive definite functions and infinitely divisible positive definite functions. In *Lecture Notes in Mathematics (Symmetric Hilbert Spaces and RelatedTopics)*, (Heidelberg, D.A., and Zürich, B.E., Eds.). Berlin.Heidelberg.New York.

Gupta, A.K., and Adler, P.M. (2006). Stereological Analysis of Fracture Networks along Cylindrical Galleries. *Mathematical Geology 38(3)*, 233-267.

Harris, S.D., McAllister, E., Knight, R.J., and Odling, N.E. (2003). Predicting the three-dimensional population characteristics of fault zones: a study using stochastic models. . *Journal of Structural Geology 25(8)*, 1281-1299.

Hatton, C.G., Main, I.G., and Meredith, P.G. (1993). A comparison of seismic and structural measurements of scaling exponents during tensile subcritical crack growth. *Journal of Structural Geology 15(12)*, 1485-1495.

Hatton, C.G., Main, I.G., and Meredith, P.G. (1994). Non-universal scaling of fracture length and opening displacement. *Nature 367*, 160-162.

Heffer, K.J., and Bevan, T.G. (1990). Scaling Relationships in Natural Fractures-data, Theory and Applications. In *Society of Petroleum Engineers paper SPE 20981, Society of Petroleum Engineers Europec 90 meeting*. The Hague, Holland.

Heuer, R.E. (1995). Estimating rock tunnel water inflow. *1995 RETC Proceedings*, (Williamson, G., and Gowring, I.M., Eds.), pp. 41-60. Random House Trade.

Heuer, R.E. (2005). Estimating rock tunnel water inflow-II. *2005 RETC Proceedings*, (Hutton, J.D., and Rogstad, W.D., Eds.). Society of Mining, Metallurgy, and Exploration, Inc., Seattle, WA.

Huang, Q., and Angelier, J. (1989). Fracture spacing and its relation to bed thickness. *Geological Magazine 126(4)*, 355-362.

Hudson, J.A., and Priest, S.D. (1979). Fracture and rock mass geometry. *International Journal of Rock Mechanics and Mining Science and Geomechanics Abstracts 16*, 339-362.

Hudson, J.A., and Priest, S.D. (1983). Discontinuity frequency in rock mass *International Journal of Rock Mechanics and Mining Science and Geomechanics Abstracts 20*, 73-89.

Huseby, O., Thovert, J.-F., and Adler, P.M. (1997). *Journal of Physics A: Mathematical and General 30(5)*, 1415.

Hwang, J.-H., and Lu, C.-C. (2007). A semi-analytical method for analyzing the tunnel water inflow. *Tunnelling and Underground Space Technology 22(1)*, 39-46.

ISRM. (1978). International society for rock mechanics commission on standardization of laboratory and field tests : Suggested methods for the quantitative description of discontinuities in rock masses. *International Journal of Rock Mechanics and Mining Science and Geomechanics Abstracts 15*, 319-368.

Istok, J. (1989). Groundwater modeling by the Finite Element Method. American Geophysical Union, Washington, DC.

Ivanova, V.M. (1995). Three-dimensional stochastic modeling of rock fracture systems. In *Civil and Environmental Engineering*, Vol. Master of Science, p. 200. Massachusetts Institute of Technology, Cambridge, MA.

Jacob, C.E., and Lohman, S.W. (1952). Nonsteady flow to a well of constant drawdown in an extensive aquifer. *Transactions - American Geophysical Union 33(4)*, 559-569.

Ji, S., and Saruwatari, K. (1998). A revised model for the relationship between joint spacing and layer thickness. *Journal of Structural Geology 20(11)*, 1495-1508.

John, P.H., and Hudson, J.A. (2000). Engineering Rock Mechanics Part2: Illustrative worked examples. Elsevier Science Inc., New York.

Johnston, J.D. (1992). The fractal geometry of veins system: the potential for ore reserve calculation. In *The Irish Minerals Industry 1980-1990--- A Review of the Decade, Galway 1990* (Earls, G.V., et al., Eds.), pp. 105-118. Irish Association for Economic Geology, Dublin.

Johnston, J.D., and McCaffrey, K.J.W. (1996). Fractal geometries of vein systems and the variation of scaling relationships with mechanism. *Journal of Structural Geology 18(2)*, 349-358.

Journel, A.G., and Deutsch, C.V. (1993). Entropy and spatial disorder. *Mathematical Geology 25(3)*, 329-355.

Kakimi, T. (1980). Magnitude-frequency relation for displacement of minor faults and its significance in crustal deformation. *Bulletin of the Geological Survey of Japan 31(10)*, 467-487.

Kawecki, M.W. (2000). Transient flow to a horizontal water well. *Ground water 38(6)*, 842-850.

Kellogg, O.D. (1953). Foundations of Potential Theory. Dover Publications, New York.

Koestler, A.G. (1994). Scaling properties of extensional fault populations - the natural gap at the medium scale. *Geological society of London, Tectonics studies group special meeting*, (Cowie, P.A., et al., Eds.), pp. 21-23. London.

Korvin, G. (1989). Fractured but Not Fractal: Fragmentation of the Gulf of Suez Basement. *Pure and Applied Geophysics 131(1-2)*, 289-305.

Kulatilake, P.H.S.W., Wathugala, D.N., and Stephansson, O. (1993). Joint network modeling with a validation exercise in Stripa Mine, Sweden. *International Journal of Rock Mechanics and Mining Science and Geomechanics Abstracts 30(5)*, 503-526.

Löw, S. (2002). Groundwater hydraulic and environmental impacts of tunnels in crystalline rocks. *Proceedings of the 9th Congress of the International Association for Engineering Geology and the Environment*, (Roy, V., and Jermy, Eds.). Durban, South Africa

La Pointe, P.R. (1980). The Suitability of Sedimentary Rock Masses for Annular Super-conductive Magnetic Energy Storage Units. In, Vol. Ph.D. University of Wisconsin, Madison.

La Pointe, P.R. (1981). Improved numerical modeling of rock masses through geostatistical charaterization. *The 22nd U.S. Symp. Rock Mech.*, (Einstein, H.H., Ed.). Massachusetts Institute of Technology, Cambridge, MA.

La Pointe, P.R. (1993). Pattern Analysis and Simulation of Joints for Rock Engineering. In *Comprehensive Rock Engineering*, (Hudson, J.A., Ed.), Vol. 3, pp. 215-240. Pergamon Press, Oxford.

Laubach, S.E. (1997). A method to detect natural fracture strike in sandstones. *AAPG Bulletin 81(4)*, 604-623.

Laubach, S.E. (2003). Practical approaches to identifying sealed and open fractures. *AAPG Bulletin 87(4)*, 561-579.

Laubach, S.E., and Gale, J.F.W. (2006). Obtaining fracture information for low-permeability (tight) gas sandstones from sidewall cores. *Journal of Petroleum Geology 29(2)*, 147-158.

Laubach, S.E., and Milliken, K.L. (1996). New fracture characterization methods for siliciclastic rocks. *Proceedings 2nd North American Rock Mechanics Symposium*, (Hassani, M.F., and Mitri, H., Eds.), pp. 1209-1213. Balkema.

Laubach, S.E., and Ward, M.E. (2006). Diagenesis in porosity evolution of opening-mode fractures, Middle Triassic to Lower Jurassic La Boca Formation, NE Mexico. *Tectonophysics 419(1-4)*, 75-97.

Lee, H.S., Cho, T.F., and Jeon, S.W. (2001). The Hydraulic Properties of Rough Rock Joint under Shear Loading. *The ISRM Regional Symposium Eurock*, (Sarkka, P., and Eloranta, P., Eds.). A. A. Balkema Publishers, Espoo, Finland.

Lei, S. (1999). An analytical solution for steady flow into a tunnel. *Ground water 37(1)*, 23-26.

Lei, S. (2000). Steady flow into a tunnel with a constant pressure head. *Ground water 38(5)*, 643-644.

Liu, E. (2005). Effects of fracture aperture and roughness on hydraulic and mechanical properties of rocks: implication of seismic characterization of fractured reservoirs. *Journal of Geophysics and Engineering 2*, 38-47.

Long, J.C.S., and Billaux, D.M. (1987). From field data to fracture network modeling: an example incorporating spatial structure. *Water resources research 23(7)*, 120 I -I 122 I 126.

Long, J.C.S., Gillespie, P., and Witherspoon, P.A. (1985). A Model for Steady Fluid Flow in Random Three-Dimensional Networks of Disc-Shaped Fractures. *Water resources research 21(8)*, 1105-1115.

Luke, Y.L. (1962). Integrals of Bessel Function. McGraw-Hill, New York.

Manev, G., and Avramova, E. (1970). On the variation of strength and resistance condition of the rocks in natural rock massif. *Proc. 2nd Cong. Int. Soc. Rock Mech.*, Vol. 3, p. 59~68. Belgrade.

Mardia, K.W. (1972). Statistics of Directional Data. Academic Press, London.

Marrett, R. (1996). Aggregate properties of fracture populations. *Journal of Structural Geology 18(2)*, 169-178.

Marrett, R. (1997). Permeability, porosity, and shear-wave anisotropy from scaling of open fracture populations. In *Fractured Reservoirs: Characterization and Modeling Guidebook*, (Hoak, T.E., et al., Eds.), pp. 217-226. Rocky Mountain Association of Geologists, Denver, Colorado.

Marrett, R., and Allmendinger, R.W. (1991). Estimates of strain due to brittle faulting: sampling of fault population. *Journal of Structural Geology 13(6)*, 735-738.

Marrett, R., and Allmendinger, R.W. (1992). Amount of extension on "small" faults: An example from the Viking graben. *Geology 20(1)*, 47-50.

Marrett, R., Gale, J.F.W., and Gomez, L.A. (2005 Manuscript). Correlation Analyses of Fracture Spatial Arrangement. *Journal of Structural Geology*.

Marrett, R., and Laubach, S.E. (1997). Diagenetic controls on fracture permeability and sealing. *International Journal of Rock Mechanics and Mining Sciences 34(3-4)*, 204.e201-204.e211.

Marrett, R., Ortega, O.J., and Kelsey, C.M. (1999). Extent of power-law scaling for natural fractures in rock. *Geology 27(9)*, 799-802.

Mauldon, M., and Dershowitz, W. (2000). A multi-dimensional system of fracture abundance measures. *Abstracts with programs - Geological Society of America 32(7)*, A474.

Mauldon, M., Dunne, W.M., and Rohrbaugh Jr., M.B. (2001). Circular scanlines and circular windows: New tools for characterizing the geometry of fracture traces. *Journal of Structural Geology 23*, 247-258.

Mauldon, M., and Mauldon, J.G. (1997). Fracture Sampling on a Cylinder: From Scanlines to Boreholes and Tunnels. *Rock Mechanics and Rock Engineering 30(3)*, 129-144.

McCaffrey, K.J.W., Johnston, J.D., and Loriga, M.A. (1994). Variation of fractal dimension in vein systems. *Geological society of London, Tectonics studies group special meeting*, (Cowie, P.A., et al., Eds.), pp. 103-105. London.

Miller, S.M. (1979). Geostatistical analysis for evaluating spatial dependence in fracture set characteristics. *Proceedings of the 16th International Symposium on Applications of Computers and Operational Research in the Mineral Industry, SME-AIME*, pp. 537-545. New York.

Murdoch, L.C., and Franco, J. (1994). The analysis of constant drawdown well using instantaneous source function. *Water resources research 30(1)*, 117-124.

Narr, W. (1996). Estimating average fracture spacing in subsurface rock. *AAPG Bulletin 80(10)*, 1565-1586.

Narr, W., and Suppe, J. (1991). Joint spacing in sedimentary rocks. *Journal of Structural Geology 13(9)*, 1037-1048.

Oda, M. (1985). Permeability Tensor for Discontinuous Rock Masses. *Geotechnique 35*, 483.

Odling, N.E. (1997). Scaling and connectivity of joint systems in sandstones from western Norway. *Journal of Structural Geology 19(10)*, 1257-1271.

Odling, N.E., Gillespie, P., Nourgine, B., Castaing, C., Chiles, J.-P., Christensen, N.P., Fillion, E., Genter, A., Olsen, C., Thrane, L., Trice, R., Aarseth, E., Walsh, J.J., and Watterson, J. (1999). Variations in fracture system geometry and their implications for fluid flow in fractured hydrocarbon reservoirs. *Petroleum Geoscience 5(4)*, 373-384.

Olson, J.E. (1993). Joint pattern development, effects of subcritical crack growth and mechanical crack interaction. . *Journal of Geophysical research 98*, 12251-12265.

Ortega, O., and Marrett, R. (2000). Prediction of macrofracture properties using microfracture information, Mesaverde Group sandstones, San Juan basin, New Mexico. *Journal of Structural Geology 22(5)*, 571-588.

Ortega, O.J. (1997). Prediction of Macrofracture properties using microfracture information, Mesaverde Group sandstone, San Juan Basin, New Mexico. In *Jackson School of Geosciences*, Vol. Master, p. 250. The University of Texas at Austin, Austin.

Ortega, O.J., Marrett, R.A., and Laubach, S.E. (2006). A scale-independent approach to fracture intensity and average spacing measurement. *AAPG Bulletin 90(2)*, 193-208.

Perrochet, P. (2005a). A simple solution to tunnel or well discharge under constant drawdown. *Hydrogeology Journal 13(5-6)*, 886-888.

Perrochet, P. (2005b). Confined flow into a tunnel during progressive drilling: an analytical solution. *Ground water 43(6)*, 943-946.

Perrochet, P., and Dematteis, A. (2007). Modeling transient discharge into a tunnel drilled in a heterogeneous formation. *Ground water 45(6)*, 786-790.

Perrochet, P., and Musy, A. (1992). A simple formula to calculate the width of hydrological buffer zones between drained agricultural plot and neture reserve areas. *Irrigation and Drainage Systems 6(1)*, 69-81.

Phillips, F.C. (1971). The Use of Stereographic Projection in Structural Geology. Edward Arnold, London.

Pollard, D.D., and Aydin, A. (1988). Progress in understanding jointing over the past century. *Geological Society of America Bulletin 100*, 1181-1204.

Polubarinova-Kochina, P.Y. (1962). Theory of groundwater movement. Princeton University Press, Princeton, N.J.

Price, N.J. (1966). Fault and Joint Development in Brittle and Semi-Brittle Rock. Pergamon, Oxford.

Priest, S.D. (1993). Discontinuity Analysis for Rock Engineering. Chapman and Hall, London.

Priest, S.D., and Hudson, J.A. (1976). Discontinuity spacings in rock. *International Journal of Rock Mechanics and Mining Science and Geomechanics Abstracts 13(5)*, 135-148.

Priest, S.D., and Hudson, J.A. (1981). Estimation of discontinuity spacing and trace length using scanline surveys. *International Journal of Rock Mechanics and Mining Science and Geomechanics Abstracts 18*, 183-197.

Ragan, D.M. (1985). Structural Geology, an Introduction to Geometrical Techniques. Wiley, Chichester.

Rasolofosaon, P.N.J., and Zinszner, B.E. (2002). Comparison between permeability anisotropy and elastic anisotropy of reservoir rocks. *Geophysics 67*, 230-240.

Raymer, J.H. (2005). Groundwater inflow into hard rock tunnels: a new look at inflow equations. *2005 RETC Proceedings*, (Hutton, J.D., and Rogstad, W.D., Eds.). Society of Mining, Metallurgy, and Exploration, Inc., Seattle, WA.

Renard, P. (2005). Approximate discharge for constant head test with recharging boundary. *Ground water 43(3)*, 439-442.

Renshaw, C.E. (1995). On the relationship between mechanical and hydraulic apertures in rough-walled fractures. *Journal of Geophysical research 100*, 24629-24636.

Ries, H. (1915). Engineering geology. Chapman and Hall, London.

Rives, T., Razack, M., Petit, J.-P., and Rawnsley, K.D. (1992). Joint spacing: analogue and numerical simulations. *Journal of Structural Geology 14(8-9)*, 925-937.

Robertson, A. (1970). The interpretation of geologic factors for use in slope theory. *Proceeding of the symposium on the theoretical background to the planning of open pit mines*, pp. 55-71. South Africa, Johannersbury.

Robinson, P.C. (1983). Connectivity of fracture systems - a percolation theory approach. *Journal of Physics A: Mathematical and General 16*, 605-614.

Rouai, M. (2006). Application of fractal geometry to 2D fracture networks in the Middle Atlas aquifer (Morocco). In *the 9th AGILE Conference on Geographic Information Science*. Visegrád, Hungary.

Rouleau, A., and Gale, J.E. (1985). Statistical characterization of the fracture system in the Stripa granite, Sweden. *International Journal of Rock Mechanics and Mining Science and Geomechanics Abstracts 22(6)*, 353-367.

Sanderson, D.J., Roberts, S., and Gumiel, P. (1994). A fractal relationship between vein thickness and gold grade in drill core from La Codosera, Spain. *Economic Geology 89(1)*, 168-173.

Santalo, L.A. (1976). Integral Geometry and Geometric Probability. Addison-Wesley Publishing Co., Reading, MA.

Scholz, C.H., and Cowie, P.A. (1990). Determination of total strain from faulting using slip measurements. *Nature 346*, 837-839.

Shaw, H.R., and Gartner, A.E. (1986). On the Graphical Interpretation of Paleoseismic Data. In *U.S. Geological Survey Open-file Report 86-394*.

Simpson, G.D.H. (2000). Synmetamorphic vein spacing distributions: characterisation and origin of a distribution of veins from NW Sardinia, Italy. *Journal of Structural Geology 22(3)*, 335-348.

Smith, L.P. (1937). Heat Flow in an Infinite Solid Bounded Internally by a Cylinder. In, Vol. 8, pp. 441-448. AIP.

Sneddon, I.N. (1976). Encyclopaedic Dictionary of Mathematics for Engineer and Applied Scientists. Pergamon Press, New York.

Snow, D.T. (1968). Rock fracture spacings, openings, and porosities. *ASCE Journal of Soil Mechanics and Foundations Div 94(SM 1)*, 73-91.

Snow, D.T. (1969). Anisotropic permeability of fractured media. *Water resources research 5*, 1273-1289.

Strack, O.D.L. (1989). Groundwater mechanics. Prentice-Hall Inc, Englewood, New Jersey.

Terzaghi, R.D. (1965). Sources of error in joint surveys. *Geotechnique 15*, 287-304.

Thiem, G. (1906). Hydrologische Methoden. Leipzig, Germany.

Tonon, F., and Chen, S. (2007). Closed-form and numerical solutions for the probability distribution function of fracture diameters. *International Journal of Rock Mechanics and Mining Sciences 44(3)*, 332-350.

Twiss, R.J., and Moores, E.M. (1992). Structural Geology. New York: W. H. Freeman, New York.

Vermilye, J.M., and Scholz, C.H. (1995). Relation between vein length and aperture. *Journal of Structural Geology 17(3)*, 423-434.

Walsh, J.J., and Watterson, J. (1988). Analysis of the relationship between displacements and dimensions of faults. *Journal of Structural Geology 10*, 239-247.

Walsh, J.J., Watterson, J., and Yielding, G. (1991). The importance of small-scale faulting in regional extension. *Nature 351*, 391-393.

Wang, H.F., and Anderson, M.P. (1982). Introduction to Groundwater modeling : Finite Difference and Finite Element Methods. W. H. Freeman and company, New York.

Warburton, P.M. (1980a). A stereological interpretation of joint trace data. *International Journal of Rock Mechanics and Mining Science and Geomechanics Abstracts 17(4)*, 181-190.

Warburton, P.M. (1980b). Stereological interpretation of joint trace data: influence of joint shape and implications for geological surveys. *International Journal of Rock Mechanics and Mining Science and Geomechanics Abstracts 17(6)*, 305-316.

Watterson, J., Walsh, J.J., Gillespie, P.A., and Easton, S. (1996). Scaling systematics of fault sizes on a large-scale range fault map. *Journal of Structural Geology 18(2/3)*, 199-214.

Williams, C.K.I. (1998). Prediction with Gaussian processes: From linear regression to linear prediction and beyond. In *Learning in graphical models*, (Jordan, M.I., Ed.), pp. 599-612. MIT Press.

Wong, T.-F., Fredrich, J.T., and Gwanmesia, G.D. (1989). Crack Aperture statistics and pore space fractal geometry of westerly granite and rutland quartzite: implications for elastic contact model of rock compressibility *Journal of Geophysical research 94(B8)*, 10,267-210,278.

Xu, C., and Dowd, P.A. (2010). A new computer code for discrete fracture network modelling. *Computers and Geosciences 36*, 292-301.

Xue, Y.Q. (1986). The principle of groundwater dynamics (in Chinese). Chinese Geological Publishing House, Peking, China.

Yielding, G., Needham, T., and Jones, H. (1996). Sampling of fault populations using sub-surface data: a review. *Journal of Structural Geology 18(2/3)*, 135-146.

Yielding, G., Walsh, J., and Watterson, J. (1992). The prediction of small-scale faulting in reservoir. *First Break 10(12)*, 449-460.

Zhang, L., and Franklin, J.A. (1993). Prediction of water flow into rock tunnels: an analytical solution assuming an hydraulic conductivity gradient. *International Journal of Rock Mechanics and Mining Sciences and Geomechanics Abstracts 30(1)*, 37-46.

VITA

Ran Chen attended Hai'an High School in Jiangsu, China. In 1996 he entered Tongji University in Shanghai, China. He received the degree of Bachelor in Civil Engineering from Tongji University in July 2000 and the degree of Master in Geotechnical Engineering from Tongji University in March 2003. During the following years he was employed as a design engineer at Shanghai Tunnel Engineering Design and Research Institute (STEDI) in Shanghai, China. In September, 2007, he entered the Graduate School at The University of Texas at Austin.

Permanent contact: ranchen2010@gmail.com

This manuscript was typed by Ran Chen.